UNIVERSAL OPERATIONS ON PROTECTED QUBITS

Doctoral thesis submitted to the faculty for

Mathematics, Computer Science and Physics

In partial fulfillment of the requirements for the degree of

Doctor of philosophy
(Physics)

Carried out at the Institute for Experimental Physics under supervision of o.Univ.-Prof. Dr. Rainer Blatt

Lukas Postler

2024

ABSTRACT

The realm of quantum mechanics exhibits phenomena, such as superposition or entanglement, that we do not encounter in our daily lives interacting with a macroscopic world. In the field of quantum information processing those unique quantum features are leveraged to solve problems that are intractable with classical computers. Over the last decades, algorithms exploiting the particularities of quantum mechanics were developed that outperform their classical counterparts in tasks like searching unstructured data or function classification. Among the most prominent applications of quantum computing is finding the prime factors of an integer. In 1994, Peter Shor proposed a quantum factorization algorithm providing a superpolynomial speedup compared to the best classical algorithm. The task of prime factorization attracts great attention as the widespread Rivest–Shamir–Adleman (RSA) encryption protocol for secure communication relies on its intractability. Applying Shor's algorithm to factorization problems used in state-of-the-art RSA encryption requires implementing billions of gate operations on thousands to millions of quantum bits, referred to as *qubits*.

The susceptibility to noise inherent in quantum computers renders the implementation of protocols actively correcting errors during a computation indispensable in large-scale applications such as factorization. The redundancy required to protect qubits against noise is achieved by distributing the information content of a single qubit to multiple qubits, forming a so-called *logical qubit*. In order to ensure that quantum error correction can suppress noise it is inevitable that errors do not spread uncontrollably when one acts on logical qubits. Protocols respecting this requirement are referred to as *fault-tolerant*.

This thesis discusses the implementation and characterization of fault-tolerant quantum error correction building blocks. A trapped-ion quantum processor hosting up to 16 qubits encoded in $^{40}\mathrm{Ca}^{+}$ ions is used to encode up to two logical qubits. Steane-type quantum error correction relying on logical auxiliary qubits is experimentally investigated and found to be beneficial compared to more commonly implemented protocols using bare auxiliary qubits. Moreover, the manipulation of encoded quantum information is demonstrated by applying gate operations to logical qubits. Although fault-tolerant protocols to manipulate logical qubits require an increased overhead compared to their non-fault-tolerant analogs, an improved performance of the fault-tolerantly implemented gate operations is observed in the experiment. Furthermore, the impact of crosstalk in quantum operations on quantum error correction protocols is studied. At noise levels currently present in the experimental setup, crosstalk is not limiting the performance of error correction procedures. However, crosstalk has to be taken into account if noise levels are decreased by future hardware improvements. Lastly, the trapped-ion quantum processor is used as a testbed for a method of quantifying spatial correlations in quantum dynamics. Comprehending the characteristics of spatial correlations in noise dynamics present in quantum computing hardware is crucial in assessing the performance of error correction procedures.

KURZFASSUNG

Werden physikalische Systeme auf kleinsten Skalen betrachtet, können Erscheinungen beobachtet werden, denen wir in unserem alltäglichen Leben nicht begegnen. Diese Phänomene, wie Superposition und Verschränkung, können im Rahmen der klassischen Physik nicht beschrieben werden, sondern erfordern eine quantenmechanische Beschreibung. In der Quanteninformationsverarbeitung werden diese Phänomene genutzt, um Problemstellungen zu lösen, die mit den Mitteln der klassischen Informationsverarbeitung nur schwer lösbar sind. Die Behandlung derartiger Probleme mit klassischen Rechnern erfordert Ressourcen, wie Speichergröße oder Rechenleistung, welche exponentiell mit der Problemgröße wachsen. In den letzten Jahrzehnten wurden Quantenalgorithmen entwickelt, deren Ressourcenbedarf im Vergleich zu klassischen Algorithmen mit der Problemgröße deutlich langsamer wächst. Einer der bedeutendsten Quantenalgorithmen ist der Faktorisierungsalgorithmus von Shor. Er erlaubt, Primfaktoren einer Zahl zu finden, wobei der Ressourcenbedarf mit zunehmender Länge der Zahl im Vergleich zum besten bekannten klassischen Algorithmus superpolynomiell langsamer wächst. Effiziente Algorithmen zur Primfaktorenzerlegung stoßen auf reges Interesse, da das weitverbreitete Rivest–Shamir–Adleman (RSA)-Verschlüsselungsverfahren darauf basiert, dass klassische Computer Primfaktoren einer ausreichend großen Zahl nicht auf brauchbaren Zeitskalen ermitteln können. Ein leistungsstarker Quantenrechner würde somit die Dechiffrierung verschlüsselter Daten ermöglichen.

Typische Schlüsselängen zur RSA-Verschlüsselung liegen zwischen 1024 und 4096 bits. Um mit dem Shor-Algorithmus Zahlen dieser Länge zu zerlegen, wird ein Quantencomputer mit Tausenden von Qubits, den Analoga zu klassischen Bits, benötigt. Auf diesen Qubits müssen Milliarden von quantenmechanischen Rechenoperationen, auch Gatteroperationen genannt, durchgeführt werden. Quantencomputer sind intrinsisch anfällig für externe Störquellen, sodass die in Qubits gespeicherte Information während einer Berechnung korrumpiert werden kann. Daher werden Protokolle zur aktiven Unterdrückung von Fehlern in Quantencomputern notwendig sein, um Probleme wie die Primfaktorenzerlegung großer Zahlen lösen zu können. Dazu wird die gespeicherte Quanteninformation auf mehrere Qubits aufgeteilt, sodass eine Wiederherstellung der Quanteninformation möglich ist, auch wenn einzelne Qubits korrumpiert sind. Die Gesamtheit der physikalischen Qubits, die den Informationsgehalt eines Qubits tragen, wird *logisches Qubit* genannt. Sind zu viele Qubits fehlerbehaftet, lässt sich die gespeicherte Information nicht wiederherstellen. Deshalb ist es wichtig, dass sich Fehler während der Manipulation logischer Qubits nicht auf weitere physikalische Qubits ausbreiten können. Protokolle, die eine Ausbreitung von Fehlern verhindern, werden als *fehlertolerant* bezeichnet.

In dieser Arbeit werden die experimentelle Realisierung und Charakterisierung grundlegender Bausteine für fehlertolerante Quanteninformationsverarbeitung demonstriert. Dazu werden in einem Ionenfallenquantencomputer bis zu zwei logische Qubits kodiert. Eines der beiden logischen Qubits agiert als Hilfsqubit und wird dazu verwendet, wiederholt Fehler auf dem anderen logischen Qubit zu detektieren und in Folge zu korrigieren. Im Vergleich zu einem verbreiteten Protokoll, welches auf *physikalischen* Hilfsqubits basiert, werden

niedrigere Fehlerraten auf dem zu korrigierenden logischen Qubit beobachtet. Weiters werden fehlertolerante Gatteroperationen auf den logischen Qubits realisiert und mit nicht fehlertoleranten Operationen verglichen. Dabei zeigt sich, dass die logische Fehlerrate bei der fehlertoleranten Implementierung niedriger ist, obwohl mehr fehlerbehaftete physikalische Qubits und Gatteroperationen benötigt werden.

Fehlerbehaftete Gatteroperationen können nicht nur auf den manipulierten physikalischen Qubits Fehler erzeugen, sondern auch auf benachbarte Qubits übersprechen. Es wird gezeigt, dass bei aktuellen Gatterfehlerraten Übersprechfehler keinen bedeutenden Beitrag zur logischen Fehlerrate leisten. Werden die Gatterfehlerraten allerdings durch experimentelle Verbesserungen gesenkt, so können Übersprechfehler durchaus relevant werden. An die Übersprechfehler angepasste Fehlerkorrekturprotokolle können in diesem Fall deutliche Verbesserungen der logischen Fehlerrate bringen. Abschließend wird ein Protokoll zur Quantifizierung räumlicher Korrelationen in Quantenprozessen auf verschiedene Fehlerprozesse des Ionenfallenquantencomputers angewendet. Wie Übersprechfehler können auch räumliche Korrelationen von Fehlerprozessen großen Einfluss auf Fehlerkorrekturprotokolle haben. Damit ist die Kenntnis über räumliche Korrelation in Fehlerprozessen eines Quantencomputers notwendig, um Fehlerkorrekturprotokolle entsprechend zu konzipieren.

DANKSAGUNG

An dieser Stelle möchte ich die Gelegenheit nutzen, mich bei den vielen Menschen zu bedanken, ohne die diese Arbeit nicht zustande gekommen wäre. Leider ist es nicht möglich, alle Menschen, die zu dieser Arbeit beigetragen haben, hier aufzulisten. Daher ein großes Dankeschön an alle, die in den folgenden Zeilen nicht namentlich genannt werden.

Zu Beginn möchte ich meiner Familie dafür danken, dass sie mich, auch abgesehen von diesem Studium, bei allen meinen Vorhaben unterstützt hat. Ich bin sehr dankbar dafür, dass ihr mir ermöglicht habt, meinen Weg im Leben zu gehen. Danke, Mama, Papa und Johannes. Ich möchte auch meiner Freundin Lisa danken. Wenn ich mit Sorgen von der Arbeit nach Hause gekommen bin, wusste ich, dass du da bist und mich unterstützt und aufbaust. Aber auch die Erfolge hast du stets gebührend mit mir gefeiert. Vielen Dank!

Ich möchte Rainer Blatt dafür danken, dass er mir die Möglichkeit gegeben hat, mein Doktoratsstudium in dieser Forschungsgruppe zu absolvieren. Du hast ein großartiges Umfeld geschaffen, um Wissen zu schaffen. Egal welche Frage, eine Antwort war immer nur wenige Schritte entfernt. Ich danke auch Martin, Philipp und Thomas, die ihren enormen Erfahrungsschatz mit mir geteilt haben. Speziell Philipp hat maßgeblich dazu beigetragen, die Ergebnisse in dieser Arbeit in eine publizierbare Form zu gießen.

Danke auch an meine Kollegen von LinTrap und Aqtion. Es hat immer unglaubliche Freude bereitet, mit euch zusammenzuarbeiten. Ich durfte sehr viel von euch lernen und der dunkle Laboralltag wurde durch euch aufgehellt. Es war schön, mit euch Erfolge und Durchbrüche im Labor zu erleben, aber auch wenn es nicht nach Plan lief, wart ihr immer da. Danke, Axel, Roman, Mike, Claire, Vanya, Christian, Thomas und Milena! Wissenschaft ist nur durch Zusammenarbeit möglich. Darum möchte ich auch allen Menschen außerhalb des Instituts danken, mit denen ich über die Jahre hinweg zusammengearbeitet habe. Spezieller Dank geht an Markus Müller und seine Arbeitsgruppe, mit der eine besonders intensive Kollaboration bestand. Vielen Dank, Friederike, Manuel und Sascha, für die großartige und erfolgreiche Zusammenarbeit.

Auch allen nichtwissenschaftlichen Mitarbeiterinnen und Mitarbeitern möchte ich herzlich danken. Danke Patricia, Renate und Verena, dass ihr mich bei allen bürokratischen Angelegenheiten stets unterstützt habt und jegliches Problem meist in kürzester Zeit zur Seite geschafft habt. Danke auch an Wolfgang und Kilian bzw. Armin und Christoph von der elektronischen und mechanischen Werkstatt für die tatkräftige Unterstützung.

Natürlich dürfen die Tarockierer Arne, Axel, Klemens, Marian und Martin in dieser Danksagung keinesfalls unerwähnt bleiben. Die Mittagspause wurde durch das Kartendreschen manchmal ein bisschen in die Länge gezogen, aber es war jede Sekunde davon wert. Danke auch an den leider viel zu selten stattgefundenen Stammtisch. Ich hoffe, ich darf auch in Zukunft noch auf ein Bier zu euch stoßen, Alex, Bassem, Lorenz, Marco, Marco und Mike. Zu guter Letzt möchte ich auch all meinen Freunden außerhalb der Universität danken. Danke, dass ihr immer für mich da wart. Ihr habt mir geholfen, einen klaren Kopf zu bewahren, wenn die Quantenphysik versucht hat, mir den Verstand zu rauben. Danke für viele schöne Stunden auf dem Fahrrad, im Schnee, in Bars oder auf Reisen.

CONTENTS

LIST OF FIGURES

LIST OF TABLES

ACRONYMS

AOD	acousto-optic deflector
AOM	acousto-optic modulator
APD	avalanche photodiode
CNOT	controlled-NOT
CSS	Calderbank-Shor-Steane
CTR	crosstalk-resistant
COM	center-of-mass
DD	dynamical decoupling
DFS	decoherence free subspace
EC	error correction
EMCCD	electron-multiplying charge-coupled device
FT	fault-tolerant
GHZ	Greenberger-Horne-Zeilinger
MC	Monte Carlo sampling
MS	Mølmer-Sørensen
NA	numerical aperture
PTA	Pauli twirling approximation
RF	radio frequency
RSA	Rivest–Shamir–Adleman
SS	subset sampling
QEC	quantum error correction
QIP	quantum information processing

1

INTRODUCTION

The emergence of information technology during the last century has played an incredibly influential role and led to an unprecedented societal transformation, affecting every aspect of our modern life. The stunning growth in computational power over the last decades was already predicted in 1965 by Gordon Moore, who estimated an increase in the number of basic computational units, called *transistors*, per device by a factor of two every second year [1]. A significant portion of this advancement can be attributed to the size reduction of the semiconductor structures in the processor, the heart of a computer. The length scale of those structures shrunk from $10\,\mu\mathrm{m}$ in the early seventies [2] to on the order of $10\,\mathrm{nm}$ in 2022 [3], allowing for a skyrocketing density of transistors. However, the once-reliable trajectory of Moore's Law faces an inevitable limit as transistors can not be realized at sub-atomic size scales [4].

There exist problems requiring resources that grow exponentially with the size of the input for which the problem is to be solved. For instance, while the state of a quantum mechanical two-level system is fully described by two complex numbers, an arrangement of 100 such systems already involves computing up to $2^{100} = 1.2676506 \times 10^{30}$ complex amplitudes. Facing the problem of simulating physical systems obeying the rules of quantum mechanics, Richard Feynman outlined this scaling issue using the memorable words [5]:

> *"And I'm not happy with all the analyses that go with just the classical theory, because nature isn't classical, dammit, and if you want to make a simulation of nature, you'd better make it quantum mechanical, and by golly it's a wonderful problem, because it doesn't look so easy."*

Using quantum mechanical systems as the centerpieces of a computer and leveraging their unique features, like superposition and entanglement, opens up new possibilities in algorithm design and potentially provides efficient solutions to many problems other than simulating quantum systems.

> *"Quantum information is a radical departure in information technology, more fundamentally different from current technology than the digital computer is from the abacus."*
>
> — *William Daniel Phillips*

A pivotal role in the development of information processing based on quantum mechanical systems, referred to as *quantum computing*, is taken by the development of several key algorithms. They not only showcase the power and versatility of quantum computers but also attracted broader attention within the scientific community. The Deutsch-Jozsa algorithm [6], proposed in 1992, is an example of an algorithm providing an exponential

speedup over any classical counterpart. Let us assume a function with an n-bit input and a one-bit output either yields the same output for every input, referred to as a *constant* function, or a *balanced* output of 0 and 1 for half of the inputs, respectively. Then, the Deutsch-Jozsa algorithm requires only a single function evaluation to classify the function as constant or balanced. On the contrary, a classical algorithm requires $2^{n-1}+1$ evaluations to classify a function as constant [7]. A function can be identified as balanced as soon as two different outputs are obtained, meaning that two evaluations are required in the best case. Admittedly, the Deutsch-Jozsa problem is kind of constructed to fit the strengths of quantum computers and is of little practical use. However, it was one of the first algorithms showing an exponential advantage of quantum computers, thus inspiring the development of further algorithms.

One of the quantum algorithms sparking the most interest, earlier and still today, is Shor's algorithm [8]. It can be used to find the prime factors of an integer N requiring a runtime polynomial in $\log(N)$. The fastest known classical algorithm exhibits a runtime that is faster than exponential in $\log(N)$ but still slower than every polynomial of $\log(N)$ [9]. The reason why Shor's algorithm attracts a lot of attention is the significance of the problem it promises to solve efficiently: Finding the prime factors of a large integer is impractical employing classical computers. This fact is used in the widely spread Rivest–Shamir–Adleman (RSA) cryptosystem [10]. When using RSA to transmit an encrypted message, the receiver of a message publicly shares a large integer N, which is the product of two prime numbers. The sender uses this number to encode the message and transmits it via a potentially eavesdropped channel. Only the receiver, knowing the prime factors of N, is able to decode the message.

Apart from the two prominent algorithms discussed exemplarily above, there are various applications in the fields of material science, many-body physics, and chemistry exploiting a quantum computer's potential [11–14]. Simulating interesting problems in those fields of research on a larger scale using classical computing is intractable.

After discussing the manifold opportunities opening up through quantum computation, let us see the formal requirements for a quantum computer's successful implementation. In 2000, DiVincenzo proposed a collection of five conditions that a physical system must fulfill in order to be considered as a platform for quantum computing [15]. In the following, the criteria proposed by DiVincenzo are reproduced in a shortened and paraphrased version:

1. The physical system has to offer a scalable way of encoding information in well-characterized quantum mechanical two-level systems called *qubits*. The interaction of the qubits with their environment and with each other should be accurately known.

2. The platform must allow for initializing the qubits in a known, simple initial state.

3. Qubits are subject to interactions with their environment, leading to the loss of a system's quantum features and to convergence to a classical system. This transition has to occur on timescales much longer than the typical time needed to manipulate the qubits.

4. Typically, a physical system offers a set of tunable interactions of the qubits with each other and with classical control. Only if any quantum algorithm can be decomposed into a sequence of these available interactions, called *quantum gates*, the physical system is suitable for implementing a quantum computer.

5. A measurement distinguishing the two qubit levels needs to be available to retrieve a computation's result.

Over the last decades, several platforms for quantum computing have been developed that, at least partially, fulfill DiVincenzo's criteria. Among others, possible candidates for quantum computing architectures are quantum dots [16, 17], nitrogen-vacancy centers [18, 19], photonic systems [20, 21], superconducting electronic circuits [22–24], or trapped neutral atoms [25, 26] and ions [27–29].

This thesis discusses the implementation of quantum computation in a trapped-ion system, where qubits are encoded in the ions' electronic state that can be manipulated via interaction with laser light. External electromagnetic fields allow trapping the ions in vacuum to isolate them from their environment. Furthermore, their charge causes an interaction between individual ions that can be utilized to couple qubits encoded in their electronic states. Many years of research and development in various academic institutions but also in industry paved the way to precise control of the internal and motional state of trapped ions. The control and isolation properties of trapped-ion systems together with the fact that different ions of the same species, and therefore the qubits encoded in them, are identical, render them a promising candidate for quantum computing.

The algorithms to solve problems like prime factorization or quantum chemistry tasks for relevant problem sizes require the implementation of billions of quantum gates [30]. As the classical control realizing the gates is not perfect and the qubits are unintentionally coupled to the environment, the implementation of a quantum algorithm is inherently noisy. A sequence of n gates, each having an error probability of p, is faulty with a probability $1-(1-p)^n$. Therefore, there is always a finite probability of implementing a faulty gate sequence, leading to the corruption of the quantum information and the algorithm's failure. Currently, none of the available quantum computing platforms offers quantum gates with error probabilities low enough for a reliable and successful execution of large-scale quantum algorithms. It is believed that the implementation of error correction (EC) mechanisms when operating quantum computers will be inevitable [31–34]. Procedures for quantum error correction (QEC) rely on redundancy to detect and correct errors stemming from noisy qubits. The information content of a single qubit is distributed among multiple physical qubits, forming a so-called *logical* qubit. Copying the quantum information is forbidden by quantum mechanics, so carefully structured entanglement between the physical qubits collectively carrying the encoded information is utilized to establish the required redundancy.

Peter Shor was not only developing seminal quantum algorithms [8] but also laid the foundation of QEC. In 1995, he proposed a scheme of encoding a logical qubit in nine physical qubits, allowing for the correction of an arbitrary error on any of the nine qubits [35]. A year later, Andrew Steane proposed a QEC code also correcting one arbitrary error using only seven qubits [36]. This seven-qubit code, called *Steane code*, is still widely used in cutting-edge QEC implementations [37–41] and also plays a substantial role in this thesis. A key element of QEC is to repeatedly map the information about errors present on the logical qubit to auxiliary qubits throughout a computation. Subsequently, the information about the present error is extracted by measuring the auxiliary qubits and the respective correction is applied to restore the error-free quantum state of the logical qubit.

In order to implement a particular quantum algorithm using logical qubits, the encoded information needs to be manipulated according to the algorithm's requirements. To maintain the computation's protection against errors, gate operations have to be applied directly to

encoded qubits. Applying gate operations to physical qubits constituting a logical qubit entails the risk of spreading errors within the logical qubit [42]. This could transform a correctable error into an uncorrectable error and lead to a corruption of the computation. Protocols preventing correctable errors from becoming uncorrectable are called *fault-tolerant (FT)*. The propagation of errors can be avoided by only applying gates that act on a single physical qubit within a logical qubit at a time, referred to as *transversal* gates [42]. However, solely using transversal gates does not allow for the implementation of arbitrary computations, and therefore, an alternative strategy for fulfilling the fourth of DiVincenzo's criteria is required [43].

In this thesis, the implementation of QEC protocols involving up to two logical qubits in a trapped-ion quantum processor is discussed. Having two logical qubits at hand certainly does not enable the implementation of quantum algorithms to solve relevant problems. Nevertheless, studying QEC on small to medium-scale devices is informative as it allows one to steer the development of next-generation quantum information processing (QIP) architectures and estimate the performance of prospective devices. This work reports on the experimental realization of the basic building blocks of error-corrected quantum computing, namely the encoding of quantum information, the repeated extraction of information about present errors and the application of gate operations to logical qubits. Furthermore, details on decisive experimental advancements to the $^{40}\mathrm{Ca}^{+}$ trapped-ion quantum processor enabling the implementation of these building blocks are provided.

This thesis is structured as follows: Chapter 2 provides a basic introduction to QIP in an architecture-agnostic fashion. Chapter 3 discusses the implementation of the basic building blocks of QIP in a trapped-ion quantum information processor and provides details about the experimental setup. The implementation of various QEC codes is described in Chapter 4. Furthermore, different methods are compared to repeatedly and fault-tolerantly read out the information about present errors on logical qubits using either physical or logical auxiliary qubits. Chapter 5 discusses the FT realization of a set of logical gates allowing for the implementation of arbitrary algorithms while circumventing the propagation of errors within a logical qubit. The set of transversal gates of the Steane code is augmented with the logical T gate, implemented by preparing a specific resource state on an auxiliary logical qubit and using transversal gates to apply the T gate on the target logical qubit. In Chapter 6, the spatial properties of noise affecting qubits in a common register are investigated in the context of QEC. Correlated errors induced via crosstalk in quantum gates, as well as correlations in the dynamics of qubits unintentionally coupled to a common environment are considered.

2

QUANTUM INFORMATION PROCESSING

As the name suggests, the field of QIP deals with processing information whose behavior is governed by the rules of quantum mechanics. Superposition and entanglement are salient features of quantum mechanics that allow time-efficient computations that are intractable for classical computers. Section 2.1 gives the mathematical framework to describe those phenomena and the underlying qubits. Section 2.2 discusses how quantum information can be manipulated, followed by an introduction to measurements, bringing the results of a quantum computation back to the classical world in Section 2.4.

2.1 From bits to qubits

The smallest unit in classical computation is a *bit*. A bit can be realized in any two-level system, e.g., a mechanical system like a light switch. The most apparent association one probably has when it comes to a physical realization of a bit is two voltage levels at the output of an electronic circuit containing transistors and other electronic components. In fact, information processing devices like smartphones or personal computers we use daily consist of such circuits. Regardless of its physical realization, the state of a bit can be described by a single-digit binary number, where the possible states are labeled 0 and 1. Consequently, the state of a system consisting of n bits can be described by n digits.

Following the term bit, the smallest unit in QIP is referred to as a quantum bit or *qubit*. In contrast to its classical analog, a general state of a qubit encoded in a quantum mechanical two-level system is described as a linear combination, in quantum mechanics referred to as superposition, of its two basis states. Using the Dirac notation [44], which allows for a convenient description of common calculations in quantum mechanics, the state of a qubit can be written as [45]

$$|\psi\rangle = \alpha\,|0\rangle + \beta\,|1\rangle\,, \tag{2.1}$$

where α and β are complex numbers. The probability to find the system in the state $|0\rangle$ ($|1\rangle$) is given by $|\alpha|^2$ ($|\beta|^2$), which implies the condition [45]

$$|\alpha|^2 + |\beta|^2 = 1. \tag{2.2}$$

Furthermore, any device probing the qubit can only be sensitive to the relative phase between α and β but cannot probe the phases of α and β directly and therefore states with the same relative phase of α and β are equivalent. Consequently $|\psi\rangle$ can be written as [45]

$$|\psi\rangle = |\alpha|\,|0\rangle + \sqrt{1-|\alpha|^2}\mathrm{e}^{\mathrm{i}(\arg(\beta)-\arg(\alpha))}\,|1\rangle = \cos\left(\frac{\theta}{2}\right)|0\rangle + \sin\left(\frac{\theta}{2}\right)\mathrm{e}^{\mathrm{i}\phi}\,|1\rangle\,, \tag{2.3}$$

with $0 \leq \theta \leq \pi$ and $0 \leq \phi < 2\pi$. The state of a single qubit

$$|\psi\rangle = \begin{pmatrix}\alpha\\ \beta\end{pmatrix} \tag{2.4}$$

is a vector in a 2-dimensional Hilbert space, where

$$|0\rangle = \begin{pmatrix}1\\ 0\end{pmatrix} \qquad \text{and} \qquad |1\rangle = \begin{pmatrix}0\\ 1\end{pmatrix} \tag{2.5}$$

are orthonormal vectors forming a basis of the Hilbert space. This basis is often referred to as the *computational basis*. On this Hilbert space, an inner product of two elements $|\psi\rangle$ and $|\phi\rangle$ is defined as [45]

$$|\psi\rangle^\dagger \cdot |\phi\rangle = \langle\psi|\phi\rangle \in \mathbb{C}, \tag{2.6}$$

where $|\psi\rangle^\dagger$ in Dirac notation is written as $\langle\psi|$. The normalization condition in Eqn. 2.2 can conveniently be written in Dirac notation as [46]

$$\langle\psi|\psi\rangle = 1. \tag{2.7}$$

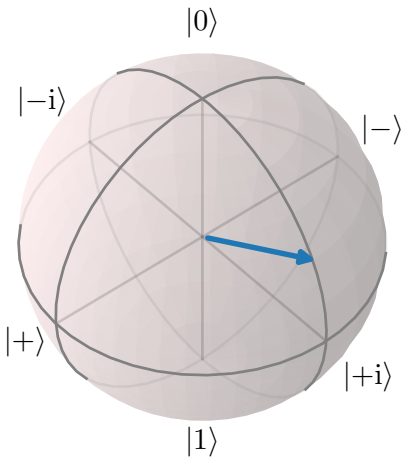

Figure 2.1: Bloch sphere representation of the single-qubit state $|\psi\rangle = \sqrt{\frac{3}{4}}\,|0\rangle + \sqrt{\frac{1}{4}}\mathrm{e}^{\mathrm{i}\frac{\pi}{2}}\,|1\rangle$. The blue arrow points to the location on the Bloch sphere that represents the state $|\psi\rangle$. The computational states $|0\rangle$ and $|1\rangle$ lie at the intersections of the positive and negative Z axis with the surface of a sphere with radius 1, respectively. Superposition states with equal probabilities of being found in $|0\rangle$ or $|1\rangle$ are located on the equator of the sphere.

An ubiquitous visual representation of a single-qubit state is given by the Bloch sphere [45], shown in Figure 2.1. Using the parametrization in Eqn. 2.3, a state can be described as the intersection of the surface of a sphere with a radius of 1 and a ray going through the center of the sphere defined by the angles θ and ϕ. The parameter θ is the angle of the ray with the Z axis, while ϕ is the angle between the X axis and the projection of the ray to the X-Y plane. In Figure 2.1, the blue arrow exemplarily represents the state

$$|\psi\rangle = \sqrt{\frac{3}{4}}\,|0\rangle + \sqrt{\frac{1}{4}}\mathrm{e}^{\mathrm{i}\frac{\pi}{2}}\,|1\rangle\,. \tag{2.8}$$

The basis states $|0\rangle$ and $|1\rangle$ are located at the poles of the Bloch sphere. The states

$$|+\rangle = \frac{1}{\sqrt{2}}\left(|0\rangle + |1\rangle\right) \qquad \text{and} \qquad |-\rangle = \frac{1}{\sqrt{2}}\left(|0\rangle - |1\rangle\right) \tag{2.9}$$

are located at the intersection of the positive and negative X axis with the sphere's surface. Analogously

$$|+\mathrm{i}\rangle = \frac{1}{\sqrt{2}}\left(|0\rangle + \mathrm{i}\,|1\rangle\right) \qquad \text{and} \qquad |-\mathrm{i}\rangle = \frac{1}{\sqrt{2}}\left(|0\rangle - \mathrm{i}\,|1\rangle\right) \tag{2.10}$$

are located at the intersections of the Y axis with the sphere's surface.

A multi-qubit quantum state is a vector in a 2^n-dimensional Hilbert space. Its computational basis states are given by the tensor product of all possible combinations of single-qubit computational basis states, e.g. [46]

$$\begin{aligned} |0\rangle \otimes |0\rangle = |00\rangle &= \begin{pmatrix} 1 \\ 0 \\ 0 \\ 0 \end{pmatrix}, & |1\rangle \otimes |0\rangle = |10\rangle &= \begin{pmatrix} 0 \\ 0 \\ 1 \\ 0 \end{pmatrix}, \\ |0\rangle \otimes |1\rangle = |01\rangle &= \begin{pmatrix} 0 \\ 1 \\ 0 \\ 0 \end{pmatrix} \qquad \text{and} & |1\rangle \otimes |1\rangle = |11\rangle &= \begin{pmatrix} 0 \\ 0 \\ 0 \\ 1 \end{pmatrix} \end{aligned} \tag{2.11}$$

for a two-qubit state. A general n-qubit state

$$\begin{aligned} |\psi\rangle_n = c_0\,|000\ldots000\rangle + c_1 \quad |100\ldots000\rangle + c_2 \quad |010\ldots000\rangle + \cdots + \\ c_{2^n-3}\,|111\ldots101\rangle + c_{2^n-2}\,|111\ldots110\rangle + c_{2^n-1}\,|111\ldots111\rangle \end{aligned} \tag{2.12}$$

is a superposition of 2^n basis states* and, therefore, requires $2^{n+1} - 2$ real parameters to be described considering the normalization of the squared amplitudes and only accounting

* According to the convention used in this thesis qubit 1 is the left-most of the computational basis bitstrings.

for relative phases between the computational basis states. The exponential growth in the dimension of the Hilbert space with the number of qubits renders simulating quantum information processors using classical computers intractable.

Qubits can be encoded in various physical systems. Among other architectures, quantum information processors have been implemented using superconducting circuits [22–24], photonic systems [20, 21], neutral atoms [25, 26], nitrogen-vacancy centers in diamonds [18, 19], and trapped ions [27–29].

2.2 Quantum operations

In order to use qubits for computation, one has to manipulate them using operations similar to bits being acted on by classical logic gates. An operation U acting on the single-qubit state $|\psi\rangle$ can be described using the basis vector notation from Eqn. 2.5 as the matrix multiplication [46]

$$|\psi'\rangle = U\,|\psi\rangle = U\begin{pmatrix}\alpha\\ \beta\end{pmatrix} = \begin{pmatrix}\alpha'\\ \beta'\end{pmatrix}, \tag{2.13}$$

with U being a 2×2 matrix. As the squared amplitudes α and β have been interpreted as probabilities, the normalization from Eqn. 2.7 also has to hold for $|\psi'\rangle$, meaning

$$\langle\psi'|\psi'\rangle = \langle\psi|U^\dagger U|\psi\rangle = 1. \tag{2.14}$$

Using $\langle\psi|\psi\rangle = 1$ imposes the condition

$$U^\dagger U = \mathbb{1} \qquad \text{with} \qquad \mathbb{1} = \begin{pmatrix}1 & 0\\ 0 & 1\end{pmatrix}, \tag{2.15}$$

meaning that U has to be unitary. From this, it follows that $U^\dagger = U^{-1}$, meaning that every quantum operation is reversible. Furthermore, a unitary matrix U can be expressed as [47]

$$U = \mathrm{e}^{-\mathrm{i}H}, \tag{2.16}$$

where $H^\dagger = H$. Such a matrix H is referred to as a *hermitian matrix*.

Figure 2.2a shows a visual representation of a quantum circuit implementing the operation U on a qubit in the state $|\psi\rangle$. The horizontal line, often referred to as *wire*, represents the quantum information encoded in a qubit flowing through the circuit.

2.2.1 *Single-qubit gates*

As shown in the previous section, general quantum operations acting on a single qubit can be described as 2×2 unitary matrices. A frequent parametrization of such an operation is given by [48]

$$U(\theta, \varphi, \lambda) = \begin{pmatrix}\cos\left(\frac{\theta}{2}\right) & -\mathrm{e}^{\mathrm{i}\lambda}\sin\left(\frac{\theta}{2}\right)\\ \mathrm{e}^{\mathrm{i}\phi}\sin\left(\frac{\theta}{2}\right) & \mathrm{e}^{\mathrm{i}(\phi+\lambda)}\cos\left(\frac{\theta}{2}\right)\end{pmatrix} \tag{2.17}$$

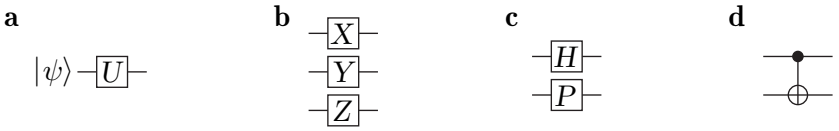

Figure 2.2: Symbols representing operations in quantum circuits. **a** Operation U acting on an input qubit in the state $|\psi\rangle$. Circuit symbols for **b** the Pauli operators X, Y, and Z, **c** the Hadamard gate H and the phase gate P and **d** the controlled-NOT (CNOT) gate.

with $\theta, \varphi, \lambda \in \mathbb{R}$ being Euler angles. Any point on the surface of the Bloch sphere, and therefore, any quantum state of the form described in Eqn. 2.1, can be rotated to any other point on the Bloch sphere. For an n-qubit state, the single-qubit unitary U acting on qubit m can be written as

$$U^{(m)} = \bigotimes_{i=1}^{n} U_i \qquad \text{with} \qquad U_i = \begin{cases} U, & \text{if } i = m \\ \mathbb{1}, & \text{otherwise} \end{cases}. \tag{2.18}$$

Operators of a similar form that are constructed as tensor products of non-trivial single-qubit operators and identity operators will be frequently used later in this thesis.

The single-qubit operations [45]

$$\sigma_x = \begin{pmatrix} 0 & 1 \\ 1 & 0 \end{pmatrix}, \qquad \sigma_y = \begin{pmatrix} 0 & -\mathrm{i} \\ \mathrm{i} & 0 \end{pmatrix}, \qquad \text{and} \qquad \sigma_z = \begin{pmatrix} 1 & 0 \\ 0 & -1 \end{pmatrix}, \tag{2.19}$$

are the so-called *Pauli operators*. Throughout this thesis, the Pauli operators are also denoted as $X \equiv \sigma_x$, $Y \equiv \sigma_y$ and $Z \equiv \sigma_z$, which is a common notation in the context of QEC. Their respective circuit symbols are shown in Figure 2.2b. The group of operators

$$\mathcal{P}_n = \{\mathrm{e}^{\mathrm{i}\epsilon\frac{\pi}{2}} \bigotimes_{i=1}^{n} \sigma \mid \epsilon \in \{0,1,2,3\},\ \sigma \in \{\mathbb{1}, X, Y, Z\}\}, \tag{2.20}$$

is referred to as the n-qubit Pauli group, which plays an important role later in this thesis. The cardinal states on the Bloch sphere $|0\rangle$, $|1\rangle$, $|+\rangle$, $|-\rangle$, $|+\mathrm{i}\rangle$ and $|-\mathrm{i}\rangle$ are eigenstates to the Pauli operators:

$$\begin{aligned} X|+\rangle &= |+\rangle & Y|+\mathrm{i}\rangle &= |+\mathrm{i}\rangle & Z|0\rangle &= |0\rangle \\ X|-\rangle &= -|-\rangle & Y|-\mathrm{i}\rangle &= -|-\mathrm{i}\rangle & Z|1\rangle &= -|1\rangle. \end{aligned} \tag{2.21}$$

Furthermore, the following relations hold:

$$\begin{aligned} XX &= \mathbb{1} & XY &= \mathrm{i}Z & XZ &= -\mathrm{i}Y \\ YX &= -\mathrm{i}Z & YY &= \mathbb{1} & YZ &= \mathrm{i}X \\ ZX &= \mathrm{i}Y & ZY &= -\mathrm{i}X & ZZ &= \mathbb{1}. \end{aligned} \tag{2.22}$$

Using the Pauli operators, a general single-qubit unitary can be parametrized as [45]

$$U = \mathrm{e}^{-i\frac{\theta}{2}\boldsymbol{a}\cdot\boldsymbol{\sigma}} = \cos\left(\frac{\theta}{2}\right)\mathbb{1} - \mathrm{i}\sin\left(\frac{\theta}{2}\right)\boldsymbol{a}\cdot\boldsymbol{\sigma}, \tag{2.23}$$

describing a rotation on the Bloch sphere around an axis with unit vector $\boldsymbol{a}$ and a rotation angle of θ. Here,

$$\boldsymbol{\sigma} = (X, Y, Z)^\intercal \tag{2.24}$$

is a vector operator consisting of the three Pauli operators. For $\theta = \pi$ and $\boldsymbol{a} = (\frac{1}{\sqrt{2}}, 0, \frac{1}{\sqrt{2}})^\intercal$ the resulting single-qubit unitary is

$$U = -\frac{\mathrm{i}}{\sqrt{2}}\begin{pmatrix} 1 & 1 \\ 1 & -1 \end{pmatrix}, \tag{2.25}$$

which is up to a global phase equivalent to the unitary

$$H = \frac{1}{\sqrt{2}}\begin{pmatrix} 1 & 1 \\ 1 & -1 \end{pmatrix}. \tag{2.26}$$

This operation is commonly referred to as Hadamard gate [45]. Applying the Hadamard gate to the computational basis state $|0\rangle$ prepares the superposition $H|0\rangle = |+\rangle$ and vice versa. Another gate that is frequently used throughout this thesis is the phase gate P, which is recovered up to a global phase, for $\theta = \frac{\pi}{2}$ and $\boldsymbol{a} = (0, 0, 1)^\intercal$:

$$P = \begin{pmatrix} 1 & 0 \\ 0 & \mathrm{i} \end{pmatrix}. \tag{2.27}$$

It implements a rotation around the Z axis by $\frac{\pi}{2}$ and turns eigenstates of X into eigenstates of Y and vice versa. Eigenstates of Z remain unchanged as these states on the Bloch sphere lie on the rotation axis. Figure 2.2c shows the circuit symbols of the Hadamard and phase gates.

Sequences of Hadamard and phase gates can implement any operator in the group

$$N(\mathcal{P}_n) = \{V \mid V\mathcal{P}_n V^\dagger = \mathcal{P}_n\} \tag{2.28}$$

for $n = 1$, where $\mathcal{P}_n$ is the n-qubit Pauli group, defined in Eqn. 2.20. With this, H and P generate the group of operators that transforms the single-qubit Pauli group into itself [49]. The state $|\psi\rangle = V|0\rangle$ is an eigenstate of a Pauli operator for all V. $N(\mathcal{P}_1)$ is the normalizer of the single-qubit Pauli group. The group $N(\mathcal{P}_n)$ is commonly referred to as the *n-qubit Clifford group*. Circuits containing only operations in the Clifford group acting on a computational basis state can be simulated efficiently using classical computers [50, 51]. Therefore, a quantum computer that only implements the Clifford group can not outperform a classical computer.

2.2.2 *Two-qubit gates*

In the previous section, operations acting non-trivially on a single qubit were discussed. Now, let us consider operations manipulating two qubits, described by unitary matrices with a dimension of 4×4. A prototypical example of a two-qubit operation that one will encounter repeatedly in this thesis is the controlled-NOT (CNOT) gate described by the unitary [45]

$$\mathrm{CNOT} = \begin{pmatrix} 1 & 0 & 0 & 0 \\ 0 & 1 & 0 & 0 \\ 0 & 0 & 0 & 1 \\ 0 & 0 & 1 & 0 \end{pmatrix} \tag{2.29}$$

with its corresponding quantum circuit symbol shown in Figure 2.2d. This operation is acting on the two-qubit computational basis states in Eqn. 2.11 as follows:

$$\begin{aligned} |00\rangle &\xrightarrow{\mathrm{CNOT}} |00\rangle\,, & |01\rangle &\xrightarrow{\mathrm{CNOT}} |01\rangle\,, \\ |10\rangle &\xrightarrow{\mathrm{CNOT}} |11\rangle\,, & |11\rangle &\xrightarrow{\mathrm{CNOT}} |10\rangle\,. \end{aligned} \tag{2.30}$$

The state of the second qubit is left unchanged whenever the first qubit is in the state $|0\rangle$. If, on the contrary, the state of the first qubit is $|1\rangle$, the second qubit is flipped from $|0\rangle$ to $|1\rangle$ and vice versa. Effectively, the first qubit controls if a bit flip, corresponding to a NOT gate in classical computing, is applied to the second qubit. Therefore, two-qubit operations allow for conditional logic to be implemented in QIP. The way the computational basis states are transformed under the application of the CNOT gate might not seem particularly remarkable, as one could have prepared the output states using single-qubit operations only. However, let us consider a different input state:

$$\frac{1}{\sqrt{2}}(|0\rangle + |1\rangle) \otimes |0\rangle = |+\rangle \otimes |0\rangle \xrightarrow{\mathrm{CNOT}} |0\rangle \otimes |0\rangle + |1\rangle \otimes |1\rangle = |00\rangle + |11\rangle\,. \tag{2.31}$$

The output state is a Bell state [45] and cannot be written as a tensor product

$$(\alpha\,|0\rangle + \beta\,|1\rangle) \otimes (\gamma\,|0\rangle + \delta\,|1\rangle) \tag{2.32}$$

of general single qubit states. States that are not separable into a tensor product of states describing the individual qubits are referred to as *entangled* [46]. For the Bell state in Eqn. 2.31 the combined system is found with equal probabilities in the states $|00\rangle$ and $|11\rangle$. Therefore, each subsystem has the same probability of being in $|0\rangle$ or $|1\rangle$, but the two subsystems are, for certain, found in the same state. Besides superposition, entanglement is a second distinctive feature between classical and quantum computation.

In this thesis, we do not discuss quantum operations that act on more than two qubits directly. However, any unitary operation acting on an arbitrary number of qubits can be decomposed into a sequence of CNOT gates in conjunction with arbitrary single-qubit operations. The following section explains how such a sequence is constructed.

2.3 Universal gate set

The goal of quantum computation is to reliably implement any desired quantum algorithm. This can be broken down into preparing the initial state $|0\rangle^{\otimes n}$ for n qubits and applying a unitary operation that transforms $|0\rangle^{\otimes n}$ into a state encoding the result of the algorithm. It is desirable to decompose this unitary operation into a finite set of gates, each acting on a limited subset of qubits: In large-scale physical systems, mechanisms manipulating qubits will always be limited to act only on a spatially bounded subset of qubits at a time. Furthermore, a finite, parameter-free set of gates offers practical advantage when designing a quantum computer as the hardware can be optimized for the implementation of this finite gate set. Apart from that, limiting the required gate operations to a finite set is crucial in error-corrected quantum computation, as will be discussed in Chapter 5. A set of gates that can approximate any desired unitary to arbitrary accuracy is referred to as *universal*.

As entanglement is a key feature of QIP, a universal set of gates has to contain a gate that can create entanglement. In order to do so, this gate has to act on more than one qubit. However, an entangling gate acting on two qubits is sufficient to decompose any n-qubit unitary operation into a finite universal set of gates [45]. For the rest of this section it will be discussed, how an arbitrary unitary can be approximated to arbitrary precision by a sequence of gates from a finite set of quantum gates. In overview, the decomposition is constructed as following:

1. In a first step, a unitary operation acting on n qubits is decomposed into unitary matrices acting only on two computational basis states, so called *two-level unitary matrices**.
2. The two-level unitaries are decomposed into CNOT gates and single-qubit operations.
3. Single-qubit unitaries are approximated to arbitrary precision by a sequence of gates in a finite set.

Each of the following subsections is dedicated to one of the aforementioned steps of decomposing a unitary operation into a sequence of gates from a finite set.

2.3.1 *Two-level unitary operations are universal*

Let us assume a unitary operation $U \in \mathrm{U}(2^n)$ acting on n qubits has to be applied in order to implement a desired quantum algorithm. The effect of U on $|0\rangle$ is given by [52]

$$U|0\rangle = \sum_{i=0}^{2^n-1} a_i |i\rangle \,, \tag{2.33}$$

* Note that two-level unitary matrices are not to be confused with two-qubit unitary matrices that act on two qubits instead of two basis states. For example, an operation transforming $|000\rangle$ to $\frac{1}{\sqrt{2}}(|000\rangle + |111\rangle)$ is a two-level unitary but is not a two-qubit unitary, as it manipulates three qubits.

where $\{|0\rangle, ..., |2^n - 1\rangle\}$* are consecutively numbered computational basis states and $a_i \in \mathbb{C}$. The state $U|0\rangle$ can be written as $V_0|0\rangle$, where V_0 is a product of $2^n - 1$ two-level unitaries [52]

$$V_0 = \prod_{k=0}^{2^n-2} V_{(0,k)}. \tag{2.34}$$

The two-level unitaries $V_{(0,k)}$ are acting as [52]

$$\begin{aligned} V_{(0,0)}|0\rangle &= a_0|0\rangle + b_0|1\rangle \\ V_{(0,1)}b_0|1\rangle &= a_1|1\rangle + b_1|2\rangle \\ &\vdots \\ V_{(0,2^n-2)}b_{2^n-3}|2^n-2\rangle &= a_{2^n-2}|2^n-2\rangle + a_{2^n-1}|2^n-1\rangle \end{aligned} \tag{2.35}$$

on the computational basis states. Note that the operator $U_0 = V_0^{-1}U$ acts trivially on the state $|0\rangle = U_0|0\rangle$ and, therefore, is of the form

$$U_0 = \begin{pmatrix} 1 & 0 & \dots & 0 \\ 0 & u_{0,(0,0)} & \dots & u_{0,(0,2^n-2)} \\ \vdots & \vdots & \ddots & \vdots \\ 0 & u_{0,(2^n-2,0)} & \dots & u_{0,(2^n-2,2^n-2)} \end{pmatrix}. \tag{2.36}$$

Next, one can construct V_1 as a product of two-level unitaries

$$V_1 = \prod_{k=1}^{2^n-2} V(1,k), \tag{2.37}$$

such that $U_0|1\rangle = V_1|1\rangle$. The unitaries $V(1,k)$ act on the subspace spanned by $\{|1\rangle \cdots |2^n - 2\rangle\}$ as

$$\begin{aligned} V_{(1,1)}|1\rangle &= a_0'|1\rangle + b_0'|2\rangle \\ V_{(1,2)}b_0'|2\rangle &= a_1'|2\rangle + b_1'|3\rangle \\ &\vdots \\ V_{(1,2^n-2)}b_{2^n-4}'|2^n-3\rangle &= a_{2^n-2}'|2^n-2\rangle + a_{2^n-1}'|2^n-1\rangle. \end{aligned} \tag{2.38}$$

Defining $U_1 = V_1^{-1}U_0$, one sees that $U_1|0\rangle = |0\rangle$ and $U_1|1\rangle = |1\rangle$.

While U acts non-trivially on all computational basis states, U_0 acts trivially on $|0\rangle$ and U_1 acts trivially on the subspace spanned by $\{|0\rangle, |1\rangle\}$. The procedure of finding products

* Note the italic typesetting here. The state $|0\rangle$ is not to be confused with the state $|0\rangle = |0\rangle^{\otimes n}$

of two-level matrices that act trivially on subspaces with increasing dimension is repeated $2^n - 1$ times in total. The matrix [52]

$$U_{2^n-2} = V_{2^n-2}U_{2^n-3} = V_{2^n-2}^{-1}V_{2^n-3}^{-1}\dots V_1^{-1}V_0^{-1}U = \mathbb{1}^{\otimes n} \tag{2.39}$$

then acts trivially on all computational basis states and $U = V_0V_1\dots V_{2^n-3}V_{2^n-2}$. This means that any n-qubit unitary U can be decomposed into $(2^n-1)+(2^n-2)+\dots+2+1 = \frac{2^n(2^n-1)}{2}$ two-level unitaries. Consequently, two-level unitaries are universal.

2.3.2 *Decomposition of two-level unitaries in CNOT and single-qubit gates*

Up to now it was shown that any unitary operator can be decomposed in a product of two-level unitary matrices. The goal of this subsection is to find sequences of CNOT and single-qubit gates implementing those two-level unitaries. Let us consider the n-qubit two-level unitary

$$V = \left(\begin{array}{ccc|cc} 1 & & 0 & & \\ & \ddots & & & 0 \\ 0 & & 1 & & \\ \hline & 0 & & V'_{0,0} & V'_{0,1} \\ & & & V'_{1,0} & V'_{1,1} \end{array}\right) \tag{2.40}$$

acting on the subspace spanned by the states

$$|i\rangle = |11\dots10\rangle \qquad \text{and} \qquad |j\rangle = |11\dots11\rangle\,. \tag{2.41}$$

This two-level unitary can be implemented using a $n-1$-qubit controlled-U gate[45]. The single-qubit unitary

$$V' = \begin{pmatrix} V'_{0,0} & V'_{0,1} \\ V'_{1,0} & V'_{1,1} \end{pmatrix} \tag{2.42}$$

is applied to qubit n if all other qubits are in the state $|1\rangle$ and the identity operator is applied otherwise. This operation, depicted in Figure 2.3a for $n = 5$, can be decomposed into $n-2$-qubit controlled-U and one-qubit controlled-U gates. The corresponding decomposition for $n = 5$ is shown in Figure 2.3b. Applying this decomposition repeatedly allows one to express the $n-1$-qubit controlled-U gate using just one-qubit controlled-U gates. The controlled-U gate with a single control qubit then again can be decomposed into CNOT gates and single-qubit gates [45], as shown in Figure 2.3c. Here, A, B, C, and D are chosen to fulfill $U = \mathrm{e}^{\mathrm{i}\alpha}AXBXC$, $ABC = \mathbb{1}$, and $D = \left(\begin{smallmatrix} 1 & 0 \\ 0 & \mathrm{e}^{\mathrm{i}\alpha} \end{smallmatrix}\right)$ [45].

Up to now, only two-level unitaries acting non-trivially on the states $|i\rangle = |11\dots10\rangle$ and $|j\rangle = |11\dots11\rangle$ were considered. To generalize this method to implementing arbitrary two-level unitaries, the limitations for the computational states the unitary is acting on have to be reduced. As a first step, let us assume the unitary acts on the subspace spanned by

$$|i\rangle = |b_1\cdots b_{n-1}0\rangle \qquad \text{and} \qquad |j\rangle = |b_1\cdots b_{n-1}1\rangle\,, \tag{2.43}$$

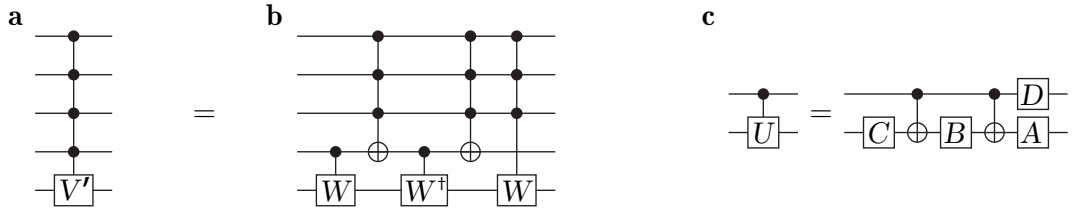

Figure 2.3: Circuits implementing two-level unitaries on the subspace spanned by $|11110\rangle$ and $|11111\rangle$. **a** A four-qubit-controlled single-qubit unitary V' implementing a two-level unitary acting on this subspace and **b** its decomposition into controlled unitaries with a single and three control qubits. Here, $W^2 = V'$ [53]. **c** Decomposition of a one-qubit controlled-U gate into CNOT gates and single-qubit operations, where $U = \mathrm{e}^{\mathrm{i}\alpha} AXBXC$, $ABC = \mathbb{1}$ and $D = \left(\begin{smallmatrix} 1 & 0 \\ 0 & \mathrm{e}^{\mathrm{i}\alpha} \end{smallmatrix}\right)$ [45].

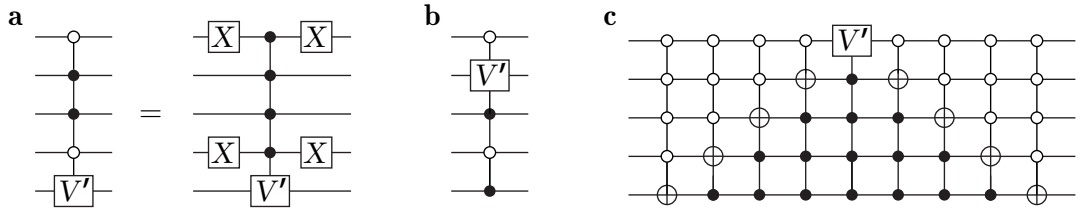

Figure 2.4: Circuits implementing two-level unitaries. **a** A controlled single-qubit unitary triggered by the state $|0110\rangle$ on the control qubits and its decomposition into the circuit from Figure 2.3a and NOT gates. **b** The same unitary acting on a different target qubit. **c** A five-qubit two-level unitary acting on the subspace spanned by $|00000\rangle$ and $|11111\rangle$ can be expressed as controlled unitaries with four control qubits.

where $b_1 \cdots b_{n-1}$ is an arbitrary $n-1$-digit bitstring. Then the $n-1$-qubit controlled-U gate has to be adapted to apply the unitary V' to qubit n, whenever the state $|b_1 \cdots b_{n-1}\rangle$ is present on the first $n-1$ qubits. This can be achieved by applying X operations before and after the controlled gate on all qubits i for which $b_i = 0$, as shown in Figure 2.4a exemplarily for $n = 5$, $|i\rangle = |01100\rangle$ and $|j\rangle = |01101\rangle$.

A further step of generalization to arbitrary two-level unitaries is to assume the basis states $|i\rangle$ and $|j\rangle$, that the two-level unitary acts on, still differ only in one qubit, but it is not the right-most one in the bitstrings i and j. In this case, the single-qubit unitary V' is just applied to a different qubit conditional on the state of the other $n-1$ qubits, as shown in Figure 2.4b for $|i\rangle = |00101\rangle$ and $|j\rangle = |01101\rangle$.

As a last step in the generalization towards decomposing arbitrary two-level unitaries, let us assume $|i\rangle$ and $|j\rangle$ differ in m different positions. Then, a sequence of $m-1$ multi-qubit CNOT gates is applied to the register. The first gate of this sequence transforms $|i\rangle$ into $|i_1\rangle$, so that i_1 and j differ in $m-1$ positions. Each of the following gates reduces the number of positions, in which i_i and j differ, again by 1. Consequently, the bitstrings i_{m-1} and j differ in only one position. After that, an $n-1$-qubit controlled-U gate is applied that implements V', composed of the four non-trivial entries of the two-level unitary, on the qubit in which i_{m-1} and j differ. Subsequently, the multi-qubit CNOT gates are applied in reverse order to undo the permutation. The multi-qubit CNOT gates can be decomposed in single-qubit and CNOT gates using the decomposition from Figures 2.3a and 2.3b. Figure 2.4c shows a circuit implementing the two-level unitary V acting on the subspace $|i\rangle = |00000\rangle$ and

$|j\rangle = |11111\rangle$. The state $|i\rangle$ undergoes the following evolution until it only differs in the left-most position from $|j\rangle$:

$$|00000\rangle \to |00001\rangle \to |00011\rangle \to |00111\rangle \to |01111\rangle\,. \tag{2.44}$$

With this, it is shown that a sequence of CNOT gates, in conjunction with single-qubit gates, can implement any two-level unitary. As products of two-level unitaries are universal, also the set of CNOT and single-qubit gates is universal.

2.3.3 *Approximation of single-qubit gates using a finite set of gates*

As mentioned in Section 2.2.1, the Hadamard gate H and phase gate P generate the single-qubit Clifford group. In the following, it is shown that expanding the set $\{H, P\}$ by the *T gate*, implementing a rotation with a rotation angle of $\frac{\pi}{4}$, allows for decomposing arbitrary single-qubit operations. Combined with the result from the previous subsection, stating that CNOT and single-qubit gates are universal, this means that the set $\{H, P, T, \mathrm{CNOT}\}$ is universal [54].

Commonly, the rotation axis of the T gate is chosen to be the Z axis. However, in this work, the T gate is defined as

$$T = \mathrm{e}^{-\mathrm{i}\frac{\pi}{8}Y} \tag{2.45}$$

which is a rotation around the Y axis. Up to single-qubit Clifford operations, T gates rotating around the Z and Y axes are equivalent.

As it is not obvious at first sight how adding a $\frac{\pi}{4}$ rotation allows approximating continuous single-qubit rotations, let us first consider the sequential application of the gate operations T and $HPTP^\dagger H^\dagger$, resulting in the rotation

$$\begin{aligned} HPTP^\dagger H^\dagger\ T &= \mathrm{e}^{\mathrm{i}\frac{\pi}{8}Z}\mathrm{e}^{-\mathrm{i}\frac{\pi}{8}Y} \\ &= \left(\cos\left(\frac{\pi}{8}\right)\mathbb{1} + \mathrm{i}\sin\left(\frac{\pi}{8}\right)Z\right)\left(\cos\left(\frac{\pi}{8}\right)\mathbb{1} - \mathrm{i}\sin\left(\frac{\pi}{8}\right)Y\right) \\ &= \cos^2\left(\frac{\pi}{8}\right)\mathbb{1} - \mathrm{i}\sin\left(\frac{\pi}{8}\right)\left[\sin\left(\frac{\pi}{8}\right)X + \cos\left(\frac{\pi}{8}\right)(Y - Z)\right]. \end{aligned} \tag{2.46}$$

This sequence of gate operations implements a rotation $R_{\boldsymbol{n}}(\theta)$ around the axis

$$\boldsymbol{n} = \frac{1}{\sqrt{1 + \cos^2\left(\frac{\pi}{8}\right)}}\left(\sin\left(\frac{\pi}{8}\right), \cos\left(\frac{\pi}{8}\right), -\cos\left(\frac{\pi}{8}\right)\right)^\intercal \tag{2.47}$$

with a rotation angle θ given by $\cos\left(\frac{\theta}{2}\right) = \cos^2\left(\frac{\pi}{8}\right)$. In Ref. [55], it is shown that θ is an irrational multiple of 2π. Any rotation around $\boldsymbol{n}$, $R_{\boldsymbol{n}}(\alpha)$ with $\alpha \in \mathbb{R}$, can be approximated to arbitrary accuracy by repeatedly applying $R_{\boldsymbol{n}}(\theta)$ [45].

As a next step towards the approximation of arbitrary single-qubit unitaries, let us consider the rotation

$$\begin{aligned} R_{\boldsymbol{m}}(\theta) &= HR_{\boldsymbol{n}}(\theta)H^\dagger \\ &= \cos^2\left(\frac{\pi}{8}\right)\mathbb{1} - \mathrm{i}\sin\left(\frac{\pi}{8}\right)\left[-\cos\left(\frac{\pi}{8}\right)(X + Y) + \sin\left(\frac{\pi}{8}\right)Z\right] \end{aligned} \tag{2.48}$$

with a different rotation axis

$$\boldsymbol{m} = \frac{1}{\sqrt{1+\cos^2\left(\frac{\pi}{8}\right)}}\left(-\cos\left(\frac{\pi}{8}\right), -\cos\left(\frac{\pi}{8}\right), \sin\left(\frac{\pi}{8}\right)\right)^\intercal \tag{2.49}$$

and a rotation angle θ. Analogously to $R_{\boldsymbol{n}}(\alpha)$, repeated implementation of $R_{\boldsymbol{m}}(\theta)$ can approximate any rotation $R_{\boldsymbol{m}}(\alpha)$ to arbitrary accuracy. Any single-qubit unitary U_{sq} can be expressed by a sequence [56]

$$U_{\mathrm{sq}} = R_1(\alpha_1)\ldots R_j(\alpha_j) \quad \text{with} \quad R_i \in \{R_{\boldsymbol{n}}, R_{\boldsymbol{m}}\}, \tag{2.50}$$

for appropriate choices of $\alpha_i \in \mathbb{R}$. Therefore, U_{sq} can be approximated by a sequence of rotations $R_{\boldsymbol{n}}$ and $R_{\boldsymbol{m}}$. The minimum number of rotations necessary to decompose any unitary is given by [56]

$$j = \left\lceil \frac{\pi}{\arccos\left(|\boldsymbol{n}^\intercal \boldsymbol{m}|\right)} \right\rceil + 1. \tag{2.51}$$

With this, the construction of an arbitrary unitary using only gates from a finite set is complete. In Section 2.3.1, it was shown that two-level unitary matrices are universal, followed by the proof that two-level unitaries can be decomposed in CNOT and single-qubit gates in Section 2.3.2. As a sequence of gates from the set $\{H, P, T\}$ allows one to approximate any single-qubit gate to arbitrary accuracy, the set $\{H, P, T, \mathrm{CNOT}\}$ is universal [54].

2.4 Measurements

A particular quantum algorithm can be implemented by applying a sequence of gates discussed above to a quantum register. The desired result is encoded in the quantum state of the register. In order to retrieve the result, the qubits of the quantum processor are *measured*. Measurements transfer the encoded quantum information to the classical world, rendering it accessible to the quantum processor's user.

A general measurement of a quantum system is described by a set of measurement operators $\{M_\lambda\}$ [45], where the index λ is the observed measurement outcome. The probability p to obtain the outcome λ, when applying the measurement described by $\{M_\lambda\}$ to a quantum state $|\psi\rangle$, is given by [45]

$$p(\lambda) = \langle\psi|M_\lambda^\dagger M_\lambda|\psi\rangle\,. \tag{2.52}$$

As the sum of all outcome probabilities

$$\sum_\lambda p(\lambda) = \sum_\lambda \langle\psi|M_\lambda^\dagger M_\lambda|\psi\rangle = \langle\psi|\sum_\lambda M_\lambda^\dagger M_\lambda|\psi\rangle \tag{2.53}$$

must be equal to 1, the measurement operators have to fulfill the following requirement [45]:

$$\sum_\lambda M_\lambda^\dagger M_\lambda = \mathbb{1}. \tag{2.54}$$

Figure 2.5: Measurements on a single qubit. **a** Projective measurement in the computational basis of a qubit in the state $|\psi\rangle$. The quantum state of the qubit is collapsed to a computational basis state, and one classical bit of information is extracted. **b** Measurement of the hermitian and unitary operator U using an auxiliary qubit. The state of the measured qubit after the measurement $|\psi'\rangle$ is an eigenstate of U.

Unlike in classical systems, in the quantum mechanical world, even an ideal measurement device will affect the measured system. For the considered measurement, after obtaining the outcome λ the system is found to be in the state [45]

$$|\psi'\rangle = \frac{M_\lambda |\psi\rangle}{\sqrt{\langle\psi|M_\lambda^\dagger M_\lambda|\psi\rangle}}. \tag{2.55}$$

A particular, however pervasive, case is a single-qubit measurement in the computational or Z basis, where

$$\begin{aligned} &\lambda_1 = +1 && \lambda_2 = -1 \\ &M_{+1} = |0\rangle\langle 0| && M_{-1} = |1\rangle\langle 1|. \end{aligned} \tag{2.56}$$

For $|\psi\rangle = \alpha|0\rangle + \beta|1\rangle$ the outcome probabilities are $p(+1) = \langle\psi|0\rangle\langle 0|\psi\rangle = |\alpha|^2$ and $p(-1) = |\beta|^2$ and the final states are, up to an irrelevant global phase, $|\psi'\rangle_{+1} = |0\rangle$ and $|\psi'\rangle_{-1} = |1\rangle$. This measurement extracts one bit of classical information from a single-qubit state and projects the output state to the computational basis as shown in Figure 2.5a.

Measurements in a different basis can be implemented by applying a unitary operation prior to the measurement. For a measurement in the basis $\{|+\rangle, |-\rangle\}$ a Hadamard gate is applied to the state

$$|\psi\rangle = \alpha|0\rangle + \beta|1\rangle = \frac{\alpha+\beta}{\sqrt{2}}|+\rangle + \frac{\alpha-\beta}{\sqrt{2}}|-\rangle \tag{2.57}$$

prior to the measurement in the computational basis discussed before. The outcome probabilities then are

$$\begin{aligned} p(+1) &= \langle\psi|H|0\rangle\langle 0|H|\psi\rangle = \langle\psi|+\rangle\langle+|\psi\rangle = \frac{|\alpha+\beta|^2}{2} \\ &\text{and} \\ p(-1) &= \langle\psi|H|1\rangle\langle 1|H|\psi\rangle = \langle\psi|-\rangle\langle-|\psi\rangle = \frac{|\alpha-\beta|^2}{2}, \end{aligned} \tag{2.58}$$

corresponding to the square of the absolute value of the amplitudes of $|+\rangle$ and $|-\rangle$ in $|\psi\rangle$. Note that the output state is still projected to $|0\rangle$ and $|1\rangle$ for measurement outcomes $+1$ and -1, respectively.

However, it might be desirable to perform a measurement that does not project the qubits it is acting on in the computational basis. For example, one could want to probe a certain property on a set of qubits that is prepared in a superposition state which is still supposed to be used after the measurement. In such a case, a measurement of a unitary and hermitian operator can be performed using an auxiliary qubit [57]. Figure 2.5b shows the circuit implementing a measurement of a single-qubit operator U on a qubit in the state $|\psi\rangle$ using an auxiliary qubit prepared to $|0\rangle$. As U is hermitian and unitary the relations $U = U^\dagger$ and $U^2 = \mathbb{1}$ hold. The cornerstone of the measurement is the application of U to the qubit to be measured conditioned on the auxiliary qubit being in the state $|1\rangle$. This controlled operation

$$U_\mathrm{C} = |0\rangle\langle 0| \otimes \mathbb{1} + |1\rangle\langle 1| \otimes U \tag{2.59}$$

is sandwiched between two Hadamard gates on the auxiliary qubit. The measurement procedure is concluded with a projective measurement of the auxiliary qubit in the computational basis described by the measurement operators

$$M_+ = |0\rangle\langle 0| \otimes \mathbb{1} \qquad \text{and} \qquad M_- = |1\rangle\langle 1| \otimes \mathbb{1}. \tag{2.60}$$

Using the measurement framework introduced above, one can calculate the probability of obtaining the measurement outcome $+1$ to be

$$\begin{aligned} p(+) &= (\langle 0| \otimes \langle\psi|) H_1 \, U_\mathrm{C} \, H_1 (M_+^\dagger M_+) H_1 \, U_\mathrm{C} \, H_1 (|0\rangle \otimes |\psi\rangle) \\ &= (\langle 0| \otimes \langle\psi|) H_1 \, U_\mathrm{C} \, H_1 (|0\rangle\langle 0| \otimes \mathbb{1}) H_1 \, U_\mathrm{C} \, H_1 (|0\rangle \otimes |\psi\rangle) \\ &= \frac{1}{2}(1 + \langle\psi|U|\psi\rangle), \end{aligned} \tag{2.61}$$

with $H_1 = H \otimes \mathbb{1}$ being a Hadamard gate on the auxiliary qubit and U_C being the controlled unitary. After obtaining the outcome $+1$, the combined system is in the state [57]

$$|\Psi'_+\rangle = |0\rangle \otimes |\psi'_+\rangle = \frac{1}{\sqrt{2(1 + \langle\psi|U|\psi\rangle)}} \, |0\rangle \otimes (\mathbb{1} + U) \, |\psi\rangle \, , \tag{2.62}$$

with $|\psi'_+\rangle = U \, |\psi'_+\rangle$ being a $+1$ eigenstate of U. Accordingly, the probability of obtaining -1 and the corresponding output state are [57]

$$\begin{gathered} p(-) = \frac{1}{2}(1 - \langle\psi|U|\psi\rangle) \\ \text{and} \\ |\Psi'_-\rangle = |1\rangle \otimes |\psi'_-\rangle = \frac{1}{\sqrt{2(1 - \langle\psi|U|\psi\rangle)}} \, |1\rangle \otimes (\mathbb{1} - U) \, |\psi\rangle \, , \end{gathered} \tag{2.63}$$

where $|\psi'_-\rangle = -U \, |\psi'_-\rangle$. Therefore, the described measurement procedure projects to $+1$ or -1 eigenstates of the measured operator while the corresponding eigenvalue can be

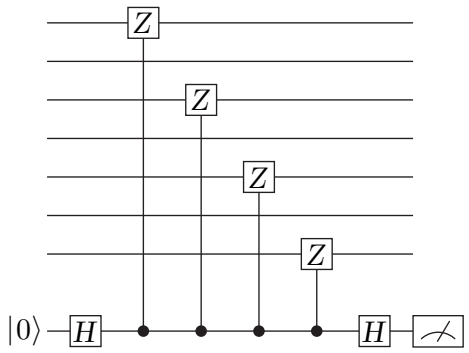

Figure 2.6: Parity measurement acting on four out of seven qubits. The expectation value of the operator $Z_1Z_3Z_5Z_7$ is determined using an auxiliary qubit.

measured using the auxiliary qubit. The same reasoning holds for n-qubit measurements with $\dim(U) = 2^n \times 2^n$ and $\dim(|\psi\rangle_{\mathrm{S}}) = 2^n$ [57].

A multi-qubit measurement used extensively throughout this thesis is a unitary measuring Pauli operators on a subset of qubits. Figure 2.6 exemplarily shows the measurement of

$$U = \bigotimes_{i=1}^{7} U_i \qquad \text{with} \qquad U_i = \begin{cases} Z, & \text{if } i \in \{1,3,5,7\} \\ \mathbb{1}, & \text{otherwise} \end{cases}. \tag{2.64}$$

A shorthand notation of this operator is $Z_1Z_3Z_5Z_7$. This measurement returns $+1$ for all computational basis states with an even number of qubits of the subset $\{1,3,5,7\}$ being in the state $|1\rangle$, e.g. $|0000000\rangle$ or $|1010000\rangle$. If the number of qubits in this subset being in the state $|1\rangle$ is odd, the measurement returns -1. At the same time, the circuit projects to the subspace with an even or odd number of qubits in $|1\rangle$. For instance, the input state

$$|\psi\rangle_{\mathrm{S}} = \frac{1}{\sqrt{4}}(|0000000\rangle + |1000000\rangle + |1000001\rangle + |0000001\rangle) \tag{2.65}$$

is projected to

$$|\psi'\rangle_{\mathrm{S},+1} = \frac{1}{\sqrt{2}}(|0000000\rangle + |1000001\rangle) \tag{2.66}$$

for a measurement outcome of $+1$ occurring with a probability of $p(+1) = 0.5$. In this example, all qubits outside the subset acted on non-trivially by U are irrelevant and set to $|0\rangle$. Such measurements are broadly used in QEC and are referred to as *parity measurements*.

2.5 Density matrix formalism

Until now, this thesis considered only systems consisting of qubits that can all be individually controlled and measured. The qubits were not coupled to an environment that cannot be acted on in a controlled fashion. The technical term describing such situations is *closed*

systems. In reality, this might not be the case. Let us consider a bipartite system consisting of subsystems A and B, but only system A is accessible. The combined system of A and B is referred to as an *open system*. For simplicity, A and B are assumed to be qubits and a general state of this system can be written as

$$|\psi\rangle_{\mathrm{AB}} = \sum_{i,m=0}^{1} \alpha_{im} \, |i\rangle_{\mathrm{A}} \otimes |m\rangle_{\mathrm{B}} \,, \tag{2.67}$$

with $\alpha_{im} \in \mathbb{C}$ and $\sum_{i,m=0}^{1} |\alpha_{im}|^2 = 1$. An observable on the accessible subsystem A acting trivially on the inaccessible subsystem B is given by

$$O_{\mathrm{AB}} = O \otimes \mathbb{1} \tag{2.68}$$

with an expectation value of [46]

$$\begin{aligned} \langle O_{\mathrm{AB}} \rangle = {}_{\mathrm{AB}}\langle\psi|O_{\mathrm{AB}}|\psi\rangle_{\mathrm{AB}} &= \Big(\sum_{j,n=0}^{1} \alpha^*_{jn} \, {}_{\mathrm{A}}\langle j| \otimes {}_{\mathrm{B}}\langle n| \Big)(O \otimes \mathbb{1}) \Big(\sum_{i,m=0}^{1} \alpha_{im} \, |i\rangle_{\mathrm{A}} \otimes |m\rangle_{\mathrm{B}} \Big) \\ &= \sum_{i,j=0}^{1} \Big(\sum_{k=0}^{1} \alpha^*_{jk} \alpha_{ik} \Big) \, {}_{\mathrm{A}}\langle j|O|i\rangle_{\mathrm{A}} . \end{aligned} \tag{2.69}$$

Using the expression for the trace of a product of matrices $\mathrm{Tr}(CD) = \sum_{i=0}^{n} \sum_{j=0}^{n} c_{ij} d_{ji}$ for $n \times n$ matrices C and D, the expectation value $\langle O_{\mathrm{AB}} \rangle$ can expressed as [52]

$$\langle O_{\mathrm{AB}} \rangle = \mathrm{Tr}(O\rho) \qquad \text{with} \qquad \rho = \sum_{i,j=0}^{1} \Big(\sum_{k=0}^{1} \alpha^*_{jk} \alpha_{ik} \Big) \, |i\rangle_{\mathrm{A}} \, {}_{\mathrm{A}}\langle j| . \tag{2.70}$$

Measuring expectation values of observables is the only available tool to gain knowledge about a quantum system. Therefore, the object ρ, referred to as the *density matrix*, describes the characteristics of subsystem A. The density matrix is a hermitian, positive semi-definite operator whose trace sums to 1 to fulfill the normalization condition for the probabilities to find the system in any of the basis states.

The density matrix ρ expressed in the basis formed by its orthogonal eigenstates $\{|e\rangle\}$ reads [52]

$$\rho = \sum_{e} p_e \, |e\rangle \, \langle e| \, . \tag{2.71}$$

where $\sum_e p_e = 1$ and $0 \leq p_e \leq 1$ as $\mathrm{Tr}(\rho) = 1$ and ρ is positive semi-definite. If there is only one non-zero coefficient $p_{e'}$, then $\rho = |e'\rangle \, \langle e'|$, and system A is referred to be in a *pure state.* The state of the combined system can be written

$$|\psi\rangle_{\mathrm{AB}} = |e'\rangle \otimes |\psi\rangle_{\mathrm{B}} \, . \tag{2.72}$$

The state $|\psi\rangle_{\mathrm{AB}}$ is a separable and, therefore, a non-entangled state. If there is more than one non-zero coefficient p_e, the state of A is a mixture of pure states with respective weights p_e. The subsystem A is in a *mixed state*, and the systems A and B are entangled.

Let us assume the two states $|\phi\rangle_{\mathrm{AB}} = \frac{1}{\sqrt{4}}(|00\rangle + |10\rangle + |01\rangle + |11\rangle)$ and $|\chi\rangle_{\mathrm{AB}} = \frac{1}{\sqrt{2}}(|00\rangle + |11\rangle)$. The corresponding density matrices for subsystem A in the computational basis read

$$\rho_\phi = \frac{1}{2}\begin{pmatrix} 1 & 1 \\ 1 & 1 \end{pmatrix} \qquad \text{and} \qquad \rho_\chi = \frac{1}{2}\begin{pmatrix} 1 & 0 \\ 0 & 1 \end{pmatrix}. \tag{2.73}$$

In the basis $\{|+\rangle, |-\rangle\}$ the density matrix ρ_ϕ reads

$$\rho_\phi = \frac{1}{2}\begin{pmatrix} 1 & 0 \\ 0 & 0 \end{pmatrix} = |+\rangle\langle+|, \tag{2.74}$$

meaning that the subsystems A and B are not entangled. In fact $|\phi\rangle_{\mathrm{AB}}$ can be written as $|{+}{+}\rangle$. In contrast, $\rho_\chi = \frac{1}{2}(|0\rangle\langle 0| + |1\rangle\langle 1|) = \frac{1}{2}(|+\rangle\langle+| + |-\rangle\langle-|)$ is a mixture of pure states, and $|\chi\rangle_{\mathrm{AB}}$ cannot be written as a product state, meaning that subsystems A and B are entangled. Performing a Z measurement on system A for the two states $|\phi\rangle_{\mathrm{AB}}$ and $|\chi\rangle_{\mathrm{AB}}$ yields the same measurement statistics with randomly selected outcomes of $+1$ and -1. However, if one measures in the X basis, the outcome will still be random for $|\chi\rangle_{\mathrm{AB}}$ but will always return $+1$ for $|\phi\rangle_{\mathrm{AB}}$, as subsystem A is in an eigenstate of X in this case.

The Pauli matrices given in Eqn. 2.19, together with the identity matrix, form a basis of the 2×2 hermitian matrices. Therefore, a single-qubit density matrix can be written as [46]

$$\rho = a_0\mathbb{1} + a_1 X + a_2 Y + a_3 Z \tag{2.75}$$

with $a_i \in \mathbb{R}$. As the Pauli matrices have a trace of 0, the coefficient a_0 has to be $\frac{1}{2}$ [52]. Furthermore, $r^2 = a_1^2 + a_2^2 + a_3^2 \leq 1$ to ensure $\det(\rho) = \frac{1}{4}(1 - r^2) \geq 0$ so that the density matrix is positive semi-definite [52]. A violation of this inequality is equivalent to the existence of negative eigenvalues of the density matrix. This is unphysical as it would correspond to a negative probability to find the system in the respective eigenstate of the density operator.

The vector $\boldsymbol{a} = (a_1, a_2, a_3)^\intercal$, with $r^2 = 1$, describes a point on the surface of the Bloch sphere, where its three components are the projections of the Bloch vector on the X, Y and Z axis. On the contrary, mixed states with $r^2 < 1$ lie within the Bloch sphere, where a higher degree of entanglement between the accessible and inaccessible subsystems leads to a quantum state closer to the origin of the Bloch sphere.

Now, one might wonder how this is relevant to the description of a quantum information processor. In the previous sections, it was assumed that the constituents of a quantum processor are perfect two-level systems. In reality, this is usually not the case. The physical systems encoding qubits can have more than two states and be undesirably coupled to an environment providing additional degrees of freedom. The density matrix formalism allows for describing the qubit's state, although there might be entanglement with other degrees of freedom.

Furthermore, the classical control system of a quantum information processor can be subject to undesired drifts in the control parameters, e.g., rotation angles or axes of gate operations. Consequently, a slightly different gate sequence is implemented when repeatedly implementing a computation. The observed quantum state prepared under fluctuating classical control can be described as a mixture of different realizations that can be treated using the density matrix formalism.

3

TRAPPED-ION QUANTUM PROCESSOR

The fundamental information carriers of a quantum information processor are physical systems providing two states that can encode a qubit. A promising candidate for such a system is atomic ions, where the quantum information is encoded in their internal electronic states [28, 29]. Due to their charge, ions exposed to electric fields see a force that can be employed to control their state of motion. Carefully engineering the properties of the electric field even allows one to trap ions in a confined spatial region [58]. Furthermore, ions create an electric field themselves, affecting other ions in spatial proximity. This interaction between trapped ions can be exploited to create entanglement between qubits encoded in the ions' electronic states. Electronic states encoding the qubit, but also external motional degrees of freedom of ions can be manipulated by illuminating the ions with laser light [59].

This chapter provides a short introduction to trapped-ion QIP. Section 3.1 discusses how ions can be spatially confined, and Section 3.2 describes how the basic building blocks of QIP introduced in the previous section can be implemented in trapped-ion systems. In Section 3.3, error processes affecting trapped-ion qubits and a framework modeling these processes are addressed.

3.1 Trapping charged particles

Applying an electric field $\boldsymbol{E} = -\nabla\phi$, where ϕ is the electric potential, to a charged particle with charge q generates a force $\boldsymbol{F} = q\boldsymbol{E}$ acting on the particle. The magnitude of the force is proportional to $|\boldsymbol{E}|$ and, for positively charged particles we are concerned with in this thesis, the direction of the force is along $\boldsymbol{E}$. One would now naïvely think that an ion trap can be constructed by creating a potential ϕ with a maximum at the desired ion position. Unfortunately, a local maximum of a static electric potential cannot exist in free space, as [60]

$$\nabla^2\phi = 0 \tag{3.1}$$

according to Gauss's law. Consequently, a charged particle cannot be trapped solely by static electric fields in free space. However, trapping the ion in free space is necessary to provide isolation of a qubit encoded in the ion's internal state from the environment. The limitation imposed by Gauss's law can be circumvented by allowing $\boldsymbol{E}$ to be time-dependent. In doing so, averaged over time a force pointing towards an equilibrium position fixed in space can be exerted on the particle. In 1953, Paul proposed a device providing two-dimensional mass-dependent confinement of charged particles and suggested using the device as a mass filter for an ion beam along the third, non-confined axis [61]. An ion trap for QIP on the contrary requires confinement in all three spatial dimensions. The macroscopic, linear Paul

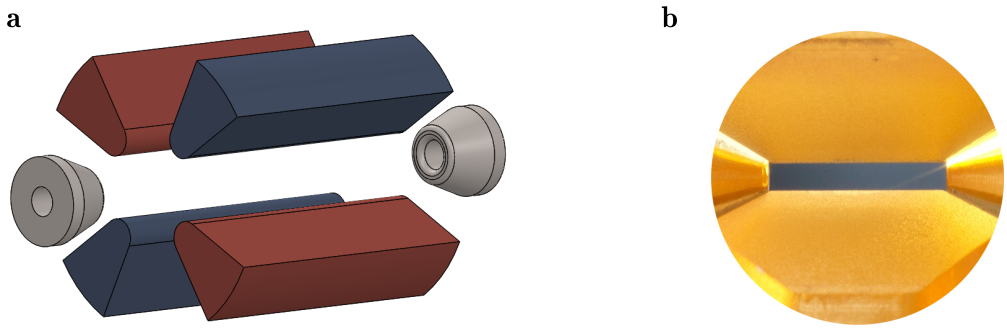

Figure 3.1: Macroscopic Paul trap. **a** Schematic depiction of the trap, where the line between the center points of the gray electrodes is referred to as the main trap axis. A radio frequency (RF) voltage is applied to the blade electrodes shown in red while the pair of blue blades are at ground potential, providing confinement in the directions orthogonal to the trap axis. A static voltage is applied to the gray electrodes aligned along the main trap axis to provide confinement in the third direction. The electrodes are not drawn to scale for better visibility of electrodes in the background. **b** Photograph of the Paul trap. At the top and bottom, the RF electrodes are shown, and the electrodes providing confinement along the main trap axis can be seen on the left and right.

trap used to obtain most of the results in this thesis is depicted schematically in Figure 3.1a and photographically in Figure 3.1b. The electrodes depicted in red and blue on the left provide confinement in two-dimensions perpendicular to the *main trap axis*, defined as the line between the center points of the gray electrodes. The colored electrodes are called *radio frequency (RF) electrodes*, whereas the gray electrodes are referred to as *endcap electrodes*. The geometry of the RF electrodes resembles the device proposed by Paul [61]. One pair of opposing electrodes is at ground potential, while an oscillating voltage is applied to the other pair. A static voltage is applied to the endcap electrodes providing confinement along the main trap axis. The time-dependent potential created by this electrode arrangement can be approximated by [62]

$$\phi(\boldsymbol{r},t) = \phi_{\mathrm{AC}} + \phi_{\mathrm{DC}} = \frac{\kappa_r V_{\mathrm{AC}}}{2R^2}(x^2 - y^2)\cos(\Omega_{\mathrm{AC}} t) + \frac{\kappa_z V_{\mathrm{DC}}}{2Z^2}(2z^2 - x^2 - y^2), \tag{3.2}$$

with $\boldsymbol{r} = (x, y, z)^\intercal$. Here, V_{AC} is the amplitude of the RF voltage with a frequency of Ω_{AC} applied to the electrodes shown in red. A static voltage of V_{DC} is applied to the gray electrodes. The distances between two opposing red/blue and gray electrodes are $2R$ and $2Z$, respectively. The prefactors κ_r and κ_z account for deviations of the electrodes' shape from hyperbolic surfaces [63, 64], originally proposed by Paul [58, 61]. Using non-hyperbolic electrodes allows one to decrease the solid angle the electrodes cover from the viewpoint of the trapped particle, facilitating the illumination of the particle with laser light.

The equation of motion of a charged particle with mass m and charge Q within the potential ϕ is given by

$$\ddot{\boldsymbol{r}} = -\frac{Q}{m}\nabla\phi(\boldsymbol{r},t). \tag{3.3}$$

It can be transformed into the standard form of the Mathieu equation

$$\frac{d^2u}{d\xi^2} + (a_u - 2q_u \cos(2\xi))u = 0 \tag{3.4}$$

for each Cartesian coordinate $u \in \{x, y, z\}$ using the substitutions

$$\begin{aligned} a_x = a_y &= -\frac{4Q\kappa_z V_{\mathrm{DC}}}{mZ^2\Omega_{\mathrm{AC}}^2}, & q_x = -q_y &= -\frac{2Q\kappa_r V_{\mathrm{AC}}}{mR^2\Omega_{\mathrm{AC}}^2}, \\ a_z &= \frac{8Q\kappa_z V_{\mathrm{DC}}}{mZ^2\Omega_{\mathrm{AC}}^2}, & q_z &= 0, \end{aligned} \tag{3.5}$$

and

$$\xi = \frac{\Omega_{\mathrm{AC}} t}{2}. \tag{3.6}$$

Given a particular set of voltages, V_{DC} and V_{AC}, the solution to the equation of motion for a range of particle masses can be a bounded trajectory. This means that for suitable initial values of particle position and momentum, the distance of the particle to the center of the trap is much smaller than R and Z for all times. Averaged over a period of the RF voltage, a force is exerted on the particle that points towards the trap center. The particle's motion can be approximated by the motion of a particle in the harmonic pseudopotential [65]

$$\Phi(\boldsymbol{r}, t) = \frac{1}{2} m \sum_{u \in \{x,y,z\}} \omega_u^2 u^2 \qquad \text{with} \qquad \omega_u = \frac{\Omega_{\mathrm{AC}}}{2} \sqrt{a_u + \frac{q_u^2}{2}}. \tag{3.7}$$

Combining Eqns. 3.5 and 3.7, one can see that the frequency of the harmonic oscillator along the z direction does not depend on the voltage applied to the RF electrodes. The Hamiltonian of a single charged particle in this harmonic potential is

$$H = \frac{1}{2} m \Big(\sum_{u \in \{x,y,z\}} \dot{u}^2 + \omega_u^2 u^2 \Big) = \sum_{u \in \{x,y,z\}} \frac{p_u^2}{2m} + \frac{1}{2} m \omega_u^2 u^2. \tag{3.8}$$

For applications in QIP, a trapped particle has to be stationary in order to render it reliably addressable with focused laser light. This means that the energy of the harmonic oscillator describing the particle's motion has to be sufficiently low, so that the oscillation amplitude is much smaller than the wavelength of the laser light. This goal can be achieved by cooling the trapped particle. Laser cooling techniques enable the reduction of the energy of the charged particle to an extent where a quantum mechanical treatment of the system is required [29]. The quantum mechanical expression for the Hamiltonian is [59]

$$H = \sum_{u \in \{x,y,z\}} \hbar \omega_u \left(\hat{a}^\dagger \hat{a} + \frac{1}{2} \right) \tag{3.9}$$

with the ladder operators [59]

$$\hat{a}_u = \frac{1}{\sqrt{2m\hbar\omega_u}} \left(m\omega_u u + \mathrm{i}p_u\right) \qquad \text{and} \qquad \hat{a}_u^\dagger = \frac{1}{\sqrt{2m\hbar\omega_u}} \left(m\omega_u u - \mathrm{i}p_u\right). \tag{3.10}$$

Therefore, a single charged particle in a Paul trap can be modeled as a three-dimensional quantum mechanical harmonic oscillator. The operator $n_u = \hat{a}_u^\dagger \hat{a}_u$ quantifies the number of excitations, referred to as *phonons*, being present in the respective direction.

If multiple particles are trapped in the same trap, the particles do not only see the external potential given by the Paul trap but also interact with each other via the Coulomb interaction [66]. The particles can be arranged as a chain along the z axis if $\frac{\omega_r}{\omega_z} > 0.73N^{0.86}$, where $\omega_r = \omega_x = \omega_y$ and N is the number of particles in the trap [67]. This gives rise to $3N$ normal modes of oscillation of the interacting particles, where N modes oscillate along the x, y and z direction each. These normal modes allow one to describe the collective motion of multiple particles trapped in the same pseudopotential. The lowest frequency normal mode along z corresponds to all ions oscillating in phase and with equal amplitude. The relative position of the ions with respect to each other does not change. Such a normal mode is referred to as *center-of-mass (COM) mode*. The motional frequency ω_z of this mode does not depend on the number of ions in the linear chain, so that the entire ion chain oscillates as a single particle would do. For the mode along the z axis next in frequency the ions oscillate with an amplitude proportional to the distance of the ions position to the trap center [66]. This mode is referred to as *breathing mode* and has an oscillation frequency of $\sqrt{3}\omega_z$. Oscillation frequencies and amplitudes for higher frequency modes can be found by numerically solving the equations of motions of the multi-particle system [66].

For the motion along the x and y directions the mode structure is inverted compared to z-axis modes, so that the highest frequency modes are the COM modes with oscillation frequencies of ω_x and ω_y, respectively. The frequency difference to the breathing modes is about $0.05\omega_z$ [68]. If ω_r is fixed, the frequency ω_z has to be decreased with increasing ion number in order for the ions to form a linear chain. In a 16-ion chain the ratio $\frac{\omega_r}{\omega_z}$ has to be larger than 7.9 [67]. Therefore, the frequency difference between motional modes is significantly smaller for motional modes along x and y compared to modes along z [68].

3.2 Ions as qubits

Encoding quantum information in electronic states of trapped ions was proven to be a viable path for QIP by several research groups [29]. Various atomic species provide states that fulfill the requirements for encoding and storing quantum information: First, the states must not decay to other electronic states on typical timescales of a computation and second, they have to allow for maintaining a fixed phase relation with respect to each other. These properties ensure that encoded quantum information is not altered unintendedly during a computation. On the other hand, the encoded information can be manipulated and read out by exposing the trapped ions to laser or microwave radiation [29]. Furthermore, atoms of the same species and isotope are identical by nature which ensures reproducibility and yields benefits when scaling up the qubit register size of a quantum information processor.

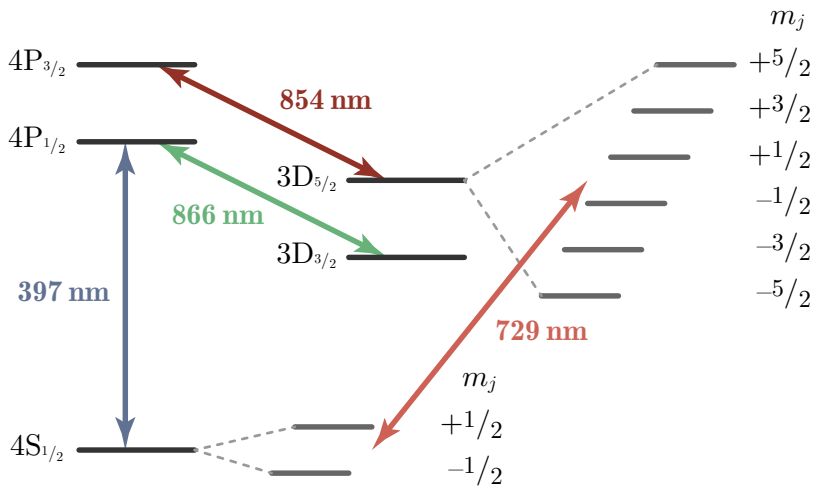

Figure 3.2: Energy scheme of $^{40}Ca^+$. On the right-hand side of $4S_{1/2}$ and $3D_{5/2}$, the splitting of the states into multiple Zeeman sublevels in an external magnetic field is shown. The usual qubit encoding used throughout most of this thesis is in the states $4S_{1/2,m_j=-1/2}$ and $3D_{5/2,m_j=-1/2}$.

3.2.1 *Encoding of quantum information in ions*

Alkaline earth metals are a common choice as atomic species in trapped-ion QIP. Singly ionized, they become hydrogen-like and provide simple energy schemes allowing for the control of the electronic state with few external controls, e.g., lasers. The energy scheme of $^{40}Ca^+$ is shown in Figure 3.2. Ions excited to the states $4P_{1/2}$ and $4P_{3/2}$ rapidly decay to the ground state $4S_{1/2}$ within nanoseconds [69, 70]. On the contrary, the transitions from the states $3D_{3/2}$ and $3D_{5/2}$ to the ground state are dipole-forbidden, rendering the latter states metastable. The lifetime of the state $3D_{5/2}$ is $T_1 = 1.168(9)\,\mathrm{s}$ [71]. In an external magnetic field all states shown in Figure 3.2 split into Zeeman sublevels, which are shown as gray horizontal lines for the states $4S_{1/2}$ and $3D_{5/2}$. A qubit can be encoded using one of the Zeeman sublevels of the ground state and a state in the Zeeman manifold of the $3D_{5/2}$, e.g., $4S_{1/2,m_j=-1/2}$ and $3D_{5/2,m_j=-1/2}$. As the transition frequency between those two states lies in the optical regime, such an encoding is referred to as *optical qubit encoding*. The numerously available Zeeman sublevels in the described trapped-ion system also allow for other qubit encodings. In this thesis, also the qubit encoding in the two ground states $4S_{1/2,m_j=-1/2}$ and $4S_{1/2,m_j=+1/2}$ is employed. This qubit encoding is called *ground-state qubit encoding*.

The electric quadrupole transition connecting the states $4S_{1/2}$ and $3D_{5/2}$ of the optical qubit encoding can be addressed by illuminating a trapped ion with light at $729\,\mathrm{nm}$. This system can be described by the Hamiltonian [72]

$$\begin{aligned} H &= H_\mathrm{p} + H_\mathrm{o} + H_\mathrm{i} \\ &= \frac{\hbar\omega_\mathrm{a}}{2}\sigma_z + \hbar\omega_\mathrm{o}\left(\hat{a}^\dagger\hat{a} + \frac{1}{2}\right) + \frac{\hbar\Omega}{2}\left(\mathrm{e}^{\mathrm{i}kx}\sigma^+\mathrm{e}^{-\mathrm{i}\omega_\mathrm{l}t} + \mathrm{e}^{-\mathrm{i}kx}\sigma^-\mathrm{e}^{\mathrm{i}\omega_\mathrm{l}t}\right). \end{aligned} \tag{3.11}$$

The Hamiltonian is given by the sum of the Hamiltonians describing the electronic state of the trapped particle H_p, the motion of the particle in the harmonic potential H_o, and

the interaction between the trapped particle with laser light H_i. Here, $\hbar\omega_\mathrm{a}$ is the energy difference between the qubit states, ω_o is the frequency of the harmonic oscillator describing the motion of the ion in the trap, Ω is the Rabi frequency, k and ω_l are the wavenumber and angular frequency of the laser field, and $\sigma_z = Z$, $\sigma^+ = \frac{1}{2}(X + \mathrm{i}Y)$ and $\sigma^- = \frac{1}{2}(X - \mathrm{i}Y)$ (see Eqn. 2.19) are spin operators. In the interaction Hamiltonian, fast-rotating terms are neglected, referred to as *rotating wave approximation* [73]. Furthermore, only one motional mode is considered and the laser light is assumed to be a plane wave. The particle oscillates along the laser light's direction of propagation, in this case presumed to be along the x direction. Expressing the ion's position x in terms of the ladder operators $\hat{a}$ and $\hat{a}^\dagger$ from Eqn. 3.10, the interaction Hamiltonian reads

$$H_\mathrm{i} = \frac{\hbar\Omega}{2}\left(\mathrm{e}^{\mathrm{i}\eta(\hat{a}+\hat{a}^\dagger)}\sigma^+\mathrm{e}^{-\mathrm{i}\omega_\mathrm{l}t} + \mathrm{e}^{-\mathrm{i}\eta(\hat{a}+\hat{a}^\dagger)}\sigma^-\mathrm{e}^{\mathrm{i}\omega_\mathrm{l}t}\right) \tag{3.12}$$

with $\eta = k\sqrt{\frac{\hbar}{2m\omega_\mathrm{o}}}$ being the *Lamb-Dicke parameter*. With $U = \mathrm{e}^{-\frac{\mathrm{i}}{\hbar}(H_\mathrm{p}+H_\mathrm{o})t}$, the Hamiltonian in the interaction picture reads

$$H_\mathrm{i}' = U^\dagger H_\mathrm{i} U = \frac{\hbar\Omega}{2}\left(\mathrm{e}^{\mathrm{i}\eta(\hat{a}'+\hat{a}'^\dagger)}\sigma^+\mathrm{e}^{-\mathrm{i}(\omega_\mathrm{l}-\omega_\mathrm{a})t} + \mathrm{e}^{-\mathrm{i}\eta(\hat{a}'+\hat{a}'^\dagger)}\sigma^-\mathrm{e}^{\mathrm{i}(\omega_\mathrm{l}-\omega_\mathrm{a})t}\right), \tag{3.13}$$

where the modified ladder operator $\hat{a}' = \hat{a}\mathrm{e}^{-\mathrm{i}\omega_\mathrm{o}t}$ is time-dependent [73]. The time-independent part of the Hamiltonian $H_\mathrm{p} + H_\mathrm{o}$ commutes with U and, therefore, coincides in the Schrödinger and interaction pictures.

In most practical cases, the *Lamb-Dicke approximation*

$$\mathrm{e}^{\mathrm{i}\eta(\hat{a}'+\hat{a}'^\dagger)} \approx 1 + \mathrm{i}\eta(\hat{a}' + \hat{a}'^\dagger) \tag{3.14}$$

is valid, leading to the approximate interaction Hamiltonian

$$H_\mathrm{i}' \approx \frac{\hbar\Omega}{2}\left(\sigma^+\mathrm{e}^{-\mathrm{i}(\omega_\mathrm{l}-\omega_\mathrm{a})t} + \sigma^-\mathrm{e}^{\mathrm{i}(\omega_\mathrm{l}-\omega_\mathrm{a})t}\right) \tag{3.15}$$

$$+ \mathrm{i}\eta\frac{\hbar\Omega}{2}\left(\hat{a}\sigma^+\mathrm{e}^{-\mathrm{i}(\omega_\mathrm{l}-\omega_\mathrm{a}+\omega_\mathrm{o})t} - \hat{a}^\dagger\sigma^-\mathrm{e}^{\mathrm{i}(\omega_\mathrm{l}-\omega_\mathrm{a}+\omega_\mathrm{o})t}\right) \tag{3.16}$$

$$+ \mathrm{i}\eta\frac{\hbar\Omega}{2}\left(\hat{a}^\dagger\sigma^+\mathrm{e}^{-\mathrm{i}(\omega_\mathrm{l}-\omega_\mathrm{a}-\omega_\mathrm{o})t} - \hat{a}\sigma^-\mathrm{e}^{\mathrm{i}(\omega_\mathrm{l}-\omega_\mathrm{a}-\omega_\mathrm{o})t}\right). \tag{3.17}$$

These three terms correspond to different processes of the system consisting of a trapped ion and an external drive, which is, in this case for the optical qubit encoding in $^{40}\mathrm{Ca}^+$, a laser:

- The term in Eqn. 3.15 is resonant if the laser frequency and the frequency of the atomic transition coincide. It only contains the atomic operators σ^+ and σ^- and, therefore, couples the electronic states encoding a qubit without acting on the harmonic oscillator. This process is referred to as a *carrier transition*.
- The second term in Eqn. 3.16 is called a *red sideband transition*. If the laser is red detuned from the atomic transition by the oscillator frequency ω_o, the ion can be excited while an excitation is removed from the harmonic oscillator and vice versa.

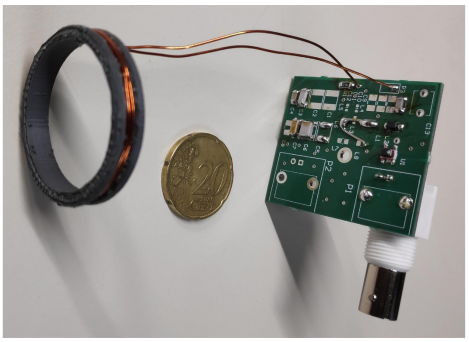

Figure 3.3: Coil and resonator circuit for directly manipulating the ground-state qubit. The coil and the resonator circuit are shown on the left and right, respectively. The drive signal with a frequency of $16.7\,\mathrm{MHz}$ is supplied via the connector on the bottom right of the image. The image shows a prototype with a slightly larger coil compared to the device used in the experiment.

- In Eqn. 3.17 the excitation of the harmonic oscillator is increased while the ion is excited if the laser is blue-detuned by ω_o from the carrier transition. This process, called *blue sideband transition*, also describes a simultaneous deexcitation of ion and harmonic oscillator.

Therefore, driving an atomic transition not only allows for changing the internal state of the ion but also affects the ion's motion in the trap. Note that in this description, only one harmonic oscillator has been taken into account for simplicity, but an extension of the framework to motional modes for multiple ions in the same potential is straightforward. Due to the collective nature of multi-ion motional modes, driving a sideband transition allows acting on the motional state of all ions trapped in a common harmonic potential.

The framework discussed above describing the interaction of a laser drive with the optical qubit can be directly transferred to the manipulation of the ground state qubit in $^{40}Ca^{+}$. In this case, the qubit can be directly manipulated by irradiating the ion chain with an RF magnetic field oscillating at the transition frequency between the two ground states. Here, the transition frequency between the states $4S_{1/2,m_j=-1/2}$ and $4S_{1/2,m_j=+1/2}$ is $16.7\,\mathrm{MHz}$. The implemented Hamiltonian is the same as the one for driving an atomic transition of a trapped ion using lasers, introduced in Eqns. 3.15 to 3.17. However, due to the long wavelength of the RF field driving the ground-state qubit transition the Lamb-Dicke parameter η is on the order of 10^{-9} in the considered setup. Therefore, sideband transitions are effectively suppressed [74]. In the following, the experimental setup to drive the ground-state qubit is discussed.

Figure 3.3 shows the antenna emitting the RF field. The coil antenna constitutes the inductor of a resonant circuit* with a resonance frequency of $16.7\,\mathrm{MHz}$, given by the magnetic field applied to the ions. The antenna, a self-made coil with a diameter of $1.2\,\mathrm{cm}$ and 10 windings, is mounted outside the vacuum chamber as close as possible to the ion chain to maximize the coupling strength. Driving the resonator with a power of $2\,\mathrm{W}$ yields a Rabi frequency of about $2\pi \times 14\,\mathrm{kHz}$. Figure 3.4 shows the probability of finding each ion in the state $4S_{1/2,m_j=-1/2}$ in a 16-ion chain plotted against the RF field irradiation duration. The difference between the maximum and minimum Rabi frequency along the ion chain

* At this point, I would like to thank Matthias Bock for providing the printed circuit board for the resonator circuit.

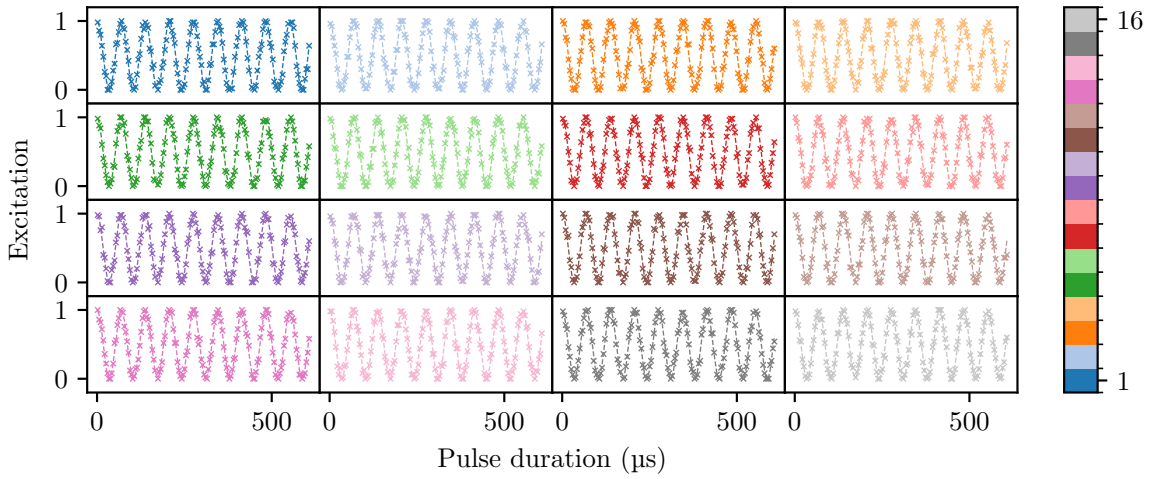

Figure 3.4: Rabi oscillations on the ground-state qubit in a 16-ion chain. The probability of finding the ion in the state $4S_{1/2,m_j=-1/2}$ is plotted against the duration of the pulse applied to the RF antenna for ion 1 in the top left and ion 16 in the bottom right corner.

normalized to the minimum Rabi frequency is $\frac{\Omega_{\max}-\Omega_{\min}}{\Omega_{\min}} = 0.002(1)$. As the coil induces an interaction that acts on the entire ion chain it is important that the Rabi frequency is as homogeneous as possible along the ion chain. Otherwise manipulations of the qubit state would act differently on different ions.

For both, the optical and ground-state qubit encoding, the transition frequency between the two qubit states depends on the magnetic field at the ion's position. Therefore, the phase relation between the drive manipulating the qubit, e.g., laser or RF drive, and the qubit itself varies in case of a fluctuating magnetic field affecting the qubit transition frequency*. This effect, referred to as *dephasing*, can be described as a $Z(\theta)$ rotation with time-dependent rotation angle. The rotation angle is given by

$$\theta(t) = \int_{t'=0}^{t} (\omega_\mathrm{d} - \omega_\mathrm{q})\, dt', \tag{3.18}$$

where ω_d and ω_q are the angular frequencies of the drive and the qubit transition, respectively. The time $t' = 0$ is defined as the start of the manipulation of the qubit. Let us assume that a qubit is prepared in the state $|+\rangle$, as shown on the Bloch sphere in Figure 3.5a. The corresponding density matrix is given by

$$\rho = |+\rangle\langle+| = \frac{1}{2}\begin{pmatrix} 1 & 1 \\ 1 & 1 \end{pmatrix}. \tag{3.19}$$

During a subsequent evolution under a fluctuating transition frequency, the Bloch vector undergoes a Z rotation as described above. By repeating this thought experiment, one ends up with different rotation angles of the Z rotation for every realization of the noise,

* Exactly the same behavior would be observed if the qubit transition frequency would be stable and the drive frequency would fluctuate. The following discussion can be directly transferred to a situation of fluctuating qubit transition drive.

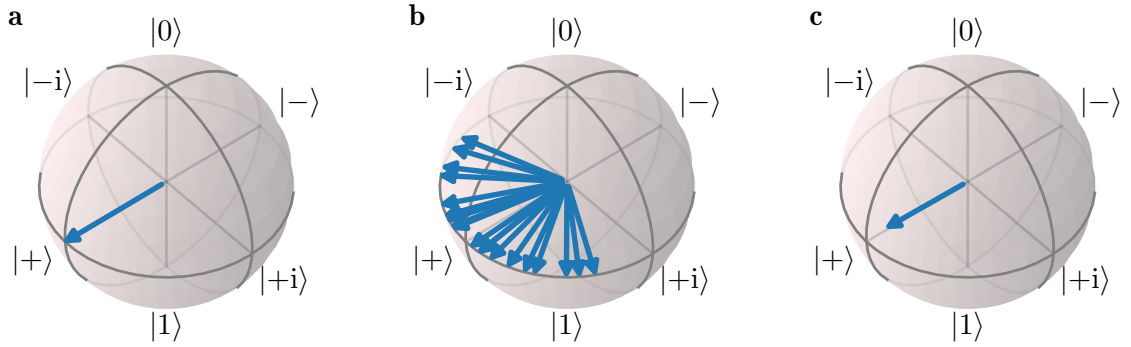

Figure 3.5: Depiction of dephasing of a single qubit on the Bloch sphere. **a** A single qubit is prepared to the superposition state $|+\rangle = \frac{1}{\sqrt{2}}(|0\rangle + |1\rangle)$. **b** Letting the qubit evolve under a fluctuating transition frequency with respect to the qubit drive introduces different rotations around the Z axis for different realizations of the stochastic process describing the transition frequency fluctuation. **c** Averaging over the realizations shown in **b** yields a Bloch vector shrunk towards the Z axis.

as depicted in Figure 3.5b. The resulting quantum state is described by a mixture of superposition states

$$\rho'(t) = \frac{1}{N}\sum_{i=1}^{N}(|0\rangle + \mathrm{e}^{\mathrm{i}\theta_i}|1\rangle)(\langle 0| + \mathrm{e}^{-\mathrm{i}\theta_i}\langle 1|), \tag{3.20}$$

where N is the number of realizations. The averaged state can be described as a Bloch vector shrunk towards the Z axis of the Bloch sphere, shown in Figure 3.5c. For white noise of the frequency difference $\omega_\mathrm{d} - \omega_\mathrm{q}$, the length of the Bloch vector shrinks exponentially with the evolution time after preparation [75]. The averaged state is described by the density matrix

$$\rho'(t) = \frac{1}{2}\begin{pmatrix} 1 & \mathrm{e}^{-\frac{t}{T_2}} \\ \mathrm{e}^{-\frac{t}{T_2}} & 1 \end{pmatrix}, \tag{3.21}$$

where t is the evolution time and T_2 is a the characteristic time constant of the dephasing process given by the magnitude of the noise.

The *coherence time* T_2 can be experimentally determined by implementing the thought experiment discussed above, called *Ramsey experiment* [76]. After the preparation of a superposition state, the qubit undergoes free evolution for a time t. After the evolution time an analysis pulse with rotation angle $\frac{\pi}{2}$ and a variable drive phase is applied, followed by a measurement of the qubit. Repeating this experiment multiple times for different analysis pulse phases leads to a sinusoidal variation of the probability to find $|1\rangle$ with the analysis phase. The amplitude of the sinusoidal curve is called *Ramsey contrast*. The Ramsey contrast is proportional to the absolute value of the off-diagonal elements of the single-qubit density matrix $\rho'(t)$ in Eqn. 3.21. Fitting an exponential function to the Ramsey contrast versus time allows one to extract the coherence time T_2.

In the setup considered here, the typical coherence time in the ground state encoding is on the order of $5\,\mathrm{ms}$. In Figure 3.6 the Ramsey contrast for different waiting times between

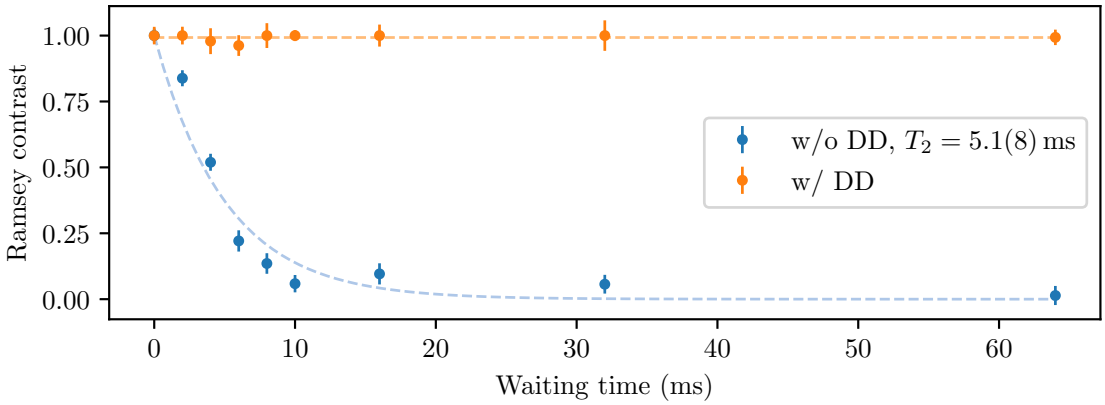

Figure 3.6: Ramsey contrast decay for the ground-state qubit encoding with and without DD. The Ramsey contrast on the vertical axis is plotted against the waiting time between the preparation and analysis pulses on the horizontal axis. Without DD (labeled *w/o DD*), the timescale of the decay is $5.1(8)\,\mathrm{ms}$. When applying an RF pulse inverting the population every $1\,\mathrm{ms}$, no significant decay can be observed for up to $64\,\mathrm{ms}$ (labeled *w/ DD*).

preparation of the superposition and the analysis pulse is shown in blue. Dephasing of the qubit during the evolution time can be mitigated by periodically exchanging the population of the two ground states, canceling the destructive effects of slow magnetic field fluctuations [77], a technique called *dynamical decoupling (DD)*. The simplest instance of a DD sequence is a single pulse with rotation angle π halfway through the evolution time. If the deviation of the qubit drive frequency from the qubit transition frequency $\delta\omega = \omega_\mathrm{d} - \omega_\mathrm{q}$ is constant during the evolution, the state of the qubit is $|-\rangle$ at the end of the evolution regardless of the magnitude of the deviation. Applying another π pulse at the end of the free evolution recovers the prepared state $|+\rangle$. If $\delta\omega$ varies on timescales shorter than the evolution time, the dephasing effect can not be fully suppressed. However, dividing the evolution time in multiple segments and applying a π pulse in the middle of each segment allows one to suppress dephasing caused by frequency deviations varying on timescales much larger than the length of each segment. For an even number of segments the qubit state returns to $|+\rangle$, whereas for an odd number of segments $|-\rangle$ is prepared at the end of the evolution time. The data shown in orange in Figure 3.6 shows the Ramsey decay for waiting times up to $64\,\mathrm{ms}$ under application of DD. The DD pulses are applied every $1\,\mathrm{ms}$ using the RF coil directly driving the ground-state qubit. Whereas the timescale of the Ramsey contrast decay is about $5\,\mathrm{ms}$ without DD, no significant decay can be observed for up to $64\,\mathrm{ms}$ if DD is applied*.

3.2.2 *State preparation*

The first objective of QIP is to prepare a defined state of the physical system encoding the qubits a quantum algorithm is supposed to act on. Translated to the situation discussed in this thesis, one has to be able to reliably prepare a trapped ion in a desired electronic state, e.g., $4\mathrm{S}_{1/2,m_j=-1/2}$.

* Stating a decoherence time in this case is not possible, as the waiting time in this measurement is not long enough to perform a reliable fit to the measured data.

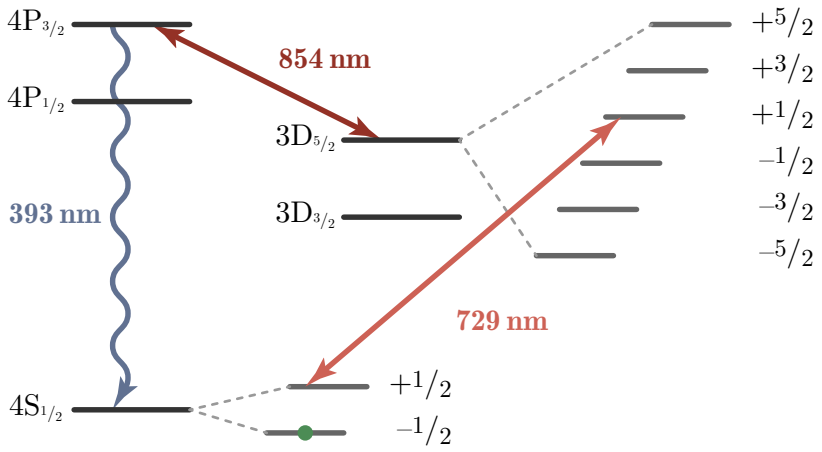

Figure 3.7: Optical pumping scheme for state initialization. Population in $4S_{1/2,m_j=+1/2}$ is excited to $3D_{5/2,m_j=+1/2}$, from where it rapidly decays back to the ground state under illumination with light resonant to the transition $3D_{5/2} \leftrightarrow 4P_{3/2}$. Population in the desired initial state $4S_{1/2,m_j=-1/2}$ (see green symbol) does not participate in this cyclic transition and population accumulates in the ground state's $m_j = -1/2$ Zeeman sublevel.

Let us assume for now that the ion under consideration is in one of the two ground states $4S_{1/2,m_j=-1/2}$ and $4S_{1/2,m_j=+1/2}$, which is an assumption that will undoubtedly be fulfilled if one waits long enough for all excited states to decay. An option to transfer the population from $4S_{1/2,m_j=+1/2}$ to $4S_{1/2,m_j=-1/2}$ would be to drive the carrier transition $4S_{1/2,m_j=+1/2} \leftrightarrow 3D_{5/2,m_j=+1/2}$, shown in Figure 3.7 as a red arrow labeled $729\,\mathrm{nm}$, and wait for the population to decay to $4S_{1/2,m_j=-1/2}$. This is quite tedious due to the long lifetime of the $3D_{5/2}$ state. The decay can be accelerated by exciting the ion to $4P_{3/2}$, which decays to $3D_{3/2}$, $3D_{5/2}$, or one of the ground states on the order of nanoseconds. This excitation can be achieved by applying light at around $854\,\mathrm{nm}$ (see dark red arrow in Figure 3.7). The dominant decay channel is the one to the ground state with a probability of ≈ 0.93 [78]. A continuous process pumping the population to $4S_{1/2,m_j=-1/2}$ can be realized by simultaneously illuminating the ion with light resonant to the transition $4S_{1/2,m_j=+1/2} \leftrightarrow 3D_{5/2,m_j=+1/2}$ and light with wavelengths of $854\,\mathrm{nm}$ and $866\,\mathrm{nm}$ (green arrow in Figure 3.2). This simultaneous illumination ensures a fast decay to the ground state while avoiding trapping population in the $3D_{3/2}$ state. As soon as population reaches the state $4S_{1/2,m_j=-1/2}$ it does not participate in the process anymore and the population is trapped there. With this scheme, a reliable preparation of the desired initial state can be realized in hundreds of microseconds.

Besides the electronic state, it is also crucial to control the motional state of trapped ions before manipulating the qubit using gate operations. The rate at which the internal state of a trapped ion can be manipulated via illumination with laser light depends on the motional state of the ion [74]. Therefore, the internal state of the ion after interaction with a laser pulse is different for different numbers of excitations $n = a^\dagger a$ of the harmonic oscillator formed by the ion in the trap. For a thermal state of the harmonic oscillator having multiple contributions with different n, the laser-ion-interaction leads to a mixed internal state of the ion. Consequently, the encoded quantum information is corrupted.

As a result, it is crucial to prepare trapped ions in a defined motional state, usually the motional ground state with $n = 0$, before starting a quantum computation. A first step towards this goal is the application of Doppler cooling on the transition $4S_{1/2} \leftrightarrow 4P_{1/2}$ [59]

with a natural linewidth of $\Gamma = 2\pi \times 20.7\,\mathrm{MHz}$ [79]. After Doppler cooling the harmonic oscillator excitation is thermally distributed. The theoretically achievable minimal mean phonon number [59] is $\bar{n} \approx 13$ and $\bar{n} \approx 1.6$ for harmonic oscillator frequencies of $2\pi\times400\,\mathrm{kHz}$ and $2\pi\times3.2\,\mathrm{MHz}$, corresponding to the typical range of oscillator frequencies in the considered experimental setup. The excitation of the harmonic oscillator can be further reduced by driving a transition whose linewidth is smaller than the harmonic oscillator's frequency. While this is not the case for the Doppler cooling transition, the qubit transition $4\mathrm{S}_{1/2} \leftrightarrow 3\mathrm{D}_{5/2}$ with a linewidth of $\Gamma = 2\pi\times0.14\,\mathrm{Hz}$ [80] fulfills this requirement. In this case, one can directly access the red sideband transition, see Eqn. 3.16, exciting the ion while reducing the phonon number by 1. A subsequent relaxation to the ground state by spontaneous emission will predominantly occur on the carrier transition [59], leaving the phonon number unchanged. This constitutes a cyclic process in which the electronic state returns to the initial state, but the phonon number is reduced. This process is commonly called *sideband cooling*.

The cooling rate in this scenario is upper-bounded by the decay rate of the excited state, which is $\approx 0.9\,\mathrm{s}^{-1}$ for $3\mathrm{D}_{5/2}$ in $^{40}\mathrm{Ca}^{+}$ [81]. Reaching a mean phonon number close to $\bar{n} = 0$ starting from the steady state after Doppler cooling would require tens of seconds. The rate can be increased by simultaneously driving the red sideband transition and illuminating the ions with light at $854\,\mathrm{nm}$, as is shown in Figure 3.8*. Tuning the Rabi frequency driving the $3\mathrm{D}_{5/2} \leftrightarrow 4P_{1/2}$ transition allows controlling the effective decay rate and, therefore, the cooling rate [82]. Cooling a single motional mode to $\bar{n} \leq 0.1$ can be achieved within hundreds of microseconds to a few milliseconds [83, 84]. Only motional modes with oscillation frequencies within tens of kilohertz from the detuning of the laser at $729\,\mathrm{nm}$ to the atomic transition are cooled. Typically, the range of motional frequencies spans more than tens of kilohertz when trapping multiple particles in an ion trap. Therefore, cooling all $3N$ modes in an N-ion chain close to the ground state requires repeating the sideband cooling procedure for multiple detunings.

The Zeeman splitting in the ground and metastable state is usually larger than the harmonic oscillator frequencies, and only two distinct Zeeman sublevels, e.g., $4\mathrm{S}_{1/2,m_j=-1/2}$ and $3\mathrm{D}_{5/2,m_j=-5/2}$, are involved in the cooling process. When using the aforementioned transition for sideband cooling, a single spontaneous emission event cannot transfer population to the state $4\mathrm{S}_{1/2,m_j=+1/2}$, where it is not involved in the cooling process anymore. However, after a decay from $4\mathrm{P}_{3/2}$ to $3\mathrm{D}_{3/2}$ or $3\mathrm{D}_{5/2}$ and subsequent excitation to $4\mathrm{P}_{3/2}$ or $4\mathrm{P}_{1/2}$, respectively, population can be transferred to $4\mathrm{S}_{1/2,m_j=+1/2}$. To bring back population trapped in this dark state to the cooling cycle and maintain the cooling rate, the cooling procedure is interleaved with optical pumping, as described above and shown in Figure 3.7. The cooling procedure for each motional mode is split into up to five sideband cooling pulses with optical pumping pulses in between.

3.2.3 *Gate operations*

From Eqns. 3.15 to 3.17, one can see that illuminating trapped ions with light close to the resonance of an electronic state transition can manipulate not only the internal state of the ions, but also the state of the ions' motion in the trap. We will now discuss how to utilize this interaction to implement single-qubit and two-qubit gate operations, as introduced in Section 2.2, on qubits encoded in electronic states of trapped ions.

* Similar to optical pumping, also light at $866\,\mathrm{nm}$ is applied to avoid trapping population in $3\mathrm{D}_{3/2}$.

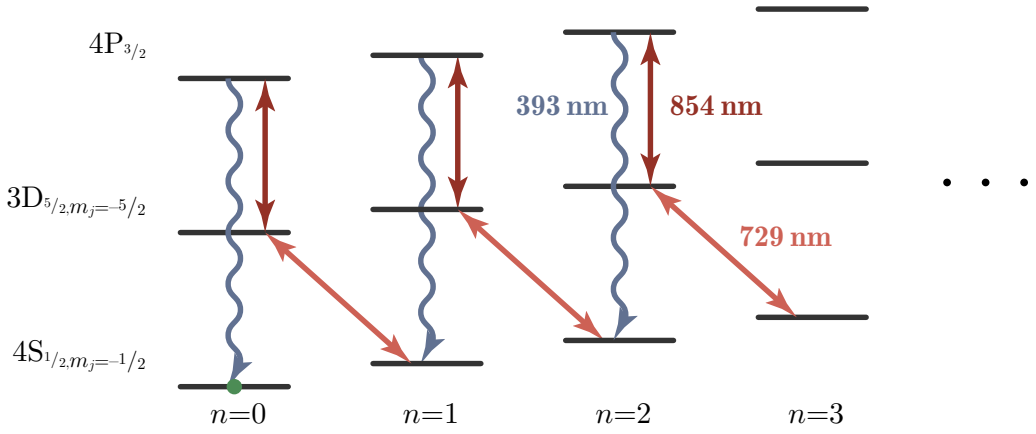

Figure 3.8: Resolved sideband cooling scheme. Illuminating a trapped ion with light resonant to the red sideband of the transition $4S_{1/2,m_j=-1/2} \leftrightarrow 3D_{5/2,m_j=-5/2}$ excites the ion while the phonon number n of the harmonic oscillator is reduced by one. After exciting the ion to $4S_{3/2}$ by illuminating it with light at $854\,\mathrm{nm}$, the ion rapidly decays back to the ground state without changing the phonon number. Population is trapped in the motional and electronic ground state (shown with a green symbol) due to the absence of a red sideband transition for population in $4S_{1/2}$ with $n = 0$.

3.2.3.1 *Single-qubit gates*

Illuminating an ion with light resonant to the transition between the two qubit states implements the following operation:

$$R_\varphi(\theta) = \mathrm{e}^{-\mathrm{i}\frac{\theta}{2}(X\cos\varphi + Y\sin\varphi)}. \tag{3.22}$$

This operation corresponds to a rotation around an axis in the equatorial plane of the Bloch sphere with a rotation angle θ, where φ is the angle between the X axis and the rotation axis. The operation can be physically realized in the experiment by controlling the amplitude and phase of a continuous-wave laser using an acousto-optic modulator (AOM). The phase of the RF signal driving the AOM is directly imprinted on the phase of the light passing through the AOM. The rotation angle θ can be controlled via the amplitude and duration of the light pulse.

Rotations around the Z axis of the Bloch sphere can be implemented by adjusting the phase of subsequent gate operations [85], often called *virtual* Z rotations. This implementation is both noise-free and instantaneous, as the application of Z rotations in software does not affect the execution time of a circuit. Virtual Z rotations in conjunction with R_φ gates in Eqn. 3.22 allow for the implementation of any single-qubit gate using the decomposition

$$U(\theta,\varphi,\lambda) = Z\left(\varphi+\frac{\pi}{2}\right)R_0(\theta)\,Z\left(\lambda-\frac{\pi}{2}\right) = \mathrm{e}^{-\mathrm{i}\frac{\varphi+\frac{\pi}{2}}{2}Z}\mathrm{e}^{-\mathrm{i}\frac{\theta}{2}X}\mathrm{e}^{-\mathrm{i}\frac{\lambda-\frac{\pi}{2}}{2}Z}, \tag{3.23}$$

where $U(\theta,\varphi,\lambda)$ is a general single-qubit unitary (see Eqn. 2.17) and $Z(\alpha)$ ($R_0(\beta)$) is a rotation around the Z (X) axis with rotation angle α (β).

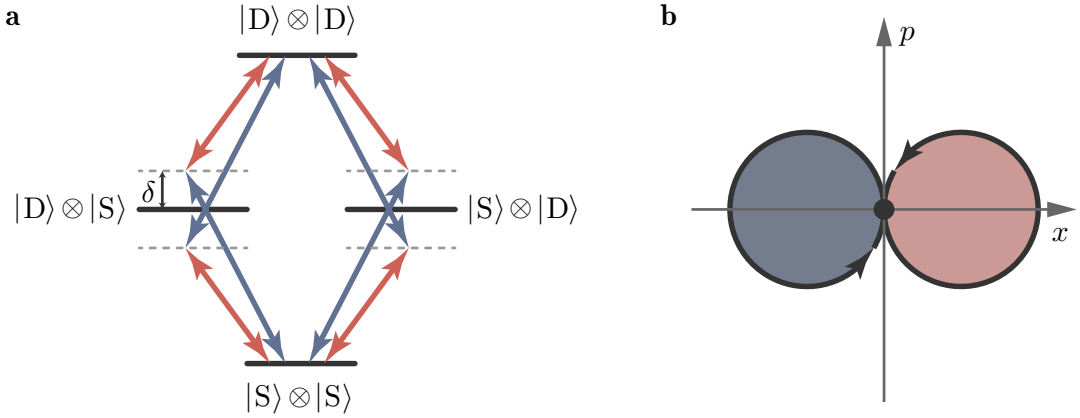

Figure 3.9: Mølmer-Sørensen interaction for two ions. **a** A bichromatic drive detuned by $+\delta$ and $-\delta$ from the transition between the qubit states $|S\rangle$ and $|D\rangle$ couples the two-qubit states $|S\rangle \otimes |S\rangle$, $|D\rangle \otimes |S\rangle$, $|S\rangle \otimes |D\rangle$ and $|D\rangle \otimes |D\rangle$. **b** Phase space trajectories of the harmonic oscillator with oscillation frequency ω_o close to the detuning δ for $+1$ (blue) and -1 (red) eigenstates of $Y^{(1,2)}$. The phase space is spanned by the two operators, $x \propto (\hat{a}^\dagger + \hat{a})$ and $p \propto \mathrm{i}(\hat{a}^\dagger - \hat{a})$. After the interaction time $t = \frac{2\pi}{\omega_\mathrm{o} - \delta}$, the harmonic oscillator returns to the initial state, and the trajectory in phase space is closed.

3.2.3.2 *Entangling gates*

In Section 3.1, the collective nature of the motion of multiple ions in a trap was discussed. The collective modes can be used to mediate an interaction between different ions in a common trap [27]. In 1999, Sørensen and Mølmer [86] suggested driving a two-photon transition on two ions between the states $|S\rangle \otimes |S\rangle$ and $|D\rangle \otimes |D\rangle$, where $|S\rangle$ and $|D\rangle$ here denote the qubit states in one of the ground states and in the Zeeman manifold of the state $3\mathrm{D}_{5/2}$, respectively. The driving fields are detuned by $\pm\delta$ from the qubit transition frequency ω_a. Figure 3.9a depicts this scenario referred to as *Mølmer-Sørensen (MS) interaction*. Red and blue arrows indicate laser light red detuned ($-\delta$) and blue detuned ($+\delta$) from the carrier transition. The interaction can be realized by illuminating the ions with light consisting of frequency components at $\omega_\mathrm{a} + \delta$ and $\omega_\mathrm{a} - \delta$, referred to as *bichromatic light*. The corresponding Hamiltonian in the interaction picture for two trapped ions reads

$$\begin{aligned} H_\mathrm{i}' \approx \sum_{i=0}^{5} \sum_{j=0}^{1} \sum_{\Delta=\pm\delta} \Bigg[& \frac{\hbar\Omega}{2} \left(\sigma^{+(j)} \mathrm{e}^{-\mathrm{i}\Delta t} + \sigma^{-(j)} \mathrm{e}^{\mathrm{i}\Delta t} \right) \\ & + \mathrm{i}\eta_i \frac{\hbar\Omega}{2} \left(\hat{a}_i \sigma^{+(j)} \mathrm{e}^{-\mathrm{i}(\Delta+\omega_{\mathrm{o},i})t} - \hat{a}_i^\dagger \sigma^{-(j)} \mathrm{e}^{\mathrm{i}(\Delta+\omega_{\mathrm{o},i})t} \right) \\ & + \mathrm{i}\eta_i \frac{\hbar\Omega}{2} \left(\hat{a}_i^\dagger \sigma^{+(j)} \mathrm{e}^{-\mathrm{i}(\Delta-\omega_{\mathrm{o},i})t} - \hat{a}_i \sigma^{-(j)} \mathrm{e}^{\mathrm{i}(\Delta-\omega_{\mathrm{o},i})t} \right) \Bigg]. \end{aligned} \tag{3.24}$$

The summation index i denotes different motional modes with Lamb-Dicke parameters η_i and oscillation frequencies $\omega_{\mathrm{o},i}$. Each of these modes is modeled as a harmonic oscillator with ladder operators $\hat{a}_i$ and $\hat{a}_i^\dagger$. The index j specifies on which of the two illuminated ions

a spin operator is acting. Assuming that the detuning Δ is set close to one of the mode frequencies $\omega_{\mathrm{o},i}$ and neglecting fast-oscillating terms, the Hamiltonian simplifies to [87]

$$H_{\mathrm{i}}' \approx -\frac{\hbar\Omega}{2}\eta(\sum_{j=0}^{1} Y^{(j)})\left[\hat{a}^\dagger \mathrm{e}^{\mathrm{i}(\omega_{\mathrm{o}}-\delta)t} + \hat{a}\mathrm{e}^{-\mathrm{i}(\omega_{\mathrm{o}}-\delta)t}\right], \tag{3.25}$$

where $Y^{(j)}$ is the Pauli operator Y acting on qubit j. Here, the index i was dropped as all modes but the one with oscillation frequency close to δ are neglected. The unitary operator, governing the evolution of the ions' electronic and motional states, of this approximated Hamiltonian can be written as [87]

$$\begin{gathered} U(t) = \hat{D}(\alpha(t)Y^{(1,2)})\mathrm{e}^{\mathrm{i}(\lambda t - \frac{\lambda}{\omega_{\mathrm{o}}-\delta}\sin(\omega_{\mathrm{o}}-\delta)t){Y^{(1,2)}}^2} \\ \text{with} \\ \alpha = \frac{\eta\Omega}{2(\omega_{\mathrm{o}}-\delta)}(\mathrm{e}^{-\mathrm{i}(\omega_{\mathrm{o}}-\delta)t}-1), \qquad Y^{(1,2)} = \sum_{j=0}^{1} Y^{(j)}, \\ \lambda = \frac{\eta^2\Omega^2}{4(\omega_{\mathrm{o}}-\delta)}, \qquad \hat{D}(\alpha) = \mathrm{e}^{\alpha\hat{a}^\dagger - \alpha^*\hat{a}}. \end{gathered} \tag{3.26}$$

This unitary describes a loop in the phase space of the harmonic oscillator with an oscillation frequency close to the detuning, as shown in Figure 3.9b. Eigenstates of the operator $Y^{(1,2)}$ with different eigenvalues undergo different trajectories in phase space, which leads to entanglement between the electronic and motional state of the trapped ions. However, at the time $t = \frac{2\pi}{\omega_{\mathrm{o}}-\delta}$ the operator $\hat{D}(\alpha(t)Y^{(1,2)})$ vanishes. At this time, the electronic state of the ions is not entangled with the harmonic oscillator*, but the illuminated ions experience a unitary evolution of the form

$$U_{\mathrm{MS}}(\theta) = \mathrm{e}^{-\mathrm{i}\frac{\theta}{2}Y\otimes Y}. \tag{3.27}$$

The rotation angle

$$\theta = -\frac{\eta^2\Omega^2}{\omega_{\mathrm{o}}-\delta}\left(t - \frac{1}{\omega_{\mathrm{o}}-\delta}\sin(\omega_{\mathrm{o}}-\delta)t\right) \tag{3.28}$$

can be controlled via the light intensity being proportional to Ω^2.

For $\theta = \frac{\pi}{2}$ the evolution of the state $|SS\rangle$ is given by

$$U_{\mathrm{MS}}\left(\frac{\pi}{2}\right)|SS\rangle = \frac{1}{\sqrt{2}}\left(|SS\rangle + \mathrm{i}\,|DD\rangle\right). \tag{3.29}$$

Therefore, the MS interaction allows for generating a maximally entangled state starting from a product state. The phase of the bichromatic light field determines the rotation axis, similar to the case of single-qubit gates in Eqn. 3.22. Up to single-qubit gates, an MS gate with $\theta = \frac{\pi}{2}$ is equivalent to a CNOT gate [88].

* The typical measurement performed at the end of a computation traces over the motional state. Therefore, entanglement between the motional and internal state of the ions leads to a mixed qubit state.

3.2.3.3 *Single-site addressing*

Implementing arbitrary algorithms in a qubit register formed by a linear chain of ions requires applying the single-qubit and entangling gates discussed above to any ion or ion pair. In the following the experimental setup to implement this selective ion-light interaction is discussed. The laser light needs to be focused so that the light field can be spatially confined to interact with a specific ion. Residual light intensity at a neighboring ion's position leads to an unintended manipulation of the neighbor ion. This erroneous effect is referred to as *crosstalk*. For typical ion-to-ion distances of $3.8\,\mu\mathrm{m}$ to $6\,\mu\mathrm{m}$, a spot size on the order of $1\,\mu\mathrm{m}$ is required. A naïve assessment using the Abbe diffraction limit yields that for a wavelength of $729\,\mathrm{nm}$ and a resolvable distance of $1\,\mu\mathrm{m}$, an optical system with an numerical aperture (NA) of ≈ 0.36 is required. Such a tightly focused laser beam has a Rayleigh length on the order of a few micrometer. This means that the focused laser beam expands rapidly with increasing distance from the focal plane of the objective. Therefore, variations in the distance between an ion and the objective along the ion chain have to be as small as possible. This is achieved by aligning the optical axis of the focusing optics perpendicular to the direction along the ion string.

Furthermore, the optical system addressing individual ions must allow for changing the target ion between two successive gates of an algorithm. Ideally, switching the focus from one ion to another can be completed on timescales similar to the duration of a single gate operation, typically a couple of microseconds for trapped-ion quantum information processors. For the implementation of entangling gates, at least two ions have to be illuminated simultaneously. Furthermore, individual control over the phase and amplitude of the light for every addressing site is required to account for previously applied virtual Z rotations and different transmission efficiencies of the optical system, respectively.

Figure 3.10: Scheme of the optical setup from the light source to the ions. The light is generated in a diode laser and is amplified in a tapered amplifier. The frequency, phase and amplitude of the light is controlled in a setup consisting of two AOMs in series. In the addressing setup the light is deflected to address individual ions before it is focused to the ion chain shown as blue dots.

In Figure 3.10, a schematic depiction of the experimental setup for individual ion addressing is shown. The continuous-wave laser light is generated in an amplified diode laser. The phase, amplitude and frequency of the light is controlled in two consecutive AOMs before being sent to the addressing setup. Here, the direction of propagation of the laser beam is changed to selectably illuminate individual ions. Then the beam is expanded in a telescope so that the necessary NA is obtained. Finally, the laser light is focused onto the ions using a high-NA objective*.

For the addressing setup we choose a system based on acousto-optic deflectors (AODs) that fulfills the requirements concerning the optical system discussed above. In an AOD

* Custom-built objective from photon gear inc. with an NA of 0.59 and an effective focal length of $34.35\,\mathrm{mm}$ at a wavelength of $729\,\mathrm{nm}$

a sound wave is generated by a transducer and propagates within a crystal leading to a periodic spatial modulation of the refractive index. The distance between two maxima of the refractive index depends on the frequency of the sound wave. Light passing through the crystal is diffracted at the grating formed by the periodic modulation of the refractive index. After the diffraction process the direction of propagation of the light is changed and also the frequency of the light is altered. Depending on the incident angle of the light, the frequency of the sound wave, typically in the RF range, is either added (*frequency upshift*) or subtracted (*frequency downshift*) from the light frequency. Furthermore, AODs provide control over the phase and amplitude of the deflected light via the RF input signal. The switching time for the AOD* used in this setup is approximately 10 µs. Furthermore, the generation of multiple deflected light beams can be straightforwardly achieved by combining multiple RF signals before routing them to the AOD.

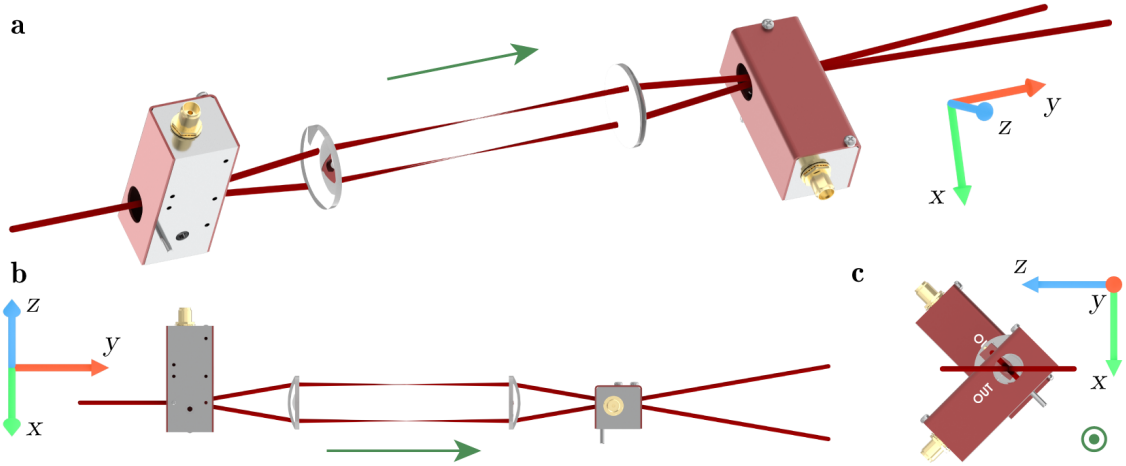

Figure 3.11: Optical setup for single-site addressing. The laser light propagates along the direction indicated by green arrows in all three subfigures. Two acousto-optic deflectors, rotated by 90° with respect to each other, deflect the laser beam without shifting its frequency. This is achieved by applying a frequency upshift in the first and a downshift in the second AOD. In between the acousto-optic deflectors, there is a 1:1 telescope that images beams with different deflection angles at the first AOD to the same spot in the second AOD. The two shown laser beams correspond to different AOD drive frequencies and, therefore, to two different ions addressed in an ion chain aligned along the Z axis. The deflection angle is exaggerated in this depiction for better visibility of the deflected beams. Subfigure **a** shows a lateral view of the setup. In **b** a view orthogonal to the optical axis is shown, whereas **c** shows a view along the optical axis in the direction opposite to the propagation direction of the laser light.

The design of the laser beam deflection setup is shown in Figure 3.11. It consists of two AODs mounted along the same optical axis. The AODs are rotated by ±45° around the optical axis, as can be seen in Figure 3.11c. For light passing through the AODs the vertical component of the deflection cancels while the horizontal deflection is added up. To ensure that beams with different deflection angles originate from the same spot in the second AOD, a 1:1 telescope is added in between the AODs. The distance between the AODs and the identical lenses is given by the focal length of the lenses, while the distance between the two lenses is twice the focal length. With this, the output beams of the setup for different RF

* AA Opto Electronic DTSXY-400-730-20

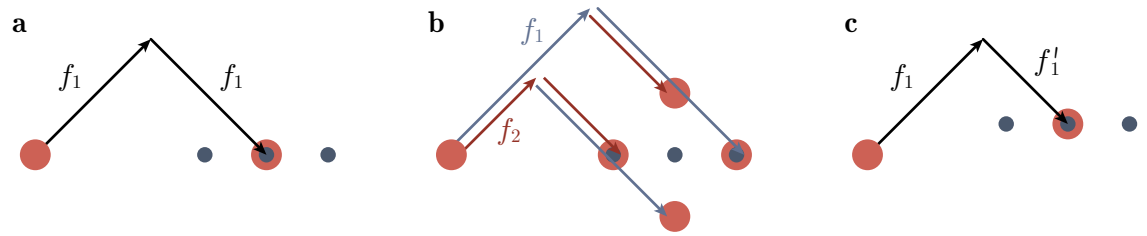

Figure 3.12: Schematic of the deflection pattern in the focal plane created by the single-site addressing system. **a** The red spot on the left is the laser beam which is not diffracted in the acousto-optic deflectors. The first AOD introduces a frequency upshift indicated by the arrow pointing to the top right, whereas the second AOD introduces a frequency downshift shown as a black arrow pointing to the bottom right. Applying RF signals with the same frequency f_1 to both acousto-optic deflectors does not introduce a frequency shift to the light transmitted through the single-site addressing system. Furthermore, the vertical components of the spatial deflection in the two acousto-optic deflectors cancel. However, the combined setup deflects the beam in the horizontal direction. The blue dots indicate the ion chain. **b** Applying two frequencies, f_1 and f_2, simultaneously to both acousto-optic deflectors creates four beam spots, where the two spots vertically displaced from the horizontal axis are detuned by $f_1 - f_2$ and $f_2 - f_1$. The frequency difference between f_1 and f_2 is exaggerated for better visibility of the four spots. **c** Introducing a detuning δ between the frequencies f_1 and $f_1' = f_1 - \delta$ used to address a single ion allows shifting the beam spot in the vertical direction.

frequencies applied to the AODs lie in the plane formed by the ion chain and the optical axis. In a prototype of the deflection setup we used achromatic lenses with a focal length of $50\,\mathrm{mm}$ for the telescope. The optical setup actually used in the trapped-ion experiment considered here is sourced from Alpine Quantum Technologies GmbH. In this setup, the lenses are designed as triplets with an effective focal length of approximately $19\,\mathrm{mm}$ to reduce aberrations.

One AOD imprints a frequency upshift to the passing light, while the other applies a frequency downshift. When driving the AODs with the same RF frequency, this results in an RF-frequency-dependent deflection of the beams, but the net frequency shift imprinted on the laser light is zero. Figure 3.12a schematically shows the deflection of a light beam with respect to the undeflected beam in the focal plane of the objective when an RF signal with frequency f_1 is applied.

For the simultaneous illumination of two ions, two RF tones with frequencies f_1 and f_2 are applied to the AODs. As can be seen in Figure 3.12b, not only the two spots that undergo frequency up- and downshifts of f_1 and f_2, respectively, but also spots that are upshifted by f_1 and downshifted by f_2 and vice versa, are present. Those spots are detuned in frequency by the difference of f_1 and f_2 with respect to the spots addressing the individual ions. Although the off-resonant spots do not lie on the ion chain's axis, they can still affect the state of the ions. Especially for the situation where two neighboring ions are illuminated, the spatial distance of the off-resonant beam spots to the illuminated ions is smaller than the inter-ion spacing potentially leading to undesired illumination of the ions with off-resonant light. However, the detuning of the off-axis spots allows for shifting them away from any carrier or sideband transition in frequency space by tuning the magnification of the telescope for beam expansion after the addressing setup (see Figure 3.10). This parameter allows tuning the ratio of the beam displacement to RF frequency change and, therefore, the

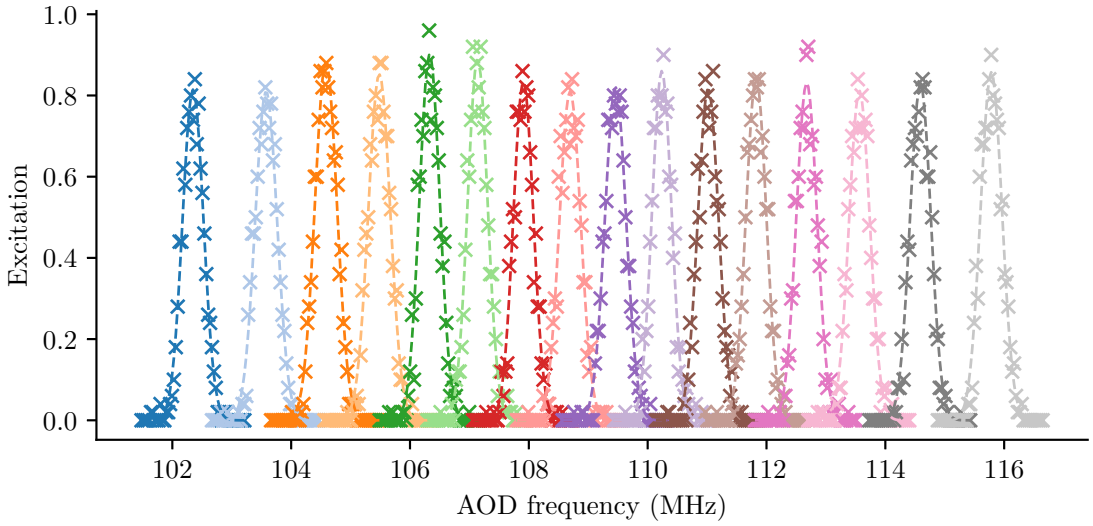

Figure 3.13: Scan of a tightly focused laser beam across a chain of 16 trapped ions. The probability of finding an ion in the excited qubit state after applying an excitation pulse is plotted against the RF signal driving the acousto-optic deflectors of the single-site addressing setup. Each color corresponds to the excitation probability of a different ion. The excitation probability of each ion is only plotted for frequencies close to the peak frequency for improved clarity.

frequency difference $f_1 - f_2$ for two illuminated ions. Besides that, the frequencies f_1 and f_2 obviously depend on the respective ion positions. Consequently, $f_1 - f_2$ depends on the inter-ion spacing and, therefore, the detuning of the off-axis beam spots can be adjusted by changing the ion trap's confinement along the trap axis.

The individual control of frequency, amplitude, and phase of each RF tone sent to the two AODs provides considerable flexibility in this addressing approach. Figure 3.12c shows a situation where a frequency shift δ is introduced between the two RF tones sent to the AODs. The first AOD is driven with a frequency f_1, while the second is driven with $f_1' = f_1 - \delta$. This effectively shifts the deflected spot in the vertical direction orthogonal to the direction along the ion chain*. Adding the frequency offset δ introduces a frequency detuning of the laser light from the atomic resonance by δ. However, this can be compensated for by shifting the laser light prior to the AOD-based addressing setup by $-\delta$, enabling two-dimensional adjustments to the beam spot position by means of RF frequency control. Furthermore, introducing a shift δ for individual ions without frequency compensation of the laser light facilitates correcting undesired carrier frequency shifts along the ion string, e.g., caused by a magnetic field gradient. This will spatially shift the beam spot with respect to the ion in the vertical direction, but as long as the shift is much smaller than the diameter of the beam spot, this effect can be neglected.

Figure 3.13 shows a scan of a single addressing beam spot resonant to the qubit transition across a 16-ion chain. On the horizontal axis, the AOD drive frequency f_1, and on the vertical axis, the probability of exciting an ion from the ground state to $3D_{5/2}$ is plotted. Different colors show the excitation probability for individual ions. The laser beam is displaced by $\approx 5\,\mu m$ for an RF frequency difference of $1\,MHz$. The distance from the left-most ion,

* The detuning δ also introduces a shift in the direction along the ion string, which can be compensated for by adjusting f_1.

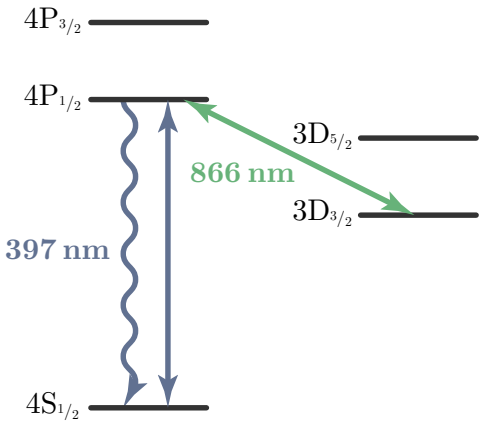

Figure 3.14: Illumination scheme for qubit state detection. When illuminating the ion chain with light at 397 nm, ions projected to the qubit state encoded in the ground state will scatter photons. Ions projected to a Zeeman sublevel of $3D_{5/2}$ instead will not scatter photons and appear dark. The ion string is additionally illuminated with light at a wavelength of 866 nm to avoid pumping initially bright ions to the dark, metastable state $3D_{3/2}$.

corresponding to the data shown in blue in Figure 3.13, to the right-most ion, corresponding to the data shown in light gray, is 66 µm.

The crosstalk to neighboring ions when addressing a specific target ion can be quantified in terms of the ratio $\epsilon = \frac{\Omega_s}{\Omega_t}$ of the Rabi frequencies at a particular spectator ion Ω_s and at the target ion Ω_t. The highest crosstalk ratios occur for next-neighbors to the target ion. A measurement of the crosstalk ratio ϵ shows a maximum and mean next-neighbor crosstalk of 0.016 and 0.009, respectively. A more detailed analysis of undesired crosstalk affecting neighbors of an illuminated ion can be found in Section 6.1.1.

3.2.4 *Qubit measurements*

Projective measurements in the computational basis in a $^{40}Ca^+$ trapped-ion quantum processor can be realized by illuminating the ions with laser light at a wavelength of 397 nm resonant to the transition $4S_{1/2} \leftrightarrow 4P_{1/2}$. For the optical qubit encoding the two computational states are $4S_{1/2,m_j=-1/2}$ and $3D_{5/2,m_j=-1/2}$. Ions projected to the qubit state encoded in the ground state will absorb a photon while getting excited to $4P_{1/2}$, as shown in Figure 3.14. From there, a decay within nanoseconds either to the ground state or to the state $3D_{3/2}$ occurs. Simultaneous illumination with light at 866 nm, repumps population decayed to $3D_{3/2}$ back to $4P_{1/2}$. This ensures that every ion, once excited to $4P_{1/2}$, eventually decays to the ground state, emitting a photon at 397 nm. This closed cycling transition allows one to scatter multiple 397 nm photons from ions in the ground state. Qubits projected to $3D_{5/2,m_j=-1/2}$ do not participate in this cyclic process and do not scatter any photons. Therefore, collecting scattered photons at 397 nm allows for the distinction between qubits being projected to either the ground state or to the metastable $3D_{5/2}$ state. This technique termed *shelved optical electron amplifier* was first demonstrated in 1986 [89]. It allows one to distinguish the ground state from a *shelved*, metastable state. The state of a single valence electron controls the emission of thousands of photons in milliseconds. The final electronic state for qubits projected to the ground state after such a projective measurement is not a certain Zeeman

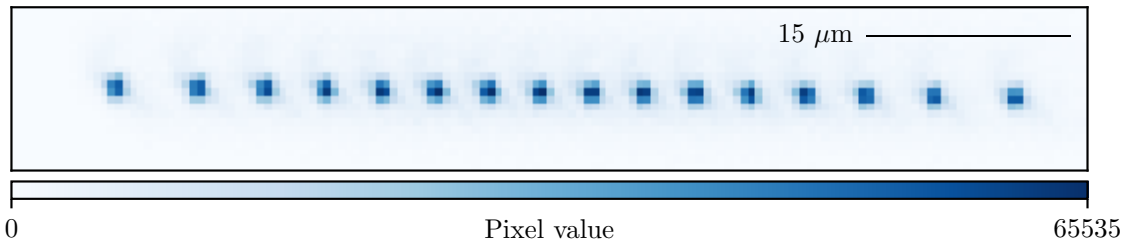

Figure 3.15: Image of a chain of 16 trapped ions captured with an EMCCD camera. The photons scattered by the ions when illuminated with light at $397\,\mathrm{nm}$ are imaged to the camera sensor using a high-NA objective. Note that the scale bar in the top right corner does not show a distance of $15\,\mu\mathrm{m}$ on the camera but at the position of the ion chain. The exposure time is $100\,\mathrm{ms}$.

sublevel but a mixture of the Zeeman sublevels with $m_j = -1/2$ and $m_j = +1/2$. On the contrary, the Zeeman state of qubits projected to $3\mathrm{D}_{5/2}$ is not affected.

For a simultaneous measurement of multiple qubits in an ion chain, all ions are simultaneously illuminated with light at $397\,\mathrm{nm}$ and $866\,\mathrm{nm}$, projecting them to either $4\mathrm{S}_{1/2}$ or $3\mathrm{D}_{5/2}$. A computational state can be assigned to each qubit by spatially resolving the photons emitted during the measurement. This can be achieved by collecting the emitted photons using an electron-multiplying charge-coupled device (EMCCD) camera*. The light emitted by the ions is imaged to the camera through the same objective that is used for single-site addressing described in Section 3.2.3.3. Figure 3.15 shows a typical image taken with an EMCCD camera of a 16-ion chain with a length of $66\,\mu\mathrm{m}$. The optical system imaging the ion chain to the camera has a magnification of ≈ 30 [84]. The number of photons scattered by an ion is proportional to the summed up value of the pixels an ion is imaged to. A computational state is assigned to each ion by comparing the summed pixel value to a threshold: If the value is above (below) the threshold the ion is assumed to be projected to $4S_{1/2}$ ($3D_{5/2}$). A histogram of the summed pixel value from 500 images with an exposure time of $250\,\mu\mathrm{s}$ for a single ion is shown in Figure 3.16. The ion is prepared in a superposition of the two computational states before detection. On the horizontal axis, the summed pixel value is plotted.

During a measurement an ion projected to the ground state scatters thousands of photons. Every photon emission process results in change of the ions momentum. The magnitude of this *recoil* is given by the momentum of the emitted photon. Due to the spatial symmetry of the emission pattern the transferred momentum averaged over many emission cycles is zero. However, the recoil leads to a random walk in the momentum space of the trapped ion causing an excitation of the harmonic oscillators describing the motion of the ions in the trap [59]. Therefore, a qubit measurement induces heating and the cooling procedure described in Section 3.2.2 has to be repeated after a measurement.

For specific algorithms, e.g., QEC protocols, it is required to measure subsets of the entire qubit register during a computation, referred to as *mid-circuit measurement*. Subsequently, additional gate operations are applied to the measured qubits but also to spectator qubits. Ideally, such a mid-circuit measurement implements an identity operation on the spectator qubits. The procedure involves measuring a subset of the qubit register, recooling the ion

* Andor iXon Ultra 897

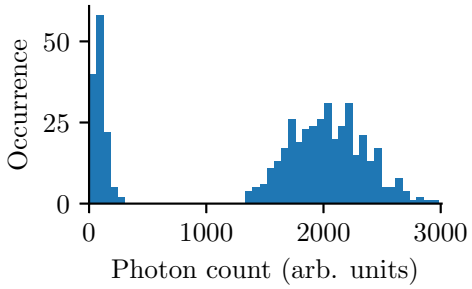

Figure 3.16: Histogram of detected photon counts of a single ion extracted from 500 images with an exposure time of 250 µs. Before detection, the ion is prepared in a superposition of the two qubit states so that bright and dark events are observed. The horizontal axis shows the pixel value output by the camera accumulated over all pixels the ion is imaged to. This quantity is proportional to the number of scattered photons.

chain after scattered photons induced motional excitation, and reinitializing the auxiliary qubits for later reuse.

The lasers at wavelengths of 397 nm, 854 nm and 866 nm required for implementing projective measurements, cooling of the ion motion, and qubit initialization are illuminating the entire ion string simultaneously. Those laser beams are referred to as *global beams*, in contrast to the addressed laser beam at 729 nm. Therefore, the standard procedures described above and in Section 3.2.2 would also undesirably affect the information encoded in spectator qubits. This can be avoided by changing the qubit encoding of spectator qubits for the different stages of the mid-circuit measurement procedure. For the projective measurement the qubit encoding is transferred from $4S_{1/2,m_j=-1/2}$ and $3D_{5/2,m_j=-1/2}$ to $3D_{5/2,m_j=-1/2}$ and $3D_{5/2,m_j=+1/2}$. A projective measurement does not affect the Zeeman sublevels of $3D_{5/2}$ and the spectator qubits stay unperturbed. The same holds true for the following Doppler cooling step, where the same lasers as for the measurement are involved. For the sideband cooling and reinitialization of the measured qubits the encoding of the spectator qubits is transferred to $4S_{1/2,m_j=-1/2}$ and $4S_{1/2,m_j=+1/2}$. A detailed description of the mid-circuit measurement procedure, including a performance characterization, can be found in Appendix A.

During the recooling step using sideband cooling, spectator qubits are encoded in the two Zeeman sublevels of the ground state. In the ground state encoding, the coherence time is on the order of 5 ms. The sideband cooling sequence after a mid-circuit measurement requires approximately 15 ms, significantly extending beyond the typical coherence time in the ground state encoding. However, dephasing of spectator qubits can be mitigated by applying the DD technique described in Section 3.2.1. When applying DD no significant decay in coherence is observed on the timescales of tens of milliseconds relevant in the context of recooling after mid-circuit measurements.

3.3 Modeling noisy trapped-ion quantum processors

All the implementations of fundamental building blocks for QIP described in the previous section are faulty to some degree. Erroneous behavior of a building block can be caused by fluctuations in the classical control system or limitations imposed by the physical system encoding the qubits. Examples of classical control limitations are magnetic field fluctuations or laser intensity noise, whereas, e.g., the limited lifetime of the metastable qubit state is a

limitation of the physical system. Developing models describing the erroneous behavior allows relating such limitations to deviations of the prepared from the ideal quantum state after implementing a quantum algorithm. Furthermore, error models allow for identifying limiting error processes and estimating a quantum processor's performance after future hardware advancements. The goal hereby is to find a model that is complex enough to capture the salient features of a noisy implementation of a quantum computation and reliably predict its outcome, while still being simplistic enough for an efficient simulation using classical computers.

3.3.1 *Idling*

Errors corrupting quantum information can occur not only when one acts on a qubit but also when a qubit is not directly involved in a particular time step of a quantum algorithm. Error processes affecting inactive qubits are referred to as *idling errors*. Such a process was already mentioned in Section 3.2.1, where ground-state qubits suffer from dephasing originating from magnetic field fluctuations during idling.

An error model for this process that is applicable to complex gate sequences on multi-qubit registers can be constructed by describing each time step of the gate sequence individually. Every idling location in a circuit is replaced by an ideal, error-free idling period followed by the probabilistic application of a Z rotation with a rotation angle of π. With this, the quantum state of a noisy implementation of a gate sequence can be described at every time step throughout the computation. The mathematical description, called *error channel*, of this model is given by the linear map

$$\rho'(t) = \mathcal{E}(\rho) = (1 - p_{\text{idle}})\rho + p_{\text{idle}} Z\rho Z. \tag{3.30}$$

Here, ρ and $\rho'(t) = \mathcal{E}(\rho)$ are the density matrices of the quantum state before and after a qubit is undergoing noisy idling. The Pauli operator Z is applied with the probability p_{idle} to the idling qubit. Instead of modeling the Z rotations that physically happen in a noisy system, a full phase-flip error is applied in a stochastic fashion. Such noise models are referred to as being *incoherent*. A major upside of such an incoherent error channel is that a quantum computation affected by the channel can be simulated efficiently using a classical computer for quantum circuits only containing Clifford gates [50, 51]. Averaging over multiple simulation runs of the noisy circuit, where the decision whether or not to apply a Z rotation is made individually for every run and idling location, produces a mixed state describing the final noisy state. For

$$p_{\text{idle}} = \frac{1}{2}(1 - \mathrm{e}^{-\frac{t}{T_2}}) \tag{3.31}$$

this channel reproduces the noise-affected density matrix $\rho'(t) = \mathcal{E}(\rho)$ of a single qubit undergoing noisy idling for a duration t from Eqn. 3.21.

Another noise process affecting a qubit's state during idling is the decay of computational basis states. For optical qubit encodings in trapped-ion quantum processors, one of the qubit states is encoded in a metastable electronic state, i.e., the state $3\mathrm{D}_{5/2,m_j=-1/2}$ for the quantum information processor discussed in this thesis. The time constant of the spontaneous decay

of a Zeeman sublevel of $3D_{5/2}$ to the ground state is $T_1 = 1.168(9)\,\mathrm{s}$ [71]. The error channel of the metastable state's decay to the other computational basis state, $4S_{1/2,m_j=-1/2}$, reads

$$\mathcal{E}(\rho) = \begin{pmatrix} 1 & 0 \\ 0 & \sqrt{1-p} \end{pmatrix} \rho \begin{pmatrix} 1 & 0 \\ 0 & \sqrt{1-p} \end{pmatrix} + \begin{pmatrix} 0 & \sqrt{p} \\ 0 & 0 \end{pmatrix} \rho \begin{pmatrix} 0 & 0 \\ \sqrt{p} & 0 \end{pmatrix}, \tag{3.32}$$

with p being the probability that the metastable state decays during the respective idling period. The decay of the metastable state to $4S_{1/2,m_j=+1/2}$, which is a state outside the computational subspace, cannot be modeled in the framework of a closed two-level system. Simulating errors involving states outside the computational subspace requires to increase the dimension of the quantum state describing the system [90].

The timescale T_1 of the metastable state's decay is on the order of one magnitude longer than the coherence time T_2 in the devices considered here, rendering this error process negligible for most practical cases. Encoding a qubit in the two Zeeman sublevels of the ground state can even eliminate the decay of computational states entirely.

3.3.2 *Gate errors*

When applying a single-qubit gate $R_\varphi(\theta)$ defined in Eqn. 3.22, two different types of errors can occur:

- The rotation angle θ can deviate from the ideal rotation angle. Physical processes that cause this are, among others, fluctuations in the laser intensity, drifts or vibrations of the focusing optics generating the tightly focused laser beam, or fluctuations in the polarization of the laser light causing a change of the coupling to the atomic transition [66].
- The rotation axis described by the angle ϕ can be affected by fluctuations of the laser phase or the magnetic field applied to the ions.

These two effects will, similar to the case of dephasing noise, shrink the Bloch vector. However, instead of shrinking towards the Z axis of the Bloch sphere, the Bloch vector shrinks towards the center of the sphere for erroneous single-qubit gates averaged over many gates. In other words, not only the off-diagonal elements of the density matrix are affected, as for dephasing noise, but also the diagonal elements are altered. Ultimately, when applying more and more single-qubit gates, the density matrix converges to the fully depolarized state

$$\rho'(t) = \frac{1}{2} \begin{pmatrix} 1 & 0 \\ 0 & 1 \end{pmatrix} \tag{3.33}$$

irrespective of the initial state. This behavior can be modeled by replacing each noisy gate with an ideal gate, followed by the incoherent error channel

$$\mathcal{E}(\rho) = (1-p_1)\rho + \frac{p_1}{3}\left(X\rho X + Y\rho Y + Z\rho Z\right). \tag{3.34}$$

With a probability of $1 - p_1$, the output state of the ideal single-qubit gate is left unchanged, while with equal probabilities of $\frac{p_1}{3}$, either an X, Y, or Z error is applied. This error channel is referred to as a *depolarizing noise channel*.

Adopting the same reasoning also for two-qubit gates, it stands to reason to model a noisy gate as an ideal gate followed by the two-qubit depolarizing noise channel

$$\mathcal{E}(\rho) = (1 - p_2)\rho + \frac{p_2}{15}\sum_{i=1}^{15} E_i \rho E_i \tag{3.35}$$

with

$$E_i \in \{\sigma_k \otimes \sigma_l, \ \ \forall \sigma_k, \sigma_l \in \{\mathbb{1}, X, Y, Z\}\} \setminus \{\mathbb{1} \otimes \mathbb{1}\}. \tag{3.36}$$

Similar to the single-qubit case, random Pauli errors are applied with an equal probability. With a probability of $\frac{p_2}{15}$, one of fifteen non-trivial bipartite tensor products of Pauli matrices is acting on the system after the ideal gate operation. Repeated application of this channel eventually leads to the fully depolarized two-qubit state. Estimated error probabilities for the data in this thesis in a 16-qubit register are $p_1 \approx 0.005$ and $p_2 \approx 0.025$.

The aforementioned gate error models neglect off-resonant excitation to Zeeman sublevels outside the computational subspace. Due to the large detuning from any transition to states outside the computational subspace of at least $6.8\,\mathrm{MHz}$ with maximal Rabi frequencies of $200\,\mathrm{kHz}$, contributions from off-resonant processes to the total error probability are negligible [91]. More gate-specific error models deviating from the generic depolarizing noise model for two-qubit operations are discussed in Section 6.1.1.

3.3.3 *Preparation and measurement errors*

The dominant error source of the state preparation scheme discussed in Section 3.2.2 is off-resonant excitation of transitions between $4\mathrm{S}_{1/2,m_j=-1/2}$ and Zeeman sublevels of $3\mathrm{D}_{5/2}$. The rate equation for the fraction of the population n_- in the desired initial state $4\mathrm{S}_{1/2,m_j=-1/2}$ is given by

$$\frac{dn_-}{dt} = c_1 n_+ - c_2 n_-, \tag{3.37}$$

where $n_+ = 1 - n_-$ is the fraction of the population in $4\mathrm{S}_{1/2,m_j=+1/2}$. The coefficient c_1 depends on the probability of the process, where population is excited from $4\mathrm{S}_{1/2,m_j=+1/2}$ and subsequently decays to $4\mathrm{S}_{1/2,m_j=-1/2}$, whereas c_2 depends on the probability of the inverse process. In equilibrium the fraction of population in $4\mathrm{S}_{1/2,m_j=-1/2}$ is given by $n_- = \frac{c_1}{c_1+c_2}$. As the laser is tuned to resonance with the transition from $4\mathrm{S}_{1/2,m_j=+1/2}$ to $3\mathrm{D}_{5/2,m_j=+1/2}$ the coefficient c_1 is much larger than the coefficient c_2. However, in this equilibrium state, some population is undesirably left in $4\mathrm{S}_{1/2,m_j=+1/2}$, outside the computational subspace of the optical qubit encoding. Modeling this leakage from the computational subspace would require extending the dimension of the modeled Hilbert space per qubit beyond two, depending on the number of non-computational states taken into account [90]. However, this extension to the error model would increase the computational effort of simulating noisy circuits and prevent the utilization of optimized and readily available simulation tools.

Therefore, an approximated error channel for noisy initialization following the spirit of the channels discussed above is used in this thesis. The channel is given by

$$\mathcal{E}(\rho) = (1 - p_{\mathrm{i}})\rho + p_{\mathrm{i}} X \rho X, \tag{3.38}$$

where a noiselessly initialized qubit is flipped with a probability p_{i}.

When measuring a qubit, the discrimination between the two computational states is done by comparing the number of collected photons from a specific ion illuminated with the detection laser beams with a threshold photon number, as described in Section 3.2.4. The measurement outcome is corrupted if the detected photon counts are below the threshold for a bright ion or above the threshold for a dark ion. One reason for such a misjudgment is the finite overlap of the Poissonian distributions of collected photons for dark and bright ions [74]. Another error mechanism is the decay of the dark computational state to the ground state during the detection procedure, leading to an increased number of detected photons [74]. Furthermore, imperfections in the optical system imaging the light from the ion chain to the camera can cause the assessment of a dark ion as bright. Thereby, photons scattered from a bright ion are imaged to pixels of the camera sensor that are associated with a different, dark ion. Without considering the details of the aforementioned error mechanisms, one can model a noisy measurement as a bit flip occurring with a probability p_{m} before a noiseless measurement. The corresponding error channel then reads

$$\mathcal{E}(\rho) = (1 - p_{\mathrm{m}})\rho + p_{\mathrm{m}} X \rho X. \tag{3.39}$$

For the data presented in this thesis the preparation and measurement error probabilities were estimated to be $p_{\mathrm{i}} = p_{\mathrm{m}} = 0.003$.

4

PROTECTING QUBITS FROM NOISE

In order to provide a practical advantage over classical computation, quantum computers will require thousands of qubits and billions of quantum gates acting on them [30, 92–95]. The required quality of gate operations to successfully execute a circuit can be very naïvely assessed as one over the number of applied gates. Hence, a gate error probability on the order of 10^{-9} is required to implement a circuit consisting of 10^9 gates. The state of a quantum mechanical system is described by continuous variables, as shown in Section 2.1. Already tiny undesired interactions with an environment change the stored quantum information. Therefore, no quantum computing architecture currently offers gate error probabilities that fulfill the requirements for large-scale computations. In contrast, in classical computing the set of possible states of a register is discrete. Each bit is either 0 or 1, usually represented by two voltage ranges. Small voltage fluctuations, e.g., due to undesired influence of the environment, do not alter the stored information. In this sense, digital logic for classical computing is intrinsically error correcting.

Furthermore, in classical computing, additional to the intrinsic EC properties, a sophisticated arsenal of tools to actively correct possible errors compromising a computation was established over the last decades. The goal of implementing procedures detecting and correcting errors is to recover the stored or transmitted information although parts of the information are corrupted. Due to the low failure rates on the order of 10^{-17} and less in classical computing hardware [45], EC is utilized predominantly in critical applications or particularly noisy transmission lines, e.g., satellite or cellular connections [96]. Large-scale quantum computation will require similar EC procedures in order to achieve the required error probabilities. The techniques developed for EC in classical computing cannot be directly applied to quantum computing owing to the peculiarities of quantum mechanics, but the field of QEC was undoubtedly inspired by ideas from its classical counterpart.

In this chapter, the basic ideas of EC for QIP are presented. Section 4.1 discusses the distinction between classical and quantum EC and introduces an instructive example of a QEC code. In Section 4.2, a framework to describe an extensive class of QEC codes, the *stabilizer formalism* [97], is introduced. Section 4.3 covers the seven-qubit Steane code [36], which has been used for most of the work presented in this thesis. Finally, Section 4.4 discusses the building blocks necessary to encode and protect logical information in a QEC code.

4.1 Introduction to quantum error correction

Redundancy in the encoding of information is a critical requirement for any sort of EC. If a part of the system is corrupted, the storage of information distributed to multiple informa-

tion carriers allows for the recovery of the encoded information. In classical information processing, the most elementary approach for EC is just copying the information. Assuming one wants to transmit a single bit, instead of sending the value 0 or 1, one sends 000 or 111, respectively. Those bitstrings consisting of the copied information are called *code words* of the EC code. An error on a single bit will alter the encoded bitstring in one position. Table 4.1 shows the effect of an error affecting a single bit (second column) on the encoded information (first column) and the corresponding corrupted bitstring (third column). In this example, we assume that errors occur independently on single bits with a probability of p. A specific error affecting m bits, termed a weight-m error, occurs with a probability p^m. Therefore, the most likely error configuration leading to a particular corrupted bitstring is the one having the lowest weight, which is a weight-1 error in this example. A procedure to recover the encoded information, assuming the lowest weight error configuration occurred, is a majority vote across the values in the transmitted bitstring. In the fourth column of the table, one can see that this successfully recovers the encoded information for errors affecting a single bit. However, any weight-2 error acting on the bitstring gives rise to a majority of bits carrying the wrong value, and therefore, the recovered value is also inverted. Although the EC procedure cannot recover the correct value for weight-2 errors, the fact that not all bits in the corrupted bitstring hold the same value still allows detecting that an error has happened. Going a step further by introducing a weight-3 error, one sees that the two code words of the code are transformed into each other, and there is no chance even to detect this error configuration. The weight of an error configuration transforming one valid code word into another is referred to as distance d of the EC code. Therefore, for a distance-d code an error affecting d bits can corrupt the encoded information while going unnoticed. In contrast, the encoded information can be successfully recovered for errors with a weight of up to [98]

$$t = \lfloor \frac{d-1}{2} \rfloor. \tag{4.1}$$

A commonly used notation for an EC code with a distance d encoding the information content of k bits in n bits is the $[n, k, d]$ notation. Such a code has 2^k different code words with a length of n each. The code introduced above is a $[3, 1, 3]$ code. Copying the encoded information to more bits than for the classical distance-3 repetition code discussed above increases the distance and, therefore, the number of correctable errors.

If QIP, it is not sufficient anymore to protect the states $|0\rangle$ (corresponding to the classical bitstring 0) and $|1\rangle$ (corresponding to 1), but also superposition states $|\psi\rangle$ of the form

$$|\psi\rangle = \alpha\,|0\rangle + \beta\,|1\rangle \tag{4.2}$$

have to be safeguarded from errors. The most naïve way to transfer the EC procedure discussed above to quantum states would be to copy the state $|\psi\rangle$. Unfortunately, there are two roadblocks ahead:

1. A mechanism of copying superposition states for all allowed values of α and β is prohibited by the no-cloning theorem [99].

2. Measuring the ensemble of copied qubits to determine the majority qubit state would collapse the superposition states to eigenstates of the respective measurement operator.

Encoded bit value	Error on bit	Corrupted bitstring	Recovered value
0	1	100	0
	2	010	0
	3	001	0
1	1	011	1
	2	101	1
	3	110	1

Table 4.1: Single bit-flip error acting on a classical error correction code. The first column shows the bit value to be encoded, and the third column shows the corrupted, encoded bitstring after an error occurs on the bit indicated in the second column. The correct value can be recovered, as shown in the third column.

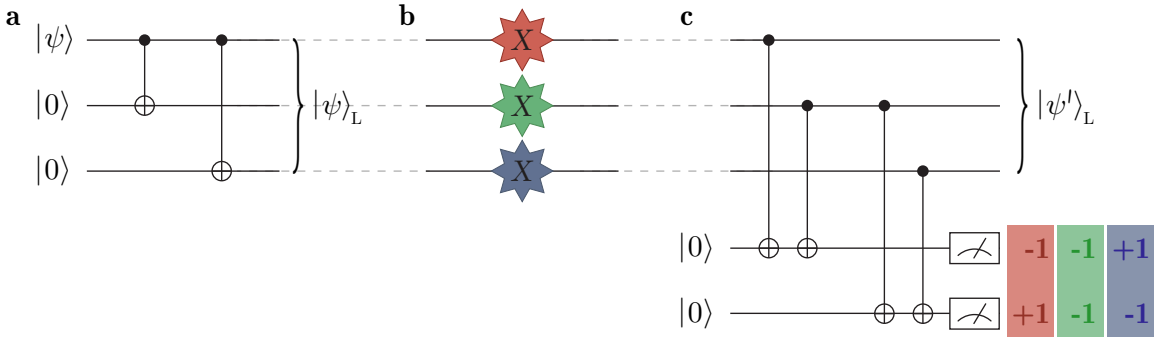

Figure 4.1: Distance-3 bit-flip repetition code. **a** Circuit encoding an arbitrary single-qubit quantum state $|\psi\rangle$ in the logical state $|\psi\rangle_L$. **b** Single-qubit X errors acting independently on the three qubits of the code. **c** Error syndrome extraction using two auxiliary qubits. The colored measurement outcomes correspond to the errors in **b** of the same color.

Therefore, the random nature of the measurement would impair the majority vote, and the encoded superposition state would be destroyed.

A way out of this dilemma is to provide the redundancy necessary to protect the encoded information by using carefully structured entanglement between multiple qubits. Probably the most basic instance of such a construction is given by:

$$|\psi\rangle = \alpha\,|0\rangle + \beta\,|1\rangle \rightarrow |\psi\rangle_L = \alpha\,|000\rangle + \beta\,|111\rangle\,. \tag{4.3}$$

The subscript L indicates that $|\psi\rangle_L$ is an encoded, also referred to as *logical*, state. Figure 4.1a shows the encoding for this so-called distance-3 bit-flip code [100]. For both error-free code words $|0\rangle_L = |000\rangle$ and $|1\rangle_L = |111\rangle$, two neighboring qubits always exhibit the same state in the computational basis. The product of the eigenvalues to the Z Pauli operator of two neighboring qubits is always $+1$*. This quantity is referred to as *parity*. For the analysis of the erroneous case, let us first restrict the possible errors to single-qubit bit-flip errors, corresponding to rotations around the X axis of the Bloch sphere with rotation angle π. An

* The products of the eigenvalues are $+1 \cdot +1 = +1$ and $-1 \cdot -1 = +1$ if both qubits are in the state $|0\rangle$ and $|1\rangle$, respectively.

error on the first qubit, as shown in Figure 4.1b in red, transforms the encoded state $|\psi\rangle_{\mathrm{L}}$ to $|\psi'\rangle_{\mathrm{L}} = \alpha\,|100\rangle + \beta\,|011\rangle$. The parity for the first two qubits then is -1, whereas the parity for the last two qubits is still $+1$. Figure 4.1c shows a circuit measuring the parity of the first two and last two qubits encoding the logical information using two additional qubits. Those additional qubits are referred to as *auxiliary qubits*, whereas the qubits holding the encoded information are called *data qubits*. Measurements of the first and second auxiliary qubit reveal the parity of the first and last two data qubits, respectively. Evaluating this set of parity measurements for the single-qubit bit-flip errors, shown in different colors in Figure 4.1b, reveals that each error has its unique set of parity measurement outcomes, referred to as *error syndrome*. If no error is present on the data qubits, the measured error syndrome is $(+1, +1)$. The parity measurements for two neighboring qubits correspond to measuring the operators Z_1Z_2 and Z_2Z_3, where Z_iZ_j is short for the tensor product of Pauli-Z operators acting on qubits i and j and the identity acting on all other qubits. According to Eqn. 2.62, in the error-free case, the state of the data qubits after measuring Z_1Z_2 and Z_2Z_3 is

$$\begin{aligned} |\psi'\rangle_{\mathrm{L}} &= \frac{1}{\sqrt{2(1 + {}_{\mathrm{L}}\langle\psi|Z_1Z_2|\psi\rangle_{\mathrm{L}})}}(\mathbb{1}^{\otimes 3} + Z_1Z_2)\,|\psi\rangle_{\mathrm{L}} = \\ &= \frac{1}{\sqrt{2(1 + {}_{\mathrm{L}}\langle\psi|Z_2Z_3|\psi\rangle_{\mathrm{L}})}}(\mathbb{1}^{\otimes 3} + Z_2Z_3)\,|\psi\rangle_{\mathrm{L}} = |\psi\rangle_{\mathrm{L}}\,. \end{aligned} \tag{4.4}$$

Therefore, measuring the parity on the two pairs does not collapse a superposition of logical basis states. Also for the erroneous cases, superposition states are unaffected. The post-measurement quantum state can be determined according to Eqn. 2.63 for parity measurements with outcome -1.

The unique correspondence of error syndrome and single bit-flip error allows restoring the original state $|\psi\rangle_{\mathrm{L}}$ by applying an X operation on the respective qubit. Let us now look into the uncorrectable case of two independent errors being present on the data qubits before the parity measurements. The recovery procedure suggests applying a correction to the third, non-erroneous qubit. After the correction, a logical bit flip is introduced as the code word $|0\rangle_{\mathrm{L}}$ is transformed into $|1\rangle_{\mathrm{L}}$ and vice versa. For an error configuration where all three qubits suffer from a bit flip, the error is not even detected, and the corruption of the logical information, termed *logical error*, goes unnoticed.

Although measurement-free protocols [101–107] seem to be a viable option for QEC, this thesis will be restricted to schemes mapping the error syndrome to auxiliary qubits which are measured subsequently. After the measurement, the error syndrome is processed in a classical computer and the appropriate correction is applied. This general structure is depicted in Figure 4.2.

This thesis will be restricted to QEC schemes mapping the error syndrome to auxiliary qubits which are measured subsequently. After the measurement, the error syndrome is processed in a classical computer and the appropriate correction is applied. This general structure is depicted in Figure 4.2. Such schemes require the ability to measure and reset a subset of qubits during the implementation of a quantum algorithm, but require fewer gate operations acting on the qubit register compared to measurement-free protocols [101–106].

Since the goal of QEC is to reduce the rate at which quantum information is corrupted, in the following the error rates of the distance-3 bit-flip code and a bare, unencoded qubit are compared. Let us assume that the probability of a bit flip occurring on a single qubit in a specific time interval is p. For independent errors the probability for a specific weight-m

Figure 4.2: Principle of error syndrome extraction and EC based on measurements of auxiliary qubits. The upper wire consisting of multiple lines symbolizes multiple physical qubits encoding one logical qubit. An encoded, potentially erroneous state $|\psi'\rangle_{\mathrm{L}}$ is coupled to a set of auxiliary qubits in the state $|\mathrm{aux}\rangle$ (depicted as the block labeled 'Syndrome extraction'). Subsequently, the auxiliary qubits are measured, and the corresponding correction is applied to the data qubits. The correction restores the error-free encoded state $|\psi\rangle_{\mathrm{L}}$ if a correctable error was present on the data register.

bit flip then is p^m. In the case of a bare physical qubit, the information stored in the state $|\psi\rangle$ will be corrupted after the respective time interval with a probability p. The same error process acting on the encoded state $|\psi\rangle_{\mathrm{L}}$ leads to one of the following four scenarios:

1. The encoded quantum state is unperturbed with a probability of $(1-p)^3$.
2. In one of three possible locations, a single qubit sustains a bit flip with a probability of $p(1-p)^2$, leading to a combined probability of $3p(1-p)^2$.
3. A two-qubit error configuration occurs with a combined probability of $3p^2(1-p)$.
4. All three qubits experience a bit flip with a probability of p^3.

After applying the EC procedure, scenarios three and four lead to logical errors. Therefore, the summed probability of finding a corrupted logical state is $3p^2(1-p)+p^3 = 3p^2-2p^3 = \mathcal{O}(p^2)$. This means that the error rate of the logical qubit is lower compared to the one of the bare physical qubit if $p < 0.5$ [45]. Thus, implementing this QEC code is beneficial, if the error rate given by undesired coupling to the environment is low enough and the time interval between EC cycles, shown in Figure 4.2, is short enough.

So far, it was shown that the quantum repetition code can correct discrete bit-flip errors. However, the control acting on qubits is continuous, meaning that an error in general also shows this continuous behavior. Imagine, for example, a coherent error $U_1^X(\theta) = \cos\frac{\theta}{2}\mathbb{1}^{\otimes 3} - \mathrm{i}\sin\frac{\theta}{2}X_1$, implementing a rotation around the X axis for the first qubit with a rotation angle θ. The perturbed encoded quantum state then reads

$$\begin{aligned} U_X^{(1)}(\theta)\,|\psi\rangle_{\mathrm{L}} = |\tilde{\psi}\rangle_{\mathrm{L}} &= \cos\frac{\theta}{2}(\alpha\,|000\rangle + \beta\,|111\rangle) - \mathrm{i}\sin\frac{\theta}{2}X_1(\alpha\,|000\rangle + \beta\,|111\rangle) \\ &= \cos\frac{\theta}{2}(\alpha\,|000\rangle + \beta\,|111\rangle) - \mathrm{i}\sin\frac{\theta}{2}(\alpha\,|100\rangle + \beta\,|011\rangle). \end{aligned} \tag{4.5}$$

A measurement of the parity operator Z_1Z_2 now projects the state either to

$$|\psi'\rangle_{\mathrm{L}} = \frac{1}{\sqrt{2(1 + {}_{\mathrm{L}}\langle\tilde{\psi}|Z_1Z_2|\tilde{\psi}\rangle_{\mathrm{L}})}}(\mathbb{1}^{\otimes 3} + Z_1Z_2)\,|\tilde{\psi}\rangle_{\mathrm{L}} = \alpha\,|000\rangle + \beta\,|111\rangle \tag{4.6}$$

with probability

$$p(+) = \frac{1}{2}(1 + {}_{\mathrm{L}}\langle\tilde{\psi}|Z_1Z_2|\tilde{\psi}\rangle_{\mathrm{L}}) = \cos^2\frac{\theta}{2} \tag{4.7}$$

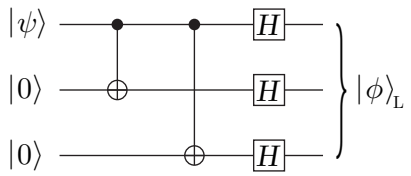

Figure 4.3: Circuit encoding an arbitrary single-qubit quantum state $|\psi\rangle$ to the logical state $|\phi\rangle_{\mathrm{L}}$ of the distance-3 phase-flip repetition code. The circuit corresponds to the encoding circuit of the bit-flip code shown in Figure 4.1a, followed by Hadamard gates on all qubits.

or to

$$|\psi'\rangle_{\mathrm{L}} = \frac{1}{\sqrt{2(1 - {}_{\mathrm{L}}\langle\tilde{\psi}|Z_1Z_2|\tilde{\psi}\rangle_{\mathrm{L}})}}(\mathbb{1}^{\otimes 3} - Z_1Z_2)\,|\tilde{\psi}\rangle_{\mathrm{L}} = \mathrm{e}^{-\mathrm{i}\frac{\pi}{2}}(\alpha\,|100\rangle + \beta\,|011\rangle) \tag{4.8}$$

with probability

$$p(-) = \frac{1}{2}(1 - {}_{\mathrm{L}}\langle\tilde{\psi}|Z_1Z_2|\tilde{\psi}\rangle_{\mathrm{L}}) = \sin^2\frac{\theta}{2}. \tag{4.9}$$

Therefore, one ends up with either no error or a bit-flip error on the first qubit. This argument holds analogously for errors acting on the other two qubits and justifies the restriction to discrete errors.

Another distinct feature of QIP compared to classical computing is a further error mechanism that maps

$$|0\rangle \to |0\rangle \qquad \text{and} \qquad |1\rangle \to -|1\rangle\,, \tag{4.10}$$

commonly referred to as *phase-flip* error. This error, effectively applying the operator Z, cannot be detected by measuring neighboring qubits' parity with respect to the Z basis but still affects the encoded information. Protection against phase-flip errors can be achieved by using the same encoding as for the bit-flip code but subsequently applying Hadamard operations to all three qubits. The encoding circuit of this code called *distance-3 phase-flip repetition code* is depicted in Figure 4.3. Applying a Hadamard operation effectively exchanges the Z and X basis. The encoded state of this new QEC code then reads

$$|\phi\rangle_{\mathrm{L}} = H_1H_2H_3\,|\psi\rangle_{\mathrm{L}} = \alpha\,|+++\rangle + \beta\,|---\rangle \tag{4.11}$$

with the code words $|0\rangle_{\mathrm{L}} = |+++\rangle$ and $|1\rangle_{\mathrm{L}} = |---\rangle$. Now, the error syndrome is determined by measuring X_1X_2 and X_2X_3. Just as for the bit-flip code, the error syndrome indicates on which qubit a phase flip has to be applied to restore the encoded information*.

4.2 Stabilizer formalism

In the previous section, bit-flip and phase-flip repetition codes were introduced and discussed in terms of the state vector of their code words. For more complex codes, this description

* Only a single phase-flip error is correctable. For a phase-flip error acting on two or three qubits the logical information is corrupted. For more details, see the analogous discussion on correctable errors for the bit-flip code.

can be cumbersome. An alternative way of describing a quantum state is by giving a set of operators to which the state is a $+1$ eigenstate [45]. The quantum state remains unchanged under the application of any operator from this set, i.e., the operators are *stabilizing* the state [45]. The concept of describing a quantum state in terms of stabilizing operators is called *stabilizer formalism* [97] and not only allows for the description of quantum states but also for an efficient treatment of a large class of QEC codes, as will be discussed later in this section.

The quantum state $|\psi\rangle$ is stabilized by an operator $S^{(i)}$ in the n-qubit Pauli group*, defined in Eqn. 2.20, if

$$S^{(i)} |\psi\rangle = |\psi\rangle \,. \tag{4.12}$$

The operator $S^{(i)}$ has as many eigenstates with eigenvalue $+1$ as it has eigenstates with eigenvalue -1. Therefore, specifying that a state has to be a $+1$ eigenstate of $S^{(i)}$ reduces the dimension of the available state space by a factor of 2 [42]. Let us consider a general two-qubit quantum state

$$|\psi\rangle = \alpha |00\rangle + \beta |10\rangle + \gamma |10\rangle + \delta |11\rangle \,, \tag{4.13}$$

which is an element of a four-dimensional Hilbert space spanned by the orthonormal basis $\{|00\rangle, |10\rangle, |01\rangle, |11\rangle\}$. Demanding that a two-qubit state $|\psi_{XX}\rangle$ is stabilized by the operator X_1X_2 implies that $|\psi_{XX}\rangle$ is an element of a two-dimensional Hilbert space spanned by $\{|10\rangle + |01\rangle, |00\rangle + |11\rangle\}$ and the state can be written as

$$|\psi_{XX}\rangle = \alpha' (|10\rangle + |01\rangle) + \beta' (|00\rangle + |11\rangle) \,. \tag{4.14}$$

The states

$$|0_{XX}\rangle = \frac{1}{\sqrt{2}} (|10\rangle + |01\rangle) \qquad \text{and} \qquad |1_{XX}\rangle = \frac{1}{\sqrt{2}} (|00\rangle + |11\rangle) \tag{4.15}$$

are orthogonal basis states of this Hilbert space. Additionally requiring that Z_1Z_2 stabilizes the state reduces the dimension of the Hilbert space to 1 and fixes the state to

$$|\psi_{XX,ZZ}\rangle = \frac{1}{\sqrt{2}} (|00\rangle + |11\rangle) \,, \tag{4.16}$$

* Note that not every quantum state can be described in terms of operators in the Pauli group stabilizing it. A state that can be described in terms of stabilizing operators is called *stabilizer state*.

being the two-qubit Greenberger-Horne-Zeilinger (GHZ) state. An n-qubit GHZ state is stabilized by the n operators

$$\begin{aligned} S^{(1)} &= \bigotimes_{i=1}^{n} X_i \\ S^{(2)} &= Z_1 Z_2 \\ S^{(3)} &= Z_2 Z_3 \\ &\vdots \\ S^{(n-1)} &= Z_{n-2} Z_{n-1} \\ S^{(n)} &= Z_{n-1} Z_n. \end{aligned} \tag{4.17}$$

In general, the group

$$\mathcal{S} = \{S^{(i)} \mid S^{(i)} |\psi\rangle = |\psi\rangle\,, \left[S^{(i)}, S^{(j)}\right] = 0 \;\forall\; (i,j)\} \subset \mathcal{P}_n. \tag{4.18}$$

is called the *stabilizer* of the n-qubit state $|\psi\rangle$. The elements of $\mathcal{S}$ are in the n-qubit Pauli group $\mathcal{P}_n$ and have to mutually commute, as applying two elements $S^{(i)}$ and $S^{(j)}$ of $\mathcal{S}$ to the state $|\psi\rangle$ has to leave the state unchanged regardless of the application order:

$$S^{(i)} S^{(j)} |\psi\rangle = S^{(i)} |\psi\rangle = |\psi\rangle = S^{(j)} |\psi\rangle = S^{(j)} S^{(i)} |\psi\rangle\,. \tag{4.19}$$

The stabilizer can be described in terms of n independent generators, so that each element in $\mathcal{S}$ can be written as a product of generators [45]. The set of generators, called the *generator*, is a convenient way of describing a group. Furthermore, it can be verified that a state is stabilized by a certain stabilizer by verifying that all elements of the generator stabilize the state.

Removing one element from the generator of the stabilizer increases the dimension of the available Hilbert space from 1 to 2, corresponding to the Hilbert space dimension of a single qubit. In the previous section, a similar situation was described: For the distance-3 bit-flip code an element of the two-dimensional Hilbert space of a single qubit was encoded in a three-qubit Hilbert space with dimension 2^3. In fact, the stabilizer generated by $\{Z_1 Z_2, Z_2 Z_3\}$ defines the distance-3 bit-flip repetition code discussed above. Generally, a set of m stabilizer generators on an n-qubit Hilbert space defines an 2^{n-m}-dimensional subspace [45], which in the context of QEC is referred to as *code space*. Measuring the expectation values of the stabilizer generators does not reveal anything about the information encoded in the code space but allows for the identification and subsequent correction of an error. The set of outcomes of the stabilizer generator measurements is called error syndrome, as already introduced above when discussing the bit flip code. Table 4.2 shows the mapping from the error syndrome to the required correction operation of the distance-3 bit-flip code for states in the code space affected by at most one single-qubit bit-flip error. The expectation values of the stabilizer generators correspond to the parity measurements shown for the bit-flip code in Figure 4.1.

Quantum state	Z_1Z_2	Z_2Z_3	Erroneous qubit	Applied correction	Quantum state after correction
$\alpha\|000\rangle + \beta\|111\rangle$	$+1$	$+1$	-	-	$\alpha\|000\rangle + \beta\|111\rangle$
$\alpha\|100\rangle + \beta\|011\rangle$	-1	$+1$	1	X_1	$\alpha\|000\rangle + \beta\|111\rangle$
$\alpha\|010\rangle + \beta\|101\rangle$	-1	-1	2	X_2	$\alpha\|000\rangle + \beta\|111\rangle$
$\alpha\|001\rangle + \beta\|110\rangle$	$+1$	-1	3	X_3	$\alpha\|000\rangle + \beta\|111\rangle$

Table 4.2: Error correction look-up table for the bit-flip code. The first column shows a state in the code space of the distance-3 bit-flip code affected by either no error or one single-qubit bit-flip error. In the second column, the expectation values of the stabilizer generators are shown. In the third column, the erroneous qubit determined from the stabilizer generator expectation values can be found. After applying the correction in the fourth column, the error-free quantum state in the fifth column is restored.

As one can see from Eqn. 4.18, the application of an operator in $\mathcal{S}$ to a state in the code space trivially retains the state in the code space, and the resulting state has the same stabilizer as the initial state. Apart from the elements in the stabilizer, there are also other operators that leave the stabilizer unchanged or, in other words, commute with every element of the stabilizer. Sticking to the bit-flip repetition code, one can see that the operators $X_1X_2X_3$ and Z_1 act as follows on the code space:

$$\begin{aligned} X_1X_2X_3(|000\rangle + |111\rangle) &= |000\rangle + |111\rangle \\ X_1X_2X_3(|000\rangle - |111\rangle) &= -(|000\rangle - |111\rangle) \\ X_1X_2X_3\,|000\rangle &= |111\rangle \\ X_1X_2X_3\,|111\rangle &= |000\rangle \end{aligned} \tag{4.20}$$

and

$$\begin{aligned} Z_1\,|000\rangle &= |000\rangle \\ Z_1\,|111\rangle &= -\,|111\rangle \\ Z_1(|000\rangle + |111\rangle) &= |000\rangle - |111\rangle \\ Z_1(|000\rangle - |111\rangle) &= |000\rangle + |111\rangle\,. \end{aligned} \tag{4.21}$$

The operators $X_\mathrm{L} = X_1X_2X_3$ and $Z_\mathrm{L} = Z_1$ act on the logical state as the corresponding single-qubit Pauli operators X and Z would act on the quantum state of a physical qubit. These operators, referred to as *logical operators*, are not unique as multiplication with an element of the stabilizer, e.g. $Z'_\mathrm{L} = Z_\mathrm{L}Z_2Z_3 = Z_1Z_2Z_3$, does not change the effect on the encoded logical information. The operators Z_L and Z'_L are termed *stabilizer equivalent*. The lowest number of qubits a logical operator acts on determines the distance of the QEC code and, therefore, the number of correctable errors, according to Eqn. 4.1. For the distance-3 bit-flip code, a single Z error corrupts a logical qubit in an uncorrectable and even undetectable way. Conversely, three X errors are necessary to change the logical state in an undetectable fashion, two errors can be detected but lead to a logical error after correction, and any single error can be corrected faithfully.

As a consequence of the fact that all states in the code space of a QEC code are $+1$ eigenstates of the stabilizer, a set of data qubits can be encoded in a QEC code by measuring all stabilizer generators of the code using additional auxiliary qubits. Subsequently, the correction corresponding to the measured error syndrome is applied to prepare the data qubits in a valid code state. This procedure prepares a logical state that depends on the initial state of the data qubits. A deterministic logical state can be prepared by additionally measuring a logical operator to project the logical qubit to an eigenstate of the operator. If the logical qubit was not projected to the desired eigenstate, a logical operator can be applied to rotate the logical qubit to the desired orthogonal eigenstate.

4.3 Steane code

The bit-flip and phase-flip repetition codes only possess the ability to either correct for X-type or Z-type errors, respectively. In general, a noisy quantum information processor will exhibit both types of errors and, therefore, a procedure facilitating the correction of X- and Z-type errors will be required. A QEC code allowing for the correction of an arbitrary single-qubit error* is the code proposed by Steane in 1996 [36]. The *Steane code* is, to this day, one of the most established and well-known QEC codes, which is reflected in the fact that it has been experimentally investigated on different quantum computing platforms in various research groups [37, 38, 40].

The Steane code encodes $k = 1$ logical qubit in $n = 7$ physical qubits and has a code distance of $d = 3$. Therefore, the Steane code is a $[\![7, 1, 3]\!]^{\dagger}$ QEC code and enables to correct any error acting on a single qubit. The stabilizer generators and logical operators

$$\begin{aligned} S_X^{(1)} &= X_1X_3X_5X_7 & S_Z^{(1)} &= Z_1Z_3Z_5Z_7 \\ S_X^{(2)} &= X_4X_5X_6X_7 & S_Z^{(2)} &= Z_4Z_5Z_6Z_7 \\ S_X^{(3)} &= X_2X_3X_6X_7 & S_Z^{(3)} &= Z_2Z_3Z_6Z_7 \\ X_{\mathrm{L}} &= X_1X_2X_3X_4X_5X_6X_7 & Z_{\mathrm{L}} &= Z_1Z_2Z_3Z_4Z_5Z_6Z_7 \end{aligned} \tag{4.22}$$

are shown in Figure 4.4. The black dots represent physical qubits. The colored tiles, also called *plaquettes*, indicate the structure of the stabilizer generators: An X- and Z-type stabilizer is defined on each plaquette. The stabilizer generators are acting on the qubits which are located on the vertices of the respective plaquette[‡]. The logical operators act on all seven qubits of the Steane code but are stabilizer equivalent to weight-3 operators. Therefore, a weight-3 operator, e.g. $X_2X_4X_6$, can transform a valid code word of the Steane code into another one.

The state vector representation of the code word $|0\rangle_{\mathrm{L}}$ ($|1\rangle_{\mathrm{L}}$) of the Steane code can be found by projecting to the $+1$ eigenspace of the stabilizer generators and the $+1$ (-1) eigenspace of the logical operator Z_{L}. In Eqn. 2.62, it was shown that the final state $|\psi'_+\rangle$

* A Y-type error is a combination of X and Z and will also be correctable in this case.

† Double square brackets are used for QEC codes to distinguish them from classical EC codes.

‡ Note that this two-dimensional structure merely illustrates the definition of the code operators and does not necessarily reflect the underlying physical architecture in an experimental implementation. All results presented in this thesis are obtained from a trapped-ion processor exhibiting a one-dimensional qubit register formed by an ion chain (see Figure 3.15). A possible qubit assignment is to number the ions consecutively starting with 1 at the left-most ion.

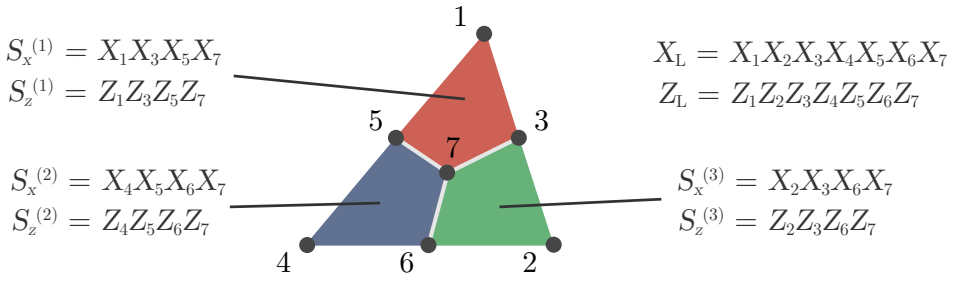

Figure 4.4: Structure of the Steane code with stabilizer generators $S_X^{(1)}$, $S_X^{(2)}$, $S_X^{(3)}$, $S_Z^{(1)}$, $S_Z^{(2)}$ and $S_Z^{(3)}$ and logical operators X_L and Z_L. Colored tiles indicate on which qubits the stabilizer generators are acting.

Error syndrome	Qubit to be corrected
$(+1,+1,+1)$	-
$(+1,+1,-1)$	2
$(+1,-1,+1)$	4
$(+1,-1,-1)$	6
$(-1,+1,+1)$	1
$(-1,+1,-1)$	3
$(-1,-1,+1)$	5
$(-1,-1,-1)$	7

Table 4.3: Error correction look-up table for the Steane Code. The first column shows the error syndrome given by the expectation values of the three stabilizer generators of either X- or Z-type and the second column shows the qubit to which a Z or X correction is supposed to be applied.

after a measurement of an operator U on a system in the state $|\psi\rangle$ with the outcome $+1$ is up to normalization given by

$$|\psi'_+\rangle \approx (\mathbb{1}^{\otimes 7} + U)\,|\psi\rangle\,. \tag{4.23}$$

The set of measurement operators to determine $|0\rangle_\mathrm{L}$ and $|1\rangle_\mathrm{L}$ are

$$\begin{gathered} U \in \{S_X^{(1)}, S_X^{(2)}, S_X^{(3)}, S_Z^{(1)}, S_Z^{(2)}, S_Z^{(3)}, Z_\mathrm{L}\} \\ \text{and} \\ U \in \{S_X^{(1)}, S_X^{(2)}, S_X^{(3)}, S_Z^{(1)}, S_Z^{(2)}, S_Z^{(3)}, -Z_\mathrm{L}\}, \end{gathered} \tag{4.24}$$

respectively. The input state $|\psi\rangle$ has to be chosen such that the probability to measure $+1$ is non-zero for all U. Particularly convenient choices of $|\psi\rangle$ to determine $|0\rangle_\mathrm{L}$ and $|1\rangle_\mathrm{L}$ are the states $|0000000\rangle$ and $|1111111\rangle$, respectively. Those states already fulfill the requirement of being a $+1$ eigenstate to the operators $S_Z^{(1)}, S_Z^{(2)}, S_Z^{(3)}, Z_\mathrm{L}$ and $S_Z^{(1)}, S_Z^{(2)}, S_Z^{(3)}, -Z_\mathrm{L}$. Therefore, the projection can be omitted for the Z-type operators. Hence, the logical basis states are given by

$$\begin{aligned} |0\rangle_\mathrm{L} = \frac{1}{\sqrt{8}} \left[\left(\mathbb{1}^{\otimes 7} + S_X^{(1)}\right)\left(\mathbb{1}^{\otimes 7} + S_X^{(2)}\right)\left(\mathbb{1}^{\otimes 7} + S_X^{(3)}\right)\right] |0000000\rangle = \\ \frac{1}{\sqrt{8}}(\,|0000000\rangle + |1010101\rangle + |0110011\rangle + |1100110\rangle + \\ |0001111\rangle + |1011010\rangle + |0111100\rangle + |1101001\rangle) \end{aligned} \tag{4.25}$$

and

$$\begin{aligned} |1\rangle_\mathrm{L} = \frac{1}{\sqrt{8}} \left[\left(\mathbb{1}^{\otimes 7} + S_X^{(1)}\right)\left(\mathbb{1}^{\otimes 7} + S_X^{(2)}\right)\left(\mathbb{1}^{\otimes 7} + S_X^{(3)}\right)\right] |1111111\rangle = \\ \frac{1}{\sqrt{8}}(\,|1111111\rangle + |0101010\rangle + |1001100\rangle + |0011001\rangle + \\ |1110000\rangle + |0100101\rangle + |1000011\rangle + |0010110\rangle). \end{aligned} \tag{4.26}$$

Errors affecting physical qubits after preparation of a state in the code space of the Steane code can be detected by measuring the expectation values of the stabilizer generators, where X-type errors affect the Z-type generators and vice versa. If there is an X (Z) error on qubit i, the parity of all Z-type (X-type) generators involving qubit i are flipped. The error location can be found by means of a look-up table shown in Table 4.3. Since the code is symmetric with respect to the X and Z basis, the error syndrome is reduced to only contain the three expectation values of generators of the same type. The syndrome found from the generators $\{S_X^{(1)}, S_X^{(2)}, S_X^{(3)}\}$ ($\{S_Z^{(1)}, S_Z^{(2)}, S_Z^{(3)}\}$) is used to infer the qubit requiring a Z (X) correction and vice versa.

As mentioned above, the expectation values of stabilizer generators are -1 for all generators involving an erroneous qubit. Therefore, weight-2 errors exist that yield the same error syndrome as single-qubit errors, e.g., X_1X_4 and X_5. In case a weight-2 error is present on the data qubits, applying the corresponding correction from Table 4.3 introduces an

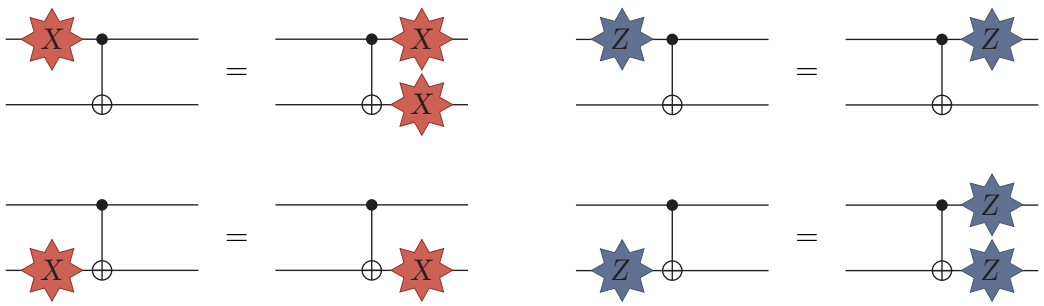

Figure 4.5: Propagation of Pauli-X and Pauli-Z errors through a CNOT gate.

additional error. The combined error operator, e.g., $X_1X_4X_5$, is stabilizer equivalent to a logical operator. Consequently, the encoded logical qubit is unintendedly manipulated and the logical information is corrupted.

4.4 Fault-tolerant circuit design

So far in this chapter, the principles of QEC were introduced and the repetition and Steane codes were discussed. It was shown that the distance-3 bit-flip code's error rate of a logical qubit can be lower than that of a bare physical qubit, given that the physical qubit error rate is low enough. With the Steane code, a QEC code was discussed that allows for correcting a single arbitrary error being present on any of the data qubits. As yet, it has been implicitly assumed that errors only occur while the logical qubit is idling. A more realistic scenario also includes errors during encoding and syndrome extraction procedures.

Encoding and syndrome extraction circuits inevitably contain entangling gates. For one thing, faulty entangling gates can introduce uncorrectable weight-2 errors directly on the two qubits they are acting on. Then again, they can also spread errors already present on the register before the entangling gate is applied. Figure 4.5 shows the propagation of X and Z errors through a CNOT gate. In the case of an X error on the control qubit, the computational basis states $|0\rangle$ and $|1\rangle$ are exchanged at the control qubit. Therefore, the X gate is applied to the target qubit when it actually should not have been applied, which introduces an X error also on the target qubit. In contrast, an X error on the target qubit does not propagate to the control, as the CNOT gate commutes with the X error. The same is true for a Z error on the control qubit. While those three cases are rather straightforward, a Z error on the target qubit is less intuitive. In this case, also the control qubit acquires a Z error [108]. Although seeming unintuitive from our daily interaction with the classical world, one can see, by multiplying the unitary matrices of the Z and CNOT gates, that a Z error acting on the target qubit before applying a CNOT gate is equivalent to Z errors on both qubits after the CNOT gate:

$$\text{CNOT } Z_2 = Z_1Z_2 \text{ CNOT}$$

$$\begin{pmatrix} 1 & 0 & 0 & 0 \\ 0 & 1 & 0 & 0 \\ 0 & 0 & 0 & 1 \\ 0 & 0 & 1 & 0 \end{pmatrix} \begin{pmatrix} 1 & 0 & 0 & 0 \\ 0 & -1 & 0 & 0 \\ 0 & 0 & 1 & 0 \\ 0 & 0 & 0 & -1 \end{pmatrix} = \begin{pmatrix} 1 & 0 & 0 & 0 \\ 0 & -1 & 0 & 0 \\ 0 & 0 & -1 & 0 \\ 0 & 0 & 0 & 1 \end{pmatrix} \begin{pmatrix} 1 & 0 & 0 & 0 \\ 0 & 1 & 0 & 0 \\ 0 & 0 & 0 & 1 \\ 0 & 0 & 1 & 0 \end{pmatrix}. \tag{4.27}$$

Error propagation can increase the weight of an error. Therefore, an error that would be correctable for a particular QEC code before propagation can become uncorrectable and can lead to corruption of the encoded logical information. Let us assume that a circuit component, like a gate operation, an idling location or a measurement, is erroneous with probability p. In this case, implementing a circuit using bare physical qubits would yield a faulty result with a probability $\mathcal{O}(p)$. In principle, using a distance-3 QEC code would suppress these errors so that the error probability scales as $\mathcal{O}(p^2)$. However, entangling gate errors and error propagation lead to the breakdown of this suppression mechanism, as single errors can propagate to higher weight, uncorrectable errors, as shown in Figure 4.5. Therefore, some logical errors occur with probability $\mathcal{O}(p)$, breaking the promise of QEC.

For a QEC code with a distance d that can correct $t = \lfloor \frac{d-1}{2} \rfloor$ errors, a quantum circuit is called *fault-tolerant (FT)* if logical errors are only caused by errors that occur with a probability of order greater than $\mathcal{O}(p^k)$. In contrast, a circuit is called *non-FT* if errors occurring with a probability of order smaller than or equal to $\mathcal{O}(p^t)$ lead to logical errors, e.g., by error propagation through entangling gates. This section discusses how entangling gate and propagation errors can lead to logical errors. Furthermore, techniques are presented that either herald the potential spreading of errors or avoid circuit constructions that are susceptible to error propagation altogether. Those techniques are summarized by the term *FT circuit design*.

For most of this thesis, fault tolerance is discussed for distance-3 QEC codes, where logical errors are admissible with a probability of order larger than $\mathcal{O}(p^2)$. This means that a single faulty circuit component cannot cause a logical error. However, FT circuit design is also essential for higher-distance QEC codes to maintain their error suppression capabilities and their promised advantage over lower-distance codes.

4.4.1 *Logical state preparation*

The first building block of error-corrected quantum computing is preparing a logical qubit with determined logical information. Section 4.2 discussed the preparation of a logical state by measuring the expectation values of the stabilizer generators. The trapped-ion device considered in this thesis allows us to efficiently implement entangling gates between any pair in the qubit register. This enables implementing the logical qubit preparation more resource-efficient compared to the preparation procedure discussed in Section 4.2.

Figure 4.6a shows the circuit for the preparation of $|0\rangle_{\mathrm{L}}$ of the Steane code [109] affected by an exemplary single-qubit error that propagates to an uncorrectable error. The Z-type error syndrome obtained for this error configuration is $(S_Z^{(1)}, S_Z^{(2)}, S_Z^{(3)}) = (+1, +1, -1)$. After naïvely applying the corresponding correction from Table 4.3 the error operator $X_1X_2X_3$ is present on the data qubits. This operator is stabilizer equivalent to the logical X operator, and therefore, a logical error is induced.

In recent years, a concept has been introduced that uses extra auxiliary qubits coupled to the data qubits to herald uncorrectable errors that are cause by a single erroneous circuit component [110–113]. According to their purpose of signaling uncorrectable errors, the extra qubits are called *flag qubits*. After preparing the encoded state and coupling the data register to the flag qubits, the flag qubits are measured. A measurement outcome of -1 reveals potential corruption, and the prepared encoded state is discarded. In this case, the

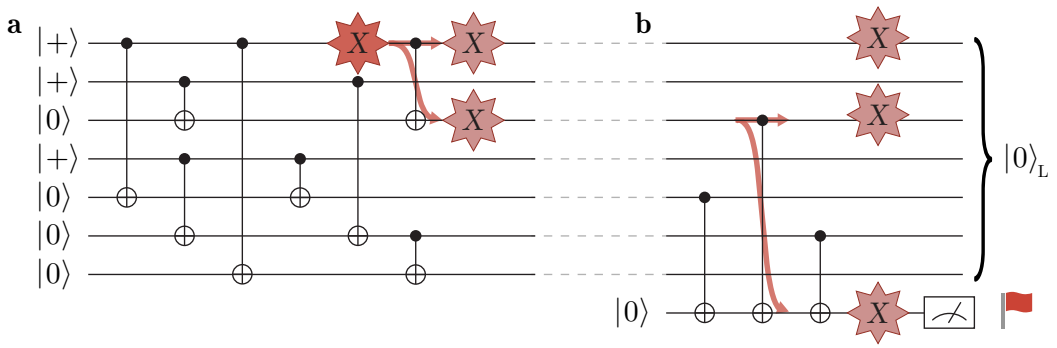

Figure 4.6: Encoding circuit for the Steane code. **a** Non-FT circuit encoding $|0\rangle_L$ [109]. **b** Verification circuit rendering the encoding FT [110]. Single error events leading to logical errors propagate to the flag qubit (bottom wire) and can be detected.

encoding block might just be repeated. If the flag-measurement outcome is $+1$, the desired encoded state is prepared up to correctable errors.

Figure 4.6b shows the verification of the encoding of a Steane code logical qubit using a flag qubit [110]. The additional circuitry shown in the figure is appended to the non-FT encoding circuit and renders the combined circuit FT. As all correctable errors proliferating to uncorrectable errors, the error shown in Figure 4.6a also propagates to the flag qubit and raises the flag, manifesting itself in a measurement outcome of -1.

4.4.2 *Error syndrome extraction*

In the procedure for syndrome extraction, namely the measurement of stabilizer generator expectation values, a similar problem arises, as has been discussed above for encoding a logical qubit. Figure 4.7a shows the non-FT circuit for measuring a weight-4 X-type operator, where the bottom qubit is the auxiliary qubit. An X error on the auxiliary qubit after the second CNOT gate will propagate to a weight-2 error on the data qubits, leading to an uncorrectable error*. The same problem can appear if the second or third CNOT gate is faulty.

A naïve approach to address this problem would be to use multiple auxiliary qubits so that only one entangling gate acts on each qubit, as depicted in Figure 4.7b. This solves the problem of error propagation, as a single error cannot create an uncorrectable error. However, here another problem arises: This circuit does not extract the parity information, but instead it projects the data qubits in the respective basis they have been measured in. Consequently, a carefully structured entangled state for QEC present on the data qubit register collapses, rendering further cycles of QEC impossible.

In the following, two different procedures are discussed that circumvent the problems arising when faulty gates and qubits are considered for error syndrome extraction. The

* Although errors before the first, after the first, or after the third CNOT gate will also propagate to higher-weight errors, they do not have to be taken into account here as they do not lead to uncorrectable errors. An X error acting on the auxiliary qubit right before the first CNOT gate propagates to all four data qubits. However, the error configuration consisting of X errors on all four data qubits is a stabilizer generator and, therefore, the encoded information is not affected. An X error on the auxiliary qubit after the first CNOT gate propagates to a weight-3 error on the data qubits which is stabilizer equivalent to a weight-1 error and, by this, correctable. A gate after the third CNOT gate propagates to a correctable weight-1 error on the data qubits.

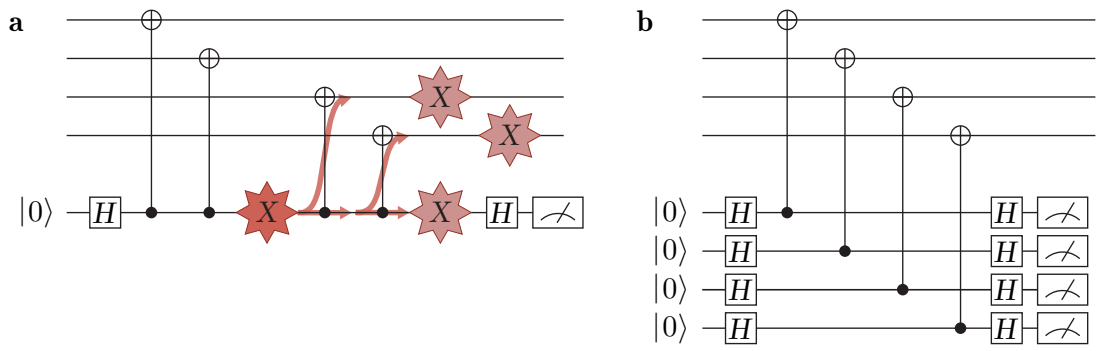

Figure 4.7: **a** Non-FT measurement of a weight-4 X-type stabilizer generator using one bare auxiliary qubit. The top four qubits are the qubits the stabilizer generator acts on. A single error acting on the auxiliary qubit between the second and third CNOT gate can proliferate to become a weight-2 error on the data qubits. **b** Coupling of the data qubits to four bare physical qubits. Although in this circuit single errors can at most propagate to become weight-1 errors on the data qubits, the circuit is unsuitable for parity measurements because it reveals too much information about the data qubits' quantum state.

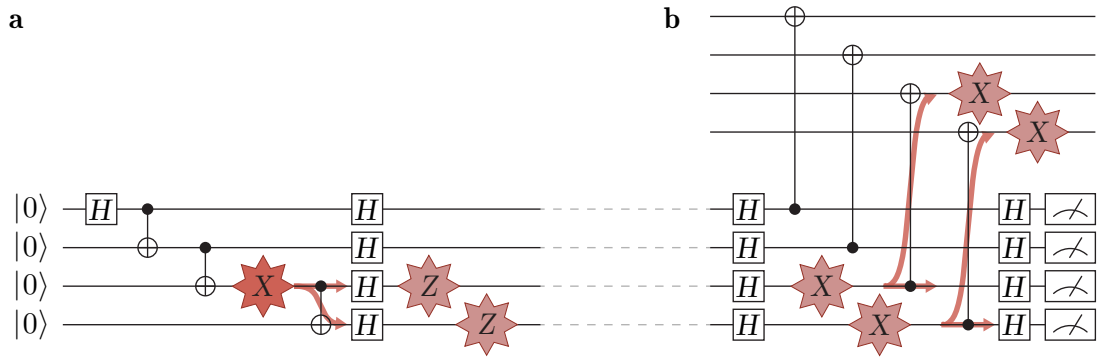

Figure 4.8: Parity measurement using a four-qubit Shor state [42]. **a** Non-FT circuit preparing the four-qubit state $|\mathrm{Shor}\rangle$. **b** Measurement of a weight-4 X operator. The top four qubits are the qubits the stabilizer generator acts on. A single fault event acting on the third auxiliary qubit during the preparation of the Shor state can propagate to a weight-2 error on the data qubits.

techniques obey the rules of fault tolerance, ensuring a scaling of the error rate with $\mathcal{O}(p^2)$ while the encoded information is kept intact.

4.4.2.1 *Steane syndrome extraction*

A first approach to tackle problematic error propagation during syndrome extraction is to further develop the idea of using multiple auxiliary qubits, ensuring that only a single entangling gate is acting on each qubit. To avoid revealing too much information, one can tailor the initial state of the auxiliary qubit register to be an entangled state [42]. A possible

auxiliary register input state proposed by Shor [35] is a superposition of all computational basis states with an even number of excitations. For four qubits, this state reads

$$|\text{Shor}\rangle = \frac{1}{\sqrt{8}} \left(|0000\rangle + |0011\rangle + |0101\rangle + |0110\rangle + |1001\rangle + |1010\rangle + |1100\rangle + |1111\rangle\right) \tag{4.28}$$

and can be prepared by applying Hadamard operations to all qubits in a four-qubit GHZ state, as shown in Figure 4.8a. This auxiliary register state can be used to measure a weight-4 X-type stabilizer generator as shown in Figure 4.8b. In the error-free case, the parity of the data qubits is +1, and the measurement procedure coupling the data qubits to the auxiliary qubits will induce an even number of bit flips on the auxiliary qubits. This maps any basis state in $|\text{Shor}\rangle$ to another basis state in $|\text{Shor}\rangle$. Therefore, the state $|\text{Shor}\rangle$ remains unchanged if there is no error present on the data qubits. Subsequent measurement of the auxiliary register will result in a projection to any of the basis states in $|\text{Shor}\rangle$ but will not project the data qubit quantum state. The outcome of the stabilizer generator measurement can be determined by multiplying the individual outcomes of the auxiliary register measurements. If an error is present on the measured data qubits, an odd number of auxiliary qubits experiences a bit flip. Therefore, every basis state in $|\text{Shor}\rangle$ is mapped to a basis state with an odd number of excitations. The product of auxiliary qubit measurement outcomes is -1 in this case, and the error is detected.

The circuit shown in Figure 4.8b ensures that single errors occurring during the coupling of the data register to the auxiliary register do not lead to logical errors. However, there is still a flaw: If the second or third CNOT gate of the Shor state preparation circuit is erroneous or a single-qubit error occurs between the CNOT gates, a weight-2 error on the auxiliary register can be induced. One does not have to worry about X errors present on the Shor state after preparation as they do not propagate to the data qubits. In the worst case, X errors present on the qubit register corrupt the outcome of the stabilizer generator measurement. This leads to a corruption of the error syndrome and the implementation of the wrong correction operation. Applying the wrong correction introduces a weight-1 error on the data register, but cannot directly lead to an uncorrectable error. On the contrary, Z errors present on the Shor state do propagate to the data register, meaning that one has to ensure the absence of two Z errors on the Shor state [42]. An error causing dangerous propagation is shown exemplarily in Figure 4.8a. Dangerous error propagation can be avoided by using an additional flag-type auxiliary qubit that measures the parity of the first and last qubit of the GHZ state before applying the Hadamard operations that rotate the GHZ state into $|\text{Shor}\rangle$ [42]. The circuit preparing this verified Shor state is shown in Figure 4.9a. There is no single error introducing two Z errors on the Shor state that does not change the parity of the first and last qubit of the GHZ state to -1. Therefore, a measurement outcome of $+1$ on the flag qubit verifies that no dangerous error propagation occurred. In other words, errors leading to dangerous error propagation will also propagate to the flag qubit. Shor states showing a flag-measurement outcome of -1 are discarded, and the state preparation is repeated. After successful preparation of the verified Shor state, the auxiliary and data registers are coupled as shown in Figure 4.9b to measure the expectation value of the stabilizer generator.

An alternative approach to verified Shor states following a similar idea has been proposed by Steane. Instead of measuring the expectation values of the stabilizer generators one by

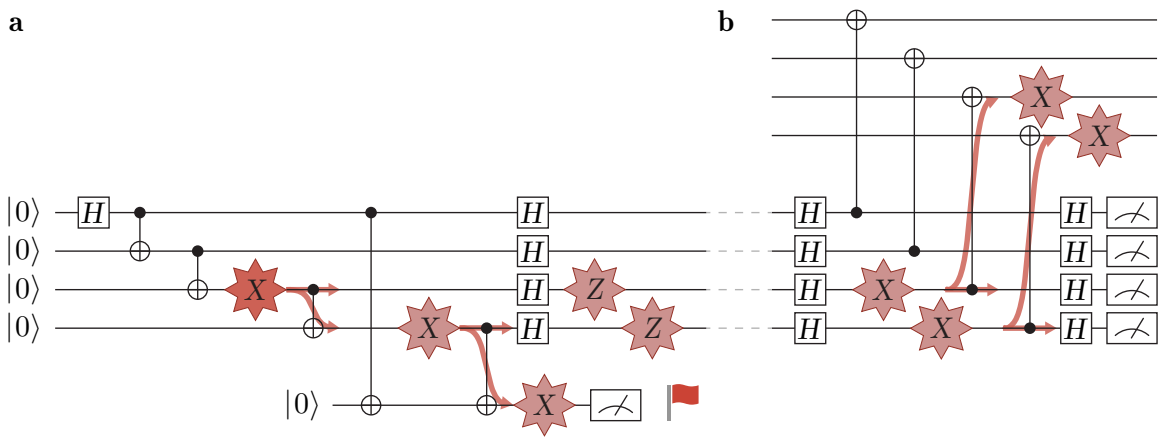

Figure 4.9: Fault-tolerant parity measurement using a four-qubit Shor state [42]. **a** Fault-tolerant circuit preparing the four-qubit state $|\text{Shor}\rangle$. **b** Measurement of a weight-4 X operator. The top four qubits are the qubits the stabilizer generator acts on. A single fault event acting on the third auxiliary qubit in **a** can propagate to a weight-2 error on the data qubits. However, an additional flag qubit coupled to the first and fourth auxiliary qubits ensures fault tolerance as it heralds errors propagating to uncorrectable errors on the data register [42].

one, he suggested determining all stabilizer generator expectation values of a particular QEC code at once [114]. The procedure to extract the error syndrome is the following:

1. The stabilizer generators $\{S^{(i)}\}$ of an n-qubit QEC code containing X and Z operators are interpreted as $2n$-qubit operators only containing Z operators. A Z operator is placed at position i of the $2n$-qubit operator for every X operator at position i of the stabilizer generator. Next a Z operator is placed at position $i+n$ for every Z operator at position i of the stabilizer generator. For example, the five-qubit stabilizer generator

$$S^{(1)} = X_1X_2Z_3Z_5 = X \otimes X \otimes Z \otimes \mathbb{1} \otimes Z \tag{4.29}$$

   is interpreted as

$$S'^{(1)} = Z_1Z_2Z_8Z_{10} = Z \otimes Z \otimes \mathbb{1} \otimes \mathbb{1} \otimes \mathbb{1} \otimes \mathbb{1} \otimes \mathbb{1} \otimes Z \otimes \mathbb{1} \otimes Z. \tag{4.30}$$

2. A $2n$-qubit auxiliary register is prepared in an equal superposition state $|\psi\rangle$ of all $2n$-qubit computational basis states that are a simultaneous $+1$ eigenstate of the operators $S'^{(i)}$:

$$|\psi\rangle \approx \sum_j |j\rangle \quad \text{with} \quad S'^{(i)}\,|j\rangle = |j\rangle \;\; \forall\, i. \tag{4.31}$$

   Here, the normalization of the state is neglected.

3. Next, the data and auxiliary registers are coupled so that errors from the data register are copied to the auxiliary qubits. To do so, the circuit shown in Figure 4.9b, expanded to act on n data and n auxiliary qubits, is applied between the data qubits and the first n

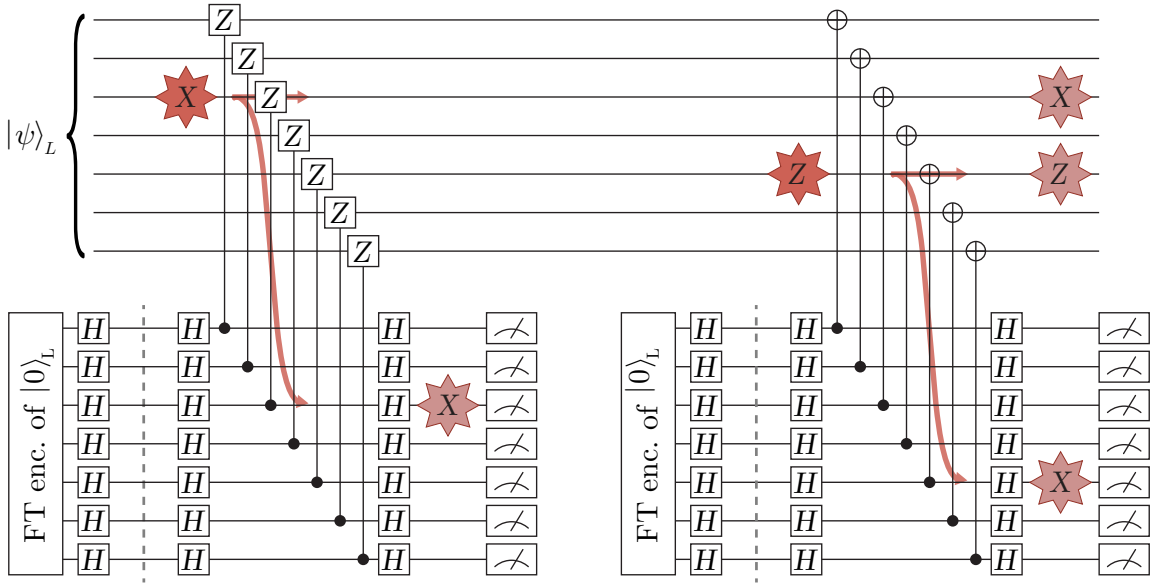

Figure 4.10: Steane syndrome extraction for the Steane code. The blocks labeled 'FT enc. of $|0\rangle_L$' contain the circuit from Figure 4.6. The Z- and X-type error syndromes are determined in the left and right parts of the circuit, respectively. A single execution of this circuit is enough to determine the entire error syndrome fault-tolerantly.

auxiliary qubits. In this step, X errors are copied to the auxiliary qubits. Subsequently, the same circuit, apart from replacing the CNOT gates with controlled-Z gates, is applied between the data qubits and the last n auxiliary qubits to copy Z errors to the auxiliary register. The following measurement projects the auxiliary register to a randomly selected computational basis state without revealing the information encoded in the data qubits.

4. The error syndrome can be extracted from the measured bitstring k. The expectation value of the stabilizer generator $S^{(i)}$ is $+1$ if $S'^{(1)}|k\rangle = |k\rangle$ and -1 if $S'^{(1)}|k\rangle = -|k\rangle$.

In the original proposal [114], Steane discussed this syndrome extraction procedure for a QEC code with stabilizer generators containing X and Z operators. Nowadays, the procedure is mostly applied to QEC codes with stabilizer generators either containing X or Z operators, called Calderbank-Shor-Steane (CSS) codes [36, 115]. For CSS codes, this syndrome extraction procedure is referred to as *Steane QEC** and greatly simplifies compared to the general case described above [116–118]: Then the X-type and Z-type syndrome can be determined sequentially and only n auxiliary qubits are required simultaneously. To determine the expectation values of the Z-type stabilizer generators $\{S_Z^{(i)}\}$ the auxiliary qubit register is prepared in a superposition of all n-qubit basis states that fulfill $S_Z'^{(i)}|j\rangle = |j\rangle$ for all stabilizers $S_Z'^{(i)} = S_Z^{(i)}$. Then, X errors are copied from the data qubits to the auxiliary register using the coupling described in step three above. The auxiliary register state for extracting the expectation values of the X-type stabilizer generators $\{S_X^{(i)}\}$ is given by a superposition of all states fulfilling $S_X'^{(i)}|j\rangle = |j\rangle$, where $S_X'^{(i)}$ is an operator acting on the

* Do not confuse Steane QEC (also termed Steane EC or Steane syndrome extraction throughout this thesis) with the Steane code. The former is a method for error syndrome extraction while the latter is a QEC code. Steane QEC can be applied to various QEC codes.

Figure 4.11: Circuit identities used to simplify QEC circuits. **a** Two consecutive applications of Hadamard operations implement the identity. **b** A measurement of Z using an auxiliary qubit can be implemented by applying a CNOT gate, where the qubit to be measured acts as the control qubit, and the auxiliary qubit is the target of the CNOT gate.

same qubits as $S_X^{(i)}$ but every X operator is replaced by a Z operator. Subsequently, Z errors are copied to the auxiliary registers. The error syndrome for the Z- and X-type stabilizer generators is calculated as described in step four of the aforementioned procedure description using the n-bit bitstrings k_z and k_x. Those bitstrings are obtained from the auxiliary register measurement after copying the X and Z errors to the auxiliary qubits.

For the Steane code, which falls into the class of CSS codes, the auxiliary register state for Steane EC is the superposition of the 16 computational basis states contained in the code words $|0\rangle_\mathrm{L}$ and $|1\rangle_\mathrm{L}$ (see Eqns. 4.25 and 4.26). This superposition state $|+\rangle_\mathrm{L} = \frac{1}{\sqrt{2}}(|0\rangle_\mathrm{L} + |1\rangle_\mathrm{L})$ can be generated by applying bitwise Hadamard operations to all physical qubits constituting a logical auxiliary qubit prepared in $|0\rangle_\mathrm{L}$. Subsequently, the X-type or Z-type errors are copied to the auxiliary register. The circuits for extracting the Z-type or X-type error syndrome are shown in Figure 4.10 on the left and right, respectively. Simplified circuits using the circuit identities shown in Figure 4.11 can be found in Appendix A. The extracted error syndrome can be decoded using the look-up table shown in Table 4.3.

In this scheme, for both types of stabilizer generators only a single CNOT acts on each auxiliary qubit, as well as each data qubit. This prevents the propagation of correctable to uncorrectable error configurations. Nevertheless, the auxiliary input state has to be verified as for Shor states. This ensures that the state preparation circuit does not introduce any uncorrectable errors. For $|0\rangle_\mathrm{L}$ of the Steane code, an FT state preparation scheme has already been presented in Section 4.4.1. One can also use this circuit, respecting FT design rules, for the preparation of $|+\rangle_\mathrm{L}$. The bitwise application of Hadamard operations necessary to transform $|0\rangle_\mathrm{L}$ to $|+\rangle_\mathrm{L}$ preserves the fault tolerance properties of the preparation circuit, as will be discussed in Chapter 5.

Steane EC requires 16 qubits (including verification flag qubits) to extract the error syndrome of the Steane code. Steane QEC minimizes the coupling between data qubits and auxiliary qubits [114]. Only 14 CNOT gates act on the data qubits, compared to 24 for syndrome extraction with bare physical qubits or verified GHZ states.

Steane EC can also be applied to the distance-3 bit-flip and phase-flip codes discussed in Section 4.1. The stabilizer generators of the bit-flip code are $\{Z_1Z_2, Z_2Z_3\}$. Computational basis states satisfying the criteria of having even parity on the qubit pairs $(1, 2)$ and $(2, 3)$ are $|000\rangle$ and $|111\rangle$, so that the auxiliary qubit state required for Steane-type EC is given by

$$|\psi\rangle_\mathrm{a} = \frac{1}{\sqrt{2}}(|000\rangle + |111\rangle). \tag{4.32}$$

Figure 4.12a depicts a complete cycle of Steane EC of the distance-3 bit-flip code. A single X error anywhere in the Steane EC procedure cannot propagate to become a weight-2 error on the data qubits. Still, single X errors can corrupt the error syndrome extracted from

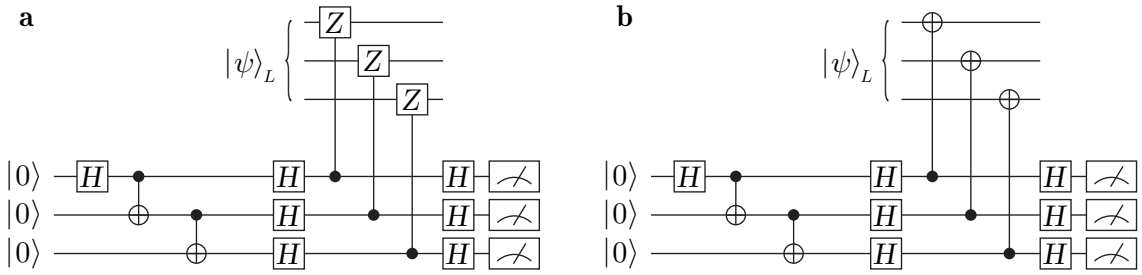

Figure 4.12: Steane syndrome extraction for the distance-3 **a** bit- and **b** phase-flip code. In both cases, the state $|\psi\rangle_{\mathrm{a}} = \frac{1}{\sqrt{2}}(|000\rangle + |111\rangle)$ is prepared on the auxiliary register before mapping errors from the data to the auxiliary register. The protocol is FT without auxiliary state verification for distance-3 repetition codes.

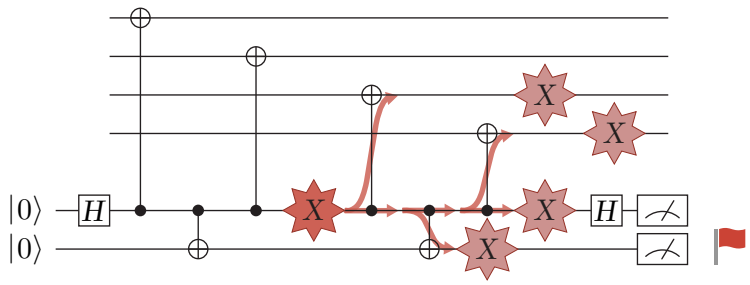

Figure 4.13: Fault-tolerant measurement of a weight-4 stabilizer generator using a single additional flag qubit [111]. Errors leading to weight-2 error configurations on the data qubits, like the single-qubit error shown, are captured by the flag qubit.

a projective measurement of the auxiliary register. However, this can at most introduce a single X error on the data qubits after applying the correction determined using the look-up table in Table 4.2. Hence, Steane EC is FT for the distance-3 bit-flip code without verification of the auxiliary state.

For the distance-3 phase-flip code, the stabilizer generators $\{X_1X_2, X_2X_3\}$ again require the input state to exhibit even parity on qubit pairs $(1, 2)$ and $(2, 3)$ in the computational basis. Therefore, the state $|\psi\rangle_{\mathrm{a}}$ given in Eqn. 4.32 is also suitable for Steane EC on the phase-flip code. The look-up table used to infer the necessary correction can be constructed from columns two to four of the bit-flip code look-up table by replacing Z with X and vice versa. The circuit for one round of syndrome extraction in the distance-3 phase-flip code is shown in Figure 4.12b.

4.4.2.2 *Flag-based syndrome extraction*

Instead of pursuing the concept of having only one entangling gate acting on each auxiliary qubit for syndrome extraction, one can also take up the paradigm of flag qubits to address dangerous error propagation. Similar to the verification of logical state preparation discussed in Section 4.4.1, extra qubits coupled to the auxiliary qubits can be used to herald correctable errors that propagate to become uncorrectable. Figure 4.13 shows a circuit for the parity measurement of a weight-4 operator using a single auxiliary and a single flag qubit [111]. Errors that propagate to weight-2 errors, like the one marked in the circuit, are also propagating to the flag qubit and are detected as the flag qubit is measured. Depending

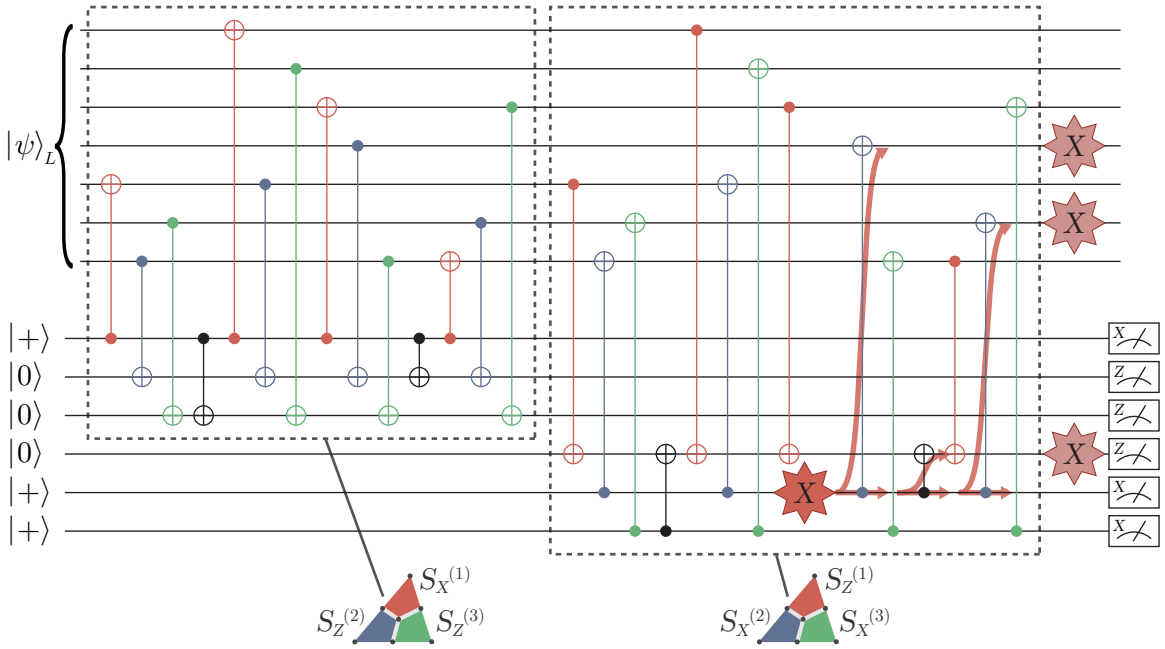

Figure 4.14: Flag syndrome extraction for the logical state $|\psi\rangle_{\mathrm{L}}$ encoded in the Steane code using six auxiliary qubits [119, 120]. The auxiliary qubits used for syndrome extraction also act as flag qubits for each other. Entangling gate operations are depicted using the color of the plaquette for which they measure the stabilizer generator expectation value. The CNOT gates shown in black establish the coupling necessary for the auxiliary qubits to act as flag qubits for each other.

on the context in which the circuit from Figure 4.13 is embedded, there are two possible ways to proceed after the measurement outcome of the flag qubit is -1: Either the run can be discarded or the two bits of information gained from the measurement in conjunction with additional measurements can be used to correct the present error on the data register. Using this scheme to measure all six stabilizer generators of the Steane code requires twelve qubits. Note that only two auxiliary qubits are required simultaneously if the expectation values of the stabilizer generators are measured sequentially.

An approach requiring fewer auxiliary qubits throughout the syndrome readout compared to the scheme shown in Figure 4.13 is proposed in Refs. [119, 120]. While still following the concept of flag fault tolerance, the auxiliary qubits act as flag qubits for each other. This allows for the measurement of all six stabilizer generators of the Steane code using only a total of six auxiliary qubits. The corresponding circuit, consisting of two blocks measuring three stabilizer generators each, is shown in Figure 4.14. For each block, entangling gates are colored corresponding to the plaquette for which they measure the stabilizer generator expectation value. The measurement outcome of this circuit is referred to as *flag syndrome* to highlight that the auxiliary qubits also act as flag qubits here. Similar to the circuit in Figure 4.13, error locations that allow for error propagation to two data qubits are to be taken care of. The CNOT gates drawn in black ensure that errors also propagate within the auxiliary register, so that auxiliary qubits can act as flag qubits for each other. One of the dangerous propagation paths is illustrated in the circuit diagram. The single-qubit X

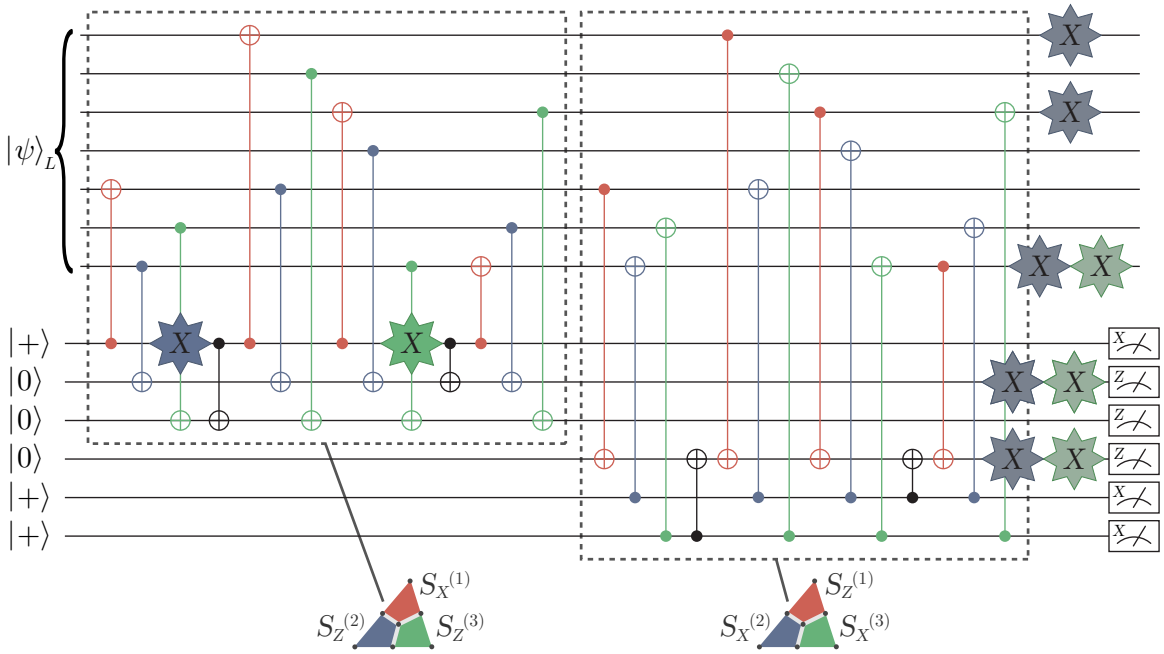

Figure 4.15: Indistinguishable errors in the flag syndrome extraction circuit for the Steane code [119, 120]. The two single-qubit X errors shown in blue and green lead to the same flag syndrome while the error on the data qubit register is different. The error propagation paths are not shown for clarity.

error on the fifth auxiliary qubit causes the two-qubit error X_4X_6 to be present on the data register. The non-trivial* flag syndrome $(S_Z^{(1)}, S_Z^{(2)}, S_Z^{(3)}) = (-1, +1, +1)^\dagger$ is obtained.

However, applying the syndrome extraction circuit shown in Figure 4.14 does not allow one to distinguish all possible errors. In Figure 4.15 two different single-qubit errors are shown that lead to the same flag syndrome $(S_Z^{(1)}, S_Z^{(2)}, S_Z^{(3)}) = (-1, -1, +1)$. The errors shown in blue and green lead to the errors $X_1X_3X_7 = S_X^{(1)}X_5$ and X_7 on the data register, respectively. To render all errors distinguishable, another round of syndrome extraction has to be implemented in case the measured flag syndrome is not trivial. This second readout can be implemented using non-FT circuits shown in Figure 4.7 as error processes introducing errors in the flag circuit from Figure 4.14 *and* in the second syndrome readout have probability $\mathcal{O}(p^2)$. A logical error with this probability scaling is acceptable as the Steane code can only correct a single error, and therefore, logical errors with probability $\mathcal{O}(p^2)$ can not be avoided in any case. A second round of syndrome extraction yields the error syndromes $(S_Z^{(1)}, S_Z^{(2)}, S_Z^{(3)}) = (-1, -1, +1)$ and $(S_Z^{(1)}, S_Z^{(2)}, S_Z^{(3)}) = (-1, -1, -1)$ for the errors shown in blue and green, respectively. Applying a correction determined using the standard look-up table for the Steane code, shown in Table 4.3, successfully corrects both errors.

For the weight-2 error shown in Figure 4.14 the second round of syndrome extraction yields $(S_Z^{(1)}, S_Z^{(2)}, S_Z^{(3)}) = (+1, +1, -1)$. Instead of applying the correction X_2, determined

* A syndrome is referred to as *trivial* if all measured expectation values are equal to $+1$. Conversely, a syndrome containing at least one expectation value of -1 is referred to as *non-trivial*.

† The part of the flag syndrome given by the expectation values of the X-type stabilizer generators is trivial for all cases discussed in this section and is omitted.

$(S_Z^{(1)}, S_Z^{(2)}, S_Z^{(3)})$	Correction
$(+1, -1, +1)$	X_3X_7
$(+1, +1, -1)$	X_4X_6

$(S_X^{(1)}, S_X^{(2)}, S_X^{(3)})$	Correction
$(+1, -1, +1)$	Z_3Z_7
$(+1, +1, -1)$	Z_4Z_6

Table 4.4: Error correction look-up table for flag-based syndrome extraction of the Steane Code. The first column shows the error syndrome of a second round of syndrome extraction after the flag-based syndrome extraction yielded a non-trivial syndrome. The second column shows the correction that is applied to the data register.

using Table 4.3, the correction X_4X_6 is applied to correct the error on the data register. A look-up table for error configurations propagating to two-qubit errors can be found in Table 4.4. For all other error syndromes and in cases where the flag and error syndromes match, the standard look-up table for the Steane code is applied.

This readout scheme only requires six physical auxiliary qubits. The number of qubits can even be reduced to three if the two blocks in Figure 4.14 are implemented sequentially and the auxiliary qubits are reused*. This means that the qubit number overhead is smaller compared to the Steane EC protocol discussed in Section 4.4.2.1. However, fewer entangling gates are required for Steane EC, allowing for lower logical error rates, if the entangling gate error rate is the dominant noise source. A more detailed discussion on the comparison of flag-based syndrome extraction and Steane syndrome extraction can be found in the next section and in Appendix A.

* This requires a procedure of reinitializing auxiliary qubits after a measurement.

4.5 Publication: Demonstration of fault-tolerant Steane quantum error correction

Demonstration of fault-tolerant Steane quantum error correction*

PRX Quantum **5**, 030326 (2024)

Lukas Postler[1], Friederike Butt[2,3], Ivan Pogorelov[1], Christian D. Marciniak[1], Sascha Heußen[2,3], Rainer Blatt[1,4,5], Philipp Schindler[1], Manuel Rispler[2,3], Markus Müller[2,3], Thomas Monz[1,4]

[1]Institut für Experimentalphysik, Universität Innsbruck, Innsbruck, Austria
[2]Institute for Quantum Information, RWTH Aachen University, Aachen, Germany
[3]Institute for Theoretical Nanoelectronics (PGI-2), Forschungszentrum Jülich, Jülich, Germany
[4]Alpine Quantum Technologies GmbH, Innsbruck, Austria
[5]Institut für Quantenoptik und Quanteninformation, Österreichische Akademie der Wissenschaften, Innsbruck, Austria

Encoding information redundantly using QEC codes allows one to overcome the inherent sensitivity to noise in quantum computers to ultimately achieve large-scale quantum computation. The Steane QEC method involves preparing an auxiliary logical qubit of the same QEC code used for the data register. The data and auxiliary registers are then coupled with a logical CNOT gate, enabling a measurement of the auxiliary register to reveal the error syndrome. This study presents the implementation of multiple rounds of FT Steane QEC on a trapped-ion quantum computer. Various QEC codes are employed, and the results are compared to a previous experimental approach utilizing flag qubits. Our experimental findings show improved logical fidelities for Steane QEC, and accompanying numerical simulations indicate an even larger performance advantage for quantum processors limited by entangling gate errors. This establishes experimental Steane QEC as a competitive paradigm for FT quantum computing.

4.5.1 *Introduction*

Quantum computing has the potential to outperform classical machines by exploiting superposition and entanglement. Quantum information is, due to unavoidable residual coupling of quantum systems to the environment, intrinsically prone to errors potentially jeopardising the computational advantages promised by quantum computing. Therefore, to achieve the goal of enhanced computational capabilities, it is crucial to safeguard quantum information, e.g. by encoding it into stabilizer codes that protect against environmental and operational noise. By repeatedly measuring the stabilizer generators, we can detect noise without disrupting the logical computational state. The error and its location within the

* The author of the present thesis carried out the experiments, analyzed the data, and wrote the manuscript. Here, the accepted version of the manuscript is printed in a slightly amended form for consistency throughout the thesis. Changes include adapting hyphenation and abbreviations.

register are mapped onto the results of the stabilizer measurements, also referred to as error syndrome. We must prevent the spread of errors by following the principles of FT circuit design, as defined in Section 4.5.2, to conduct quantum computation on the encoded level while maintaining the expected scaling of logical error rates with physical error rates. This requirement implies experimental challenges in FT logical state preparation, FT logical gates, and FT EC.

Recent progress in achieving error-corrected universal quantum computation has been made through the development of FT QEC components in leading hardware architectures. In superconducting systems, significant strides have been made towards operating Kitaev's surface code, resulting in an operation fidelity that exceeds the break-even point [121–124]. Additionally, FT magic state preparation has been demonstrated in a superconducting experiment with fidelity beyond break-even [125]. Ion-trap experiments have demonstrated FT stabilizer readout [126], FT control of single logical qubits [127], and FT repetitive QEC cycles [38], with subsequent efforts aimed at implementing universal FT logical gate sets [39, 128]. Meanwhile, practical experimental benefits of fault tolerance have been demonstrated in error-detecting codes, such as FT non-Clifford gates on multiple logical qubits in both superconducting and trapped-ion devices [129], FT one-bit addition as a small logical algorithm on three logical qubits [130], the realization of Grover search utilizing encoded qubits in a trapped-ion device [131], and the very recent demonstration of a larger logical quantum processor with neutral atoms [40].

The backbone of the successful operation of an FT quantum processor is an efficient implementation of QEC cycles. Steane QEC minimizes the coupling between data and auxiliary qubits and therefore also perturbations of the data register. Thus it is a promising candidate for the efficient extraction of error syndromes on scalable error-correcting codes.

4.5.2 *Fault-tolerant quantum error correction*

Given operations acting on logically encoded qubits, such as initialization, gate operations, and measurements, have to be constructed in a way that prevents dangerous propagation of errors. An error configuration is dangerous when an otherwise correctable number of errors spreads via entangling gates and turns into an error supported on a number of qubits (referred to as the weight of the error) beyond the number of errors the code can correct. A circuit where this is precluded by design is called an FT implementation and hence we refer to the corresponding operations as FT. In particular, this applies to the QEC block itself, where the necessary coupling to auxiliary qubits unavoidably feeds back to the data qubits. Any coupling can then potentially induce errors if the auxiliary qubit or the coupling itself is faulty. A method to extract the error syndrome, which minimizes the interaction between the logical data qubit(s) and the auxiliary qubit(s), was formulated by Steane [114]. The key idea is to prepare an auxiliary *logical* qubit using the same code as the data qubit and to couple both logical qubits via a transversal logical CNOT gate, i.e. in a bitwise manner. This guarantees that if any single physical operation is faulty, at most one error per encoded logical qubit block is introduced. Specifically, first, an auxiliary logical qubit is prepared in a superposition of its basis logical states $|+\rangle_L = \frac{1}{\sqrt{2}}(|0\rangle_L + |1\rangle_L)$ and a transversal $\mathrm{C}^{\mathrm{data}}\mathrm{NOT}^{\mathrm{aux}}$ is applied, as illustrated in Figure 4.16A. In the error-free case, the CNOT will act trivially on both encoded qubits as $\mathrm{CNOT}_L|\psi\rangle_L|+\rangle_L = |\psi\rangle_L|+\rangle_L$. However, if a single bit flip is present on the ith qubit comprising the logical data qubit (denoted

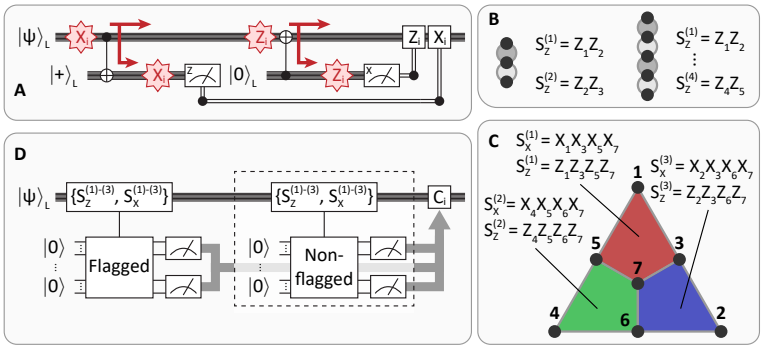

Figure 4.16: Quantum error correction codes and methods for syndrome extraction. (**A**) In Steane-type EC, an auxiliary logical qubit is prepared in $|+\rangle_L$, then coupled to the initial logical qubit $|\psi\rangle_L$ with a transversal CNOT gate, and then measured in the computational basis. This procedure is repeated for an auxiliary logical qubit in $|0\rangle_L$ with an inverted transversal CNOT gate. A correction is applied to the corresponding data qubits based on the syndrome which is extracted from the measurements performed on the auxiliary logical qubit. (**B**) The repetition code encodes one logical qubit and its stabilizer generators are weight-2 Pauli-operators defined between neighboring qubits on a line. (**C**) The seven-qubit color code encodes one logical qubit into seven physical qubits. A code state is a $+1$ eigenstate of all six weight-4 stabilizer generators $\{S_X^{(i)}, S_Z^{(i)}\}$ defined on the colored plaquettes. Pauli-X (-Z) on all qubits corresponds to the logical operator X_L (Z_L), which is up to multiplication with stabilizer generators equivalent to weight-3 operators. (**D**) Flag-EC includes the measurement of the stabilizer generators with flagged circuits. In case of non-trivial measurement outcomes of the flagged circuits, repeating the measurement of stabilizer generators is necessary. Different variants of flag-based QEC require different numbers of simultaneously available auxiliary qubits and remeasuring procedures. The flag-QEC procedure used in this work is described in Appendix A.1.1.

as (X_i^{data})), this will be copied onto the ith qubit comprising the logical auxiliary qubit (denoted as (X_i^{aux})) as

$$\begin{aligned} &\text{CNOT}_L(X_i^{\text{data}} \otimes \mathbb{1})|\psi\rangle_L \otimes |+\rangle_L \\ &= X_i^{\text{data}}|\psi\rangle_L \otimes X_i^{\text{aux}}|+\rangle_L. \end{aligned} \tag{4.33}$$

The transversal CNOT gate is FT by construction since it introduces at most one error on each encoded block. The entire circuit is therefore FT if one additionally verifies that only a correctable number of errors is present on the auxiliary logical qubit. The syndrome can then be reconstructed from the outcomes of the projective measurement of the auxiliary logical qubit in a single shot. One can identify the appropriate recovery operation based on a decoder such as the lookup table for the seven-qubit color shown as Table A.1 in Appendix A.1.1. Just as an auxiliary logical qubit in $|+\rangle_L$ detects propagated X errors, it detects propagated Z errors when prepared in $|0\rangle_L$ and acted upon with a transversal $\text{C}^{\text{aux}}\text{NOT}^{\text{data}}$ in a second half-cycle. In this second half-cycle Z errors are copied from the data qubit to the auxiliary qubit such that measuring the auxiliary qubits reveals the entire X syndrome simultaneously, just as the first half-cycle reveals the entire Z syndrome. This Steane-type QEC is to be seen in contrast to measuring each stabilizer individually, where due to fault tolerance requirements one has to resort to either verified GHZ states

or flag schemes for the auxiliary qubits [35, 111]. Moreover, the syndrome measurement has to be repeated for specific measurement outcomes to avoid single faults leading to high-weight errors, which requires the conditional execution of circuits. In our experiment and simulation, in order to benchmark against the Steane-type QEC, we implement the flagged syndrome extraction protocol of [120], which was previously realized experimentally in [38]. The circuits that are used in the implementation are shown in Figure A.4.

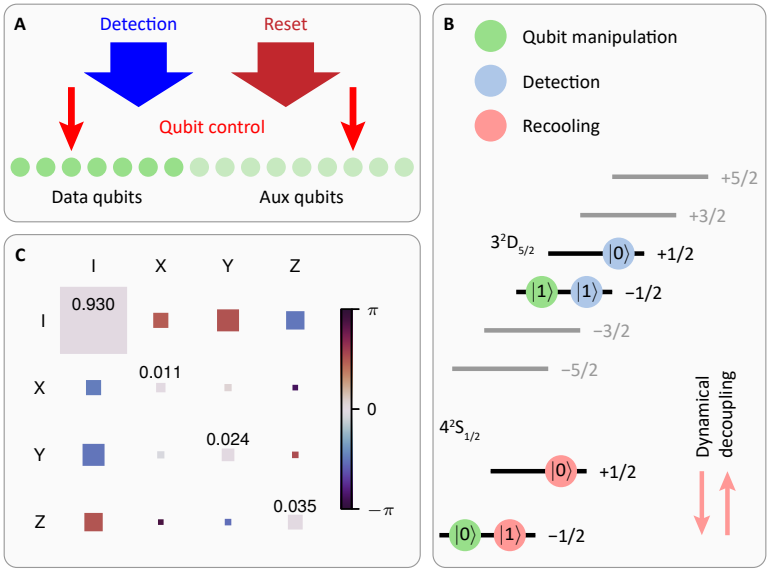

Figure 4.17: Experimental methods for mid-circuit measurements. **A** The qubit register is split into data qubit and auxiliary qubit segments. Tightly focused laser beams addressing up to two individual ions simultaneously are available to manipulate the optical qubit, while qubit state detection and reset lasers illuminate the entire register. (**B**) Different qubit encodings are used prior to and during different steps of the mid-circuit measurement procedure illustrated by symbols of different coloring. For qubit manipulation the qubits are encoded in two Zeeman sublevels of two different electronic states (green). The data qubit encoding is transferred to two Zeeman sublevels of the same electronic state to either decouple from laser light used to project to the computational basis during mid-circuit measurements (blue), or to be able to perform recooling on auxiliary qubits after a mid-circuit measurement (red). While the qubit is encoded in the ground-state manifold (red), we extend the coherence time via DD by applying RF fields. (**C**) Chi matrix representation [45] of the process acting on data qubits during mid-circuit measurements averaged over all data qubits. The area and the color coding of the squares corresponds to the absolute value and the phase of an element of the chi matrix, respectively. The values on the diagonal of the averaged chi matrix are used to inform the error model (see Appendix A.2).

In this article, we report the implementation of Steane syndrome extraction in a trapped-ion experiment. Central to the implementation of Steane QEC is the transversal logical CNOT, which in our experiment can be performed between all qubits owing to all-to-all qubit connectivity. Transversal CNOT gates have already been demonstrated in a trapped-ion experiment [39] and even their error propagation properties have been exploited in a neutral-atom quantum processor [40]. In this work, we employ transversal CNOT gates to repeatedly perform single-shot syndrome extraction on different error-correcting codes. As a first step, we investigate the bit-flip and phase-flip repetition codes with code distances

3 and 5 each. While the repetition code protects only against either Pauli-X or -Z errors, the syndrome extraction procedure is the same as for leading QEC codes such as surface and color codes. We can therefore experimentally explore the scaling of Steane QEC for codes of increasing distance. Furthermore, we demonstrate Steane syndrome extraction for a complete quantum error correcting code by applying it to the seven-qubit color code. We perform up to five and three full cycles of syndrome extraction for the repetition code and seven-qubit color code, respectively.

4.5.3 *Experimental setup*

All experimental results presented in this manuscript are implemented in a trapped-ion quantum processor. Sixteen $^{40}Ca^{+}$ ions are trapped in a macroscopic linear Paul trap, where the electronic state of the ions is controlled via laser pulses, as illustrated in Figure 4.17A. Each ion encodes one qubit in the electronic states $|0\rangle = |4^2S_{1/2}, m_J = -1/2\rangle$ and $|1\rangle = |3^2D_{5/2}, m_J = -1/2\rangle$ (see Figure 4.17B) connected via an optical quadrupole transition at a wavelength of 729 nm. Coulomb interaction between the ions gives rise to collective motional modes of the ions, which are used to mediate entangling operations between any desired pair of qubits. The available universal gate set and its error characteristics are described in more detail in Appendix A.3.

For the repeated application of QEC blocks to encoded qubits it is necessary to have the ability to extract the error syndrome by performing measurements on a subset of qubits. Measurements on these auxiliary qubits are designed in a way that minimizes the perturbation of the logical information stored in the data qubits. Furthermore, it is beneficial to have the capability of reusing measured qubits by reinitializing them to a defined state in the computational subspace, especially with the limited quantum register sizes of noisy intermediate-scale quantum devices. Viable approaches to implement these procedures in trapped-ion quantum processors are introducing a second atomic species [132–134], or moving ions to a distinct region of the trap [126, 135] for mid-circuit measurements allowing state readout of auxiliary qubits while keeping data qubits unperturbed. In this work we make use of multiple Zeeman sublevels in the states $|4^2S_{1/2}\rangle$ and $|3^2D_{5/2}\rangle$ (see Figure 4.17) for the implementation of mid-circuit measurements and subsequent reinitialization [136–138].

The first step of this procedure is the detection of the auxiliary qubits by electron shelving [83]. All data qubits are encoded in the states shown as blue symbols in Figure 4.17B to retain the phase relation of data qubit superposition states and to prevent scattering out of the computational subspace. Scattering photons from auxiliary qubits projected to $|0\rangle$ heat up the ion string, therefore a Doppler cooling pulse, acting on the same atomic transition also used for auxiliary qubit state detection, is applied. However, further cooling close to the motional ground state using resolved sideband cooling [83] is necessary for the implementation of high-fidelity gates after mid-circuit measurements. The sideband cooling procedure involves illumination with laser light that would lead to incoherent relaxation of both states marked with blue symbols to the respective ground states marked as red symbols. Therefore, the data qubit encoding is coherently transferred to the two Zeeman sublevels of the ground state portrayed as red symbols in Figure 4.17B. Subsequent to sideband cooling a final optical pumping step is used to reinitialize all auxiliary qubits that are supposed to be reused. Finally we restore the encoding of the data qubits to the states shown as green symbols, where further gate operations on the optical qubit can be implemented. A more detailed description of the procedure can be found in Appendix A.3.

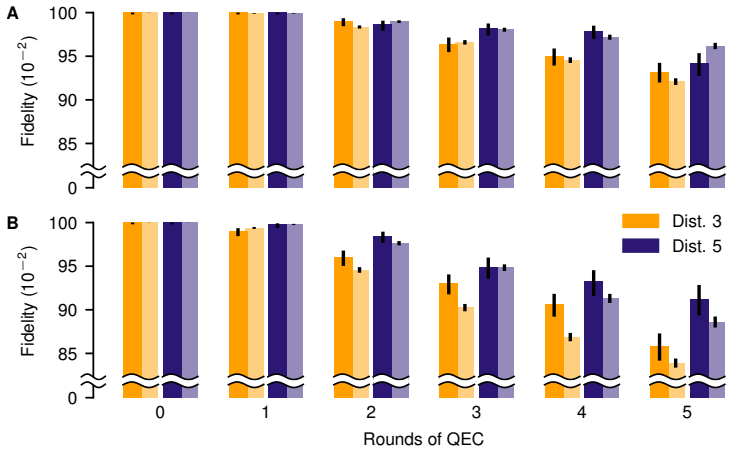

Figure 4.18: Logical fidelities for bit- and phase-flip repetition code for distances 3 and 5. Fidelities for up to 5 rounds of Steane-type EC for the distance-3 and distance-5 (**A**) bit-flip and (**B**) phase-flip code. Round 0 corresponds to the encoding of the logical state with no extra round of QEC. The experimental and simulation results are depicted with darker and lighter shades, respectively. The error bars shown in this and all following data figures are calculated as described in Appendix A.4. All data is available on Zenodo, see data availability statement 4.5.6.4.

The duration of the mid-circuit detection procedure is dominated by the sideband cooling step with a duration on the order of the coherence time. Therefore, a DD sequence [77, 139] is performed on the data qubits during the recooling procedure. This decoupling is implemented with a resonant RF antenna driving the transition between the two ground states on the entire register simultaneously, where the data qubits are encoded during sideband cooling (red symbols). A refocusing pulse is applied approximately every millisecond in between cooling pulses for different motional modes. Figure 4.17C shows the process matrix [45] of the evolution of data qubits during a full mid-circuit measurement procedure including DD averaged over all data qubits.

4.5.4 *Steane QEC for the repetition code and the seven-qubit color code*

In this section we show the application of Steane QEC to 1D repetition codes and the 2D seven-qubit color code. First, we study the scaling of Steane QEC with code distance, by presenting results for distances 3 and 5 for both the bit- and phase-flip repetition code. The structure of the codes and the stabilizer generators are illustrated in Figure 4.16B. Despite their simplicity, these codes share key properties, such as syndrome extraction, logical processing, and error suppression with fully-fledged topological QEC codes. Consequently, they routinely form a testbed for the latter [121, 140]. One round of EC in repetition codes consists of only one half of the cycle illustrated in Figure 4.16A since the codes can only correct either X or Z errors. For example for Steane-type QEC on the distance-3 bit-flip code, a logical state $|\psi\rangle_L$ is encoded in $|000\rangle$. The auxiliary logical qubit is prepared in a three-qubit GHZ state $|+\rangle_L = (|000\rangle + |111\rangle)/\sqrt{2}$. If, for example, an X fault occurs on the first qubit, this will propagate onto the auxiliary logical qubit when the auxiliary qubit is coupled to the logical data qubit with a transversal CNOT gate. A final projective measurement of the auxiliary logical qubit in the Z basis projects the state onto either $|011\rangle$ or $|100\rangle$. We can extract

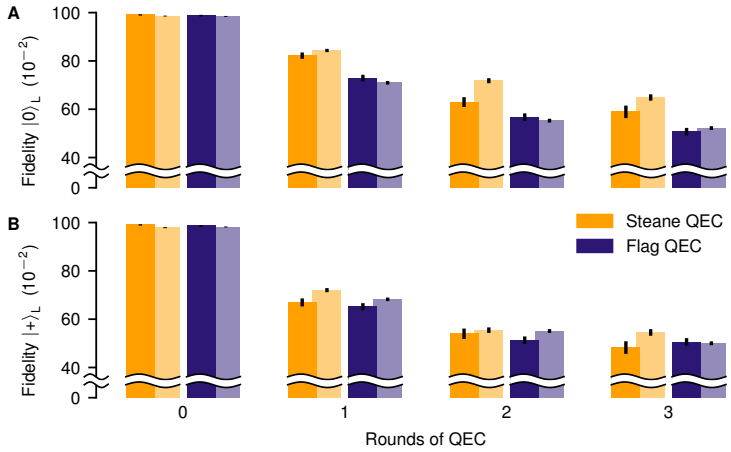

Figure 4.19: Logical fidelities for syndrome extraction on the seven-qubit color code. Logical fidelities obtained from Steane-type and flag-based QEC for the logical input state (**A**) $|0\rangle_L$ and (**B**) $|+\rangle_L$. Round 0 corresponds to the encoding of the logical state with no extra round of QEC. The experimental and simulation results are depicted with darker and lighter shades, respectively.

the stabilizer values $S_Z^{(1)} = Z_1Z_2$ and $S_Z^{(2)} = Z_2Z_3$, as given in Appendix A.1.2, by checking the parity of this measurement outcome. It is then possible to identify the initial fault on the first qubit based on the syndrome $(S_Z^{(1)}, S_Z^{(2)}) = (-1, 1)$. For the distance-5 repetition code, the auxiliary logical state has to be verified to ensure that no single fault has caused a weight-2 error configuration on the auxiliary GHZ state. We do this by coupling a single flag qubit to the prepared auxiliary qubit, heralding weight-2 error configurations, as shown in Figure A.7 in Appendix A.1.2. No verification is required for $d = 3$, since any single fault only results in a correctable error configuration on each encoded block. The phase flip code can be treated completely analogously to the bit-flip code. Figure 4.18 shows the probability to recover the target logical state, within the correction capabilities of the respective QEC code, for the bit- and phase-flip code with distances $d = \{3, 5\}$. We refer to this probability as logical fidelity (see Appendix A.5). Corrections suggested by the repeated syndrome extraction are accounted for via a Pauli frame update [141]. We can identify that increasing the code distance from 3 to 5 improves logical fidelities for both the bit- and the phase-flip code. Lower fidelities for the phase flip code compared to the bit-flip code can be attributed to dephasing on idling qubits. Experimental results are accompanied by Monte Carlo sampling (MC) simulations using an experimentally informed effective noise model. The model accounts for errors on single-qubit gates, two-qubit gates, qubit initialization, and measurements with error rates $p_{1q} = 3.6 \cdot 10^{-3}$, $p_{2q} = 2.7 \cdot 10^{-2}$, $p_{\text{init}} = 3 \cdot 10^{-3}$ and $p_{\text{meas}} = 3 \cdot 10^{-3}$, respectively. Furthermore, during mid-circuit measurements the remaining qubits experience noise which we model as asymmetric depolarizing noise with error probabilities $p^{(x)}_{\text{mid-circ}} = 1.1 \cdot 10^{-2}$, $p^{(y)}_{\text{mid-circ}} = 2.4 \cdot 10^{-2}$, $p^{(z)}_{\text{mid-circ}} = 3.5 \cdot 10^{-2}$, acting on all idling data qubits independently. These error probabilities are extracted from the experimental process matrix, quantifying the effect of mid-circuit measurements on idling (data) qubits, shown in Figure 4.17C. A more detailed description of the error model can be found in Appendix A.2. The simulation data obtained with this relatively simple multi-parameter, incoherent noise model shows

good agreement with the experimental data, which indicates that it captures the experiment well for the given error rates.

Going a step further, we now apply the above-described Steane-type QEC to the seven-qubit color code [36, 37, 142], shown in Figure 4.16C, and compare its performance to the previously used flag-based QEC scheme [38, 120, 128]. In the latter, the syndrome information is extracted by measuring stabilizers using additional auxiliary physical qubits, as illustrated in Figure 4.16D. The seven-qubit color code $[[7, 1, 3]]$ is the smallest topological color code and encodes a single logical qubit while allowing the correction of a single arbitrary Pauli error. It has the highly desirable property of admitting a transversal and thus FT implementation of the entire Clifford group. Physical qubits are placed on the vertices of a two-dimensional graph and the encoded logical qubit is defined as the simultaneous $+1$ eigenstate of the six indicated stabilizer generators. A single flag qubit is used to verify the prepared logical state such that unsuccessful preparations can be discarded [110, 128] analogous to usage in the distance-5 repetition code. The encoding circuit and lookup table are given in Appendix A.1.1.

Figure 4.19 shows the logical fidelities we obtained experimentally and numerically from MC simulations. We find an advantageous performance in terms of fidelity for Steane-type QEC compared to the flag-based QEC scheme, where the performance benefit of Steane QEC is more pronounced for the state $|0\rangle_L$. The reason for this asymmetry is that the dominating error source in the experimental setup at hand is asymmetric depolarizing noise on the data qubits during mid-circuit measurements. Additionally dephasing of data qubits is taking place during the implementation of gates on the auxiliary qubits (see Table A.3 in Appendix A.2). This conflates the logical failure rates for the different protocols and partially veils the advantage of Steane QEC, which is most pronounced in the regime of dominating two-qubit error rates. Therefore, we estimate the projected advantage of Steane-type QEC by numerically simulating logical error rates in a setting where the only noise source are two-qubit gate errors. In this regime, we find that the logical error rate of Steane-type QEC is suppressed by as much as a factor of 2, compared to flag-type QEC (see Figure A.5 in Appendix A.1.1). Experimental improvements like an extended coherence time on the order of seconds [143–145] or composite pulses robust against laser amplitude noise and crosstalk [146, 147] could further mitigate perturbations of idling data qubits during mid-circuit measurements and therefore extend the advantage in logical fidelity offered by the Steane-type over flag-type QEC also in the present experimental setup. Additional results on the extraction of only the Z (X) syndrome for the logical state $|0\rangle_L$ ($|+\rangle_L$) are presented in Appendix A.6.

4.5.5 *Conclusions and Outlook*

In this work we show practical advantage of Steane over flag-based QEC in a noisy intermediate-scale trapped-ion quantum processor. We have implemented up to five rounds of Steane QEC for bit-flip and phase-flip repetition codes with distances 3 and 5, and observe an improvement of the logical fidelity with larger distances. This increase in spite of larger qubit and gate overhead per logical qubit shows that both codes were operated below their respective thresholds. We further demonstrated an advantage of repeated Steane QEC on the seven-qubit color code, where multiple complete rounds of EC including repeated mid-circuit measurements present substantial experimental challenges. Numerical simulations based on a multi-parameter depolarizing error model, informed by experimentally estimated

error rates of basic quantum operations, underpin this finding and capture the features in the experimental data. The improved QEC performance has been achieved without the necessity to make any changes to the hardware, but is rooted in the carefully crafted quantum circuit design underlying the Steane-type QEC approach. The present implementation is currently limited by errors during mid-circuit measurements. Therefore, the benefit of Steane QEC will increase up to the numerically anticipated margin of about a factor of 2, if the error rate of the mid-circuit measurement procedure becomes smaller than the entangling gate errors.

The results presented in this work establish Steane QEC as a new paradigm in experimental QEC by showing reduced error rates of encoded qubits compared to other QEC protocols. The demonstrated Steane-type QEC approach is especially relevant in the context of the emergence of larger qubit registers with efficient implementations of entangling logical gates on various platforms. In architectures that allow for a parallel application of two-qubit gates acting on distinct subsets of qubits, a transversal CNOT gate and, therefore, the extraction of Z-type and X-type error syndromes can each be implemented within one circuit time step. We believe Steane QEC will play a pivotal role towards large-scale FT quantum computation owing to its increased logical fidelities and modularity, allowing to harness the emerging capabilities of efficiently and fault-tolerantly coupled logical qubits as building blocks.

4.5.6 *Acknowledgments*

Please also note the preprint entitled 'Comparing Shor and Steane Error Correction Using the Bacon-Shor Code' by S. Huang, K. R. Brown, and M. Cetina on related work.

4.5.6.1 *Funding:*

We gratefully acknowledge support by the European Union's Horizon Europe research and innovation program under Grant Agreement Number 101114305 ("MILLENION-SGA1" EU Project), the US Army Research Office through Grant Number W911NF-21-1-0007, the European Union's Horizon Europe research and innovation program under Grant Agreement Number 101046968 (BRISQ), the ERC Starting Grant QCosmo under Grant Number 948893, the ERC Starting Grant QNets through Grant Number 804247, the Austrian Science Fund under Project Number F7109 (SFB BeyondC), the Austrian Research Promotion Agency under Contracts Number 896213 (ITAQC) and 897481 (HPQC), the Office of the Director of National Intelligence (ODNI), Intelligence Advanced Research Projects Activity (IARPA), via the U.S. Army Research Office through Grant Number W911NF-16-1-0070 under the LogiQ program, and by IARPA and the Army Research Office, under the Entangled Logical Qubits program through Cooperative Agreement Number W911NF-23-2-0216. This research is also part of the Munich Quantum Valley (K-8), which is supported by the Bavarian state government with funds from the Hightech Agenda Bayern Plus. We further receive support from the IQI GmbH, and by the German ministry of science and education (BMBF) via the VDI within the project IQuAn, and by the Deutsche Forschungsgemeinschaft (DFG, German Research Foundation) under Germany's Excellence Strategy 'Cluster of Excellence Matter and Light for Quantum Computing (ML4Q) EXC 2004/1' 390534769.

The views and conclusions contained in this document are those of the authors and should not be interpreted as representing the official policies, either expressed or implied, of IARPA, the Army Research Office, or the U.S. Government. The U.S. Government is authorized to

4.5.6.2 *Authors contribution:*

L.P. and I.P. carried out the experiments. L.P., I.P., C.D.M., P.S. and T.M. contributed to the experimental setup. L.P., F.B. and M.R. analyzed the data. F.B., S.H. and M.R. performed the numerical simulations. F.B., S.H. and M.R. performed circuit analysis, characterization and theory modeling. L.P., F.B., I.P., C.D.M., S.H., P.S. and M.R. wrote the manuscript, with contributions from all authors. R.B., P.S., M.R., M.M. and T.M. supervised the project.

4.5.6.3 *Competing interests:*

R.B. and T.M. are founders of Alpine Quantum Technologies GmbH, a commercially oriented quantum computing company.

4.5.6.4 *Data and materials availability:*

The data underlying the findings of this work are available at https://doi.org/10.5281/zenodo.10390470. All codes used for data analysis are available from the corresponding author upon reasonable request.

5

FAULT-TOLERANT GATE OPERATIONS

The previous chapter discussed how quantum information can be encoded and protected against undesired interaction with the environment. Respecting FT design principles in the design of QEC circuits ensures that idling errors on logical qubits can be suppressed compared to errors on physical qubits. Let us assume p is the error probability of a single component in a quantum circuit, e.g., a single gate. Then, for a distance-3 QEC code, the logical error probability scales as $\mathcal{O}(p^2)$ compared to $\mathcal{O}(p)$ for a physical qubit. However, a quantum computer only implementing idling operations is obviously of limited use. In order to implement a quantum algorithm, encoded information has to be manipulated by applying gate operations to the qubit register. A naïve approach would be to transfer the stored information from logical qubits to physical qubits, referred to as *decoding* the information, before applying gate operations to the physical qubits. Subsequently, the qubits can be encoded again to protect them from noise. However, this means that error processes during the application of the gate operation can corrupt the physical qubits with a probability scaling as $\mathcal{O}(p)$. This would clearly counteract the efforts of making the encoding and error correction procedures FT. Consequently, gate operations that act directly on encoded, and hence protected, information are necessary to maintain the suppression of errors a QEC code offers. In this chapter, the FT implementation of single-qubit and two-qubit gate operations for logical qubits encoded in the Steane code is discussed.

5.1 Transversal logical gates

As was shown in Section 4.4, a correctable error can potentially become uncorrectable due to error propagation caused by entangling gates. In turn, single-qubit gates acting individually, or *bitwise*, on all physical qubits constituting a logical qubit, cannot increase the weight of an error. Furthermore, one faulty single-qubit gate cannot introduce an uncorrectable error with a weight higher than one*. In other words, any operation being applied bitwise, commonly referred to as *transversal*, intrinsically respects FT design principles. Figure 5.1a shows the transversal application of a Hadamard operation. In Section 4.4.2.1, it was already used that a bitwise Hadamard gate applied to the state $|0\rangle_{\mathrm{L}}$ of the Steane code acts as a Hadamard gate on the encoded logical information. This can be understood by analyzing

* In case an error is already present on the register before the single-qubit gate is applied, a faulty gate can lead to an uncorrectable error. However, such events occur with a probability scaling as $\mathcal{O}(p^2)$ and are therefore tolerable.

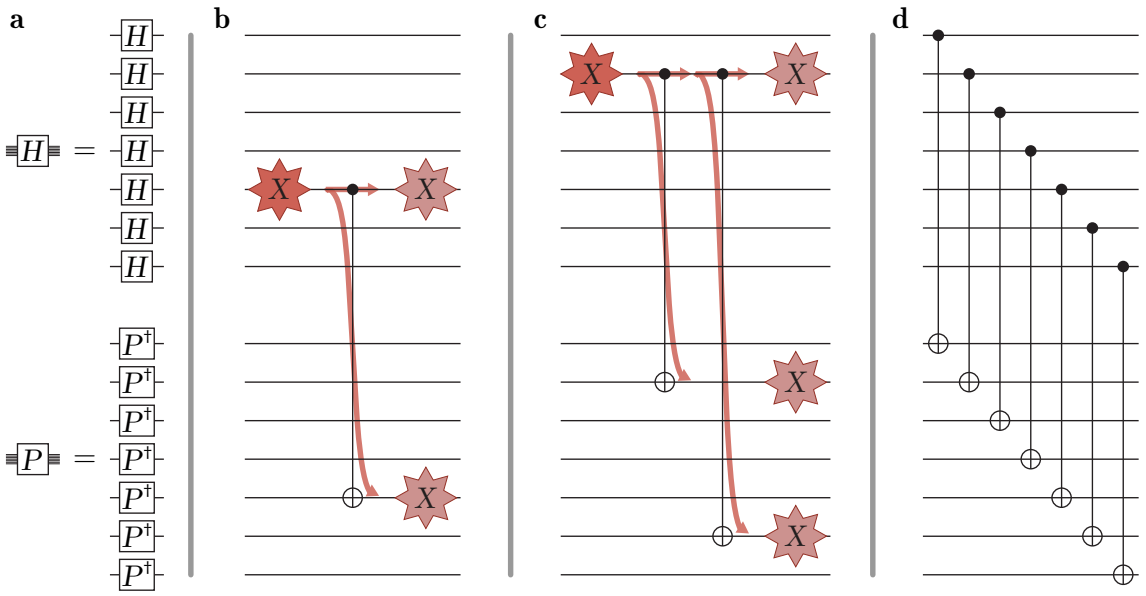

Figure 5.1: Transversal gate operations and error propagation in the Steane code. **a** Transversal Hadamard and phase gate. Note that the logical phase gate P_{L} is implemented by applying bitwise $P^\dagger$ gates. **b** A single physical CNOT gate acting on two logical qubits. A correctable error propagates to two errors that can be corrected individually on the two logical qubits. **c** Two entangling gates acting on a single physical qubit. A weight-1 error on the first logical qubit propagates to a weight-1 error on the first and an uncorrectable weight-2 error on the second logical qubit. **d** The transversal CNOT gate only allows for errors of the type shown in **b** and, therefore, is FT.

the effect of a transversal Hadamard gate on the stabilizer and the logical operators. A single-qubit Hadamard gate transforms single-qubit Pauli matrices X and Z as

$$HXH^\dagger = Z \qquad HZH^\dagger = X. \tag{5.1}$$

Therefore, a transversal Hadamard gate on all seven physical qubits of the Steane code transforms the X-type stabilizer generators to Z-type operators acting on the same qubit support and vice versa. Consequently, the stabilizer generators from Figure 4.4 are just permuted. Therefore, the resulting state is still in the code space and a valid encoded state. Furthermore, the logical operator X_{L} is transformed into Z_{L} and vice versa. This implies that the transversal Hadamard gate acts on a logical qubit as a Hadamard gate acts on a single qubit. Therefore, a Hadamard gate $H_{\mathrm{L}} = H^{\otimes 7}$ on a logical qubit encoded in the Steane code can be implemented by applying Hadamard gates on all seven physical qubits.

As shown in Chapter 2, the Hadamard gate is particularly interesting in conjunction with the phase gate P defined in Eqn. 2.27. Together they generate the single-qubit Clifford group, defined in Eqn. 2.28. The phase gate transforms single-qubit Pauli matrices as

$$PXP^\dagger = iXZ \qquad PZP^\dagger = Z. \tag{5.2}$$

The Z-type stabilizer generators of the Steane code are left unchanged, while the weight-4 X-type generators are transformed to weight-4 XZ-type operators with $\mathrm{i}^4 = 1$. These

operators are stabilizer equivalent to the original X-type generators*, which means that a state remains in the code space under the application of a transversal phase gate. The logical operators are transformed as

$$P^{\otimes 7} X_{\mathrm{L}} P^{\dagger \otimes 7} = -i(XZ)^{\otimes 7} \qquad P^{\otimes 7} Z_{\mathrm{L}} P^{\dagger \otimes 7} = Z_{\mathrm{L}}. \tag{5.3}$$

Comparing Eqns. 5.2 and 5.3, one sees that the gate $P^{\otimes 7}$ acts as $P_{\mathrm{L}}^{\dagger}$ on the logical qubit because $\mathrm{i}^7 = -\mathrm{i}$, and consequently $P_{\mathrm{L}} = P^{\dagger \otimes 7}$, as shown in the lower part of Figure 5.1a. Hence, the effect of transversally applied single-qubit gates on the logical information does not necessarily correspond to the effect the physically applied gate has on a single qubit. Transversal implementations of the Hadamard and phase gate provide means to implement any single-qubit Clifford gate intrinsically FT in the Steane code.

The concept of transversal single-qubit operations being FT relies on the absence of entangling operations that may cause uncorrectable errors from a single error event. This does not leave one very hopeful to find such a straightforward FT implementation when it comes to entangling gates between logical qubits, as they will unavoidably comprise physical entangling gates. However, the situation is different for gates acting on two qubits compared to single-qubit logical gates: A single error event may well cause higher-weight errors as long as the weight of the error *per logical qubit* is low enough to be correctable. In Figure 5.1b, a single physical CNOT gate acting on two logical qubits of the Steane code is shown. Although a single-qubit error propagates to affect two physical qubits, the two errors are correctable independently on the two logical qubits. This is true as long as each physical qubit is acted upon only by one entangling gate. On the contrary, in Figure 5.1c two entangling gates act on a single physical qubit and, therefore, a single error can lead to an uncorrectable error. The most obvious approach to finding a logical entangling gate is to apply entangling gates pairwise between corresponding physical qubits of two logical qubits. This is shown in Figure 5.1d, where CNOT gates are applied in a transversal fashion to encoded qubits. The depicted circuit acts as an entangling gate on logical qubits if two requirements, similar as for the single-qubit case, are fulfilled: First, the stabilizer of the two logical qubits has to be unchanged to ensure that the output quantum state is in the code space for valid input states. And second, the logical operators of the two qubits have to be transformed in a way that the operation acts as an entangling gate on the encoded information.

Let us discuss the aforementioned requirements for the application of a transversal CNOT gate to two logical qubits encoded in the Steane code. For single-qubit Pauli operators X_i and Z_i, where $i \in \{1, 2\}$ denotes the qubit on which the operator acts, the effect of a CNOT gate is given by

$$\begin{aligned} \mathrm{CNOT}\ X_1\ \mathrm{CNOT}^{\dagger} &= X_1 X_2 \qquad & \mathrm{CNOT}\ X_2\ \mathrm{CNOT}^{\dagger} &= X_2 \\ \mathrm{CNOT}\ Z_1\ \mathrm{CNOT}^{\dagger} &= Z_1 \qquad & \mathrm{CNOT}\ Z_2\ \mathrm{CNOT}^{\dagger} &= Z_1 Z_2. \end{aligned} \tag{5.4}$$

* Multiplying an XZ-type stabilizer generator with the Z-type generator acting on the same qubits yields the original X-type stabilizer generators, as $XZ \cdot Z = X \cdot ZZ = X \cdot \mathbb{1} = X$.

The stabilizer generators of the two logical qubits encoded in 14 physical qubits are given by the tensor product of the generators acting on one logical qubit with the identity acting on the other qubit. Therefore, the twelve stabilizer generators are

$$\begin{aligned} S_{X,1}^{(j)} &= S_X^{(j)} \otimes \mathbb{1}^{\otimes 7} & S_{X,2}^{(j)} &= \mathbb{1}^{\otimes 7} \otimes S_X^{(j)} \\ S_{Z,1}^{(j)} &= S_Z^{(j)} \otimes \mathbb{1}^{\otimes 7} & S_{Z,2}^{(j)} &= \mathbb{1}^{\otimes 7} \otimes S_Z^{(j)} \end{aligned} \tag{5.5}$$

for $j \in \{1, 2, 3\}$. Applying a transversal CNOT gate, denoted as $\mathrm{CNOT_L}$, transforms the stabilizer generators listed above into

$$\begin{aligned} \mathrm{CNOT_L}\, S_{X,1}^{(j)}\, \mathrm{CNOT_L^\dagger} &= S_X^{(j)} \otimes S_X^{(j)} & \mathrm{CNOT_L}\, S_{X,2}^{(j)}\, \mathrm{CNOT_L^\dagger} &= S_{X,2}^{(j)} \\ \mathrm{CNOT_L}\, S_{Z,1}^{(j)}\, \mathrm{CNOT_L^\dagger} &= S_{Z,1}^{(j)} & \mathrm{CNOT_L}\, S_{Z,2}^{(j)}\, \mathrm{CNOT_L^\dagger} &= S_Z^{(j)} \otimes S_Z^{(j)}. \end{aligned} \tag{5.6}$$

The six generators, $S_{X,2}^{(j)}$ and $S_{Z,1}^{(j)}$, remain unchanged compared to the stabilizer generators before applying $\mathrm{CNOT_L}$, shown in Eqn. 5.5. The generators $S_{X,1}^{(j)}$ and $S_{Z,2}^{(j)}$ are transformed into operators acting on both logical qubits. However, the stabilizer generators from Eqn. 5.5 can be recovered by multiplying $S_X^{(j)} \otimes S_X^{(j)}$ and $S_Z^{(j)} \otimes S_Z^{(j)}$ with the other two stabilizer generators $S_{X,2}^{(j)}$ and $S_{Z,1}^{(j)}$, respectively*. Therefore, a transversal CNOT gate in the Steane code leaves the stabilizer invariant and is a valid logical operation. According to Eqn. 5.4 the logical operators $X_{\mathrm{L},1} = X_\mathrm{L} \otimes \mathbb{1}^{\otimes 7}$, $X_{\mathrm{L},2} = \mathbb{1}^{\otimes 7} \otimes X_\mathrm{L}$, $Z_{\mathrm{L},1} = Z_\mathrm{L} \otimes \mathbb{1}^{\otimes 7}$ and $Z_{\mathrm{L},2} = \mathbb{1}^{\otimes 7} \otimes Z_\mathrm{L}$ are transformed as

$$\begin{aligned} \mathrm{CNOT_L} X_{\mathrm{L},1} \mathrm{CNOT_L^\dagger} &= X_{\mathrm{L},1} X_{\mathrm{L},2} & \mathrm{CNOT_L} X_{\mathrm{L},2} \mathrm{CNOT_L^\dagger} &= X_{\mathrm{L},2} \\ \mathrm{CNOT_L} Z_{\mathrm{L},1} \mathrm{CNOT_L^\dagger} &= Z_{\mathrm{L},1} & \mathrm{CNOT_L} Z_{\mathrm{L},2} \mathrm{CNOT_L^\dagger} &= Z_{\mathrm{L},1} Z_{\mathrm{L},2}, \end{aligned} \tag{5.7}$$

meaning that a transversal CNOT gate also acts as a CNOT gate on the encoded logical information. Together with the transversal single-qubit gates discussed above, the CNOT gate generates the n-qubit Clifford group [49]. With that, the Steane code has the property that it provides a transversal, and therefore intrinsically FT, implementation of the Clifford group.

5.2 Non-transversal logical gates

In Section 2.3, it was shown that a finite set of quantum gates is sufficient to approximate any unitary operation to arbitrary precision, meaning that any quantum algorithm can be implemented only using gates from this finite set. This is crucial in FT quantum computers: As has been discussed in the previous section, it is neither trivial nor desirable to find a new physical implementation for every unitary operation applied to logical qubits. The requirement on logical gate operations, that any valid code state is transformed into another valid code state, restricts the set of gates that can be implemented transversally.

The set of gates $\{H, P, \mathrm{CNOT}\}$ identified in the previous section to have a transversal implementation in the Steane code only generates the Clifford group. In Section 2.3, this

* The product of elements of the stabilizer is in the stabilizer as well, as the stabilizer is a group.

set of gates was expanded by the non-Clifford T gate to obtain a universal set of gates [54]. However, there is no way of constructing the T gate in a transversal fashion in the Steane code. Hence, the Steane code does not provide means to perform universal FT quantum computation only using transversal gates. But this is by no means just a shortcoming of the Steane code. In fact, Eastin and Knill's no-go theorem [43] shows that a transversal gate set for any QEC code cannot be universal. As sobering as this may sound, this theorem does not forbid universal FT quantum computing: It just states that this is not achievable with a single QEC code using only transversal gate operations. Viable ways to circumvent this hurdle are, e.g., code switching, where the encoded information is transferred between QEC codes having a complementary set of transversal gates [148–150], or magic state injection.

This section discusses how the T gate can be implemented fault-tolerantly for logical qubits encoded in the Steane code employing magic state injection. Utilizing the concept of flag qubits, which has already proven to be helpful in achieving fault tolerance in Section 4.4, along with transversal gates, forms the backbone of the discussed T gate construction. The overall approach is to avoid the application of physical gate operations which allow for the emergence of uncorrectable errors from correctable errors through error propagation. This is achieved by outsourcing most of the complexity of the T gate operation to the preparation of a resource state on a logical auxiliary qubit. Subsequently, only transversal operations are used to apply the T gate to the logical data qubit.

The resource state required in the scheme discussed in this thesis is given by*

$$|H\rangle = \cos\left(\frac{\pi}{8}\right)|0\rangle + \sin\left(\frac{\pi}{8}\right)|1\rangle\,. \tag{5.8}$$

The state $|H\rangle$ is referred to as a *magic state* because, on one hand, it can be used to achieve universality and, on the other hand, a higher fidelity instance of such a state can be produced from multiple lower quality instances via magic state distillation [151]. Furthermore, $|H\rangle$ is the $+1$ eigenstate of the Hadamard operator:

$$\begin{aligned} H|H\rangle &= \frac{1}{\sqrt{2}}\begin{pmatrix}1 & 1\\ 1 & -1\end{pmatrix}\begin{pmatrix}\cos\left(\frac{\pi}{8}\right)\\ \sin\left(\frac{\pi}{8}\right)\end{pmatrix} = \frac{1}{\sqrt{2}}\begin{pmatrix}\cos\left(\frac{\pi}{8}\right)+\sin\left(\frac{\pi}{8}\right)\\ \cos\left(\frac{\pi}{8}\right)-\sin\left(\frac{\pi}{8}\right)\end{pmatrix} \\ &= \begin{pmatrix}\cos\left(-\frac{\pi}{8}\right)\\ -\sin\left(-\frac{\pi}{8}\right)\end{pmatrix} = \begin{pmatrix}\cos\left(\frac{\pi}{8}\right)\\ \sin\left(\frac{\pi}{8}\right)\end{pmatrix} = |H\rangle\,. \end{aligned} \tag{5.9}$$

The T gate

$$T = \mathrm{e}^{-\mathrm{i}\frac{\pi}{8}Y} = \begin{pmatrix}\cos\left(\frac{\pi}{8}\right) & -\sin\left(\frac{\pi}{8}\right)\\ \sin\left(\frac{\pi}{8}\right) & \cos\left(\frac{\pi}{8}\right)\end{pmatrix} \tag{5.10}$$

* For now, physical qubit states and operations acting on physical qubits are considered for simplicity of the notation, but all concepts can be directly applied to logical qubits.

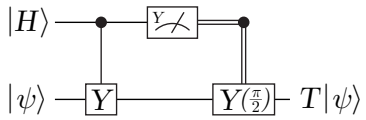

Figure 5.2: Implementation of a T gate using magic state injection [119]. The resource state $|H\rangle$ is prepared on an auxiliary qubit. Subsequently, Clifford operations, a measurement, and a single-qubit operation conditioned on the measurement outcome are applied to implement a T gate on the target qubit in the state $|\psi\rangle$.

can be applied to a data qubit in an arbitrary state $|\psi\rangle = \alpha\,|0\rangle + \beta\,|1\rangle$ by preparing an auxiliary qubit in $|H\rangle$ and employing the circuit shown in Figure 5.2. The application of the controlled-Y gate CY acts on the input state as

$$\begin{aligned}
\mathrm{CY}\ |H\rangle \otimes |\psi\rangle &= \mathrm{CY}\ \left(\cos\left(\frac{\pi}{8}\right)|0\rangle + \sin\left(\frac{\pi}{8}\right)|1\rangle\right) \otimes |\psi\rangle \\
&= \cos\left(\frac{\pi}{8}\right)|0\rangle \otimes |\psi\rangle + \sin\left(\frac{\pi}{8}\right)|1\rangle \otimes Y\,|\psi\rangle \\
&= \frac{1}{\sqrt{2}}\Big[\,|+i\rangle \otimes \left(\cos\left(\frac{\pi}{8}\right)|\psi\rangle - \mathrm{i}\sin\left(\frac{\pi}{8}\right) Y\,|\psi\rangle\right) \\
&\qquad + |-i\rangle \otimes \left(\cos\left(\frac{\pi}{8}\right)|\psi\rangle + \mathrm{i}\sin\left(\frac{\pi}{8}\right) Y\,|\psi\rangle\right)\Big].
\end{aligned} \tag{5.11}$$

The subsequent measurement of the auxiliary qubit in the Y basis projects the auxiliary qubit to either $|+i\rangle$ or $|-i\rangle$ and affects the state of the data qubit accordingly. In case the measurement outcome is $+1$, the state of the data qubit is

$$\begin{aligned}
|\psi'\rangle &= \cos\left(\frac{\pi}{8}\right)|\psi\rangle - \mathrm{i}\sin\left(\frac{\pi}{8}\right) Y\,|\psi\rangle \\
&= \left(\alpha\cos\left(\frac{\pi}{8}\right) - \beta\sin\left(\frac{\pi}{8}\right)\right)|0\rangle + \left(\alpha\sin\left(\frac{\pi}{8}\right) + \beta\cos\left(\frac{\pi}{8}\right)\right)|1\rangle = T\,|\psi\rangle\,,
\end{aligned} \tag{5.12}$$

In this case, the output state $|\psi'\rangle$ is rotated around the Y axis by $\frac{\pi}{4}$ compared to the input state $|\psi\rangle$. Therefore, a T gate is applied to the data qubit and the final state is $T\,|\psi\rangle$.

In case the measurement outcome is -1, the conditional Y rotation with a rotation angle of $\frac{\pi}{2}$ is applied, leading to the final state

$$\begin{aligned}
Y\left(\frac{\pi}{2}\right)|\psi'\rangle &= Y\left(\frac{\pi}{2}\right)\Big[\left(\alpha\cos\left(\frac{\pi}{8}\right) + \beta\sin\left(\frac{\pi}{8}\right)\right)|0\rangle \\
&\qquad + \left(-\alpha\sin\left(\frac{\pi}{8}\right) + \beta\cos\left(\frac{\pi}{8}\right)\right)|1\rangle\Big] \\
&= \left(\alpha\cos\left(\frac{\pi}{8}\right) - \beta\sin\left(\frac{\pi}{8}\right)\right)|0\rangle \\
&\quad + \left(\alpha\sin\left(\frac{\pi}{8}\right) + \beta\cos\left(\frac{\pi}{8}\right)\right)|1\rangle = T\,|\psi\rangle\,.
\end{aligned} \tag{5.13}$$

Also in this case, the T gate is applied to the data qubit.

In order to transfer this concept, referred to as *magic state injection*, to fault-tolerantly operated logical qubits, all building blocks of the scheme have to be FT. In the Steane code,

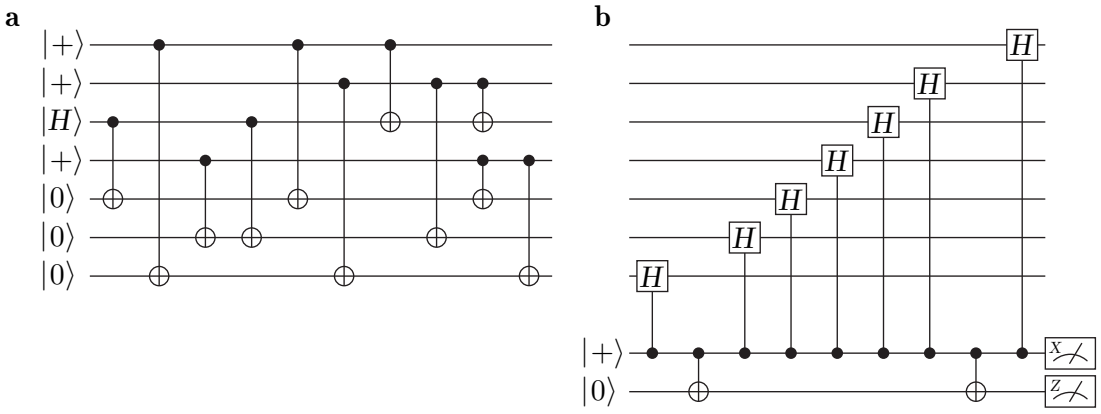

Figure 5.3: **a** Non-FT circuit preparing the magic state $|H\rangle_{\mathrm{L,nf}}$ [110, 119] and **b** FT measurement of the Hadamard operator H_{L} using a single flag qubit [119].

Figure 5.4: High-level description of the circuit for the FT preparation of the magic state $|H\rangle_{\mathrm{L}}$ [110, 119]. In a first step, the magic state is prepared non-fault-tolerantly, followed by an FT Hadamard measurement and an error detection block. The low-level circuits corresponding to the three blocks can be found in Figures 5.3a, 5.3b, and 4.14.

the controlled-Y gate and the conditional single-qubit Y rotation are intrinsically FT as they are Clifford gates. Furthermore, the measurement of the logical auxiliary qubit in the Y basis is FT. It consists of a Clifford gate and a transversal measurement of the physical qubits constituting the logical auxiliary qubit in the computational basis. The only missing building block of the injection procedure is thus the preparation of $|H\rangle_{\mathrm{L}}$ in an FT fashion.

The state preparation procedure discussed in this thesis prepares $|H\rangle_{\mathrm{L}}$ utilizing flag qubits [110, 119]. In a first step, the magic state $|H\rangle_{\mathrm{L,nf}}$ is prepared in the Steane code using the circuit in Figure 5.3a. This state preparation is not FT, as there are two-qubit gates acting within a logical qubit enabling the propagation of a single error to a logical error.

In the spirit of flag fault tolerance, two circuit blocks are appended to allow for the detection of dangerously propagating errors. A high-level schematic of the overall procedure is shown in Figure 5.4. The first block labeled $|\boldsymbol{H}\rangle_{\mathbf{L,nf}}$ is the non-FT magic state preparation, the block labeled $\mathbf{M}_{\boldsymbol{H}}$ is an FT measurement of the logical Hadamard operator shown in Figure 5.3b, and the block labeled **ED** is the flag-based FT circuit to measure all six stabilizer generators of the Steane code presented in Figure 4.14. In order to render the circuit FT, all eight* physical auxiliary qubits act as flag qubits. The state preparation is discarded if any of the auxiliary qubit measurements yields the outcome -1.

In the following the fault-tolerance proof of the magic state preparation circuit from Ref. [119] is sketched. For this, single errors occurring during the three circuit blocks shown in Figure 5.4 are considered.

A single error in the non-FT preparation block can propagate to become a higher-weight error. Any resulting weight-2 error of either X- or Z-type is stabilizer equivalent to a single-

* Two auxiliary qubits are used for the logical Hadamard measurement, and six auxiliary qubits are used for the stabilizer generator measurement.

qubit error in conjunction with a logical error, e.g., $X_3X_6 = S_X^{(1)}S_X^{(2)}S_X^{(3)}X_{\mathrm{L}}X_5$. A weight-3 error after the non-FT magic state preparation is equivalent to either a single-qubit error or a logical operator, e.g., $X_4X_5X_7 = S_X^{(2)}X_6$ or $X_3X_5X_6 = S_X^{(1)}S_X^{(2)}S_X^{(3)}X_{\mathrm{L}}$. Any single-qubit error, also in conjunction with a logical operator, is detected in the error detection block labeled **ED**. This leads to a measurement outcome of -1 for at least one of the six flag qubits of the error detection block and the preparation is discarded. States affected by a logical operator are either projected to the $+1$ eigenstate of the logical Hadamard operator or lead to measurement outcome of -1 of the first auxiliary qubit in the block $\mathbf{M}_{\boldsymbol{H}}$. Therefore, all accepted states affected by a single-error in the non-FT magic state preparation result in a error-free preparation of $|H\rangle_{\mathrm{L}}$.

Let us now consider an error in the logical Hadamard measurement $\mathbf{M}_{\boldsymbol{H}}$. A single error causing an error on the data qubits of weight larger than 1 also propagates to the second auxiliary qubit of the Hadamard measurement block. All weight-1 errors are discarded in the following error-detection block. With this, all accepted final states are $|H\rangle_{\mathrm{L}}$.

Finally, single errors during the error-detection block are considered. Errors propagating to errors of weight larger than 1 are captured by the six auxiliary qubits acting as flag qubits for each other. Errors that are not detected by the auxiliary qubits are of weight-1. Therefore, they are correctable and do not lead to a logical error. Consequently, a single-error during any of the three circuit blocks $|\boldsymbol{H}\rangle_{\mathbf{L,nf}}$, $\mathbf{M}_{\boldsymbol{H}}$ and **ED** does not lead to a logical error and the preparation procedure is FT.

The FT magic state preparation scheme, in conjunction with the transversal implementation of the Clifford group, allows for universal FT quantum computation using logical qubits encoded in the Steane code. Although the complexity of this T gate construction might seem high compared to transversal gate operations, the overhead required for this preparation of magic states can be orders of magnitude lower compared to competing, state-of-the-art protocols [119].

5.3 Publication: Demonstration of fault-tolerant universal quantum gate operations

Demonstration of fault-tolerant universal quantum gate operations*

Nature **605**, 675-680 (2022)

Lukas Postler[1], Sascha Heußen[2,3], Ivan Pogorelov[1], Manuel Rispler[2,3], Thomas Feldker[1,4], Michael Meth[1], Christian D. Marciniak[1], Roman Stricker[1], Martin Ringbauer[1], Rainer Blatt[1,5], Philipp Schindler[1], Markus Müller[2,3], Thomas Monz[1,4]

[1]Institute for Experimental Physics, University of Innsbruck, Innsbruck, Austria
[2]Institute for Quantum Information, RWTH Aachen University, Aachen, Germany
[3]Institute for Theoretical Nanoelectronics (PGI-2), Forschungszentrum Jülich, Jülich, Germany
[4]Alpine Quantum Technologies GmbH, Innsbruck, Austria
[5]Institute for Quantum Optics and Quantum Information, Austrian Academy of Sciences, Innsbruck, Austria

Quantum computers can be protected from noise by encoding the logical quantum information redundantly into multiple qubits using error correcting codes [45, 152]. When manipulating the logical quantum states, it is imperative that errors caused by imperfect operations do not spread uncontrollably through the quantum register. This requires that all operations on the quantum register obey an FT circuit design [31, 35, 116] which, in general, increases the complexity of the implementation. Here, we demonstrate an FT universal set of gates on two logical qubits in a trapped-ion quantum computer. In particular, we make use of the recently introduced paradigm of flag fault tolerance, where the absence or presence of dangerous errors is heralded by usage of few auxiliary 'flag' qubits [111, 112, 119, 120, 153]. We perform a logical two-qubit CNOT gate between two instances of the seven qubit color code [36, 142], and we also fault-tolerantly prepare a logical magic state [110, 119]. We then realize an FT logical T-gate by injecting the magic state via teleportation from one logical qubit onto the other [151]. We observe the hallmark feature of fault tolerance, a superior performance compared to a non-FT implementation. In combination with recently demonstrated repeated QEC cycles [38, 154] these results open the door to error-corrected universal quantum computation.

5.3.1 *Introduction*

Quantum computers promise to efficiently solve important computational tasks that are beyond the capabilities of classical computers, such as prime factorization or the simulation

* The author of the present thesis carried out the experiments, analyzed the data, and wrote the manuscript. Here, the accepted version of the manuscript is printed in a slightly amended form for consistency throughout the thesis. Changes include adapting hyphenation and abbreviations and updating references that were only available as preprints at the time of publication.

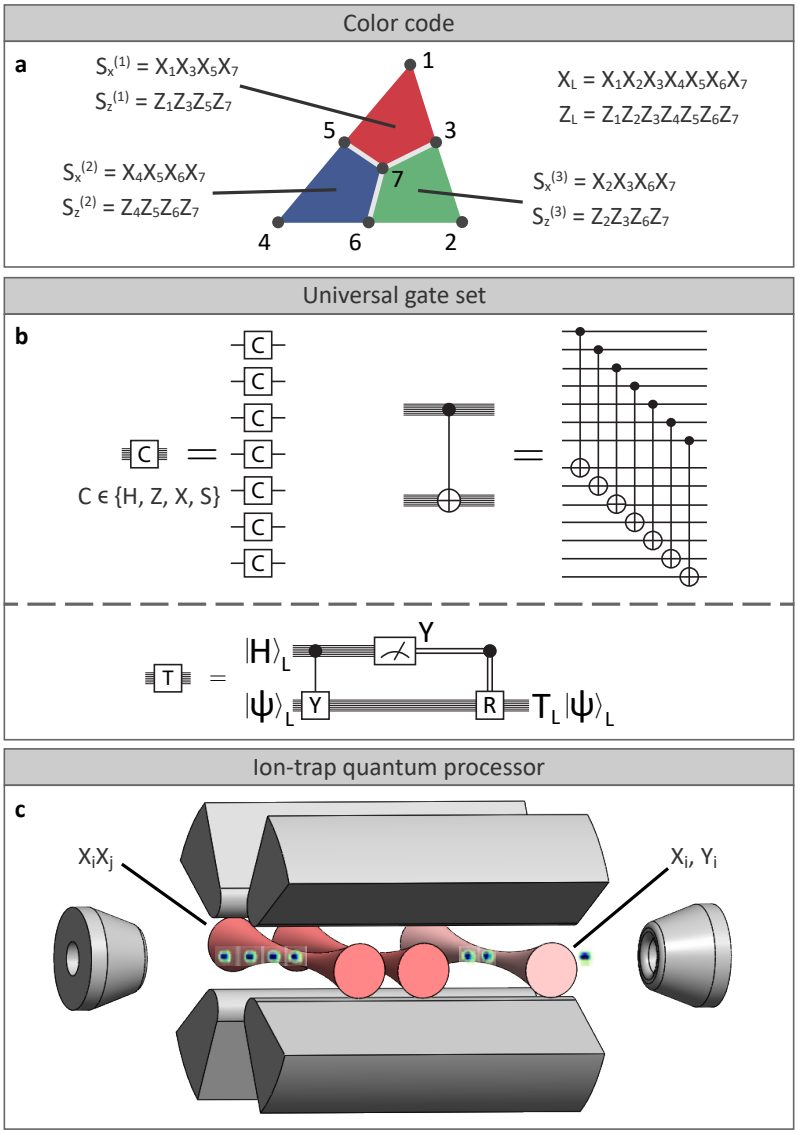

Figure 5.5: Quantum error correction code, logical gates and experimental system. (a) Seven-qubit color code encoding one logical qubit in seven physical qubits. The six weight-4 operators $\{S_x^{(i)}, S_z^{(i)}\}$, $i = 1, 2, 3$, are the stabilizer generators and the weight-7 operators are logical operators Z_L and X_L. (b) Universal gate set consisting of Clifford gates (above dashed line) and the T-gate. Whereas the Clifford group is transversal in the color code, magic state injection can be used to realize the FT T-gate. The magic state $|H\rangle_L$ is prepared fault-tolerantly and subsequently teleported onto the target qubit in an arbitrary state $|\Psi\rangle_L$, effectively implementing a T-gate on the target qubit. (c) Schematic 3D model of the ion-trap quantum processor. Single and any pair i, j of ions can be addressed simultaneously by steerable tightly focused laser beams. This enables entangling (darker shaded beams) but also single-qubit (lighter) gates.

of complex quantum systems [5, 155]. A digital quantum computer will offer a native gate set, which is comprised of the operations that can be physically executed in hardware. Remarkably, finite sets of native gates are sufficient to compose *any* operation to an arbitrary desired precision, rendering such gate sets *universal* [45]. A fundamental challenge is to keep the quantum computation coherent, while all components of the quantum computer such as physical qubits, gate operations and measurements are inherently prone to errors. This roadblock towards large-scale quantum computation can be lifted with the circuit design principle of *quantum fault tolerance* [31, 35, 116, 152]. The central idea is to use QEC codes, where many physical qubits together comprise so-called logical qubits such that the logical information is distributed non-locally and thereby protected from decoherence and errors due to finite control accuracy. By ingenuity of code design, it thus becomes possible to suppress logical decoherence arbitrarily by adding redundancy, once the physical noise level falls below some threshold [156]. Arbitrary logical quantum computation demands that a universal logical gate set has to be synthesized from physical gates, which presents new challenges. To prevent previously localized errors from spreading over the entire qubit register and destroying the computation, logical gates have to be designed with fault tolerance guarantees: For QEC codes with the potential to correct at least one arbitrary single error, this means that a single error occurring at any location (initialization, gate or measurement) in a particular circuit may under no circumstances turn into a non-correctable error on two or more qubits. When assuming for simplicity that every location has some error probability p, the logical failure rate without fault tolerance will scale as $p_L \propto Np$ with N the number of error locations in the circuit that lead to a logical error. While adding further gates and qubits for fault tolerance increases the number of circuit locations, the logical failure rate will now scale with $p_L \propto N'p^2$, i.e. it is quadratically suppressed in p, where N' now denotes the number of pairs of locations where two errors lead to a logical error. This entails one of the hallmark features of FT implementations: despite adding more (noisy) qubits and gates, the quality of the encoded information can be improved, if the physical noise level is sufficiently low. Certain QEC codes facilitate an FT implementation of some gates by acting on all physical qubits individually – called a transversal logical gate. However, a universal gate set with all gates having a transversal unitary implementation is forbidden by a no-go theorem [43]. This leads to the difficulty that to reach universal FT computation at least one logical gate must be implemented by other means, such as magic state injection [151] or code switching [157]. Fulfilling fault tolerance requirements for these approaches typically implies a substantial resource overhead [158].

The growing experimental effort towards FT quantum computation has seen tremendous advances: Non-FT logical state preparation and transversal single-qubit logical gate operations were shown in a seven qubit experiment with trapped ions [37], whereas non-FT two-qubit gates have been demonstrated in error detection codes [159, 160]. State preparation of a topological surface code state [161], repetitive stabilizer measurements in an error-detecting surface code [162, 163] and exponential error suppression in a repetition code [121] have been demonstrated in superconducting architectures. Shortly following a theory proposal towards demonstrations of fault tolerance in small systems [164], experiments showed state preparation using error detection codes and post-selection [165–167], and recently EC for FT state preparation and an FT logical single-qubit Clifford gate [127]. Theory works have substantially reduced the resource requirements for fault tolerance by the concept of flag fault tolerance [111, 112, 119, 120, 153]. Here, dedicated auxiliary qubits are introduced, which signal the presence of dangerous errors. This concept was used to demonstrate FT

operation of the five-qubit code in an NV center-based quantum processor [154], and FT parity check measurements [126] and repetitive rounds of FT QEC cycles [38] with trapped ions. In the present work, alongside the operation of single-qubit logical Clifford gates, we demonstrate the FT implementation of a logical CNOT gate between two logical color code qubits, thereby realizing the entire Clifford group fault-tolerantly. Since this is all one can hope for regarding transversal implementations, to obtain the non-Clifford gate required for universality, we amend the gate set by a T-gate. For this, in a first step we prepare a magic state fault-tolerantly by the use of flag qubits, as proposed in [119]. Finally, using this fault-tolerantly prepared magic state and the transversal logical CNOT gate, we perform FT magic state injection, thus demonstrating a universal FT gate set.

We work with the seven-qubit color code, illustrated in Figure 5.5a, which is the smallest member of the code family of topological 2D color codes [142] and is also known as the Steane code [36]. It hosts one logical qubit and can be formulated as a stabilizer code on seven physical qubits, with logical states encoded in the joint $+1$ eigenspace of six weight-4 Pauli operators. The logical operators are $X_L = X^{\otimes 7}$ and $Z_L = Z^{\otimes 7}$, which are stabilizer-equivalent to weight three operators, e.g. $Z_L \simeq Z_1 Z_2 Z_3$, rendering it a distance 3 code. This entails that all single-qubit errors can be corrected, but weight-2 errors on the code will lead to logical failures. Besides a transversal CNOT gate, remarkably it also admits the transversal implementation of the Hadamard gate H and the phase gate S. Consequently the entire Clifford group can be implemented transversally (see Figure 5.5b) [45]. The required magic resource state to enable T-gate injection can be prepared fault-tolerantly thanks to a recently proposed protocol [119].

The experiments presented in this work have been performed in a 16-qubit ion-trap quantum information processor [84] shown schematically in Figure 5.5c. The native gate set is composed of entangling MS operations [168] and single-qubit rotations around an arbitrary axis in the equatorial plane of the Bloch sphere with error rates of $p_2 = 2.5 \times 10^{-2}$ and $p_1 = 5 \times 10^{-3}$, respectively. Error rates for state initialization and measurement are estimated at $p_i, p_m = 3 \times 10^{-3}$. A more detailed discussion on the experimental setup can be found in Appendix B. For better readability, all circuits shown in this work are provided in standard CNOT gates, as these are equivalent to MS gates up to local Clifford operations [169]. All experimental results are accompanied by MC simulations, for which we model imperfections as uniform depolarizing noise on single-qubit gates, initialization and measurement as well as two-qubit gates with independent physical error rates p_1, p_i, p_m, p_2, respectively, as described in Appendix B.

5.3.2 *Initializing and characterizing the logical qubit*

We start by experimentally preparing the logical state $|0\rangle_L$ as the $+1$ eigenstate of the logical Z operator Z_L by implementing the circuit shown in Figure 5.6a. The first part of the circuit encodes a logical qubit in a non-FT fashion. To render this encoding circuit FT, a verification step is added (see Figure 5.6a) [110, 170]. An additional auxiliary qubit is used to herald a successful logical qubit initialization, meaning that for a measurement outcome of $+1$ no single error anywhere in the encoding circuit can have led to uncorrectable errors on the data qubit register. For a measurement outcome of -1 of the flag qubit the initialization is aborted and repeated.

We analyze the quality of the information encoded in a logical qubit in terms of logical operator expectation values. After a projective measurement, the outcome of the logical

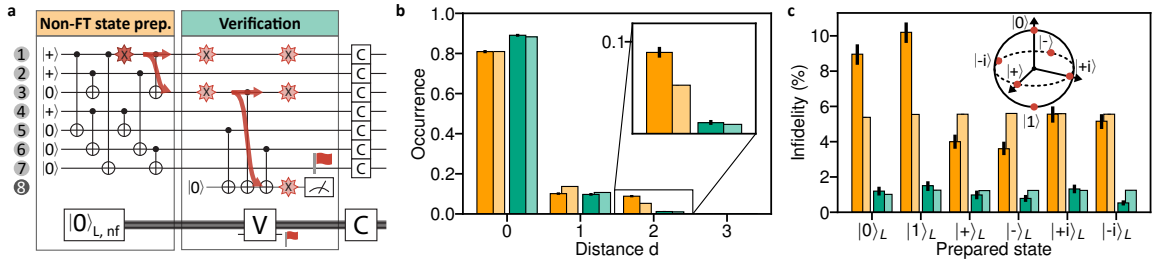

Figure 5.6: Fault-tolerant preparation of a logical basis state $|0\rangle_L$ and logical Clifford operations. (a) Logical Pauli states are prepared fault-tolerantly in three steps: First $|0\rangle_L$ is prepared by a non-FT circuit. A single error, e.g. a bit flip on qubit 1, can propagate to other qubits, here qubit 3, resulting in an uncorrectable weight-2 error and therefore causing a logical error. Fault tolerance is ensured through verification (V) of the state by coupling to an additional flag auxiliary qubit. This qubit, when measured as $|0\rangle$, signals that the correct state has been prepared fault-tolerantly, i.e. up to single-qubit errors. To prepare a logical Pauli eigenstate other than $|0\rangle_L$ an additional transversal Clifford gate needs to be applied. (b) Relative occurrence rates of logical output states of distance d to the target state $|0\rangle_L$ for non-FT (orange) and FT (turquoise) initialization. Example states of $d = 1, 2, 3$ are $X_0 |0\rangle_L$, $X_0X_1 |0\rangle_L$, $X_0X_1X_2 |0\rangle_L$. Simulation results are depicted by lighter colored bars. As described in the main text, all circuit elements are subject to depolarizing noise in numerical simulations. (c) Logical infidelities of all six logical Pauli eigenstates (red markers on Bloch sphere) including an ideal round of EC performed in post-processing (experimental/simulation results depicted darker/lighter).

operators is corrected according to the measured error syndrome, effectively performing a Pauli frame update [141, 171] described in Appendix B. The updated measurement outcomes are categorized by their minimum Hamming distance d to any constituent state of the logical zero state (see Appendix B) of 0, 1, 2 and 3. For outcomes with a minimum Hamming distance of 0 or 1 the logical state is recoverable, whereas for distances 2 and 3 an uncorrectable logical error is induced. The relative occurrence of outcomes associated to those four categories for the initialization of $|0\rangle_L$ is shown in Figure 5.6b. The verification circuit significantly suppresses the occurrence of errors leading to logical errors, resulting in decreased relative occurrences for outcomes with distance 2 and 3 by a factor of more than 7. A figure of merit describing the quality of the encoded state is the logical state fidelity, i.e. the overlap of the measured with the target logical Bloch vector (see Appendix B). The logical infidelity is decreased from 0.090(6) to 0.012(2) by introducing the verification of the initialization, showing a clear signature that an FT implementation outperforms its non-FT counterpart. The acceptance rate heralded by a $+1$ outcome of the flag measurement is 78.9(5)%. This behavior is in good qualitative agreement with numerical simulations which yield infidelities of 0.0538(2) and 0.0101(1) for the non-FT and FT circuits respectively, and an acceptance rate of 84.42(4)%.

5.3.3 *Transversal fault-tolerant operations*

The transversality of the Clifford group as a property of the color code allows for the preparation of the six cardinal states on the Bloch sphere, referred to as Pauli eigenstates herein, by applying single-qubit rotations corresponding to the respective logical gate to all qubits in the data register (see Figure 5.5b). For both experimental data but also results of

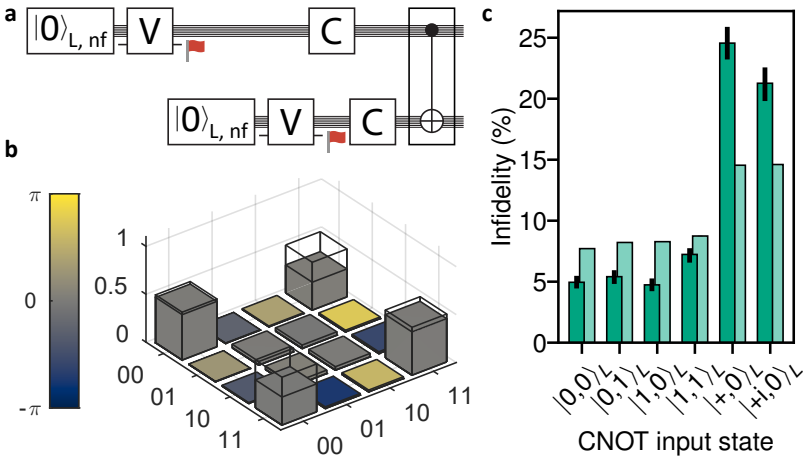

Figure 5.7: Fault-tolerant implementation of a logical entangling gate. (a) To estimate the performance of the logical CNOT gate we fault-tolerantly prepare six different logical two-qubit input states and apply the transversal CNOT gate (framed gate at the end of the circuit). (b) Logical state tomography after applying the CNOT gate to the $|+,0\rangle$ state. The phase of the complex amplitudes is encoded in the color of the 3D bar plot and the wireframes depict ideal results. (c) Logical infidelities for six different input states of the CNOT gate (experimental/simulation results depicted darker/lighter).

numerical simulations, the verification of the initialization reduces the logical infidelity of all six Pauli eigenstates, as can be seen in Figure 5.6c. The definition of the logical fidelity and a discussion on the variation of the logical infidelity for different Pauli eigenstates can be found in Appendix B. The average logical infidelity for the FT circuit is 0.011(1) with an acceptance rate of 80.6(2)%, while simulations suggest an average infidelity of 0.01203(4). The six stabilizer generators were measured projectively to verify the preparation of the correct encoded states for the Pauli states. The averaged expectation value of the X-(Z-)type stabilizers is 0.826(3) (0.760(3)) for the FT and 0.842(3) (0.790(3)) for the non-FT preparation scheme. Further details on the measured stabilizer generators can be found in Appendix B.7.

In Figure 5.7 the implementation of a two-qubit gate acting on two logical qubits prepared as described above, requiring 29 entangling gates on 16 qubits, is illustrated. The transversal logical CNOT gate is implemented by sequentially applying CNOT gates to corresponding pairs of physical qubits of the two logical qubits (see also Figure 5.5b). A single error on any of the physical qubits propagates to at most one error on each of the logical qubits and therefore remains correctable, thereby ensuring fault tolerance of the gate realization. Applying the logical CNOT gate to the input state $|+,0\rangle_L$ yields the logical Bell state $\frac{1}{\sqrt{2}}(|0,0\rangle_L + |1,1\rangle_L)$ depicted in Figure 5.7b, showing a logical fidelity of 0.754(13) (see Appendix B). Figure 5.7c shows the logical infidelity for six different input states. It reveals that the infidelity of output states is higher if the control qubit is in a superposition state, thus leading to an entangled outcome, compared to cases in which the outcome is a basis state of the logical two-qubit computational basis. This increased error rate is well-described by numerical simulations based on the circuit noise model: The average logical infidelity is 0.110^{+3}_{-4} and $0.1035(1)$ for the experimental implementation and the numerical simulation, respectively.

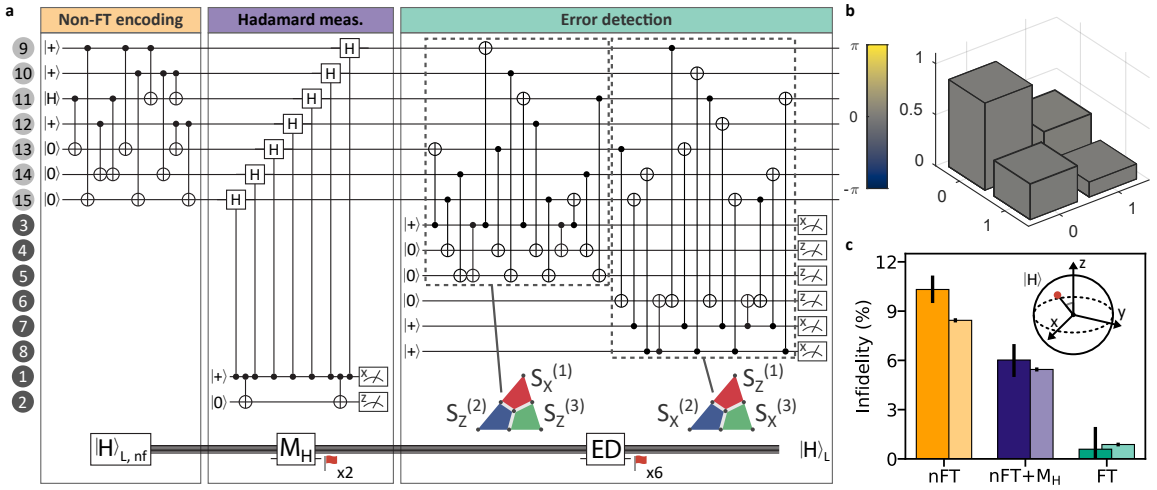

Figure 5.8: Fault-tolerant generation of a logical magic state $|H\rangle_L$ (see Eqn. 5.15). (a) The magic state is prepared non-fault-tolerantly in a first step, where a physical magic state $|H\rangle$ is mapped to the logical state $|H\rangle_{L,\mathrm{nf}}$ encoded in the data qubits at positions 9 to 15 in the ion string (see labels at left of circuit). Thereafter, an FT measurement of the Hadamard operator (M_H) is carried out. Two auxiliary qubits herald that the prepared state is a $+1$ eigenstate of the Hadamard operator but also that no dangerous error occurred during the measurement. The magic state preparation is concluded with an error detection block that measures the three X- and Z-type stabilizers each in an FT fashion. The first part of the error detection circuit (first dashed box), measures $S_X^{(1)}$, $S_Z^{(2)}$ and $S_Z^{(3)}$, whereas the second part measures $S_Z^{(1}$, $S_X^{(2)}$ and $S_X^{(2)}$. The magic state preparation is discarded and repeated in case of a non-trivial syndrome of the eight auxiliary qubits 1 to 8. (b) Logical state tomography (see Section 5.3.3) after FT magic state preparation. The phase of the complex amplitudes is encoded in the color of the 3D bar plot and the wireframes depict ideal results. Phase deviations from the ideal density matrix are smaller than $50\,\mathrm{mrad}$ while amplitude deviations are smaller than 0.007. (c) The decrease in infidelity of the logical magic state (red marker on Bloch sphere) after each step of the FT preparation procedure is observed experimentally and captured by depolarizing noise simulations (experimental/simulation results depicted darker/lighter).

5.3.4 *Universal fault-tolerant operations*

The ability to perform a $\pi/4$-rotation about any axis is known to be sufficient to augment the set of Clifford gates, which are transversal in the color code, to a universal gate set. The logical T-gate

$$T_L = e^{-i\frac{\pi}{8}Y_L} \tag{5.14}$$

performs a $\pi/4$-rotation about the Y axis* and can be implemented by magic state injection as shown in Figure 5.5b. It consists of the logical CNOT operation we have demonstrated in the

* Note that choosing this rotation axis is Clifford-equivalent to the more conventional T-gate where the $\pi/4$-rotation is performed about the Z axis.

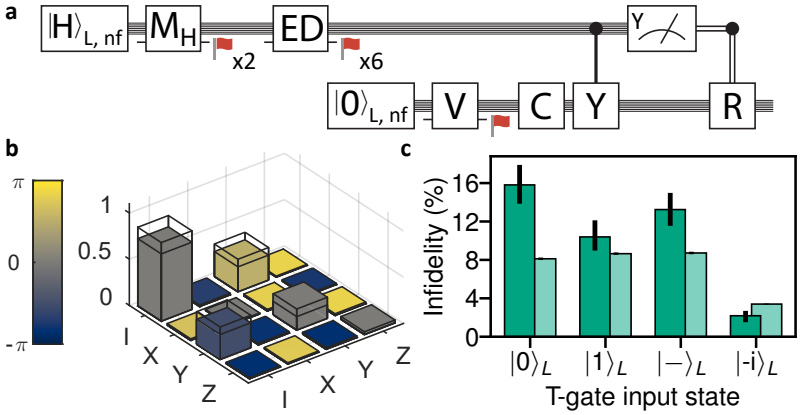

Figure 5.9: Fault-tolerant T-gate injection. (a) After preparing the logical magic state fault-tolerantly the logical T-gate is applied via logical gate teleportation onto a second register that has a logical Pauli state prepared. Conditional application of $R \equiv R_Y(\pi/2)$ is done in post-processing. (b) Logical process matrix of the experimental logical T-gate. The phase of the complex amplitudes is encoded in the color of the 3D bar plot and the wireframes depict ideal results. (c) Infidelities of the data qubit state when applying the logical T-gate to several logical Pauli input states (experimental/simulation results depicted darker/lighter). Infidelity is the lowest for the $|-i\rangle_L$ state since it is an eigenstate of the T-gate.

preceding section, a logical measurement and single-qubit Clifford operation conditioned on the logical measurement outcome. First preparing and then injecting the logical magic state

$$|H\rangle_L = \cos(\pi/8)\,|0\rangle_L + \sin(\pi/8)\,|1\rangle_L \tag{5.15}$$

enables gate teleportation of the logical non-Clifford T-gate. The logical magic state in Eqn. 5.15 is the $+1$ eigenstate of the logical Hadamard operator.

Recently, a resource-efficient procedure to prepare a magic state using FT circuits following the flag fault tolerance paradigm has been proposed [110, 119]. The procedure consists of the following steps, depicted in Figure 5.8a: we begin with a non-FT preparation of the magic state $|H\rangle_{L,\mathrm{nf}}$, as recently demonstrated also in [38] (shown in subbox "Non-FT encoding"). Next, a measurement of the logical Hadamard operator is performed, which projects input states onto the $+1$ eigenspace and discards states that are eigenstates with eigenvalue -1 (subbox "Hadamard meas."). The latter may be caused by single faults in the circuit (e.g. faults in the initial state preparation of $|H\rangle$ for physical qubit 11), thus rendering the circuit non-FT if -1 eigenstates are not discarded in this step. Here both auxiliary qubits (qubits 1 and 2) are utilized as flag qubits. The syndrome measurement auxiliary qubit flags when the -1 eigenstate has erroneously been prepared, the second auxiliary qubit flags when a dangerous fault has occurred that may corrupt the state. The last step is a complete EC cycle, consisting of fault-tolerantly measuring all six stabilizers of the color code using one flag qubit per stabilizer as suggested in [112]. The EC block is used to sort out faulty states whenever any flag qubit is measured as -1 and thus enables error detection (ED) (subbox "Error detection"). The resulting states after performing all three steps are guaranteed to be the correct logical magic state $|H\rangle_L$ up to correctable single-qubit errors

provided at most one fault has occurred anywhere in the circuit. The generated state is accepted as valid if all eight flag qubits indicate that no harmful error has happened.

In Figure 5.8b the reconstructed density matrix of the fault-tolerantly prepared magic state is shown and its ideal numerical values can be found in Appendix B, whereat we prepared the magic state up to local operations, which we account for in post-processing. Figure 5.8c shows the logical infidelity of the magic state, which clearly decreases after each preparation step in both experiment and simulation. Each step of the magic state initialization process improves the quality of the generated logical state. After the full FT initialization procedure, a logical infidelity of 0.006^{+14}_{-5} for the magic state $|H\rangle_L$ with an acceptance rate of 13.7(3)% is found in the experimental realization, whereas numerical simulations predict approximately 27%, see Appendix B for discussion.

Next, the FT magic state initialization is followed by transversal Clifford operations to fault-tolerantly teleport the logical magic state, thereby resulting in a realization of an FT logical T-gate. For this, we perform an in-sequence measurement of the flag qubits for the magic state generation as sketched in Figure 5.9a. In the case of heralded successful magic state generation, the auxiliary qubits are in a well-defined state after the measurement and can directly be re-used to encode a second logical qubit in $|0\rangle_L$ using the FT protocol from Figure 5.6a. We then apply a transversal Clifford operation on this second logical qubit to prepare one of the logical initial states $|0\rangle_L$, $|1\rangle_L$, $|-\rangle_L$, $|-i\rangle_L$. Finally, the transversal controlled-Y operation is applied on the second register and all physical qubits are measured. The measurement outcome for the logical Y operator of the control qubit in the first register is then extracted and the conditional Y$(\pi/2)$-rotation R to the target qubit in the second register is applied in post-processing, see Appendix B for details. By measuring the logical state of the target register for the four different initial states, it is possible to reconstruct the logical process matrix, shown in Figure 5.9b with the ideal values explained in Appendix B. Figure 5.9c shows the logical infidelities for the different input states, yielding a mean infidelity of 0.10(1). It is expected and indeed observed experimentally that the best fidelity is achieved for the logical Y eigenstate $|-i\rangle_L$ as it is an eigenstate of the T-gate. Infidelities for the three other logical input states are slightly higher, which qualitatively agrees with the numerical simulations.

5.3.5 *Discussion and Outlook*

In this work we have demonstrated the first FT implementation of a universal set of single- and two-qubit logical gates. We were able to witness a hallmark feature of FT circuit design, namely an improvement of the performance of encoded qubits, despite the FT implementations of encoding and manipulation requiring an increased gate count and complexity of the underlying circuits. The resource-efficient implementation of these FT operations is enabled by the all-to-all qubit connectivity in the present trapped ion architecture, allowing for entangling operations between arbitrary pairs of qubits. Predictions from numerical simulations based on a relatively simple, generic and architecture-agnostic depolarizing circuit noise model, only informed by estimated experimental error rates, approximate the experimental findings well. The largest deviations between experimental behavior and and numerical predictions were observed for the logical CNOT gate. A more extensive characterization of this logical entangling gate and the other FT gadgets, together with more sophisticated and validated theoretical noise models will be subject to future investigations, and is imperative for designing future QEC architectures and procedures.

On the way towards error-protected universal quantum computation on even more robust logical qubits, further milestones ahead are the incorporation of repetitive QEC cycles [38, 172] into the FT logical gate operations demonstrated in our work. Another hurdle to be taken is the demonstration of EC and FT gate operations for larger-distance logical qubits [119].

5.3.6 *Data availability*

The data underlying the findings of this work and the quantum circuits are available at https://doi.org/10.5281/zenodo.6244536.

5.3.7 *Code availability*

All codes used for data analysis are available from the corresponding author upon reasonable request.

5.3.8 *Acknowledgements*

We gratefully acknowledge support by the EU Quantum Technology Flagship grant AQTION under Grant Agreement number 820495, and by the US Army Research Office through Grant No. W911NF-21-1-0007. We also acknowledge funding by the Austrian Science Fund (FWF), through the SFB BeyondC (FWF Project No. F7109), by the Austrian Research Promotion Agency (FFG) contract 872766, and by the IQI GmbH. M.R. acknowledges funding from the European Union's Horizon 2020 research and innovation programme under the Marie Skłodowska-Curie grant agreement No. 840450. M.Müller acknowledges support by the ERC Starting Grant QNets Grant Number 804247. S.H. acknowledges funding by the Deutsche Forschungsgemeinschaft (DFG, German Research Foundation) under Germany's Excellence Strategy – Cluster of Excellence Matter and Light for Quantum Computing (ML4Q) EXC 2004/1 – 390534769. The research is also based upon work supported by the Office of the Director of National Intelligence (ODNI), Intelligence Advanced Research Projects Activity (IARPA), via the US Army Research Office Grant No. W911NF-16-1-0070. The views and conclusions contained herein are those of the authors and should not be interpreted as necessarily representing the official policies or endorsements, either expressed or implied, of the ODNI, IARPA, or the US Government. The US Government is authorized to reproduce and distribute reprints for Governmental purposes notwithstanding any copyright annotation thereon. Any opinions, findings, and conclusions or recommendations expressed in this material are those of the author(s) and do not necessarily reflect the view of the US Army Research Office.

5.3.9 *Author contributions*

L.P., I.P. and T.F. carried out the experiments. L.P., I.P., T.F., M.Meth, C.D.M., R.S., M.Ringbauer, P.S. and T.M. contributed to the experimental setup. L.P. analyzed the data. S.H. performed the numerical simulations. S.H., M.Rispler and M.Müller performed circuit analysis, characterization and theory modelling. L.P., S.H., I.P., M.Rispler, P.S. and M.Müller wrote the manuscript, with contributions from all authors. R.B., P.S., M.Müller and T.M. supervised the project.

5.3.10 *Competing interests*

T.M., R.B. and T.F. are connected to Alpine Quantum Technologies, a commercially oriented quantum computing company.

6

CHARACTERIZATION AND MODELING OF SPATIALLY CORRELATED NOISE

In Chapters 3 to 5, a generic error model was introduced and applied to quantum circuits in the context of QEC. In this model, noisy quantum gate operations are replaced by an ideal implementation of the gate followed by the probabilistic application of Pauli errors on the qubits the gate acts on. Furthermore, idling errors are modeled as an incoherent dephasing process by probabilistically applying Z errors independently on all idling qubits. Such a model does not necessarily reflect the microscopic noise processes taking place in a physical implementation of a quantum information processor like the trapped-ion device considered in this thesis.

This chapter considers two effects introducing noise processes that are spatially correlated: In Section 6.1, the undesired manipulation of spectator qubits in spatial proximity to the target qubits of a quantum operation, referred to as *crosstalk*, is discussed. A more refined error model taking crosstalk errors into account is introduced. Section 6.2 discusses idling processes, where the noise acting on spectator qubits is correlated across the qubit register. The effect of correlated noise on the performance of a QEC code is investigated. Furthermore, a method for the quantification of spatial correlations in error processes, analog to the quantification of entanglement in quantum states, is introduced.

6.1 Crosstalk in quantum operations

In the quantum information processor considered here, gate operations are implemented by illuminating a single ion or a pair of ions in a chain with steerable, tightly focused laser beams. However, the laser beam has a finite diameter at the position of the target ion, so that neighboring ions see residual light intensity. A limit on the ability to confine the laser light to the target ions is given by the design of the focusing optics. In the focal spot of a Gaussian beam focused by a lens with a numerical aperture NA the intensity of the light drops to a fraction $\frac{1}{e^2}$ of the peak intensity at a distance [173]

$$w = \frac{\lambda}{\pi} \frac{1}{\arcsin(\mathrm{NA})} \tag{6.1}$$

from the center of the focused spot. Here, λ is the wavelength of the light and it is assumed that the laser propagates in vacuum. Therefore, the NA of the optics has to be chosen to allow for the desired suppression of leakage light at neighboring ion positions.

The spot radius w from Eqn. 6.1 is a theoretical lower limit assuming defect-free optical elements and perfect alignment. However, a realistic optical system always exhibits mis-

alignment and errors in the surface shape of the used optics. When light passes through optics that are not ideally aligned or optics with an erroneous surface, the wavefront of the light is distorted. A distortion of the wavefront along the beam path leads to a deviation of the intensity profile in the focal spot from the ideal unperturbed beam spot.

Figure 6.1 shows the two-dimensional electric field amplitude distribution of the tightly focused addressing beam in the focal plane. The profile is measured by scanning the focused beam across an ion using the beam steering setup described in Section 3.2.3.3 and measuring the Rabi frequency on the optical-qubit transition. The Rabi frequency is proportional to the electric field amplitude of the laser field at the ion position. One can see that there is a residual light field at horizontal distances from the intensity maximum of approximately $3.8\,\mu\mathrm{m}$ to $6\,\mu\mathrm{m}$ corresponding to typical inter-ion distances along the ion chain. Therefore, whenever one is acting on a specific target ion, neighboring spectator qubits will experience an interaction with the laser light, which induces errors in the encoded quantum information.

The undesired interaction predominantly affects spectator qubits, which are direct neighbors to the target qubits of a certain gate operation. Hence, the induced errors exhibit a spatial correlation given by the structure of the quantum circuit. Crosstalk in entangling gate operations can lead to error propagation to spectator qubits in spatial proximity to the target qubits of the respective gate. Therefore, fault-tolerance properties of a QEC circuit can be affected by crosstalk errors. In the publication presented in the following section, the effect of crosstalk on QEC protocols is studied and the error model discussed in Section 3.3 is extended to account for crosstalk in single- and two-qubit gates.

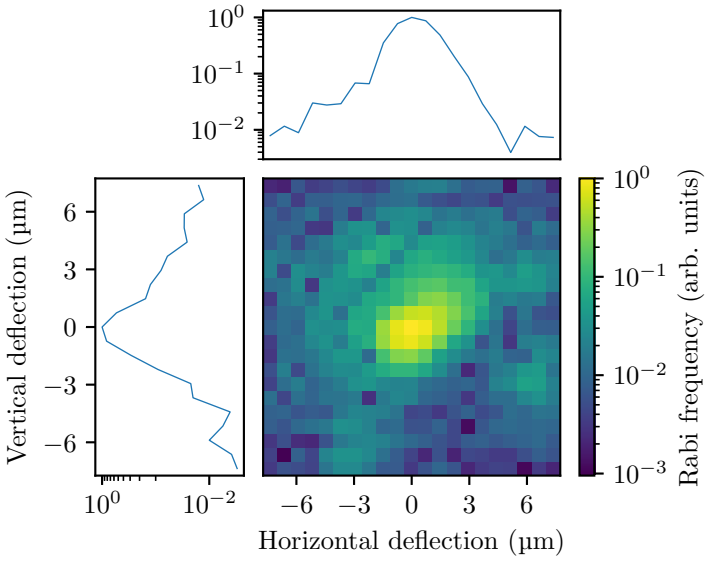

Figure 6.1: Scan of a tightly focused laser beam across a trapped ion in two dimensions. For a given vertical and horizontal deflection with respect to the calibrated ion position the Rabi frequency normalized to the maximum Rabi frequency is measured. Aberrations caused by imperfections in the optical system focusing the laser beam lead to a tail of the central peak to the top-right and patches with relative Rabi frequencies on the order of 10^{-1} towards the edges of the scan area. The line plots on top and on the left of the color plot are Rabi frequency profiles through the center of the color plot along the horizontal and vertical axis, respectively.

6.1.1 *Publication: Strategies for a practical advantage of fault-tolerant circuit design in noisy trapped-ion quantum computers*

Strategies for practical advantage of fault-tolerant circuit design in noisy trapped-ion quantum computers*

Physical Review A **107**, 042422 (2018)

Sascha Heußen[1,2], Lukas Postler[3], Manuel Rispler[1,2], Ivan Pogorelov[3], Christian D. Marciniak[3], Thomas Monz[3,4], Philipp Schindler[3], Markus Müller[1,2]

[1]Institute for Quantum Information, RWTH Aachen University, Aachen, Germany
[2]Institute for Theoretical Nanoelectronics (PGI-2), Forschungszentrum Jülich, Jülich, Germany
[3]Institut für Experimentalphysik, Universität Innsbruck, Innsbruck, Austria
[4]Alpine Quantum Technologies GmbH, Innsbruck, Austria

Fault-tolerant QEC provides a strategy to protect information processed by a quantum computer against noise which would otherwise corrupt the data. An FT universal quantum computer must implement a universal gate set on the logical level in order to perform arbitrary calculations to in principle unlimited precision. In this manuscript, we characterize the recent demonstration of an FT universal gate set in a trapped-ion quantum computer [Postler et al. Nature 605.7911 (2022)] and identify aspects to improve the design of experimental setups to reach an advantage of logical over physical qubit operation. We show that various criteria to assess the break-even point for FT quantum operations are within reach for the ion trap quantum computing architecture under consideration. Furthermore, we analyze the influence of crosstalk in entangling gates for logical state preparation circuits. These circuits can be designed to respect fault tolerance for specific microscopic noise models. We find that an experimentally-informed depolarizing noise model captures the essential noise dynamics of the FT experiment that we consider, and crosstalk is negligible in the currently accessible regime of physical error rates. For deterministic Pauli state preparation, we provide an FT unitary logical qubit initialization circuit, which can be realized without in-sequence measurement and feed-forward of classical information. Additionally, we show that non-deterministic state preparation schemes, i.e. repeat until success, for logical Pauli and magic states perform with higher logical fidelity over their deterministic counterparts for the current and anticipated future regime of physical error rates. Our results offer guidance on improvements of physical qubit operations and validate the experimentally-informed noise model as a tool to predict logical failure rates in quantum computing architectures based on trapped ions.

* The author of the present thesis carried out the experiments and wrote the manuscript. Here, the accepted version of the manuscript is printed in a slightly amended form for consistency throughout the thesis. Changes include adapting hyphenation and abbreviations and updating references that were only available as preprints at the time of publication.

6.1.1.1 *Introduction*

The toolbox of quantum fault tolerance provides a key on the way towards universal quantum computation [174]. By careful circuit design this allows one to contain the effect of faults stemming from the fundamentally noisy hardware of real physical quantum systems. Here, the ideal computation takes place in a subspace (dubbed the *logical* subspace) of the (much larger) *physical* Hilbert space, where the logical information is typically encoded in non-local degrees of freedom of a QEC code and protected against local noise [152]. Avenues to experimental investigation of FT design principles have been opened up by recent leaps in quantum computing experiments and the development of the theory of flag fault tolerance, where dedicated auxiliary qubits flag the presence or absence of dangerous error patterns [111, 112, 119, 120, 153]. In trapped-ion systems, code state preparation [37], FT error detection [167], FT stabilizer readout [126], FT operation of one logical qubit [127] as well as logical entangling gates [160] and repetitive QEC cycles [38] were achieved. The state of the art now lies in FT universal gate sets [128] (reprinted in Section 5.3) conjoined with repetitive QEC cycles [39]. In superconducting qubits, this evolution is paralleled, where code state preparation [161, 165], error detecting QEC cycles [162], logical gates in an error detecting code [163] and the operation of a surface code with QEC cycles [122] and higher-distance surface codes [124] were demonstrated. Other qubit platforms are showing greatly increasing capabilities recently along similar directions [154, 175].

Central to the task of FT operation of a quantum processor are a) the ability to initialize logical states, i.e. QEC code states, b) to measure their error syndrome, c) to perform logical gates using a universal set of gates, and d) to determine logical measurement outcomes. All these tasks have to be implemented fault-tolerantly, i.e. in such a way that they do not introduce errors beyond what can be tolerated by the QEC code. Furthermore, the noise level of all operations needs to be below a (model-dependent) threshold [116, 156]. A major concern is the proliferation of errors due to the application of entangling operations when implementing a logical gate. A landmark result that emerged from fault tolerance theory is that FT logical gate operations typically fall into two categories. On the one hand, some gate operations can be relatively straightforward to compose by transversal implementations, where the logical gate operation can be synthesized by independent bitwise action on the qubit register, thus avoiding any need for entangling operations within the logical qubit block. On the other hand, there are always gates that defy this realization and require special treatment, as dictated by the no-go theorem of Eastin and Knill [43, 151]. For the platform of trapped-ion qubits, the ability to perform a universal gate set on the logical level has recently become experimental reality as part of a demonstration by Ref. [128]. In the present work, we provide an extensive analysis to put this experiment into a broader context of current and projected experimental capabilities.

6.1.1.2 *Outline and summary of main results*

This paper is structured as follows: In Section 6.1.1.3, we discuss the trapped-ion setup and give an overview over the physics that provide the basis for defining qubit states as well as single-qubit and entangling operations. We lay out how this leads us to an experimentally-motivated noise model, building on and extending the model used in Ref. [128]. Also, we introduce the circuit sampling technique of subset sampling (SS) and discuss how it fares compared to conventional MC. In Section 6.1.1.4, we discuss one of the key aspects of

FT circuit design, namely in what scenario and parameter regime they become useful by outperforming their non-FT or bare physical counterparts. We discuss which parameters the logical qubit performance can and should be compared to and present how FT circuits for logical Pauli eigenstate preparation as well as logical magic state preparation perform on those scales. We find in Section 6.1.1.4.1, that under our current noise levels, the Pauli state preparation is already on the edge to the break-even point of outperforming the physical initialization operation. The logical magic state preparation is already below one of the relevant break-even points, namely the physical entangling gate error rate with current noise parameters. By a scaling analysis of the physical error rates, we find that both will be brought to the sub-threshold regime with moderate hardware improvements. We extend the discussion in Section 6.1.1.4.2 by comparing non-deterministic circuits, where runs with flag events are discarded, to deterministic circuits, where runs with flag events are instead treated with further circuitry to maintain fault tolerance. We find that the added circuitry reduces the logical fidelity substantially and discuss the scenarios where either might be preferential. In Section 6.1.1.5, we discuss the relevance of crosstalk, where we explain the notion of entangling crosstalk and the corresponding error channel. We study its potentially detrimental effect on QEC under current and projected experimental noise. We find that it does not constitute a major noise source at current noise levels but might become relevant at lower error rates. Nevertheless, we demonstrate how a specific type of entangling crosstalk can be mitigated by carefully designing the circuit. In Section 6.1.1.6, we calculate the quantum state fidelity of a single logical qubit under different noise models. From the comparison of different performance metrics we conclude that the logical fidelity is the appropriate measure and the central figure of merit used for quantifying the logical qubit performance.

6.1.1.3 *Trapped-ion based quantum processors*

One of the most promising system architectures for FT quantum information processors is trapped-ion based devices [29, 59, 176, 177]. These devices offer mature hardware, high-fidelity operations and all-to-all qubit connectivity. For register sizes of up to around 20 qubits [39, 84] any arbitrary pair of qubits in the register can be natively entangled with a single quantum operation, facilitating certain quantum algorithms or rather reducing the overhead of their implementation drastically [178]. This is achieved by exploiting a long-range interaction between the ions mediated by a collective motional mode of the ion Coulomb crystal. Even larger registers can be realized by subdividing the register into smaller segments, each providing all-to-all connectivity [179]. Interactions between such subsections can be realized by spatially rearranging the segments and single ions within the segments. Individual ions can be moved within the device for reconfiguration, an operation referred to as shuttling, via the application of time-dependent voltages to electrodes of the ion trap. Fault-tolerant gadgets have already been demonstrated in setups following this ion-shuttling based approach [38, 39, 126]. For the remainder of this section we will focus on a system hosting a static ion string that provides all-to-all connectivity in a register of 16 qubits [84]. In the following we will discuss the native gate set and noise processes of the device.

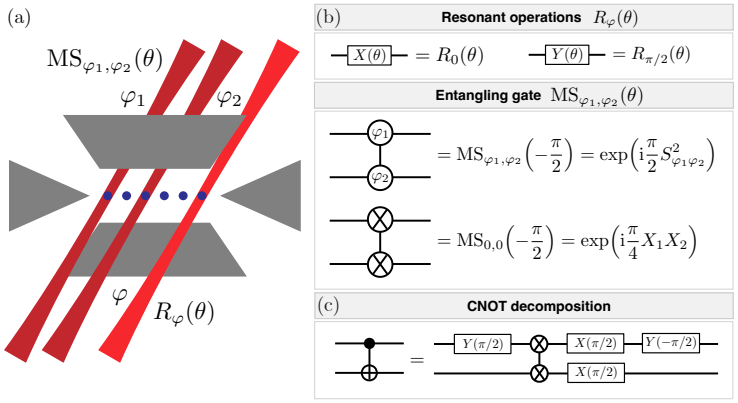

Figure 6.2: Trapped-ion device architecture and native gate set. (a) Trapped ions (blue dots) are suspended in a macroscopic linear Paul trap. Tightly focused laser beams allow for the implementation of single-qubit rotations (lighter-shaded red laser beam) and entangling operations on arbitrary pairs (darker-shaded beams). (b) The native gate set consists of resonant single-qubit operations implementing rotations around an axis in the equatorial plane of the Bloch sphere, where the rotation axis in controlled via the phase φ of the laser pulse. The rotation angle θ is controlled via the pulse area of the laser pulse. The native entangling operation is realized via an MS-type interaction. Z operations can be implemented in software by updating the phase of subsequent light pulses on the respective ion through individual control of the light phase. This allows for the implementation of generalized MS-type gates $\mathrm{MS}_{\varphi_1,\varphi_2}(\theta)$. (c) Decomposition of a CNOT gate into an MS gate and local operations.

6.1.1.3.1 *Static ion chain quantum processor*

The system under consideration uses a macroscopic Paul trap [84]. A suitable set of RF and static voltages applied to the trap electrodes ensures that trapped ions form a one-dimensional crystal, where their equilibrium positions are determined by the interplay of the trapping forces and the Coulomb interaction between the ions [66]. Each trapped $^{40}\mathrm{Ca}^+$ ion hosts a qubit in the Zeeman sublevels $4S_{1/2,m_j=-1/2} = |0\rangle$ and $3D_{5/2,m_j=-1/2} = |1\rangle$ of the ground state and a metastable excited state with a lifetime of $T_1 \approx 1.2\,\mathrm{s}$ [80]. As can be seen in Figure 6.2, a tightly focused laser beam addressing this quadrupole transition allows for individual control of the qubits in the register. The native gate set of the apparatus consists of the following three types of operations:

- **Resonant operations:** A laser pulse resonant to the qubit transition with variable phase and pulse area implements rotations $R^{(i)}_\varphi(\theta) = \exp(-\mathrm{i}\frac{\theta}{2}(X_i\cos\varphi + Y_i\sin\varphi))$ around an axis in the equatorial plane of the Bloch sphere, where X_i and Y_i are single-qubit Pauli matrices acting on qubit i. The rotation angle θ is controlled via the duration and intensity of the laser pulse, and the angle of the rotation axis with respect to the X axis φ is controlled via the pulse phase. A pulse length of about $15\,\mu\mathrm{s}$ is required to implement a rotation angle of $\pi/2$.

- **Entangling operations:** Entangling operations acting on an arbitrary pair of ions are realized by illuminating the respective ions with a bichromatic light field slightly detuned from a COM radial mode, effectively applying an MS interaction to the respective ions [168]. The phase of the light illuminating the ion pair can be controlled individ-

ually, which allows for the implementation of the unitary operations $\mathrm{MS}_{\varphi_1,\varphi_2}(\theta) = \exp\left(-\mathrm{i}\theta S^2_{\varphi_1,\varphi_2}\right)$ with $S_{\varphi_1,\varphi_2} = \frac{1}{2}\left(X_1\cos\varphi_1 + X_2\cos\varphi_2 + Y_1\sin\varphi_1 + Y_2\sin\varphi_2\right)$. A rotation angle of $\theta = -\pi/2$ renders the operation maximally entangling and makes the MS gate operation equivalent to a CNOT up to local operations [88]. The native implementation of this entangling gate we use provides only negative values of θ due to the spectral structure of the collective motional modes. We want to note that the symbol introduced in the second panel of Figure 6.2b widely used throughout this work refers to an XX-rotation with $\theta = -\pi/2$.

- **Virtual Z operations:** Z rotations are implemented in software by manipulating a phase register in the classical control hardware [180] that keeps track of Z operations for each ion. The phases of all subsequent single-qubit and entangling operations are shifted according to the state of the phase register [85].

Currently, the setup under consideration does not allow for parallel execution of gate operations, as a simultaneous illumination of only up to two ions is possible. This restriction is mainly due to a limited number of RF sources controlling the beam steering optics available in the control hardware and laser power limitations, as the light intensity illuminating an ion decreases quadratically with the number of addressed ions [181]. Modifications to the addressing setup would eliminate this technical limitation and facilitate parallel execution of gate operations [39, 182].

6.1.1.3.2 *Noise modeling and simulation*

In this section, we discuss noise processes affecting the performance of the quantum processor under consideration and introduce theoretical models describing these processes. We analyze their influence on the performance of FT circuits and estimate necessary improvements to achieve a break-even of FT encoded qubits with respect to bare physical qubits.

Idling noise. A fundamental noise process affecting all implementations of physical qubits is idling noise altering the quantum state of a qubit, which is not target of an operation at the respective time. Thereby the effect on idling qubits is not dependent on the target qubits of the respective operation, in contrast to crosstalk discussed later in this section. For trapped-ion architectures utilizing metastable electronic states, three processes are affecting the state of idling qubits: As the qubit state $|1\rangle$ is encoded in a metastable excited state its population decays exponentially. First, it either decays to $|0\rangle$, referred to as amplitude damping, or, second, it leaks out of the computational subspace while decaying to the Zeeman sublevel $4S_{1/2,m_j=+1/2}$. The rates of these processes are governed by the lifetime of the metastable state T_1. Third, fluctuations in the laser frequency or magnetic field during idle time lead to dephasing on a timescale of $T_2 \approx 100\,\mathrm{ms}$*.

Due to the predominance of dephasing over amplitude damping and leakage, the incoherent noise channel for idling qubits can be modeled by Pauli-Z faults and reads

$$\mathcal{E}_{\text{idle,deph}}(\rho) = (1 - p_{\text{idle}})\rho + p_{\text{idle}} Z\rho Z. \tag{6.2}$$

* Typical values for the experimental dephasing time vary between $30\,\mathrm{ms}$ and $200\,\mathrm{ms}$ from day to day depending on the electromagnetic environment being present.

A more accurate model could also include effects of correlated dephasing which were reported in previous investigations [183–185]. However, as idling is only a weak source of failure in our setup we do not expect a difference between correlated and uncorrelated idling noise. Thus, we choose to model the dephasing noise as uncorrelated on the individual physical qubits. The physical error rate for idling faults p_{idle} depends on the execution time t of the gate performed on a subset of ions and the coherence time T_2. The incoherent probabilities for the dephasing process on idling qubits is given by

$$p_{\text{idle}} = \frac{1}{2}\left(1 - \exp\left(-\frac{t}{T_2}\right)\right). \tag{6.3}$$

The table below shows typical execution times of various operations in the setup considered and the associated physical error rates for idling qubits during these operations.

operation	time t	p_{idle}
single-qubit rotation	$15\,\mu\text{s}$	7.5×10^{-5}
MS gate	$200\,\mu\text{s}$	1.0×10^{-3}
measurement	$300\,\mu\text{s}$	1.5×10^{-3}

In the current ion trap architecture, all experiments for FT state preparation are performed with both auxiliary and data qubit measurements deferred to the end of the circuit, as described in Ref. [128], so that no idling faults occur during the measurements. Simulations presented in Section 6.1.1.4 partly contain in-sequence measurements which are modelled with the respective idling error rate. All in-sequence measurements are modeled to have the same idling error rate, although measurements showing at least one bright ion are usually followed by a recooling sequence with a duration on the order of milliseconds [181]. As idling is not the dominant error source we neglect this dependence of the idling error rate on the outcome of a measurement.

Single-qubit operations. As virtual Z operations are noiseless [85], the only erroneous single-qubit operations are resonant operations. We characterize resonant single-qubit operations experimentally via randomized benchmarking [186]. For different ions in a 16-qubit register, the fidelity of a single-qubit rotation ranges from $0.9969(4)$ to $0.9980(3)$ with a mean of 0.9976 and a standard deviation of 2.4×10^{-4}. Combined randomized benchmarking data for sequences of up to 20 Clifford operations per qubit for all 16 qubits are shown in Figure 6.3, data for individual qubits can be found in Appendix C.5. Faults affecting single-qubit operations acting on a state ρ are modeled as depolarizing noise, hence the modeled noise channel reads

$$\mathcal{E}^{(1)}_{\text{dpl}}(\rho) = (1 - p_1)\rho + \frac{p_1}{3}(X\rho X + Y\rho Y + Z\rho Z). \tag{6.4}$$

With a probability $1 - p_1$ the ideal operation is implemented and with a probability p_1 a fault operator, randomly drawn from the set of Pauli operations $\{X, Y, Z\}$, is applied subsequently to the ideal gate. For the theory model we choose $p_1 = 0.005$ for better comparability with Ref. [128] although recent improvements on the experimental setup slightly increased the fidelity of single-qubit operations.

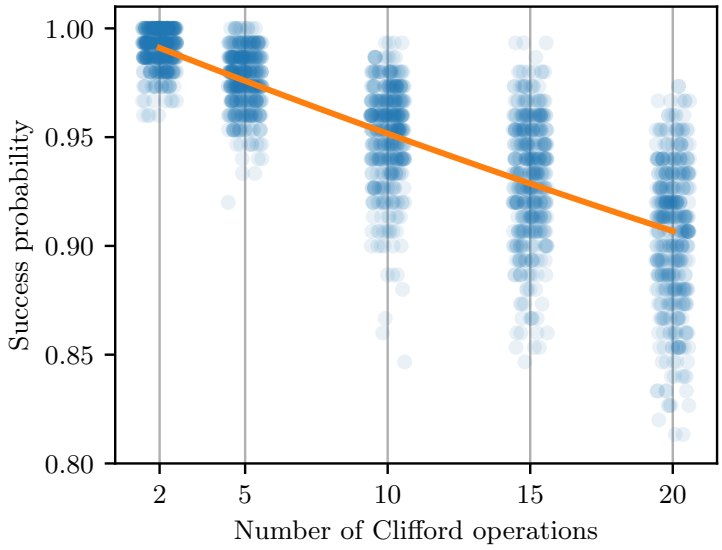

Figure 6.3: Single-qubit gate benchmarking. Experimental success probabilities of randomized benchmarking sequences containing up to 20 Clifford operations in a 16-qubit register. The scatter on the horizontal axis around the sequence lengths 2, 5, 10, 15 and 20 is introduced for better visibility of the success probability of the individual random sequences. The discretization on the vertical axis is given by averaging over 150 executions per random sequence. For brevity data from 16 qubits is combined to a single dataset. The underlying data for individual qubits can be found in Appendix C.5. The decay fitted to the combined data suggests a single-qubit gate fidelity of $0.99760(8)$, where the given error is the 95% confidence interval.

Entangling operations. In the system under consideration, entangling operations are based on the COM motional mode, which offers equal coupling to all qubits in the register. Nevertheless, unwanted coupling to higher order modes with different coupling strengths along the ion string can potentially lead to a varying fidelity for different qubit pairs in the register. To avoid benchmarking on all possible ion pairs, the mean fidelity of a single entangling gate $\mathcal{F}_{\mathrm{tq}} = 0.975(3)$ is estimated from the quantum state fidelity of the GHZ state $|\psi_{\mathrm{GHZ}}\rangle = (|0\rangle^{\otimes 16} - i\,|1\rangle^{\otimes 16})/\sqrt{2}$ prepared across the entire register. A more detailed description of this procedure can be found in Appendix C.6. Although this method does not constitute a rigorous characterization of the underlying individual gates, it can still provide insights about the system performance in terms of entanglement generation [187].

Microscopic noise models have been derived in previous works, considering amplitude fluctuations or gate miscalibrations in particular [170] as well as thermal errors or motional heating [188] and incoherent overrotations [189]. However, for simplicity, we apply depolarizing noise to two-qubit gates, as we do for single-qubit operations since our arguments of advantageous FT quantum computation primarily regard the appropriate FT design of quantum circuits. Depolarizing noise is considered the most general and architecture-agnostic incoherent noise channel because the fault operators of the depolarizing noise channels form a basis in the space of single- and two-qubit unitaries respectively. The modeled error channel for depolarizing noise on entangling gates reads

$$\mathcal{E}^{(2)}_{\mathrm{dpl}}(\rho) = (1-p_2)\rho + \frac{p_2}{15}\sum_{i=1}^{15} E_2^{(i)}\rho E_2^{(i)} \tag{6.5}$$
$$E_2 = \{\sigma_k \otimes \sigma_l, \forall k,l \in \{0,1,2,3\}\} \setminus \{I \otimes I\}.$$

With a probability p_2 one of fifteen non-trivial weight-2 Pauli faults is added to the ideal entangling gate. We choose $p_2 = 0.025$ as estimated from the GHZ state preparation. Although overrotations have been identified as a dominant source of error in ion trap quantum processors before [190, 191], we find in Section 6.1.1.4 that depolarizing noise does not perform worse at estimating logical failure rates than an incoherent overrotation noise model. The latter takes into account the physical nature of optical qubit operations, i.e. laser driven rotations around a given Pauli axis (see Appendix C.1). We provide further comparison between overrotations and depolarizing noise through quantum state fidelity calculations in Section 6.1.1.6.

Crosstalk. Another noise process is the unintended manipulation of qubits in spatial proximity to a target qubit, which we refer to in this work as crosstalk. The physical process causing this is leakage light from the tightly focused laser beam, where the main contributions are aberrations caused by imperfect optical systems. In Figure 6.4a we depict a Fourier optics calculation [192] of the profiles of the electric field amplitude being proportional to the Rabi frequency of a resonant operation. We show the electric field around the target ion position for an ideally focused Gaussian beam, but also for beams affected by coma, spherical aberration and astigmatism [193]. The parametrization of the electric field amplitude is $E_\varphi(\mathbf{x}) = E(\mathbf{x})\exp(i\varphi)$, where $\mathbf{x}$ is the position in a plane orthogonal to the beam propagation at the ion location and $E(\mathbf{x})$ is a positive, real number. The magnitudes of the aberrations in this example are chosen to give peak-to-valley wavefront distortions of 2λ and do not necessarily reflect the situation in the experiment. Figure 6.4b shows the

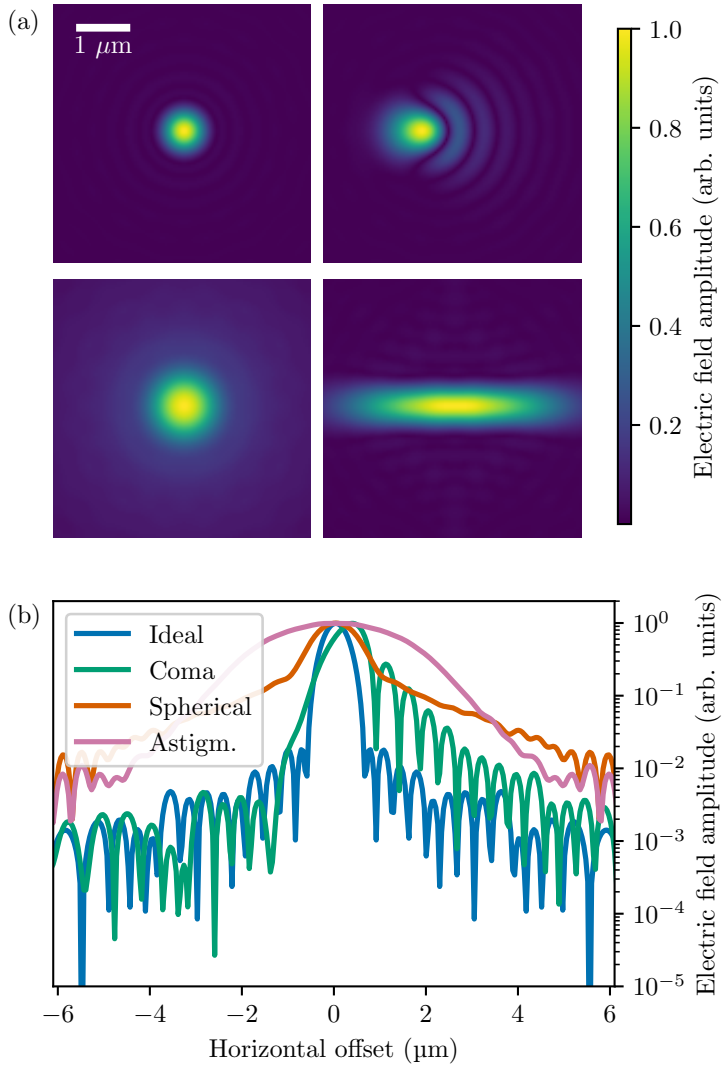

Figure 6.4: Electric field crosstalk. Fourier optics calculation of aberrations affecting a tightly focused laser beam. We simulate light with a wavelength of $\lambda = 729\,\mathrm{nm}$ illuminating an objective with an aperture diameter of $40\,\mathrm{mm}$ and a focal length of $20\,\mathrm{mm}$. Aberrations are introduced by distorting the input wavefront, where the peak-to-valley phase deviation compared to a plane wave amounts to 2λ. (a) In the upper left image the ideal electric field amplitude $E(\mathbf{x})$ of an aberration-freely focused Gaussian beam is depicted. The other color plots show the effect of different types of aberrations, namely coma (upper right), spherical aberration (lower left) and astigmatism (lower right). The increased diameter of the field distribution leads to increased leakage light at neighboring ions. (b) Cut along the horizontal axis of the field distributions shown in a) through the maximum intensity point for the ideal and the three aberrated spots.

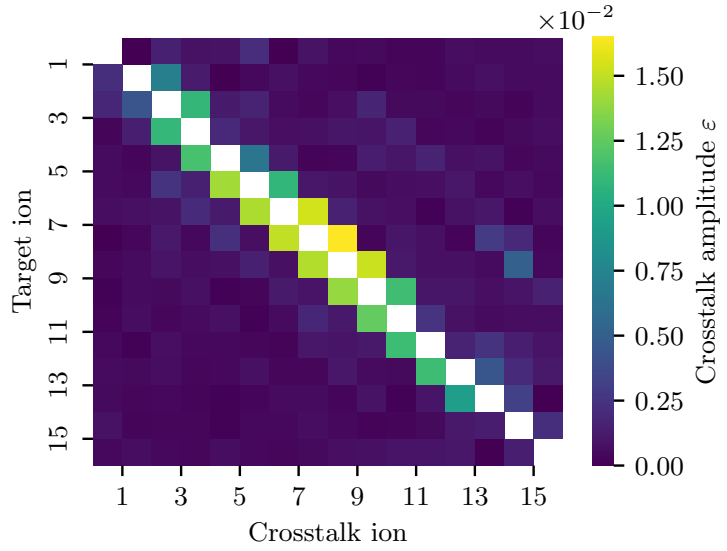

Figure 6.5: Ion-string crosstalk amplitude. Measured ratio ε of crosstalk to target Rabi frequency for resonant operations acting on all 16 qubits, with a maximum and mean next-neighbor crosstalk ratio of 1.6×10^{-2} and 0.9×10^{-2} respectively.

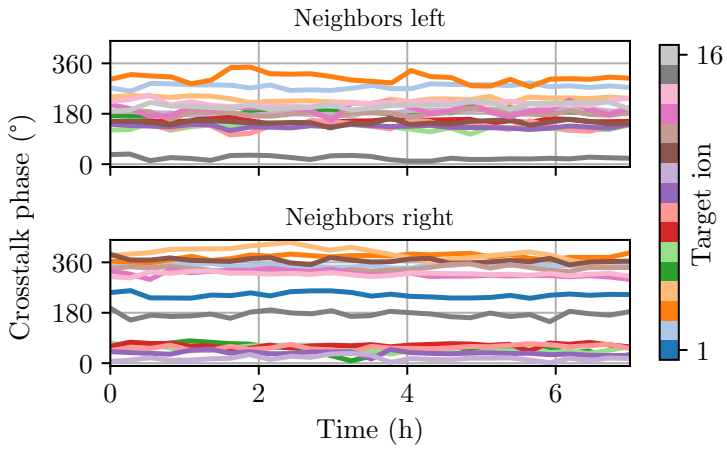

Figure 6.6: Ion-string crosstalk phase. Measurement of the phase difference between target and crosstalk light field in a 16-qubit ion crystal. The crosstalk phase covers the whole interval $[0, 2\pi]$ for different target-neighbor-pairs, but is stable up to tens of degrees over hours.

calculated electric field amplitude along the ion string, where an offset of zero corresponds to the position of the target ion. In a 16-ion crystal the distances to neighboring ions in the discussed setup are typically around $4\,\mu\mathrm{m}$. As a figure of merit for the magnitude of the effect of this crosstalk we use the ratio $\varepsilon = \Omega_n/\Omega$ of the Rabi frequencies of the unintended manipulation at a neighboring ion Ω_n and the target operation Ω. In the experimental setup under consideration the maximum nearest-neighbor crosstalk ratio is $\varepsilon_{\max} = 1.6 \times 10^{-2}$ while the mean over the register is $\varepsilon_{\mathrm{mean}} = 0.9 \times 10^{-2}$ in a 16-qubit register with an axial trap frequency of $400\,\mathrm{kHz}$. The inter-ion distances range from $3.6\,\mu\mathrm{m}$ in the center to $5.7\,\mu\mathrm{m}$ at the edge of the ion chain. Crosstalk ratios ε for the 16-qubit register are shown in Figure 6.5. We neglect crosstalk to non-nearest neighbors in our model as the measured mean Rabi frequency ratio is more than an order of magnitude lower than between direct neighbors.

It is crucial to note that the phase of the leakage light can significantly differ from the phase of the light at the target ion position. Aberrations that distort the wavefronts at the input of the focusing optics propagate to the ion string in the focal plane and lead to an electric field distribution around the target ion with spatially variable phase. This phase is experimentally accessible via a Ramsey-type experiment, where a superposition state is prepared with leakage light by illuminating a neighboring ion and subsequently its phase is analyzed by applying a resonant single-qubit operation with varied phase to the qubit affected by crosstalk. As can be seen in Figure 6.6, the measured phase difference between target and neighboring ion varies across the whole interval of all possible values $[0, 2\pi]$ for different target ions. The wavefront distortions likely stem from non-ideal alignment of the optical setup and surface imperfections in the beam path, and therefore the phase difference of neighboring ions is stable on the timescale of hours.

Based on the aforementioned experimental observations we model crosstalk noise as follows in simulations: When a resonant single-qubit gate is applied to a target ion with a rotation angle $\theta = \Omega t$, where Ω is the Rabi frequency and t is the gate duration, nearest neighbor ions see a resonant operation with a rotation angle $\theta_n = \varepsilon\theta$. After Pauli twirling (see Appendix C.1), this leads to the incoherent error process

$$\mathcal{E}(\rho) = \cos^2\frac{\varepsilon\theta}{2}\rho + \sin^2\frac{\varepsilon\theta}{2}\left(\cos^2\varphi X\rho X + \sin^2\varphi Y\rho Y\right) \tag{6.6}$$

for the neighboring ions, where φ is the light phase at the respective neighbor ion position. As the phase relation between the light at the target ion and neighbor ion position varies along the ion chain (see Figure 6.6), we average over all possible crosstalk phases to obtain the incoherent noise channel

$$\mathcal{E}_{\mathrm{c}_1}(\rho) = (1 - p_{\mathrm{c}_1})\rho + \frac{p_{\mathrm{c}_1}}{2}\left(X\rho X + Y\rho Y\right) \tag{6.7}$$

for each single-qubit crosstalk location. Here $p_{\mathrm{c}_1} = \sin^2\frac{\varepsilon\theta}{2}$ with $\varepsilon = 1 \times 10^{-2}$ is the probability that crosstalk induces an error on a neighboring qubit. Applying the same reasoning to model crosstalk errors for two-qubit gates gives the channel

$$\begin{aligned}\mathcal{E}_{\mathrm{c}_2}(\rho) = (1 - p_{\mathrm{c}_2})\rho + \frac{p_{\mathrm{c}_2}}{4}\left(X_tX_n\rho X_tX_n + X_tY_n\rho X_tY_n\right.\\ \left. + Y_tX_n\rho Y_tX_n + Y_tY_n\rho Y_tY_n\right)\end{aligned} \tag{6.8}$$

for any pair of target and neighbor ions denoted by subscripts t and n respectively with $p_{c_2} = \sin^2 \frac{\varepsilon\pi}{4}$. An illustration of all target-neighbor locations can be found in Figure C.1.

State preparation and measurement. Measurements in the Z basis are performed by illuminating the ion chain with light resonant to the $4S_{1/2}$ to $4P_{1/2}$ transition, leading to fluorescence light emitted by ions projected to $|0\rangle$ and no emitted photons from ions projected to $|1\rangle$ [83]. Measurement errors are caused by the overlap between bright and dark count distributions originating from the intrinsic overlap of the Poissonian distributions of dark and bright state fluorescence counts and by the probability that an ion decays from the metastable excited state during the detection time [74]. State initialization of the qubit to $4S_{1/2,m_j=-1/2}$ is achieved by frequency-resolved optical pumping on the quadrupole transition. The ions are illuminated with light resonant to the transition from $4S_{1/2,m_j=+1/2}$ to $3D_{1/2,m_j=-3/2}$, while a repumping laser is broadening the transition [194]. Typical probabilities for initialization and measurement faults in the setup considered are around 3×10^{-3} [83]. Both initialization and measurement errors are again modeled as depolarizing noise. Therefore, the model is the same as in Eqn. 6.4 with error probabilities $p_i = p_m = 4.5 \times 10^{-3}$, corresponding to a flip error probability of 3×10^{-3} for initialization and measurement, respectively.

All of the above-mentioned noise models are discussed in more detail in Appendix C.1 alongside coherent overrotations and coherent crosstalk on MS gates. Since it is known that QEC decoheres noise through encoding and stabilizer measurement, although coherent by nature [195, 196], we mainly focus on incoherent noise in this manuscript.

Numerical methods. In Section 6.1.1.4, we estimate logical failure rates of logical state preparation protocols by performing numerical simulations of both stochastic incoherent Pauli noise models and coherent noise as described above. We provide results of numerical simulations for logical failure rates under both *depolarizing noise* on single-qubit gates, two-qubit gates, physical qubit initialization and measurement as well as an *extended noise* model. It includes dephasing noise on idling qubits and crosstalk on both single- and two-qubit gates on top of said depolarizing noise. We use stabilizer simulations [51] for Pauli state preparation with incoherent noise and statevector simulations otherwise, i.e. either for magic state preparation or when applying coherent noise to either type of state preparation. If applicable, stabilizer simulations are advantageous since they allow for simulation of Clifford circuits in polynomial time according to the Gottesman-Knill-theorem [50]. The exponentially large n-qubit Hilbert space of dimension 2^n poses a numerical challenge for statevector simulations which run slowly and consume an exponential amount of memory with growing number of qubits n. All simulations in this work are performed using a modified version of the python package "PECOS" [197, 198]. The effect of incoherent noise is treated by means of direct MC and SS which is an importance sampling technique. Both methods have a preferential range of applicability: MC is used for larger physical error rates, SS achieves accurate estimates with well-defined confidence intervals for lower physical error rates and is especially useful for extracting scaling behavior (see Appendix C.2 for details on both methods).

6.1.1.4 *Protocols for FT advantage over physical qubits*

The paradigm of FT circuit design holds the promise to maintain coherence within a quantum computation where many physical qubits are involved and suffer the influence of noise [31]: Faults on individual components of a quantum circuit must not cause errors, which cannot be corrected by the QEC code, on the qubits holding the logical information.

There exist errors E *at the end* of the circuit, resulting from faults which happen at locations *within* the circuit, that have weight $\mathrm{wt}(E)$ larger than $t = \lfloor \frac{d-1}{2} \rfloor$. They are thus uncorrectable and will lead to failure of the QEC procedure. Here $d = 2t + 1$ is the distance of the QEC code and the weight is the number of qubits on which the error E acts. There will always exist configurations of $t + 1$ faults that cause logical failure, i.e. lead to application of an unintended logical operator when performing QEC because $\mathrm{wt}(E) > t$.

Up to t faults can be in principle prevented from propagating to cause more than the correctable amount of t errors by advantageous circuit design. By unfortunate circuit design though, large distance logical states could also be corrupted by propagation of lower order faults. In this case, one could encode into lower distance logical states directly instead of using such circuits. We denote fault tolerance towards up to t faults as "level-t FT" or "FTt". Assume that faults at any circuit location happen independently with probability p. Then the logical failure rate p_L of FT implementations of a distance d QEC code scales as $p_L \propto p^{t+1}$ in the limit of low physical error rate $p \to 0$. For level-t FT all fault configurations up to order p^t must only cause correctable errors*. Note that the weight of the *error* determines whether or not it is correctable and the probability of occurrence for the microscopic *fault* configuration that propagates to an uncorrectable error determines its order in the polynomial for p_L.

In this work, we discuss FT schemes of level $t = 1$ which thus display a quadratic dependence of the logical failure rate $p_L \propto p^2$ as $p \to 0$. This scaling of FT implementations is contrasting non-FT circuits or operation of physical qubits where single faults can cause uncorrectable errors, thus leading to a linear scaling of the logical failure rate $p_L \propto p$ at low physical error rates p. Although FT circuits may involve more (noisy) qubits and gates than their non-FT counterparts, fault tolerance ensures that there exists a regime of physical error rates where the polynomial dependence leads to lower logical failure rates than non-FT and physical qubit implementation [116, 156].

The Steane code [36] shown in Figure 6.7 is the smallest representative of the family of topological color codes [142, 199]. As a [[7,1,3]] code, it encodes $n = 7$ physical qubits into a single logical qubit with distance $d = 3$ allowing for correction of $t = 1$ arbitrary Pauli errors while $t + 1 = 2$ or more errors lead to logical failure [45]. It has low resource overhead needed for FT universal qubit operations: Not only are all Clifford gates transversal and thus inherently FT in the Steane code. Also, the non-Clifford T-gate can be added to the logical gate set, for instance, by magic state injection [151]. Pauli rotations with angle $\pi/4$, i.e. the T-gate, can be performed fault-tolerantly in this way as long as an appropriate magic state is available as a resource. The injection circuit then only requires Clifford operations, which are suitable for the Steane code as they respect the FT requirements stated above. Different strategies for logical qubit initialization in the logical zero state and a logical magic state are addressed in this section.

The logical qubit is encoded in the $[[7, 1, 3]]$ Steane code defined by the six stabilizer generators

$$\begin{aligned} K_1^X &= X_4X_5X_6X_7 & K_1^Z &= Z_4Z_5Z_6Z_7 \\ K_2^X &= X_1X_3X_5X_7 & K_2^Z &= Z_1Z_3Z_5Z_7 \\ K_3^X &= X_2X_3X_6X_7 & K_3^Z &= Z_2Z_3Z_6Z_7 \end{aligned} \tag{6.9}$$

* While there might exist particular higher order fault configurations where faults annihilate each other and do not cause uncorrectable errors, it cannot be guaranteed that *all* such faults only cause correctable errors.

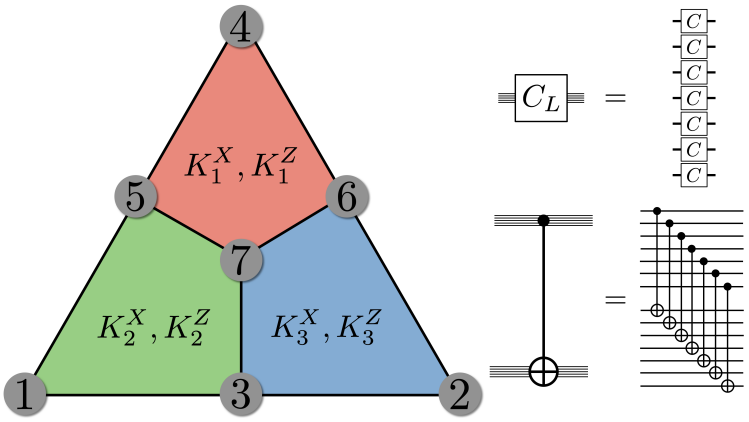

Figure 6.7: Steane code. *Left:* The Steane code is the smallest representative of the family of topological color codes. As a [[7,1,3]] code, it uses seven physical qubits to encode a single logical qubit with distance $d = 3$ allowing for correction of $t = \lfloor \frac{d-1}{2} \rfloor = 1$ arbitrary Pauli error. Physical qubits sit on the vertices of the graph. Stabilizer generators K_i are plaquettes spanning four physical qubits with mutual overlap of two qubits and are given by Eqn. 6.9. The X- and Z-type stabilizers are symmetric. *Right*: All gates of the Clifford group can be implemented transversally and thus fault-tolerantly in the Steane code and larger distance 2D color codes.

which are symmetric under exchange of X and Z. Any code state $|\psi\rangle_L$ is a +1 eigenstate of all stabilizers and thus stays invariant under application of any stabilizer. As a consequence, Pauli operators acting on code states can be multiplied by stabilizers without changing their effect on the code state. Two Pauli operators that only differ by multiplication with stabilizers are thus called stabilizer equivalent. Since the stabilizer generators exclusively consist of X or Z operators each, the Steane code belongs to the class of CSS codes [115, 200]. The transversality of the Hadamard and the CNOT gates follows directly from these two properties, respectively. The logical operators can be chosen as $X_L = X^{\otimes 7}$ and $Z_L = Z^{\otimes 7}$. By multiplication with stabilizers they can be expressed as weight-3 operators reflecting the fact that the Steane code can correct a single Pauli error. Single Pauli errors X_i and Z_j on any two single qubits $i \neq j$ can be corrected independently, or – as a consequence – a single Y-type error since $Y_i \simeq X_i Z_i$ (for $i = j$). Each possible syndrome measurement outcome is mapped to a unique recovery operation, which guarantees the correction of all single Pauli errors, with a look up table as shown in Table 6.1.

However, this mapping becomes non-unique if weight-2 errors can also occur. If two different errors map to the same syndrome then the recovery operation may cause erroneous application of a logical operator as a result of the EC attempt. As an example of such a logical failure, consider the error $E = X_3 X_5$. The Z syndrome will be measured as $-+-$ and by the look up table we would apply $R = X_6$ as a recovery operation. The total operator $RE = X_3 X_5 X_6$ is a logical operator since it is stabilizer equivalent to X_L given above.*

Transversal implementation such as for Clifford gates shown in Figure 6.7 directly ensures that single faults will at most cause a weight-1 error in each encoded logical qubit because transversal gates never couple two qubits from the same block. The weight-1 errors in each block can then independently be corrected in QEC.

* The chained error and correction operators RE correspond to X applied to all physical qubits multiplied by all three X-type generators $RE = K_1^X K_2^X K_3^X X_L$.

K_1^Z, K_2^Z, K_3^Z	recovery R
$+++$	I
$++-$	X_2
$+-+$	X_1
$+--$	X_3
$-++$	X_4
$-+-$	X_6
$--+$	X_5
$---$	X_7

Table 6.1: Look up table for the seven qubit Steane code as shown in Figure 6.7. $+$ and $-$ indicate a positive and negative expectation value of the respective stabilizer operator. All six of them form the error syndrome $(K_1^X, K_2^X, K_3^X, K_1^Z, K_2^Z, K_3^Z)$. Only the Z-type syndromes and corresponding X-type recoveries are shown. Since the Steane code is symmetric under exchange of X and Z, the Z-type recoveries from X syndrome measurements can be applied analogously. The two three-bit syndromes (K_1^X, K_2^X, K_3^X) and (K_1^Z, K_2^Z, K_3^Z) are sufficient to correct all single Pauli errors.

In this work, we use unitary encoding circuits for the initialization of logical qubits. This is in contrast to initialization procedures which rely on in-sequence stabilizer measurements and feed-forward of syndrome information. Unitary encoding circuits typically prepare logical states with fewer entangling gates at the cost of needing large connectivity between the data qubits which is provided natively in our trapped-ion architecture. These circuits allow for deterministic preparation of the code state since they avoid data qubit measurements altogether. Nonetheless, due to the large degree of inter-qubit connectivity, faults that happen on entangling gates might propagate throughout the circuit and cause uncorrectable errors as a result. This is illustrated e.g. for the encoding circuit in Figure 6.8. For FT state preparation in the Steane code the goal is to avoid such single fault events being able to cause weight-2 errors to occur on the final data qubit state. We can achieve FT by making use of recently introduced flag circuits [111, 112]. Here, additional auxiliary qubits called flag qubits are coupled to the data qubit block. Their measurement outcomes herald the potential presence of uncorrectable errors on the data qubit state. We refer to a flag measurement of -1 as a "triggered flag" and call the $+1$ measurement outcome a "clear flag".

In the remainder of this section, we analyze both deterministic and non-deterministic protocols for FT state preparation. Deterministic protocols, although they may contain measurement operations, always terminate with the data qubits prepared in the desired logical state in each individual protocol execution. They are designed to tolerate all possible faults of order $\mathcal{O}(p^1)$ (FT1). With non-deterministic protocols instead, a fraction of preparation runs is discarded when measurements of one or more flag qubits indicate that an erroneous state has been prepared. This cannot be foreseen a priori due to the stochastic nature of noise. Depending on whether the chosen protocol is deterministic or not, a flagged state is either corrected using an appropriate recovery operation, or is discarded. This recovery operation is chosen conditioned on triggered flags and is different from the look up table 6.1 used when flags are clear. Non-deterministic protocols typically exhibit lower logical failure rates as they contain fewer gates at the cost of repeatedly executing the circuit in case of triggered flags. On the other hand, deterministic protocols perform worse due to their larger

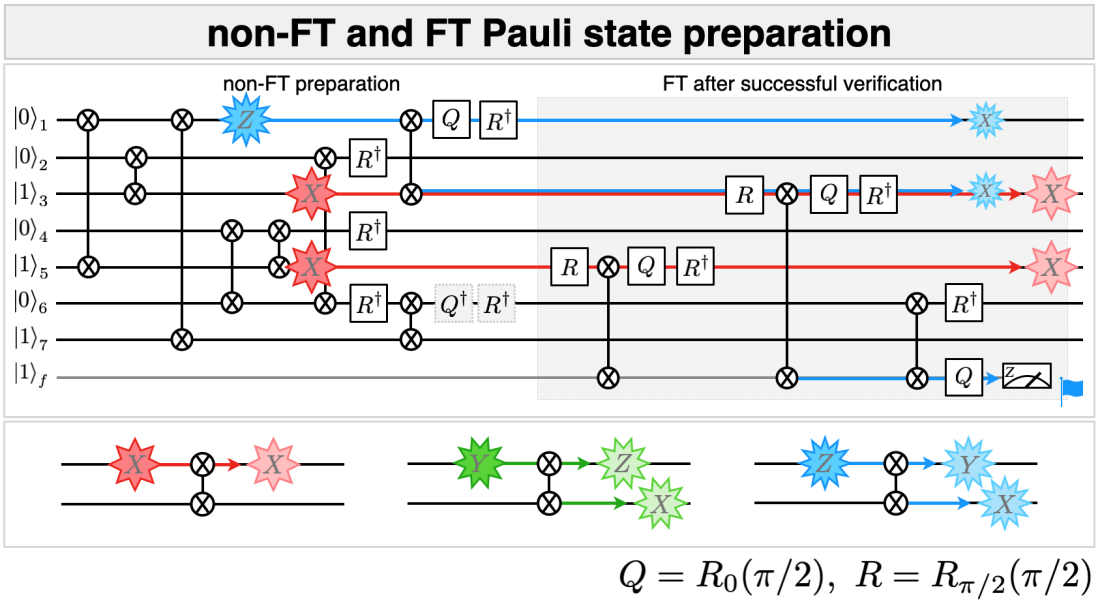

Figure 6.8: Pauli state preparation circuits. The logical zero state of the Steane code can be initialized using MS gates and single-qubit rotations about the X and Y axes. After the first block the $|0\rangle_L$ state is prepared non-fault-tolerantly (non-FT) on the data qubits 1 to 7. An example of a single Z_1 fault which can cause an uncorrectable error is shown as 12-cornered star (blue). The second block, shaded gray, couples to an additional flag qubit which heralds successful FT state preparation. The Z_1 will propagate and trigger the flag. When the flag qubit is clear, it is guaranteed that $|0\rangle_L$ is prepared up to a weight-1 error. Crosstalk faults, such as X_3X_5 (red 8-cornered stars), can devastate the FT property (cf. Section 6.1.1.5). Initialization of physical qubits as $|1\rangle$ is done by first initializing them as $|0\rangle$ and then performing an X rotation of angle π. The last two gates $Q^\dagger$ and $R^\dagger$ (shaded grey) of the first block are only needed for non-FT but not for FT state preparation. General propagation rules for Pauli faults through MS gates are shown in the lower panel.

qubit overhead or circuit depth. In the remainder of this section we theoretically investigate both types of protocols for Pauli and magic state preparation. For the non-deterministic preparation circuits used in the experiment [128], we provide a scaling analysis of their logical failure rates dependent on physical error parameters in order to estimate how much improvement of physical operations is needed to experimentally achieve lower infidelities than physical qubits.

6.1.1.4.1 *Non-deterministic state preparation*

In the following, we introduce and discuss circuits for non-deterministic FT state preparation for both Pauli and magic states. For both types of states we provide an evaluation of logical failure rate scaling with physical error parameters obtained via numerical simulations of the two different noise models described in Section 6.1.1.3.2. We assess the performance of FT protocols compared to physical qubit operations to estimate break-even points of FT advantage, i.e. identify for which physical error parameters the infidelity of logical states is lower than their respective physical qubit counterparts.

Logical Pauli states. The circuit shown in Figure 6.8 is used to prepare the $|0\rangle_L$ state which is the $+1$ eigenstate of the logical Z operator Z_L and also – as any code state – the

$+1$ eigenstate to all stabilizers including the generating plaquette operators in Figure 6.7 [110, 170]. The entangling MS gates prepare the plaquette eigenstates in an interleaved way which minimizes the number of gates. MS gates 1, 3 and 7 prepare K_2, MS gates 2, 6 and 8 are needed for preparation of K_3 and MS gates 4, 5 and 8 are involved in preparing K_1 (counting left to right and top to bottom) [201]. After executing the first block of the circuit, the state is prepared non-fault-tolerantly, meaning that single faults can still corrupt the $|0\rangle_L$ state, e.g. the fault Z_1 after the third MS gate would propagate to the uncorrectable error X_1X_3 at the end of the first block. Fault tolerance is achieved by running the second block which acts as verification. Here, the flag qubit couples to the data qubits, effectively measuring a weight-3 logical Z operator. This logical Z operator must be chosen such that any weight-2 error resulting from a single fault will trigger the flag. If the flag is triggered the state is discarded and another trial must be run until the flag is clear. The flag qubit measurement heralds uncorrectable errors such as the one caused by the aforementioned Z_1 fault. The error will propagate through the second MS gate of the verification block to $X_1X_3X_f$ so that the flag will be triggered.

Crosstalk is known to be a major source of failure in ion trap quantum computers as described in Section 6.1.1.3. The effect of crosstalk in general does not respect the FT circuit design principle [83, 172, 202]. As an example, consider the FT Pauli preparation circuit in Figure 6.8. Here, a X_3X_5 crosstalk fault can occur after the fifth MS gate under the noise channel in Eqn. 6.8. It will propagate through the circuit and cause an uncorrectable weight-2 X error on the data qubits without triggering the flag. This illustrates that even though logical failure rates of FT circuits are expected to scale quadratically, there exists a linear term in the expansion of p_L caused by dangerous crosstalk fault locations which will eventually destroy the advantageous scaling behavior (for more details on the microscopic crosstalk noise model and its fault operators see Appendix C.1).

After successfully preparing the logical zero state $|0\rangle_L$, any of the remaining five cardinal states on the Bloch sphere $|1\rangle_L$, $|+\rangle_L$, $|-\rangle_L$, $|+\mathrm{i}\rangle_L$ and $|-\mathrm{i}\rangle_L$ can be reached by subsequently applying the appropriate logical single-qubit rotation to $|0\rangle_L$. As all Clifford gates can be realized transversally and are thus FT in the Steane code, so is the full preparation procedure for any of the six Pauli states.

Logical magic state. It is known that Clifford gates are not sufficient to implement single-qubit rotations of an arbitrary angle on the Bloch sphere. Therefore, the Clifford gates alone cannot be used for universal quantum computation. In order to reach universality, the Solovay-Kitaev-theorem states that any point on the logical Bloch sphere can be reached with in principle arbitrary precision when a $\pi/4$-rotation about an arbitrarily-chosen axis is available [203, 204]. We choose to implement a logical T-gate as

$$T_L = \exp\left(-\mathrm{i}\frac{\pi}{8}Y_L\right) \tag{6.10}$$

a rotation about the Y axis because the corresponding magic state

$$|H\rangle_L = \cos\left(\frac{\pi}{8}\right)|0\rangle_L + \sin\left(\frac{\pi}{8}\right)|1\rangle_L . \tag{6.11}$$

is the $+1$ eigenstate to the logical Hadamard operator H_L. Thus, the logical magic state can be prepared by FT measurement of H_L which will project the data qubit state onto

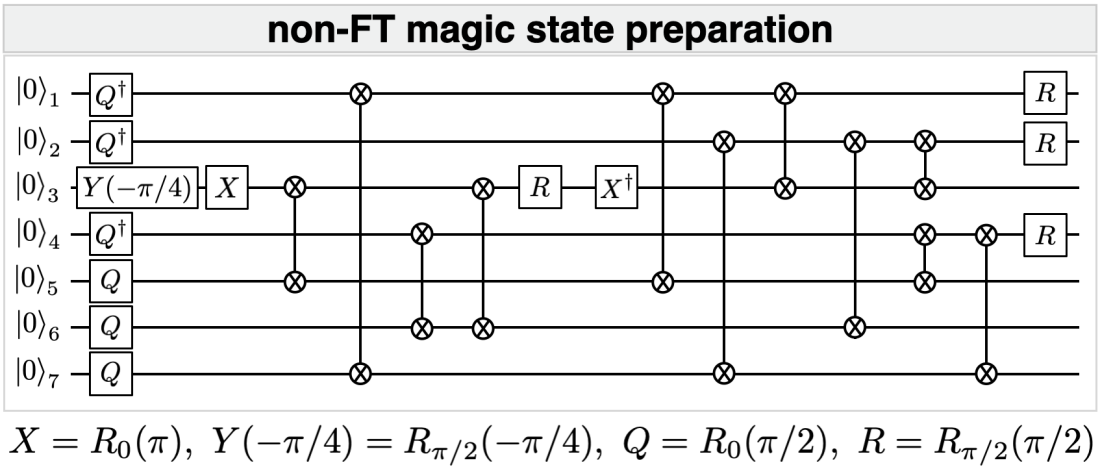

Figure 6.9: Non-FT magic state preparation circuit. The physical magic state is prepared on qubit 3 and then grown into the encoded $|H\rangle_L$ state of the Steane code. Hermitian-conjugate rotation operators amount to rotations in the respective opposite direction. For coherent rotation noise simulation, the direction of rotation affects the overall logical failure rate.

$|H\rangle_L$ if the measurement outcome is $+1$. When $|H\rangle_L$ is available, T_L can be implemented by magic state injection, which only requires Clifford gates [119]. Because all Clifford gates are transversal in the Steane code, preparing $|H\rangle_L$ fault-tolerantly with high fidelity is the crucial step for implementing the FT universal gate set.

The principle of repeat until success is also employed for magic state preparation in the non-deterministic protocol given by Ref. [119]. The circuit in Figure 6.9 prepares the magic state $|H\rangle_L$ non-fault-tolerantly, analogous to the first step of FT Pauli state preparation. Verification of the prepared state consists of two steps. First, the logical Hadamard operator is measured, which projects the data qubit state to the H_L axis. The flag circuit shown as part of the sequence in Figure 6.10 is used to measure H_L fault-tolerantly. Any dangerous fault which could occur on the measurement qubit in this block will trigger the flag. Transversality of H_L ensures that faults on single data qubits will not spread to higher-weight errors. The measurement qubit itself is also interpreted as a flag in this protocol so that a run that prepares the -1 eigenstate of H_L is discarded as well. Second, one round of FT parallel stabilizer readout, given in a CNOT version by Ref. [120], flags all other potentially dangerous faults. In this step, we measure X and Z stabilizers in an interleaved way, which is more resource-efficient because of its reduced number of 28 entangling gates compared to sequential stabilizer measurements (at least 48 entangling gates). Firstly two Z and one X stabilizer, K_2^X, K_1^Z and K_3^Z, are measured; then, in the second half, the remaining stabilizers K_2^Z, K_1^X and K_3^X are measured via one auxiliary qubit each. The auxiliary qubits are coupled to each other by four additional entangling gates. The interleaved arrangement of entangling gates used for each of the individual stabilizer measurements permits that the auxiliary qubits act simultaneously as both readout and flag qubits. This means that the circuit can be used for error detection: If an error is already present before running the circuit, the auxiliary qubits will indicate a non-trivial syndrome. If a dangerous fault happens during the circuit and it acts on an otherwise ideal input state, the auxiliary qubits act as flags and will be triggered. Thus the circuit can be used to verify that the logical qubit is in the $+1$ eigenstate of all stabilizers, without introducing additional faults if all flags are clear. All three blocks as shown in Figure 6.10 need to be run and the state is accepted only

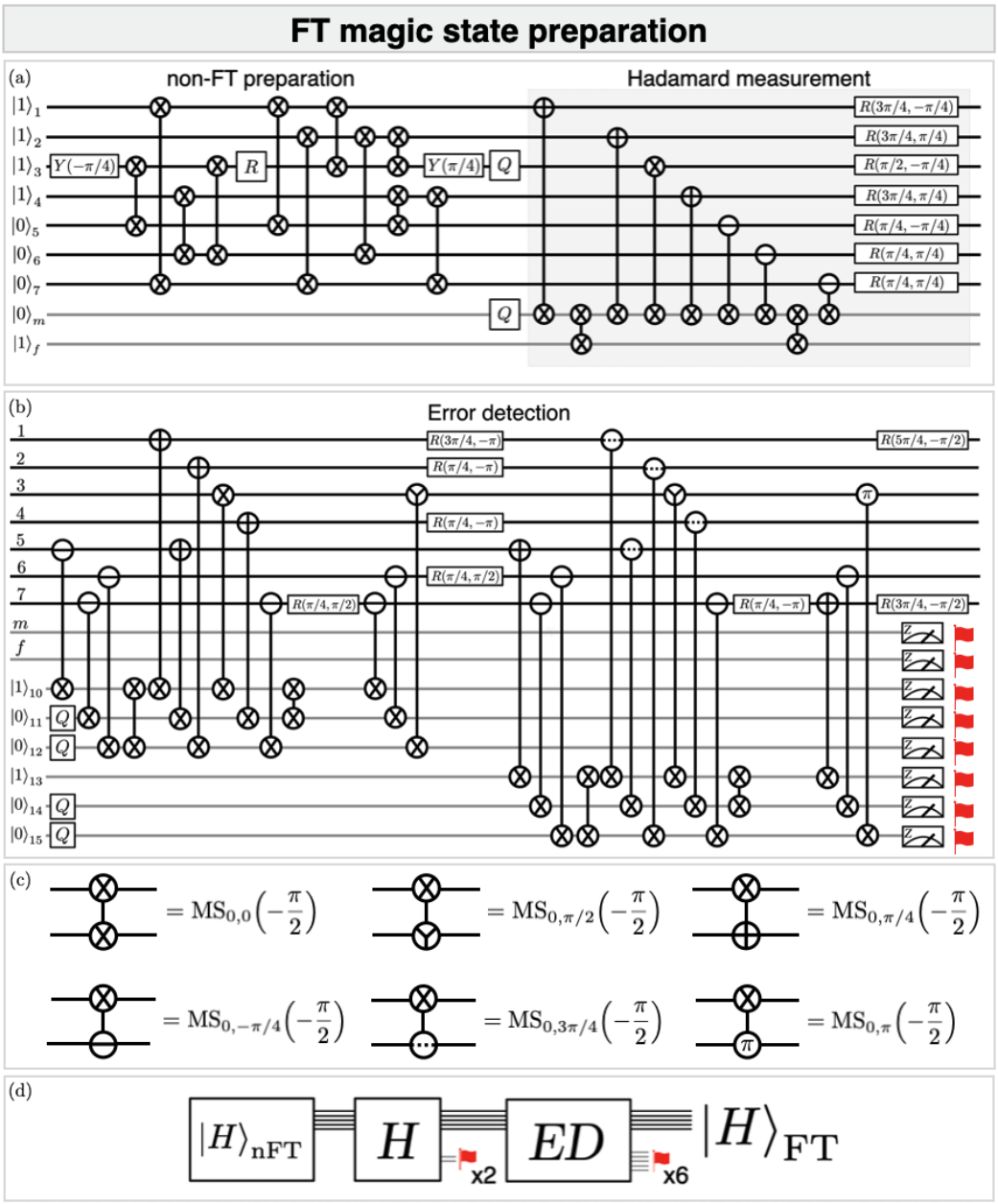

Figure 6.10: Fault-tolerant magic state preparation circuit. The logical magic state is prepared fault-tolerantly after executing all three circuit blocks. Single-qubit Z rotations are absorbed into phases of MS gates and single-qubit rotations*. (a) Non-FT magic state preparation is followed by a flag-FT measurement of the logical Hadamard operator. The flag qubits herald dangerous faults which may happen during preparation or measurement. Note that the single-qubit rotations in the non-FT preparation block differ from Figure 6.9 since they were optimized in conjunction with the subsequent Hadamard measurement block. (b) Flag-FT parallel syndrome readout circuit. Auxiliary qubits act as flags. If any flag is measured as -1 the state is discarded. (c) Phase-shifted MS gates with six different phases on their respective data qubit are used in the circuit (cf. Figure 6.2). (d) Sequence of logical building blocks of the FT magic state preparation protocol acting on data qubits and flag qubits.

* For an accepted state the single-qubit Z rotations $R_Z^{(1)}(-3\pi/4)R_Z^{(2)}(-3\pi/4)R_Z^{(3)}(-\pi)R_Z^{(4)}(-3\pi/4)R_Z^{(5)}(-3\pi/4)$ $R_Z^{(6)}(\pi/4)R_Z^{(7)}(-\pi/4)$ need to be applied (in software) to the data qubits 1 to 7.

if none of the eight flag qubits is triggered. The compiled version of this protocol into MS gate circuits contains single-qubit Z rotations and thus the phases φ_1, φ_2 of the MS gates $\mathrm{MS}_{\varphi_1,\varphi_2}(-\pi/2)$ and the phase φ of single-qubit rotations $R(\varphi, \theta)$ in Figure 6.10 are adjusted as described in Section 6.1.1.3.1 (also see Eqns. C.43 and C.44).

Scaling results. As illustrated above, the regime of advantageous FT implementation is to be found at low physical error rates due to its quadratic scaling behavior with physical error rate as compared to linear scaling of physical qubits or logical error rates of non-FT protocols. In order to demonstrate the capabilities of FT state preparation protocols to outperform non-FT implementations, we show the scaling of logical failure rates dependent on the set of physical error rates described above. We provide an easily accessible overall idea of scaling behavior, such that we can estimate the necessary improvements of trapped-ion operation fidelities, by introducing a single parameter λ to uniformly scale all physical error parameters as

$$\lambda \cdot (p_1, p_2, p_i, p_m, \dots). \tag{6.12}$$

Claiming FT advantage over physical qubits must be specifically justified for a given hardware implementation because in different experimental setups one encounters different physical phenomena, which realize the physical gate operations or even the physical qubit to begin with. One criterion to judge upon FT advantage, suggested in Ref. [164], is that the logical operation realized within a given hardware architecture should be compared to the corresponding physical operation as it could be realized in exactly that same hardware architecture. For the initialization of the logical qubit, we compare logical zero state preparation to the physical qubit initialization error rate and logical magic state preparation to first initializing the physical qubit to $|0\rangle$ followed by a physical Y rotation by an angle $\pi/4$, which is the most straightforward way to prepare the physical magic state $|H\rangle = T|0\rangle$. Here we opt to provide the said comparison with the same physical error parameters achieved in our ion trap setup for both the logical and corresponding physical operation.* Additionally to the, more rigorous, comparison of logical to physical operations, another break-even criterion is derived from comparing logical failure rates with the MS gate error rate p_2, as done previously e.g. in Refs. [205] and [206], since the overall noise in our experiment is dominated by the error rate p_2.†

Our definition of the logical failure rate $p_L(\lambda)$ is the logical infidelity $1 - F_L$. It reflects the probability to falsely conclude, by measurement of logical operators, that the desired state has been prepared correctly (up to correctable errors) when in fact the wrong logical information is output on the data qubits. The logical fidelity F_L is determined by the expectation value of the projector $P_{\pm O}$ onto the respective axis $O \in \{Z_L, H_L\}$ of the logical Bloch sphere

$$P_{\pm O} = \frac{I \pm O}{2} \tag{6.13}$$

* Another possibility is to compare to the best possible hardware implementation of the corresponding physical operation. In our ion trap even lower physical error rates could be achieved with smaller ion registers.

† Rigorous comparison with p_2 in the sense of Ref. [164] would require comparing a physical CNOT gate to an error-corrected logical CNOT gate. In our architecture we may realize the logical gate by seven transversal CNOT gates followed by a round of QEC on both logical qubits. We note that the logical error rate of this approach is dominated by the QEC block since it contains most of the procedure's entangling gates. As a consequence, the logical error rate of a QEC block serves as a proxy to the full logical CNOT gate error rate.

for the logical zero or the logical magic state respectively. For a single preparation of the $|0\rangle_L$ state, the expectation value $\langle P_{Z_L}\rangle$ after one round of ideal EC may only take the values 0 or 1. Dangerous X errors are either correctly recovered from or will result in a logical X operator after ideal EC ($\langle 0|1\rangle = 0,\ \langle 0|0\rangle = 1$). For the logical magic state, logical errors of all three Pauli types $X,\ Y$ and Z can be present on the state after ideal EC. A logical Y flip causes the output state to flip from the correct magic state $|H\rangle_L$ to the orthogonal -1 Hadamard eigenstate $|-H\rangle_L$ ($\langle H|Y|H\rangle = 0$). Logical X- and Z-flipped states still have finite overlap with $|H\rangle_L$ thus contributing a finite value to the logical infidelity ($\langle H|X|H\rangle = 1/\sqrt{2},\ \langle H|Z|H\rangle = 1/\sqrt{2}$). We discuss fidelity measures further in Section 6.1.1.6. For flag circuits, all preparation rounds, which trigger a flag and are thus discarded, do not contribute to the logical failure rate.

In Figure 6.11a we show the uniform scaling of all physical error parameters with the scaling parameter $\lambda \in [10^{-4}, 10^{1}]$ for the non-FT and FT Pauli state preparation compared to physical qubit parameters. The first is the rate $2p_i/3$ at which depolarizing noise of strength p_i causes failure of initializing a physical qubit to $|0\rangle$. The second is the MS gate error rate p_2. We observe that the FT preparation achieves lower logical failure rates than both the non-FT preparation and physical MS gate error rate for all values of λ. It is larger than the physical qubit initialization error rate for $\lambda \gtrsim 0.3$ and lower than the physical qubit initialization error rate for $\lambda \lesssim 0.3$. Within the interval $\lambda \in [10^{-1}, 10^{1}]$, i.e. with one order of magnitude stability around the experimentally achieved physical error parameters at $\lambda = 1$, the simulations with the four parameter depolarizing noise model quantitatively agree with the extended noise model. It is only at very low physical error parameters $\lambda \lesssim 10^{-1}$ that the extended noise simulation deviates from the depolarizing noise estimation. This is because crosstalk, which does not respect the FT properties of the circuit, becomes the dominant source of failure in this domain. The scaling becomes linear here with extended noise whereas the quadratic scaling of depolarizing noise continues for all $\lambda \to 0$. In this regime of low λ, we cannot rely on predictions made from the depolarizing noise model. In the experimentally accessible regime around $\lambda = 1$ the depolarizing noise prediction is as reliable as the extended noise model.

It is known from previous investigations of incoherent noise in general and crosstalk in particular that incoherent Pauli noise may underestimate logical failure rates [172, 207–209]. For the experimental error parameters at $\lambda = 1$ coherent overrotation noise on MS gates in the FT Pauli state preparation circuit causes an infidelity of $0.0116(7)$ which is larger than the incoherent depolarizing noise $0.0076(5)$ or an incoherent XX-overrotation channel $0.0082(6)$. When also adding coherent XX-type crosstalk, as given by Eqn. C.58, infidelity increases to $0.0141(7)$, while the experimentally measured value is 0.012^{+5}_{-4}.

The scaling behavior of the magic state preparation protocols, which we show with depolarizing and extended noise in Figure 6.11b, exhibits qualitatively similar features as the Pauli state preparation described above. In our setup, the physical qubit criterion of first initializing the qubit to $|0\rangle$ and then applying a physical T-gate is stricter than claiming to beat the MS gate error rate p_2 for our specific physical error parameter values. Both physical qubit criteria yield lower p_L than the non-FT circuit for all observed values of the uniform scaling parameter λ. Remarkably, the simulation data for the FT magic state preparation suggests that its logical failure rate p_L is lower than for both physical operations within the full λ-interval. In the regime of low physical error rates $\lambda \lesssim 0.03$ we find that the advantage of the FT implementation over both physical qubit criteria, i.e. the offset between the parallel

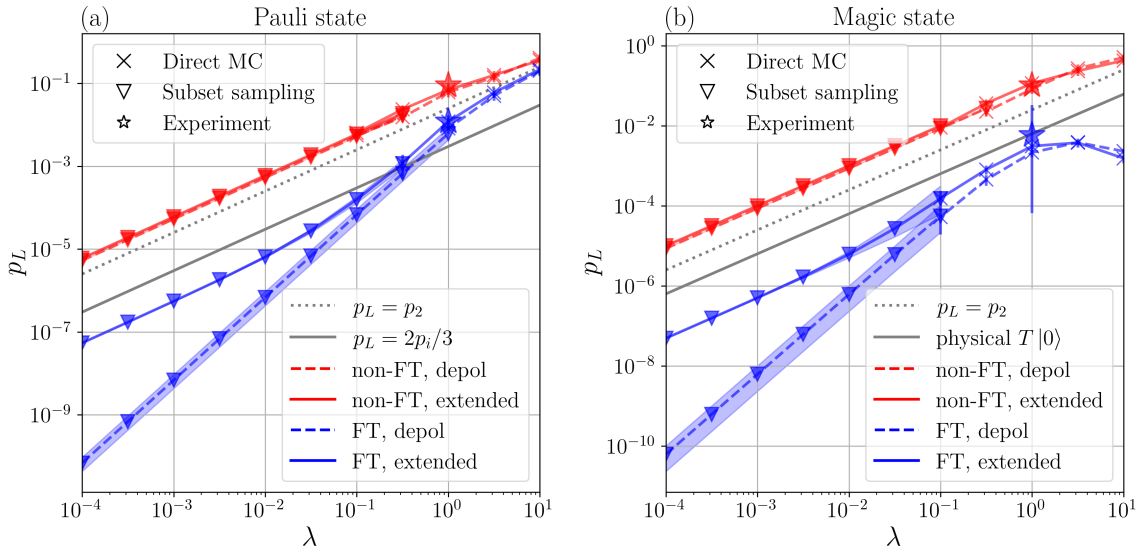

Figure 6.11: Logical state scaling. Uniform scaling with a factor λ of all physical error parameters in the non-FT and FT state preparation circuits alongside with parameters of physical qubits (both initialization – gray, dotted – and entangling operation – gray, solid). For numerical simulations, we employ direct MC (cross markers) and SS (triangle markers) with subsets up to $w_{\max} = 3$ in their preferential domain of physical error rates (see Appendix C.2 for a more detailed discussion). At the experimentally achieved rates $\lambda = 1$ (star marker) the models coincide in their prediction of logical failure rates within uncertainty intervals. (a) **Pauli state.** We compare the extended noise model containing idling and crosstalk (solid lines with markers) to depolarizing noise on single and two-qubit gates, initialization and measurements (dashed lines with markers). For each MC data point and subset failure rate we sample at least 100 times and until the uncertainty of the respective logical failure rate estimator is below a relative error of 0.5 but at most 10^4 times. (b) **Magic state.** Logical failure rates using the extended noise model and the depolarizing noise model are shown. We sample at least 100 times for each MC data point and subset failure rates of the non-FT circuits and the FT circuit with extended noise. For the FT circuit with depolarizing noise we use at least 1000 samples for each subset failure rate. We sample at most 10^4 times for the non-FT circuits and up to 10^5 times for the FT circuits or until a relative error of 0.3 for the FT circuit under depolarizing noise and 0.5 for the other cases is reached. The left-most MC data point of the FT depolarizing line is obtained from 2×10^5 samples. For FT preparation at $\lambda = 10^1$ the logical failure rate decreases again which is related to the fact that most runs are discarded.

lines, is of more than one order of magnitude. This implies that we surely beat the physical qubit criteria despite the destructive phase averaged crosstalk noise.

From the preceding analysis we conclude that the depolarizing noise model is well suited to predict experimentally measured logical infidelities. With future improvements of physical ion trap operations, more complex noise models should be taken into account. Only moderate experimental improvements, smaller than one order of magnitude, are needed in order to reach FT advantage over physical qubits judged by comparison with the corresponding physical qubit state preparations. We now move on to discuss deterministic protocols for FT state preparation.

6.1.1.4.2 *Deterministic state preparation*

The FT state preparation procedures discussed so far can be modified such that state preparation is deterministic, i.e. states never need to be discarded. If the acceptance rate of a non-deterministic protocol becomes too low, they might become experimentally unfeasible, e.g. due to cycle time constraints, although the fidelity of accepted states is high. With sufficiently low physical error parameters, the additional qubit and gate overhead that deterministic protocols require may not cause a severe increase of logical failure rates. The deterministic protocols for Pauli and magic state preparation, which we will discuss, make use of the fact that the flag has been triggered which limits the number of errors which can be present on the data qubits. The measurement information of the flag qubit is used to conditionally apply additional operator measurements. As long as all errors that are not stabilizer equivalent can be distinguished by those measurements, the combined flag and syndrome information can then be used to correct all errors that are caused by single faults in the circuit, thus preserving the FT property.

Logical Pauli state. In the following we lay out a new protocol for deterministic FT Pauli state preparation. The desired $|0\rangle_L$ state can still be recovered even when the flag is triggered instead of discarding the flagged state as in the non-deterministic case. While a single error is still tolerable, a weight-2 error leads to application of an erroneous recovery operation which causes logical failure when using the look up table decoder from Table 6.1. Instead, we may extend the look up table decoder to prioritize two-qubit recovery operations when the flag is triggered. These two-qubit errors make up the so-called flag error set. By exhaustively placing all single faults on the FT encoding circuit, we find that only two dangerous data qubit errors, namely X_1X_3 and X_4X_5, that are not stabilizer equivalent can propagate to the final data qubit state. For example, they can be caused respectively by faults Y_1X_3 on the last MS gate and Z_4X_5 on the fifth MS gate of the non-FT block in Figure 6.8 which also trigger the flag. All other resulting data qubit errors are, if not stabilizer equivalent to either X_1X_3 or X_4X_5, equivalent to a weight-1 error or a logical Z operator. The latter acts trivially on the logical zero state that is being prepared. Additionally, given that the flag is triggered, we find that the only weight-1 errors that can result on the data qubits from a single fault are X_3, X_5 and X_6.

The two dangerous errors X_1X_3 and X_4X_5 can be distinguished by measuring only two additional stabilizers. Their syndrome will not be confused with the syndromes of the single-qubit errors because the triggered flag restricts the number of errors that can occur. A pictorial illustration of the protocol with stabilizer measurement conditioned on the classical flag information is shown in Figure 6.12a. For the correction procedure, the look up table 6.2 can be applied.

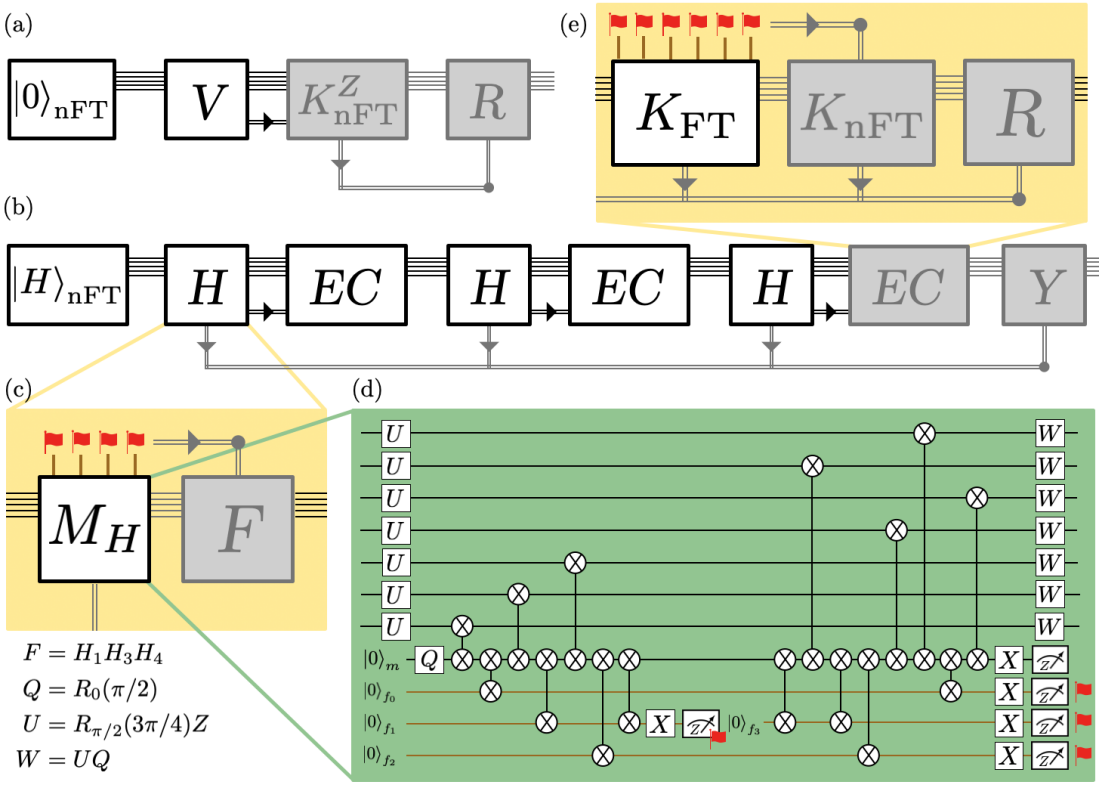

Figure 6.12: Deterministic FT state preparation. Schemes with logical building blocks acting on registers of data qubits and auxiliary qubits. Shaded blocks are only applied conditioned on classical measurement information. (a) $|0\rangle_L$: The non-FT encoding and verification blocks ($|0\rangle_{\mathrm{nFT}}$ and V, see Figure 6.8) are followed by additional measurements of Z stabilizers if the flag is triggered. Measuring with a single auxiliary qubit is sufficient to preserve the FT property of the scheme. A recovery operation R is applied according to the modified look up table 6.2 depending on how many stabilizers are measured (block K^Z_{nFT}). When the flag is clear no additional measurements and recovery are performed. (b) $|H\rangle_L$: Non-FT magic state preparation is followed by three repetitions of Hadamard measurement and FT EC. The last EC block is only executed if the third Hadamard measurement yields a non-trivial result. Finally, a logical Y flip (block Y) is applied to the data qubits if the Hadamard expectation value is measured as -1 in the second and the third round. (c) Four flag qubits are necessary to correct all dangerous errors that can happen during the Hadamard measurement. Our compiled MS gate circuit used to measure the logical Hadamard operator is shown in (d). If and only if the flag pattern $f_0, f_2, f_3 \in \{-+-, --+, ---\}$ the extra operation $F = H_1H_3H_4$ must be applied immediately after the Hadamard measurement to guarantee error distinguishability (see example in Appendix C.3). (e) If and only if the FT parallel syndrome readout (block K_{FT}, see Figure C.4) flags we proceed by measuring the syndrome with single auxiliary qubits (K_{nFT}, see Figure C.5). The recovery R is chosen from the Hadamard error set (Table C.1) when any flag of M_H is triggered. Otherwise, R is determined by the flag error set $\{X_3X_7, X_4X_6, Z_3Z_7, Z_4Z_6\}$ if a matching syndrome, $-++$ or $++-$ for X or Z stabilizers respectively, is measured, otherwise the standard Steane code look up table 6.1 is applied.

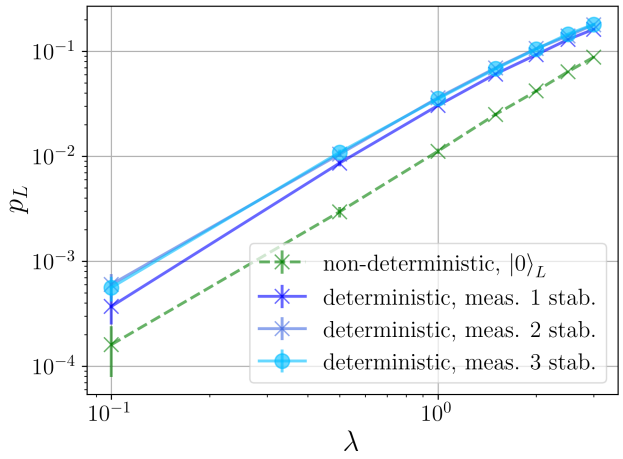

Figure 6.13: Deterministic Pauli state scaling. Uniform scaling under extended noise with a factor λ of all physical error rates for the FT flag preparation circuit of $|0\rangle_L$ and the deterministic extension where stabilizers are measured with single auxiliary qubits. For each of the 10^5 MC samples, the preparation is repeated until the flag qubit is clear. The non-deterministic circuit yields lower logical error rates then the deterministic procedure. Since both scale quadratically, there will not be a crossover point at lower λ. The lines for measuring two and three stabilizers lie on top of each other.

data qubit error	K_1^Z	K_2^Z, K_3^Z	R_2	K_{123}^Z	R_1
X_1X_3	$+$	$+-$	X_1X_3	$-$	X_7
X_4X_5	$+$	$-+$	X_4X_5	$-$	X_7
X_6X_7	$+$	$-+$	X_4X_5	$-$	X_7
X_6	$-$	$+-$	X_1X_3	$+$	I
X_5	$-$	$-+$	X_4X_5	$+$	I
X_3	$+$	$--$	X_3	$+$	I

Table 6.2: Modified look up table for deterministic Pauli state preparation. It is used instead of Table 6.1 if and only if the flag is triggered. All errors can be corrected, allowing for a residual weight-1 error, when measuring either the single stabilizer $K_{123}^Z = Z_1Z_2Z_4Z_7$ or the two stabilizers $K_2^Z = Z_1Z_3Z_5Z_7$ and $K_3^Z = Z_2Z_3Z_6Z_7$ or all three stabilizer generators, including $K_1^Z = Z_4Z_5Z_6Z_7$. The recovery R_1 is applied when only K_{123}^Z is measured. R_2 is the recovery operation when K_2^Z and K_3^Z are measured.

Applying the recovery $R_2 = X_4X_5$ when measuring the reduced syndrome $(K_2^Z, K_3^Z) = -+$ will not cause a logical failure because either the X_4X_5 error is corrected or the product of error and recovery will be $X_4X_5X_5$ in case the data qubit error was X_5. The result is the weight-1 error X_4 so FT is respected. From this example, we see that measuring K_1^Z is not necessary to correct the weight-2 errors. The same holds if the actual error is X_6X_7 since it is stabilizer equivalent to X_4X_5.

Moreover, we find that measuring only the stabilizer operator $K_{123}^Z = K_1^Z \times K_2^Z \times K_3^Z = Z_1Z_2Z_4Z_7$ is sufficient to neutralize the dangerous weight-2 errors. As shown in Table 6.2, its expectation value is $+1$ for the correctable weight-1 errors and -1 for both uncorrectable weight-2 errors. By applying the recovery operation $R_1 = X_7$, both errors X_1X_3 and X_6X_7 are turned into correctable weight-1 errors X_5 and X_6 respectively. Note that a single

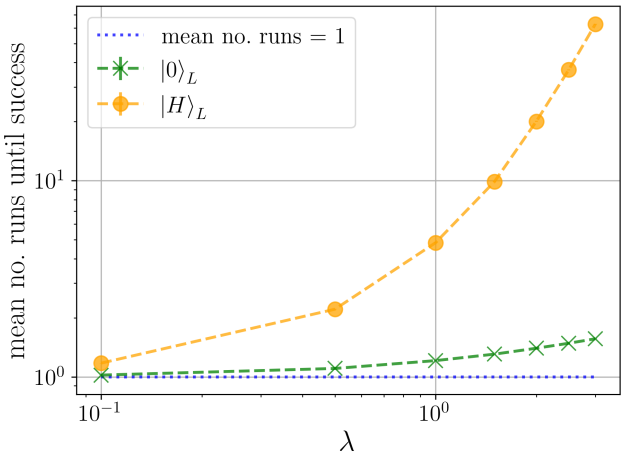

Figure 6.14: Repetition overhead for non-deterministic state preparation. Averaged number of repetitions until the prepared state is accepted, i.e. all flags measured as $+1$. Preparation of the magic state $|H\rangle_L$ on average needs more trials than the Pauli state $|0\rangle_L$. Deterministic state preparation schemes succeed after a single run by definition. Uncertainties on data points are smaller than the marker sizes.

auxiliary qubit is sufficient for syndrome readout since an additional fault happening in this step – on top of the fault that already happened to trigger the flag – would render the overall fault configuration to be of order p^2 so FT1 is not violated. The result of these additional measurements is a deterministic FT way to prepare the logical zero state of the Steane code. Given the flag has been triggered, we are able to correct all weight-2 errors possibly present on the data qubit state by measuring a reduced set of stabilizers*. Of course, it is also possible to measure all three stabilizer generators and by the full three-bit syndrome uniquely distinguish all weight-1 and weight-2 errors given in Table 6.2.

Analogously to the previous scaling analysis, we show the scaling behavior of the deterministic and non-deterministic FT Pauli state preparation in Figure 6.13. The uniform scaling parameter λ of all physical error parameters, including crosstalk, varies between 0.1 and 3. Both schemes scale quadratically in this interval due to their FT property. Nonetheless the non-deterministic scheme, where only non-flagged states are accepted, has a logical failure rate one order of magnitude lower than the deterministic schemes where either two or three stabilizer measurements are performed in case the flag is triggered. It is ensured that there cannot be another crossover point at lower values of λ since the vertical offset between the curves is determined by the coefficient of the quadratic term. Figure 6.14 shows the average number of times the non-deterministic preparation needs to be repeated until the state is accepted. While for the deterministic scheme this value is equal to one by construction, we see that for increasing $\lambda \in [0.1, 3]$ the mean number of necessary repetitions moderately grows from $1.020(1)$ to $1.563(6)$ which is feasible for experimental implementation. The number of repetitions translates to an increase of required entangling gates, shown in Figure 6.15, from approximately 11 to 17.2 for the non-deterministic protocol and from approximately 11 to 12.5 for the deterministic protocol on average. In case of a

* We note that the measurement of the flag qubit and the auxiliary qubit for K^Z_{123} can be avoided completely so that the state preparation circuit works deterministically without in-sequence measurements or feed-forward of measurement information by applying the R_1 recovery through a Toffoli gate controlled by the two auxiliary qubits. The FT property remains intact this way since the Toffoli only couples to a single data qubit.

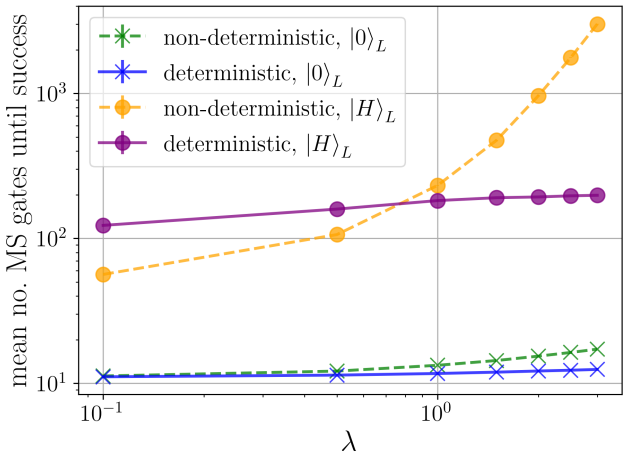

Figure 6.15: Entangling gate overhead for FT logical state preparation. Averaged number of entangling gates needed until the prepared state is accepted. For the non-deterministic protocols this amounts to all flags being clear. Deterministic protocols realize different circuit sequences depending on in-sequence measurement outcomes. The increase in average MS gate count is moderate for the deterministic protocols. For the non-deterministic FT magic state preparation the increase is over two orders of magnitude. It requires fewer MS gates on average than the deterministic FT magic state preparation protocol for $\lambda \lesssim 0.8$. Uncertainties on data points are smaller than the marker sizes.

triggered flag, the deterministic protocol will proceed with just the measurement of K^Z_{123}, requiring 4 additional MS gates, instead of repeating the preparation circuit with 11 MS gates.

We conclude that using the non-deterministic state preparation protocol is preferable in the examined range of λ and below since it yields logical failure rates one order of magnitude lower than the deterministic state preparation at the cost of a moderate number of repetitions, given that the necessary repetition times are permitted by other experimental constraints.

Logical magic state. The protocol for deterministic FT magic state preparation has been pointed out in Ref. [119]. We provide a compiled version into MS gates visualized in Figure 6.12b and discuss the expected performance for current and anticipated future trapped-ion physical error parameters.

After preparing the logical magic state non-fault-tolerantly, we measure the logical Hadamard operator three times, each involving the use of four flag qubits to distinguish all possible errors resulting from a fault triggering flags. The measurement circuit labeled M_H is shown in Figure 6.12c with the detailed MS compilation given in Figure 6.12d. For the flag patterns, i.e. combinations of flag qubit measurement outcomes, $f_0, f_2, f_3 \in \{-+-, --+, ---\}$ an additional operator $F = H_1 H_3 H_4$ must be applied to guarantee error distinguishability. Hadamard-type errors on four data qubits, which can arise from a single X fault on the measurement qubit of the circuit in Figure 6.12d, cannot be corrected using the six-bit syndrome if F were not applied. Triggered by the aforementioned flag patterns, F transforms a dangerous error into a lower weight error which can then be corrected by the subsequent EC block (see an explicit example in Appendix C.3).

After each Hadamard measurement, a full round of FT EC must be performed before the logical Hadamard can be measured again. The EC block, shown in Figure 6.12e consists of the flag-FT parallel readout circuit (K_{FT}) which we previously used to discard erroneous states

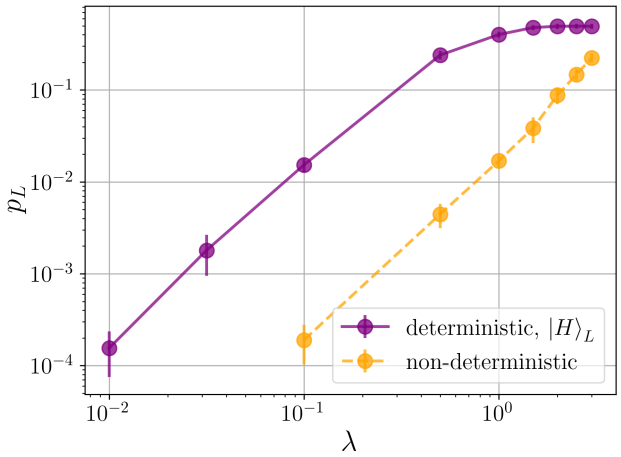

Figure 6.16: Deterministic magic state scaling. Comparison of deterministic and non-deterministic FT magic state preparation for physical error rates uniformly scaled with parameter λ. The significant overhead of the deterministic scheme leads to a logical failure rate approximately two orders of magnitude larger than for the non-deterministic scheme at low λ. For the deterministic scheme we use $(1000, 10^4, 10^5)$ samples for the data points at $(\lambda > 0.1,\ 0.01 < \lambda \leq 0.1,\ \lambda = 0.01)$. For the non-deterministic scheme we use $(1000, 10^4, 10^5)$ samples for the data points at $(\lambda > 1,\ 0.1 < \lambda \leq 1,\ \lambda = 0.1)$.

in the non-deterministic protocol. Now, it is followed by an additional block of syndrome readout with single auxiliary qubits (K_{nFT}, compiled with the CNOT decomposition of Figure 6.2c) in case any flag is triggered. If the flags of M_H are triggered and the syndrome is not trivial we apply a recovery operation according to the Hadamard look up table C.1 given in Appendix C.3. Here, the full six-bit syndrome is necessary to identify the correct recovery operation despite the CSS property of the Steane code. If all Hadamard flags are clear or the syndrome is not in the Hadamard look up table but the parallel readout circuit K_{FT} yields a triggered flag, we make use of the flag error set $\text{FES} = \{X_3X_7, X_4X_6, Z_3Z_7, Z_4Z_6\}$ to correct weight-2 errors of both X- and Z-type informed by the Z and X syndrome measured by K_{nFT} respectively. The flag error set is formed by all dangerous errors that can result from single faults in the K_{FT}-block that trigger a flag. If the syndromes measured by the two blocks K_{FT} and K_{nFT} agree, we apply the recovery from the standard look up table (Table 6.1). The third EC block can be omitted in case the third Hadamard measurement yields a $+1$ measurement outcome and no flags are triggered.

In the end, a logical Y_L-correction is applied dependent on the three Hadamard measurement outcomes. It is applied if the three consecutive Hadamard measurements are either $---$ or $+--$, otherwise no additional correction is applied. These corrections take into account logical operators that can arise from single faults in the non-FT preparation circuit (Figure 6.9) already. A detailed derivation is given in the Appendix of Ref. [119].

As for the logical zero state, we show the comparison of logical failure rates achieved by the deterministic and non-deterministic protocol over the uniform scaling range $\lambda \in [0.1, 3]$ and subjected to extended noise in Figure 6.16. While the non-deterministic scheme scales quadratically over the entire range of λ, the deterministic scheme just transitions towards quadratic scaling at low physical error parameters. For $\lambda \leq 1$ the advantage in logical failure rates of the non-deterministic over the deterministic scheme is as large as approximately two orders of magnitude. This is due to the gate overhead that the deterministic scheme

requires. On the other hand, employing the non-deterministic scheme demands a repetition overhead which we show in Figure 6.14. Although at low λ the mean number of repetitions until the FT magic state is accepted approaches 1, at scaling factors $\lambda = 1$ and $\lambda = 3$ we need approximately 5 and 63 repetitions on average respectively. From Figure 6.15, it is clear that the number of necessary MS gates also increases drastically through the repetition procedure. While the non-deterministic protocol requires only 56 MS gates at $\lambda = 0.1$ on average, the deterministic protocol uses on average approximately 113 MS gates at $\lambda = 0.1$ and 198 MS gates at $\lambda = 3$ due to more frequent flag events and thus more realizations of the full EC sequence. Due to the larger number of repetitions at $\lambda = 3$ the mean number of MS gates increases to a large value of approximately 3010. At $\lambda = 1$ the deterministic protocol requires approximately 182 MS gates on average; slightly less then the approximately 232 MS gates needed on average for the non-deterministic protocol.

The trade-off between deterministic and non-deterministic protocols includes on the one hand preparing the logical state with high fidelity while on the other hand also keeping acceptance rates high or equivalently keeping the required number of circuit repetitions sufficiently low. For the FT magic state preparation the trade-off between logical fidelity and gate overhead is more pronounced than for the Pauli state. In order to use the non-deterministic protocol in an experimental realization and benefit from its low logical failure rate, one must be able to tolerate the potentially large repetition overhead for the algorithm aimed to be performed. When the deterministic protocol is used, the runtime of a quantum algorithm can be bounded at the expense of the large gate overhead which deteriorates the resulting logical failure rate compared to the non-deterministic protocol.

For scale-up to multiple logical qubits, scheduling aspects may become relevant for the specific physical architecture at hand. Deterministic logical state preparation can be performed in parallel, if the experiment permits, and all logical states will be prepared after constant time. When L logical qubits are prepared non-deterministically, the waiting time until all logical qubits are verified is limited by the logical qubit which needs the most repetitions until accepted. On average, preparing the qubits non-deterministically is advantageous if the average number of repetitions (see Figure 6.14) for a given set of physical error parameters a_λ leads to a smaller total state preparation time $a_\lambda t_n < t_d$, assuming that a single trial takes time t_n, than using the deterministic scheme taking time t_d. Even if one is lacking parallel operation capabilities, the waiting time of the other $L - 1$ logical qubits – while one logical qubit is being prepared – does not need to be detrimental to the overall fidelity: An additional round of QEC can be performed on each logical qubit before feeding it into a subsequent logical building block. Moreover, it is not required with our protocols that successful state preparations coincide in time.

Suppose that we are capable of preparing L logical qubits, using the non-deterministic Pauli state preparation protocol, when we only need k accepted logical qubits in order to use them to run a quantum algorithm. With flag rate f, the number of logical qubits that are rejected due to flag events after a runs of the non-deterministic encoding circuit is Lf^a. As a consequence, the number of logical qubits L needed to accept k logical qubits on average at flag rate f after a trials is given by

$$k = L(1 - f^a) \tag{6.14}$$

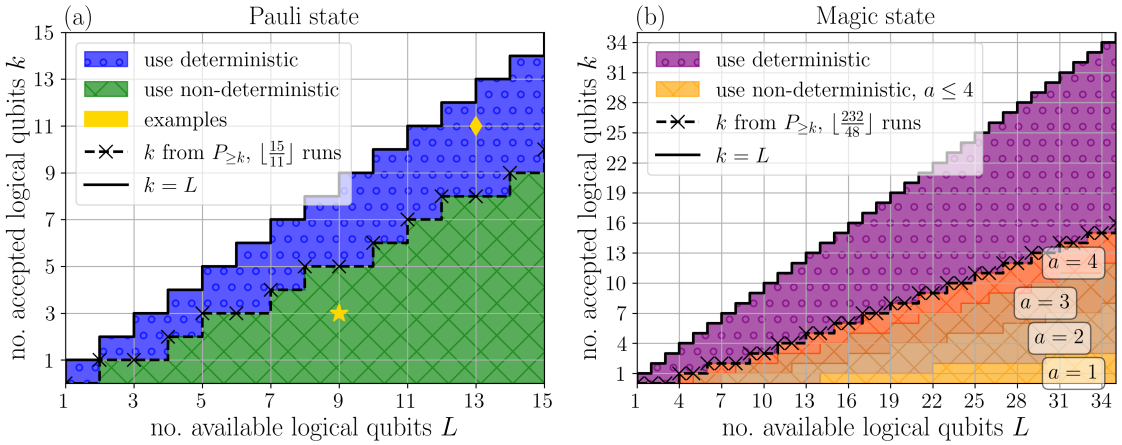

Figure 6.17: Preparation time advantage. Non-deterministic logical state preparation schemes (crosses) have a preparation time advantage over the deterministic schemes (small circles) as long as the number of entangling gates needed until k out of L logical qubits are accepted is lower than for the deterministic scheme. The deterministic schemes always prepare $k = L$ logical qubits (solid black lines). The boundaries between regimes of advantage of either scheme (dashed lines with crosses) are calculated at our respective flag rates at $\lambda = 1$ using Eqn. 6.19 with $P_{\geq k} \geq 95\%$ and $a = a^* = \lfloor t_d/t_n \rfloor$. In the region above this line using the deterministic scheme is advantageous since the non-deterministic scheme would take more MS gates for the same result of k logical qubits. (a) **Pauli state.** Running the non-deterministic scheme twice already takes 2×11 MS gates – more than the 15 MS gates needed for the deterministic scheme. Thus we compare the expected number of accepted logical qubits k at our flag rate $f = 0.17$ when L logical qubits can be prepared for one circuit run of either scheme. For example, to prepare at least 3 out of 9 logical qubits correctly the non-deterministic scheme is sufficient (star marker) while the deterministic scheme should be used if, e.g., at least 11 out of 13 logical qubits need to be accepted (diamond marker). (b) **Magic state.** At our flag rate $f = 0.8$, we can run the non-deterministic magic state preparation at most $\lfloor 232/48 \rfloor = 4$ times and stay below the number of entangling gates used by the deterministic scheme on average. Regions of accepted logical qubit number after 1, 2, 3 and 4 runs are shown in shades of orange.

and the number of runs a needed to accept k out of L logical qubits on average at flag rate f reads

$$a = \frac{\log(1 - k/L)}{\log f}. \tag{6.15}$$

Since all logical qubit preparations are independent from another, the probability $P_{\geq k}$ that at least k out of L logical qubits are prepared correctly after a runs is given by the cumulative binomial distribution with success probability $1 - f^a$

$$\begin{aligned} P_{\geq k} &= \sum_{j=k}^{L} \binom{L}{j} (1 - f^a)^j (f^a)^{L-j} && (6.16)\\ &= 1 - \sum_{j=0}^{k-1} \binom{L}{j} (1 - f^a)^j (f^a)^{L-j} && (6.17)\\ &= 1 - \sum_{j=0}^{k-1} B(L, j, 1 - f^a) && (6.18)\\ &= 1 - I_{f^a}(L - k + 1, k) && (6.19) \end{aligned}$$

where we use the regularized incomplete Beta function I [210, 211]. We can extract the number of necessary qubits L or the number of circuit runs a to obtain k accepted qubits with a desired probability $P_{\geq k}$ by numerical inspection of Eqn. 6.19.

It is advantageous to use the non-deterministic preparation procedure as long as after at most $a^* = \lfloor t_d/t_n \rfloor$ preparation attempts the number of accepted qubits k, either on average or with probability $P_{\geq k}$, is sufficient to perform the desired quantum algorithm. For our logical Pauli state preparation schemes, we have $t_d/t_n = 15/11 \approx 1.4$ when using the number of entangling gates as a proxy for the circuit execution time. So if more than a^* trials were needed, there would be no savings in the number of entangling gates over the deterministic scheme anymore. In Figure 6.17 we show the number of accepted logical qubits k given that L logical qubits can be prepared and highlight which of the two schemes is advantageous in terms of preparation time. While the deterministic scheme will always prepare $k = L$ logical qubits, Eqns. 6.14 and 6.19 provide the expected number on average or – here – with a 95% probability $P_{\geq k}$, which we show for the Pauli state at flag rate $f = 0.17$ in Figure 6.17a. For the logical magic state, the large number of MS gates used by the deterministic scheme on average at $\lambda = 1$ allows one to run up to 4 trials of the non-deterministic scheme since the fraction of entangling gates is $t_d/t_n = 232/48 \approx 4.8$. The expected number of accepted logical magic states after up to 4 runs is compared to the deterministic scheme in Figure 6.17b.

6.1.1.5 *Influence of entangling crosstalk on logical states*

We have seen in the previous discussion of FT circuits that crosstalk in general does not respect the FT property and thus can lead to linear scaling effects in the logical failure rates detrimental to the FT property of – otherwise – FT circuits. Crosstalk on single-qubit gates does not cause correlated faults but mere single-qubit faults on neighboring qubits. After entangling gates however, crosstalk fault operators of Pauli weight-2 can potentially

propagate to cause uncorrectable weight-2 errors at the end of the circuit. Preserving the quadratic scaling behavior in the logical failure rate is thus essential when aiming for advantage of FT circuits over their non-FT counterparts or physical qubits, which scale linearly. In this section we demonstrate that, for the FT Pauli preparation circuit, it is actually possible to find circuit implementations which show quadratic scaling of their logical failure rate and thus respect fault tolerance despite the presence of crosstalk. Our argument is derived from the CSS property of the Steane code.

As long as not more than a single fault occurs, accepted states from the FT Pauli state preparation circuit are guaranteed to be the correct $|0\rangle_L$ state up to a single correctable error. XX-type crosstalk on a target-neighbor location $t,\ n$ of an MS gate acting on target qubits t_1 and t_2 is described by the channel

$$\mathcal{E}_{\text{xct}}(\rho) = (1 - p_{\text{c}_2})\rho + p_{\text{c}_2} X_t X_n \rho X_t X_n. \tag{6.20}$$

In the presence of XX-type crosstalk fault tolerance can be uphold if all XX faults can be made to propagate to correctable errors at the end of the circuit.* Since the local rotations that stem from the CNOT decomposition into MS gates rotate X-fault operators on the control qubit to Z faults (see Figure 6.8), some of the resulting error operators may be correctable because a single Z and a single X error are correctable distinctly in the Steane code. An example of this effect can be seen for an X_2X_7 fault after the second MS gate in Figure 6.18 which becomes an Z_2X_7 error at the end of the circuit. The Steane code can correct Z_2 and X_7 independently. Consequentially, it is desirable to choose a qubit mapping of the FT encoding circuit that reduces the number of neighbor locations around the control qubits and allows for detection of dangerous crosstalk faults by the flag verification qubit. Robustness against crosstalk faults via optimal qubit mapping has been shown before by searching for Hamiltonian paths in a qubit mapping graph for a comparative code study with realistic ion trap noise [190].

We distinguish these types of circuits by calling them *crosstalk-resistant (CTR)* and *non-CTR*. Qubit indices can be relabeled to obtain a CTR circuit for FT preparation of the $|0\rangle_L$ state using MS gates as given in Figure 6.18. After relabeling, the new stabilizers have support on qubits $(1, 4, 6, 7)$, $(2, 5, 6, 7)$ and $(3, 4, 5, 7)$. The X_3X_5 crosstalk fault after the fifth MS gate, discussed as an example in Section 6.1.1.4, will now trigger the flag as opposed to the non-CTR circuit in Figure 6.8 so that the output state with the dangerous error $Z_3X_5X_7$ will be discarded. A CTR circuit for FT magic state preparation was not found.

In Figure 6.19 we present the CTR property of the Pauli circuit and compare its logical failure rate to the non-deterministic, non-CTR FT Pauli state preparation from Figure 6.11a. Extended noise is applied to both circuits. While, as before, there is no visible distinction between logical failure rates in an interval of approximately $\lambda \in [10^{-1}, 10^{1}]$, the non-CTR circuit transits from quadratic scaling to a linear scaling for $\lambda \lesssim 10^{-2}$ because crosstalk destroys the FT property. The CTR circuit continues to scale quadratically for all $\lambda \to 0$ under the influence of XX-type crosstalk on MS gates. XX-type crosstalk is only a valid description of the actual physical processes if crosstalk phases are zero on all ions.

We have shown in Figure 6.6 that in reality the crosstalk phases, although constant over time, vary over a large range of angles. To take this fact into account, we replace the XX-type

* Note that $\mathcal{E}_{\text{xct}}$ is a special case of Eqn. C.50 with all phases equal to zero. The incoherent error probability is shifted $p_{\text{c}_2} \to 4p_{\text{c}_2}$ for crosstalk locations which involve common neighbor ions. Also see Appendix C.1 for a more detailed discussion.

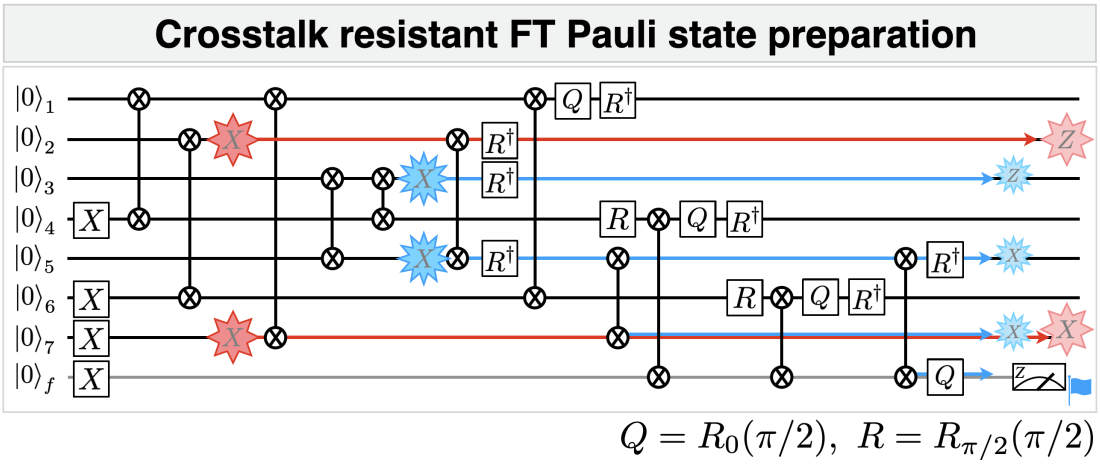

Figure 6.18: Crosstalk-resistant FT Pauli state preparation. There is no single XX-type fault placed at any crosstalk location which causes an output state with X error of weight greater than one and does not also trigger the flag. The Steane code is capable of correcting a weight-1 X and Z error each. XX-faults are prevented by local rotations from resulting in a weight-2 error. An example of such a fault on the second MS gate is depicted by the red 8-cornered stars. The resulting two weight-1 errors are Z_2 and X_7. The previously (Figure 6.8) dangerous X_3X_5 fault after the fifth MS gate (blue 12-cornered stars) now triggers the flag.

crosstalk $\mathcal{E}_{\text{xct}}$ by the phase averaged crosstalk channel (Eqn. 6.8, derived in Appendix C.1) which applies fault operators XX, XY, YX and YY with equal probability to each crosstalk location. In Figure 6.19 we show the scaling behavior for the same two circuits under the influence of the phase averaged crosstalk channel. Not only is the logical failure rate larger than for XX-type crosstalk alone. Now both the non-CTR and CTR circuit scale linearly at low λ because the XY- and YY-type crosstalk faults can cause logical failures. The distinction between the two circuits is barely visible anymore. However, at $\lambda = 1$ all four circuit models agree with the experimentally measured value of logical infidelity.

To conclude this section, we note that the existence of the CTR Pauli encoding circuit is a special case which does not generalize to arbitrary quantum circuits. While fundamentally valid, the CTR characteristic cannot be upheld in our experimental setting since crosstalk phases will always mix the different X- and Y-type contributions even if they are constant over long times. As a consequence, it can not be guaranteed that the quadratic scaling behavior of FT circuits in the presence of crosstalk does actually lead to an advantage over physical qubits; minimization of crosstalk in physical operations is imperative.

6.1.1.6 *Quantum state fidelity of logical qubits*

While the logical fidelity is a good quantity to assess the degree of successful state preparation as a measure of operational performance in QEC, in this section we assess the quantum state of the logical qubit in a more general way by calculating its *quantum state fidelity* [45].

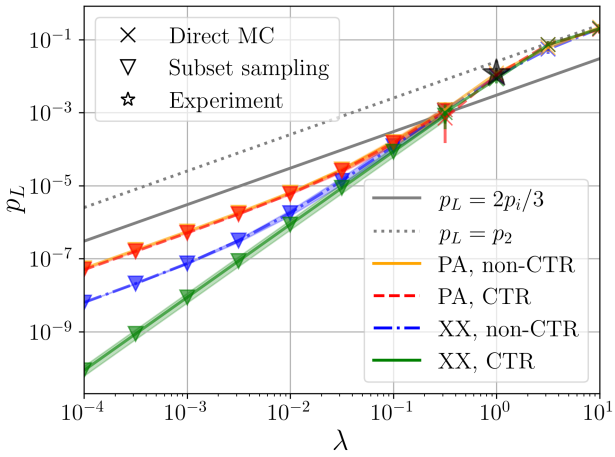

Figure 6.19: Crosstalk-resistant Pauli state scaling. Uniform scaling with a factor λ of all physical error parameters under XX-type crosstalk (XX) and phase averaged crosstalk (PA) in the FT Pauli state preparation circuit with an XX-crosstalk-resistant (CTR) and non-crosstalk-resistant (non-CTR) qubit mapping. Lines for the two state preparations with PA overlap. For numerical simulations, we employ direct MC (cross markers) and SS (triangle markers) in their preferential domain of physical error rates. The experimentally measured value (star marker) lies at $\lambda = 1$. In this regime of physical error rates, all four curves coincide within their confidence intervals. At lower values of λ crosstalk becomes a dominant source of failure causing linear scaling if CTR does not hold. Error rates of physical operations are shown for comparison (gray lines without markers) as in Figure 6.11. For each MC data point and subset failure rate we sample at least 100 times or until the uncertainty of the respective logical failure rate estimator is below a relative error of 0.5 but at most 10^4 times. All subsets up to $w_{\max} = 3$ are taken into account for SS.

The quantum state fidelity of a stabilizer state is defined as the mean of expectation values of all operators that form the stabilizer group W_k

$$\mathcal{F}(\rho_t, \rho) = \frac{1}{128}\sum_{k=1}^{128}\langle W_k\rangle \tag{6.21}$$

with a target state $\rho_t = |t\rangle\langle t|$ and $\rho = |\psi\rangle\langle\psi|$ a stabilizer state such that $W_k|\psi\rangle = \pm|\psi\rangle$. The stabilizer group of the Steane code contains $128 = 2^7$ stabilizer operators and is generated by the stabilizer generators in Eqn. 6.9 that define the logical qubit. The code space population p_{CS} is defined analogously but only involves averaging over the 64 code space stabilizer expectation values

$$p_{\text{CS}} = \frac{1}{64}\sum_{k=1}^{64}\langle W_k\rangle \tag{6.22}$$

and contains no logical operators which would fix the logical state within the code space [37]. More detail on the derivation of the quantum state fidelity of stabilizer states is given in Appendix C.4.

Since the largest physical error rate in our model is the infidelity of the MS gate, we expect the MS gate dynamics to dominantly influence the quantum state fidelity and, as a consequence, the logical failure rate. Thus, in the following, we compare the quantum state fidelity for noisy logical qubit preparation using depolarizing noise versus incoherent overrotation noise on MS gates. The MS gate is a rotation about the two-qubit XX axis and it would thus be consistent to model MS gate noise by the overrotation channel given by Eqn. C.62. The depolarizing noise channel is often used instead due to its general, hardware-agnostic structure but by introducing faults of all Pauli types it might overestimate the effect of MS gate errors compared to overrotations. It was previously expected that overrotation is the more accurate noise model [189].

The table below shows values for the quantum state fidelity $\mathcal{F}$ and code space population p_{CS} with 95% confidence intervals of a single logical qubit in the $|0\rangle_L$ state prepared by the FT circuit in Figure 6.8.

noise	$\mathcal{F}$	p_{CS}
depolarizing	82.63(3)%	82.62(4)%
overrotation	86.18(3)%	86.20(4)%
experiment	82.7(11)%	83.1(15)%

In Figure 6.20 we compare experimental data to numerical simulations with the depolarizing noise model as described before for a single logical qubit with MS gate errors modeled as either depolarizing or overrotation noise. For each of the stabilizer operators we determine the deviation $\sqrt{(\langle S_i\rangle_{\text{exp}} - \langle S_i\rangle_{\text{sim}})^2}$ of the simulated expectation value $\langle S_i\rangle_{\text{sim}}$ with both noise models to the experimentally measured expectation value $\langle S_i\rangle_{\text{exp}}$. We observe that the distribution of deviations is very similar for both noise channels. While most stabilizer expectation values deviate little from the experimental values, individual stabilizer expectation value deviations can be as high as approximately 20% for depolarizing

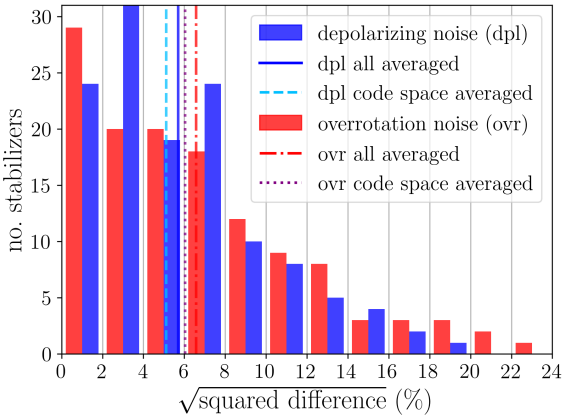

Figure 6.20: Stabilizer estimation under different MS noise models. Distributions for depolarizing (blue) and overrotation (red) noise models of the deviation $\sqrt{(\langle S_i\rangle_{\text{exp}} - \langle S_i\rangle_{\text{sim}})^2}$ of all 128 stabilizer expectation values of the logical qubit in simulation to experiment. Each bin has a width of 2%. Mean values which correspond to quantum state fidelities and code space population for both noise models are indicated as vertical lines and deviate from experimental values by approximately 6%. Individual stabilizer expectation value estimates differ to up to 24%. All simulation data is generated by direct MC sampling until 10^5 states are accepted. Each stabilizer has been measured 100 times in the experiment.

noise and 24% for overrotation noise. The averaged deviations (RMS) for all 64 or 128 expectation values, i.e. for the code space population and quantum state fidelity respectively, are $6.0(15)\%$ and $6.6(11)\%$ with overrotation noise but for depolarizing noise yield the lower values of $5.1(15)\%$ and $5.7(11)\%$.

It is evident that incoherent overrotation noise does not provide a more accurate description of MS gate errors than depolarizing noise for the circuits used in our experiment. Respecting the FT property of the state preparation circuit on the logical level appears to be the more relevant characteristic of noise than its microscopic structure. This is in stark contrast to the detrimental effect that crosstalk can exert when it does not respect fault tolerance. The effect of crosstalk strongly depends on the microscopic structure which differs between the XX-type and phase average model discussed in the previous section. We stress that the logical fidelity is an appropriate quantity to compare the agreement of experimental data to noise simulations and that computing the full quantum state fidelity does not provide additional information about the QEC procedure.

6.1.1.7 *Conclusions & Outlook*

We provided a detailed numerical study and analysis of future potential for FT universal gate set implementations. Incoherent Pauli noise simulations suggest that reaching thresholds of FT advantage over physical qubits need improvements on physical error rates of less than an order of magnitude. Currently the logical error rate is limited predominantly by entangling gate errors in the experimental setup under consideration in this work. Crosstalk on MS gates is not a substantial source of error for the advantage of FT over non-FT circuit implementation in our ion trap architecture at current noise levels. However, we give a crosstalk resistant qubit mapping for FT Pauli state preparation which keeps scaling quadratically under XX-type crosstalk as physical error rates are scaled to zero opposed

to the usual circuits where crosstalk typically breaks the FT property. We showed that the microscopic structure of crosstalk affects the scaling of logical error rates.

Therefore choosing a different set of physical gates could also make available crosstalk resistant circuits for the realization of other logical building blocks. Furthermore, crosstalk errors could be suppressed by utilizing inherently crosstalk insensitive gate operations like composite pulses [212, 213], or active suppression schemes, where additional laser fields are applied to the qubit register that destructively interfere with unwanted leakage light at neighboring ion positions. Exploiting the fact that for each ion a global phase can be freely chosen might allow for crosstalk resistant qubit mappings even in the case of random but constant crosstalk phases. However, this method does not provide enough degrees of freedom to directly control the effective crosstalk phase for both neighbors of all qubits in the register. Further investigations are needed to clarify if crosstalk resistant mappings for various logical building blocks can be found using this technique.

Also, we have found that deterministic state preparation schemes for Pauli and magic state preparation do not outperform non-deterministic ones at current physical error rates and are not expected to do so even with improvements on physical error rates due to their larger gate count. The repetition overhead needed for non-deterministic state preparation is moderate for both the Pauli and magic state at current noise levels.

Our analysis validates depolarizing noise as an appropriate effective model for FT logical state preparation in the ion trap system from Ref. [84]. Flag circuits are recognized as a promising paradigm to reach the break-even point where FT circuits will outperform physical qubits [39]. Not only is the depolarizing noise model sufficient to predict logical failure rates but also the average over stabilizer expectation values for a single logical qubit initialized to its logical zero state. Individual stabilizer expectation values can be estimated to about 24% relative uncertainty. The detailed crosstalk investigation provided in this work illustrates the value of considering aspects specific to the physical architecture realizing the quantum computer. We point out that for long protocols with deep circuits such as the deterministic FT magic state preparation scheme, coherent errors might build up and cause an additional source of logical failure. The effect of coherent noise to the logical failure rate of such circuits is a subject for further studies.

In the future, effective noise models for different quantum computing architectures and logical building blocks will aid in the characterization of FT universal quantum computers. Simulating large distance logical qubits can help to better understand relevant error processes and facilitate practical realization of error-corrected logical qubit operations below the pseudothreshold.

Data availability

The data underlying the findings of this work are available at https://doi.org/10.5281/zenodo.7565571.

Code availability

All codes used for data analysis are available from the corresponding author upon reasonable request.

Author contributions

S.H. performed the numerical simulations and analyzed the data. S.H., M.R. and M.M. performed characterization and theory modeling. L.P. and I.P. carried out the experiments. L.P., I.P., C.D.M., P.S. and T.M. contributed to the experimental setup. S.H., L.P. and M.R. wrote the manuscript, with contributions from all authors. T.M., P.S. and M.M. supervised the project.

Acknowledgements

We gratefully acknowledge support by the EU Quantum Technology Flagship grant under Grant Agreement No. 820495 (AQTION), the US Army Research Office through grant number W911NF-21-1-0007, the European Union's Horizon Europe research and innovation program under Grant Agreement No. 101046968 (BRISQ), the ERC Starting Grant QCosmo under Grant No. 948893, the ERC Starting Grant QNets through Grant Number 804247, the Austrian Science Fund under Project No. F7109 (SFB BeyondC), the Austrian Research Promotion Agency under Contracts No. 896213 (ITAQC) and by the Office of the Director of National Intelligence (ODNI), Intelligence Advanced Research Projects Activity (IARPA), via the U.S. Army Research Office through Grant No. W911NF-16-1-0070. This research is also part of the Munich Quantum Valley (K-8), which is supported by the Bavarian state government with funds from the Hightech Agenda Bayern Plus. We further receive support from the IQI GMBH. The views and conclusions contained herein are those of the authors and should not be interpreted as necessarily representing the official policies or endorsements, either expressed or implied, of the ODNI, IARPA, or the US Government. The US Government is authorized to reproduce and distribute reprints for Governmental purposes notwithstanding any copyright annotation thereon. Any opinions, findings, and conclusions or recommendations expressed in this material are those of the author(s) and do not necessarily reflect the view of the US Army Research Office. S.H. would like to thank Josias Old for valuable discussions on deterministic preparation circuits. S.H. acknowledges funding by the Deutsche Forschungsgemeinschaft (DFG, German Research Foundation) under Germany's Excellence Strategy 'Cluster of Excellence Matter and Light for Quantum Computing (ML4Q) EXC 2004/1' 390534769. The numerical simulations were performed with the aid of computing resources at Forschungszentrum Jülich.

6.2 Spatial correlations in idling noise

In Section 3.3, erroneous idling was modeled as an independent dephasing process for each spectator qubit. This dephasing is caused by the interaction of a qubit with its environment. In the setup considered in this thesis, the dominant contribution to idling errors is dephasing caused by magnetic field fluctuations originating from the environment surrounding the apparatus. The distance from the noise source to the qubit register and the wavelength of the noise are large compared to the length scale of the qubit register. Thus, it is quite conceivable that different qubits in the register are subject to similar disturbances introduced by the fluctuating magnetic field. The assumption that noise processes on different qubits are independent from each other does not hold in this case, but instead the dephasing processes along the ion chain are correlated.

6.2.1 *Quantum error correction under correlated noise*

A QEC code with a distance d can correct all errors with a weight of up to $t = \lfloor \frac{d-1}{2} \rfloor$. Now the question is whether the occurrence rate of error configurations exceeding the weight t depends on the spatial correlation properties of the noise acting on the physical qubits encoding a logical qubit. In other words: Can two error processes, that are indistinguishable when looking only at a single qubit but differ when considering the effect on multiple qubits, lead to different failure rates of a logical qubit?

To answer this question, let us consider dephasing of an idling logical qubit encoded in the Steane code. The logical state $|+\rangle_{\mathrm{L}}$ is prepared noiselessly using the circuit from Figure 4.6a followed by a transversal logical operation. Subsequently, dephasing is simulated by applying Z rotations with a rotation angle $\theta^{(i)}$ to each individual qubit i. Simplistically assuming that the magnetic field fluctuation is a white noise process the rotation angles for different realization of the simulation are distributed according to a Lorentz distribution with the probability density function

$$f(\theta, \gamma) = \frac{1}{\pi\gamma \left[1 + \left(\frac{\theta}{\gamma}\right)^2\right]}. \tag{6.23}$$

For uncorrelated noise, the rotation angle is sampled independently for each qubit from the Lorentz distribution, whereas in the case of correlated noise, the same rotation angle $\theta^{(i)} = \theta$ is chosen for all qubits. Finally, an error-free measurement in the X basis is performed on all seven qubits. This allows one to calculate the expectation values of the X-type stabilizer generators and the logical X operator. An ideal round of EC is applied by multiplying the logical X expectation value by -1 if any of the stabilizer generator expectation values is -1. The error introduced by the noisy idling process is correctable if the outcome of the logical X measurement is $+1$ after EC. Figure 6.21 shows the probability of a $+1$-outcome p_{+1} for different noise magnitudes γ obtained from a numerical simulation. For small noise magnitudes, correlated noise yields significantly lower success probabilities. In this regime, even the scaling of the success probability with regard to the noise magnitude differs for the different noise models.

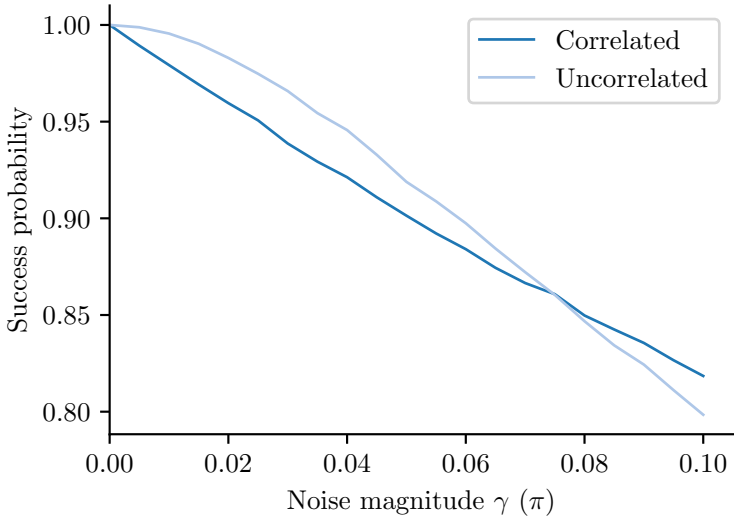

Figure 6.21: Numerical simulation of the probability of recovering the correct logical state for a logical qubit encoded in the Steane code exposed to idling noise. A logical qubit is prepared noiselessly in $|+\rangle_{\mathrm{L}}$ before being exposed to correlated or uncorrelated dephasing noise. The probability of obtaining a measurement outcome of $+1$ for the logical X operator averaged over 100000 noise realizations is plotted against the noise magnitude γ.

This simplified toy model only considering perfectly correlated and perfectly uncorrelated dephasing noise already shows that the presence of spatial correlations in noise processes heavily affects the performance of QEC protocols. Disregarding correlation effects in the design of error models can lead to underestimating the logical failure probability, especially in a regime where the correlated noise process is the dominant error source. Given the impact of correlations on QEC, it is not surprising that a few years after the proposal of the first QEC codes, the effect of spatial correlations of noise on large-scale quantum computation was already studied. It was shown that long-range spatial correlations can compromise the performance of QEC or even render FT quantum computation unfeasible [214–220]. However, adapting the utilized QEC codes can recover the performance of QEC to a large extent [214, 217, 220].

6.2.2 *Quantifying spatial correlations of quantum dynamics*

Considering the effect spatial correlations have on the operation of an FT quantum information processor, it is crucial to have protocols at hand that allow one to characterize the magnitude and distance-dependence of correlations in noise dynamics. In Ref [183] a measure $\bar{I}$ quantifying spatial correlations in quantum dynamics is proposed. The construction and properties of this measure are discussed in the following.

Let us consider a quantum process, e.g., a spatially correlated noise process, acting on a composite system $\mathrm{S} = \mathrm{A} \otimes \mathrm{B}$ consisting of subsystems A and B. The process one wants to characterize in terms of spatial correlations can be described as a completely positive and trace-preserving map $\mathcal{E}_{\mathrm{S}}$. Without loss of generality, it is assumed that the Hilbert spaces associated with the subsystems A and B both have dimension d. Hence, the dimension of the Hilbert space of the combined system S is d^2. A cornerstone in the construction of the measure $\bar{I}$ is the Choi-Jamiołkowski isomorphism [221, 222], which provides a one-to-one

mapping between a quantum map $\mathcal{E}_\mathrm{S}$ and a quantum state in an extended Hilbert space with dimension d^4. The considered system S is extended by an auxiliary system $S' = A'B'$ of the same dimension. The state [183]

$$|\Phi^+\rangle = \frac{1}{d}\sum_{i=0}^{d^2-1} |i\rangle_\mathrm{S} \otimes |i\rangle_{\mathrm{S}'} \tag{6.24}$$

is a maximally entangled state between the systems S and S′. Here, $|i\rangle$ denotes the i-th state of the consecutively numbered computational basis $\{|0\rangle, ..., |d^2 - 1\rangle\}$*. Applying $\mathcal{E}_\mathrm{S}$ to the subsystem S after the preparation of the maximally entangled state yields the density matrix of the Choi-Jamiołkowski state [183]

$$\rho_S^\mathrm{CJ} = \mathcal{E}_\mathrm{S} \otimes \mathbb{1}_{\mathrm{S}'} \left(|\Phi^+\rangle \langle\Phi^+|\right). \tag{6.25}$$

Note that it is not required to implement the auxiliary system S′ physically to determine $\rho_\mathrm{S}^\mathrm{CJ}$ experimentally. Instead the dynamics $\mathcal{E}_\mathrm{S}$ can be fully characterized by quantum process tomography [45] on the system S and $\rho_\mathrm{S}^\mathrm{CJ}$ can be determined in classical post-processing.

This detour via the Choi-Jamiołkowski isomorphism allows for the transfer of the tools available for the characterization of quantum states to quantum dynamics. If the dynamics $\mathcal{E}_\mathrm{S}$ with respect to the subsystems A and B is uncorrelated, then the state $\rho_\mathrm{S}^\mathrm{CJ}$ is uncorrelated with respect to AA′ and BB′. Similar to the quantum mutual information [45] characterizing correlations in quantum states, a measure for spatial correlations in quantum dynamics can then be defined as [183]

$$\bar{I}(\mathcal{E}_\mathrm{S}) = \frac{1}{4\log_\mathrm{e} d}\left[S\left(\rho_\mathrm{S}^\mathrm{CJ}|_{\mathrm{AA}'}\right) + S\left(\rho_\mathrm{S}^\mathrm{CJ}|_{\mathrm{BB}'}\right) - S\left(\rho_\mathrm{S}^\mathrm{CJ}\right)\right], \tag{6.26}$$

where $S(\cdot) = -[(\cdot)\log_\mathrm{e}(\cdot)]$ is the von Neumann entropy, and $\rho_\mathrm{S}^\mathrm{CJ}|_{\mathrm{AA}'} = \mathrm{Tr}_{\mathrm{BB}'}(\rho_\mathrm{S}^\mathrm{CJ})$ and $\rho_\mathrm{S}^\mathrm{CJ}|_{\mathrm{BB}'} = \mathrm{Tr}_{\mathrm{AA}'}(\rho_\mathrm{S}^\mathrm{CJ})$ denote the partial traces of the Choi-Jamiołkowski state with respect to the partitions BB′ and AA′, respectively.

The spatial correlation measure $\bar{I}(\mathcal{E}_\mathrm{S})$ fulfills the following criteria [183]:

1. A process $\mathcal{E}_\mathrm{S}$ is called uncorrelated if it can be decomposed as $\mathcal{E}_\mathrm{S} = \mathcal{E}_\mathrm{A} \otimes \mathcal{E}_\mathrm{B}$. The measure $\bar{I}(\mathcal{E}_\mathrm{S}) = 0$ if and only if such a decomposition is possible.
2. The measure $\bar{I}(\mathcal{E}_\mathrm{S}) \in [0, 1]$ is bounded.
3. For uncorrelated unitary maps $\mathcal{L}_\mathrm{A}(\cdot) = U_\mathrm{A}(\cdot)U_\mathrm{A}^\dagger$, $\mathcal{L}_\mathrm{B}(\cdot) = U_\mathrm{B}(\cdot)U_\mathrm{B}^\dagger$, $\mathcal{R}_\mathrm{A}(\cdot) = V_\mathrm{A}(\cdot)V_\mathrm{A}^\dagger$, and $\mathcal{R}_\mathrm{B}(\cdot) = V_\mathrm{B}(\cdot)V_\mathrm{B}^\dagger$ the inequality

$$\bar{I}(\mathcal{E}_\mathrm{S}) \geq \bar{I}\left[(\mathcal{L}_\mathrm{A} \otimes \mathcal{L}_\mathrm{B})\,\mathcal{E}_\mathrm{S}\,(\mathcal{R}_\mathrm{A} \otimes \mathcal{R}_\mathrm{B})\right] \tag{6.27}$$

holds. This means that composing a map $\mathcal{E}_\mathrm{S}$ with uncorrelated unitary maps cannot increase the measure $\bar{I}(\mathcal{E}_\mathrm{S})$.

* Note the italic typesetting here. For a two-qubit system, the numbered computational basis states read $|0\rangle = |0\rangle \otimes |0\rangle$, $|1\rangle = |1\rangle \otimes |0\rangle$, $|2\rangle = |0\rangle \otimes |1\rangle$ and $|3\rangle = |1\rangle \otimes |1\rangle$.

The measure allows for the certification of the presence of spatial correlations in idling dynamics and facilitates determining their distance dependence. In case the measure suggests the presence of correlations potentially impairing the implementation of QEC protocols, an error model and methods for estimating its parameters tailored to the correlated idling noise of the specific device have to be developed. Note that it is not clear how this measure can directly be used to inform more elaborate error models for idling processes in quantum information processors.

6.2.3 *Publication: Experimental quantification of spatial correlations in quantum dynamics*

Experimental quantification of spatial correlations in quantum dynamics*

Quantum **2**, 90 (2018)

Lukas Postler†[1], Ángel Rivas†[2,3], Philipp Schindler[1], Alexander Erhard[1], Roman Stricker[1], Daniel Nigg[1], Thomas Monz[1], Rainer Blatt[1,4], and Markus Müller[5]

[1]Institut für Experimentalphysik, Universität Innsbruck, Technikerstr. 25, A-6020 Innsbruck, Austria
[2]Departamento de Física Teórica I, Universidad Complutense, 28040 Madrid, Spain
[3]CCS-Center for Computational Simulation, Campus de Montegancedo UPM, 28660 Boadilla del Monte, Madrid, Spain
[4]Institut für Quantenoptik und Quanteninformation, Österreichische Akademie der Wissenschaften, Otto-Hittmair-Platz 1, A-6020 Innsbruck, Austria
[5]Department of Physics, College of Science, Swansea University, Singleton Park, Swansea - SA2 8PP, United Kingdom

Correlations between different partitions of quantum systems play a central role in a variety of many-body quantum systems, and they have been studied exhaustively in experimental and theoretical research. Here, we investigate *dynamical* correlations in the time evolution of multiple parts of a composite quantum system. A rigorous measure to quantify correlations in quantum dynamics based on a full tomographic reconstruction of the quantum process has been introduced recently [Á. Rivas et al., New Journal of Physics, 17(6) 062001 (2015).]. In this work, we derive a lower bound for this correlation measure, which does not require full knowledge of the quantum dynamics. Furthermore, we also extend the correlation measure to multipartite systems. We directly apply the developed methods to a trapped ion quantum information processor to experimentally characterize the correlations in quantum dynamics for two- and four-qubit systems. The method proposed and demonstrated in this work is scalable, platform-independent and applicable to other composite quantum systems and QIP architectures. We apply the method to estimate spatial correlations in environmental noise processes, which are crucial for the performance of QEC procedures.

* The author of the present thesis carried out the experiments and wrote the manuscript. Daniel Nigg carried out preliminary experiments and discussed them in his PhD thesis [223]. Here, the accepted version of the manuscript is printed in a slightly amended form for consistency throughout the thesis. Changes include adapting hyphenation and abbreviations and updating references that were only available as preprints at the time of publication.

† These authors contributed equally to this work.

6.2.3.1 *Introduction*

Correlations play a central role in quantum physics. A wide range of quantum effects including apparently disconnected topics, such as Bell inequalities or quantum phase transitions, can be analyzed by considering correlations. In most of the cases these correlations refer to those shared between different parties of a multipartite quantum state, i.e. describing the statistics of a system's observables at a given time. These correlations, both classical and quantum, have been extensively studied, quantified, and classified (see for instance [224–226]). A different kind of correlations, subject of less attention, are dynamical correlations. These account for the fact that the dynamics of one part of a system may not be statistically independent from the dynamics of the other parts. Dynamical correlations in quantum systems are the basis of many phenomena ranging from super-radiance [227] over super-decoherence [228] to sub-radiance [229] in atomic gases. Furthermore, the study of dynamical correlations is of central importance in various research areas, such as e.g. photosynthesis and excitation transfer dynamics [230–235], driven-dissipative phase transitions [236–240] and quantum metrology [241].

In the context of quantum information, the treatment of spatial correlations is highly important, but usually limited to the extreme cases of either completely uncorrelated noise with an independent noise source for each qubit, or completely correlated noise modeled by a single noise source with equal strength on all qubits [242]. One consequence of the latter type of correlations are decoherence free subspaces (DFSs) [243–247], which can be exploited in QIP to extend the storage time of quantum states in noisy systems. Understanding and quantifying these dynamical correlations is highly relevant for the performance of QEC protocols [242], as correlated errors can undermine the FT operation of quantum error correcting procedures [42]. Here, theory studies focusing on *spatially* correlated noise [214–220] have shown that in particular the distance-dependence of correlated noise can be crucial as to whether or not modified versions of the threshold theorem [35, 42] do hold. It is crucial that not only the noise strength is below a critical value, but also that (unwanted) interactions between qubits decay sufficiently quickly with increasing distance. In order to assess whether or not these conditions are met in experimental quantum processors, theoretically well-founded and practically applicable methods to characterize the *strength* as well as the *distance-dependence* of spatial correlations are required. Such tools become particularly important in scalable QIP architectures: There, it is forseeable that the noise environment will not be fully correlated in processors consisting of multiple smaller units that are interconnected by quantum channels. Noisy connection channels may introduce spatial correlations in the system's dynamics. Similar considerations apply in distributed quantum systems that are interconnected by flying qubits.

Recently, we proposed and explored a measure to rigorously quantify dynamical correlations [183]. Inspired by the metrics that can be employed to quantify the amount of correlations within quantum states, a method to quantify dynamical correlations from tomographic data was proposed with the following features:

1. It is a normalized quantity that is zero if and only if the dynamics are uncorrelated. In particular, it is constructed in terms of an information measure and does not rely on any assumptions or a priori knowledge of the underlying dynamics.

2. The quantifier introduces a hierarchy of quantum dynamics by enforcing a partial order relation between dynamics, i.e. a way to quantitatively compare whether one

bipartite dynamic is more or less correlated (with respect to the evolution of its parts) than another. This partial ordering is known as a *fundamental law of a resource theory* [224, 248–254]. This law states that the amount of correlations of some given dynamics cannot increase by adding uncorrelated dynamics to it, i.e. a process for the quantifier equals zero. This ordering property for the amount of dynamical correlations is analogous to the fundamental law in the resource theory of entanglement [224, 226]. There, it refers to the fact that entanglement cannot increase under application of local operations and classical communication (LOCC).

3. The measure establishes a rigorous theoretical framework that allows for a definition and the study of *maximally correlated dynamics* and the properties that such dynamics need to fulfill [183]. Again, the concept of maximally correlated dynamics is analogous to the one of maximally entangled states in the resource theory of entanglement.

Whereas the proposed quantifier for dynamical correlations [183] allows one to study correlated dynamics in a variety of contexts, its general applicability comes at the price of requiring full knowledge of the quantum dynamics. Experimentally, this requires quantum process tomography of the full system which is only feasible in small-scale systems, and has been experimentally demonstrated for up to three qubits [255], and quickly becomes impractical for quantum systems of larger size. Within this work, we therefore derive a efficiently measurable lower bound of the quantifier applicable also to larger systems.

By applying the quantifier to a two-qubit trapped-ion quantum information processor the amount of correlations is extracted from a reconstructed process matrix. Furthermore, the quantifier's lower bound is determined for dynamics in systems consisting of four trapped-ion qubits. We investigate in detail the noise dynamics and its correlations for different physical encodings of the qubits that lead to different correlation characteristics. Our findings underline the importance of experimentally informed choices of qubit encodings in the presence of spatially correlated noise in the context of quantum computing and QEC.

The presented work is structured as follows: In Section 6.2.3.2 we introduce and review the correlation measure proposed in [183]. We present the derivation of a lower bound of the measure in Section 6.2.3.3, followed by a generalization to multipartite systems in Section 6.2.3.4. Finally, we present an investigation of noise dynamics in a trapped-ion system in Section 6.2.3.5.

6.2.3.2 *Measure for Spatial Correlations in Quantum Dynamics*

In the following we review the correlation measure suggested in [183], which is based on the Choi-Jamiołkowski isomorphism [221, 222], providing a one-to-one mapping of the *dynamics* in a quantum system to a quantum *state* of a larger system. The mathematical construction underlying the isomorphism can be summarized as follows: consider a bipartite system $\mathrm{S} = \mathrm{S}_1 \otimes \mathrm{S}_2$, as shown in Figure 6.22. Then, the idea is to initially prepare a pair of maximally entangled states $|\psi^+\rangle = \frac{1}{\sqrt{d}} \sum_{k=0}^{d-1} |kk\rangle$ between every part S_1 and S_2 with two respective ancilla systems S_1' and S_2' of the same dimension,

$$|\Phi_{\mathrm{SS}'}\rangle \equiv |\psi^+\rangle_{\mathrm{S}_1\mathrm{S}_1'} |\psi^+\rangle_{\mathrm{S}_2\mathrm{S}_2'} = \frac{1}{d} \sum_{k=0}^{d-1} |kk\rangle \sum_{l=0}^{d-1} |ll\rangle \,, \tag{6.28}$$

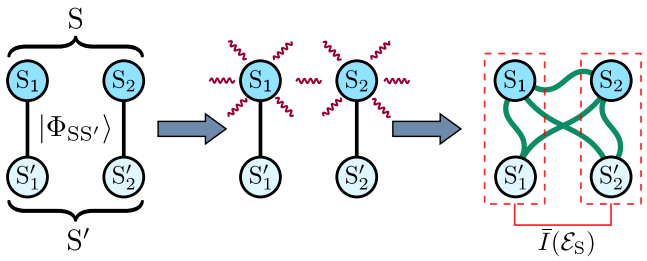

Figure 6.22: Schematic illustration of the measurement of $\bar{I}$ in a composite system S. At the beginning of the protocol subsystems S_1 and S_2 are maximally entangled with S'_1 and S'_2, respectively. The dynamics of interest is subsequently acting on S and leaves the whole system in a product state or a correlated state with respect to $\mathrm{S}_1\mathrm{S}'_1|\mathrm{S}_2\mathrm{S}'_2$ depending on the amount of correlations in the dynamics.

where d is the dimension of the subsystems S_1 and S_2, assumed to be the same for both of them for simplicity. Then the part $\mathrm{S} = \mathrm{S}_1 \otimes \mathrm{S}_2$ of the state $|\Phi_{\mathrm{SS}'}\rangle$ evolves according to a dynamical process that is given by the map $\mathcal{E}_\mathrm{S}$, and which leaves the part $\mathrm{S}' = \mathrm{S}'_1 \otimes \mathrm{S}'_2$ unperturbed. After the evolution, the final Choi-Jamiołkowski state $\rho_\mathrm{S}^\mathrm{CJ} = \mathcal{E}_\mathrm{S} \otimes \mathbb{1}_{\mathrm{S}'_1\mathrm{S}'_2}(|\Phi_{\mathrm{SS}'}\rangle\langle\Phi_{\mathrm{SS}'}|)$ is a product state with respect to the bipartition $\mathrm{S}_1\mathrm{S}'_1|\mathrm{S}_2\mathrm{S}'_2$, $\rho_\mathrm{S}^\mathrm{CJ} = \rho_{\mathrm{S}_1\mathrm{S}'_1} \otimes \rho_{\mathrm{S}_2\mathrm{S}'_2}$, if and only if the dynamics are uncorrelated, $\mathcal{E}_\mathrm{S} = \mathcal{E}_{\mathrm{S}_1} \otimes \mathcal{E}_{\mathrm{S}_2}$. This result follows from the one-to-one correspondence between the map $\mathcal{E}_\mathrm{S}$ and $\rho_\mathrm{S}^\mathrm{CJ}$. In contrast, if the process on the composite system is correlated, then the resulting state $\rho_\mathrm{S}^\mathrm{CJ}$ is correlated as well. A quantifier $\bar{I}$ which suitably reflects the amount of correlations in $\rho_\mathrm{S}^\mathrm{CJ}$ and thus in the process $\mathcal{E}_\mathrm{S}$ is the quantum mutual information [45], given by the following definition:

$$\bar{I}(\mathcal{E}_\mathrm{S}) := \frac{1}{4\log d}\left[S\left(\rho_\mathrm{S}^\mathrm{CJ}|_{\mathrm{S}_1\mathrm{S}'_1}\right) + S\left(\rho_\mathrm{S}^\mathrm{CJ}|_{\mathrm{S}_2\mathrm{S}'_2}\right) - S(\rho_\mathrm{S}^\mathrm{CJ})\right], \tag{6.29}$$

with $S(\cdot) = -\operatorname{Tr}[(\cdot)\log(\cdot)]$ the von Neumann entropy evaluated for $\rho_\mathrm{S}^\mathrm{CJ}$ and the reduced density operators $\rho_\mathrm{S}^\mathrm{CJ}|_{\mathrm{S}_1\mathrm{S}'_1} := \operatorname{Tr}_{\mathrm{S}_2\mathrm{S}'_2}\left(\rho_\mathrm{S}^\mathrm{CJ}\right)$ and $\rho_\mathrm{S}^\mathrm{CJ}|_{\mathrm{S}_2\mathrm{S}'_2} := \operatorname{Tr}_{\mathrm{S}_1\mathrm{S}'_1}\left(\rho_\mathrm{S}^\mathrm{CJ}\right)$.

Leaving aside the normalization factor $\frac{1}{4\log d}$, this quantifier can be intuitively understood as the amount of information that is needed to distinguish the actual dynamics $\mathcal{E}_\mathrm{S}$ from the individual dynamics of its parts $\mathcal{E}_{\mathrm{S}_1} \otimes \mathcal{E}_{\mathrm{S}_2}$ [256]. Namely, the information that is lost when $\mathcal{E}_{\mathrm{S}_1} \otimes \mathcal{E}_{\mathrm{S}_2}$ is taken as an approximation of $\mathcal{E}_\mathrm{S}$. The normalized quantity $\bar{I} \in [0, 1]$ quantifies this information relative to the maximum value it can take on all possible processes.

Furthermore, $\bar{I}$ fulfills the equation

$$\bar{I}\left[(\mathcal{L}_{\mathrm{S}_1} \otimes \mathcal{L}_{\mathrm{S}_2})(\mathcal{E}_\mathrm{S})(\mathcal{R}_{\mathrm{S}_1} \otimes \mathcal{R}_{\mathrm{S}_2})\right] \leq \bar{I}(\mathcal{E}_\mathrm{S}) \tag{6.30}$$

for all local dynamical maps $\mathcal{L}_{\mathrm{S}_1}$, $\mathcal{L}_{\mathrm{S}_2}$, $\mathcal{R}_{\mathrm{S}_1}$, and $\mathcal{R}_{\mathrm{S}_2}$ that might act before and after the actual, possibly correlated dynamics $\mathcal{E}_\mathrm{S}$ [183]. Equation 6.30 states that the amount of correlations of the dynamics $\mathcal{E}_\mathrm{S}$ cannot increase by composition with uncorrelated maps. In other words, if a process is a composition of a correlated and an uncorrelated part, the amount of correlations in the composition has to be equal or smaller than the amount of correlation that is inherent to the correlated part. In fact, this is the fundamental law of the resource theory of correlated dynamics [183], where the correlations are considered as a resource, and the operations which do not increase the amount of this resource are uncorrelated maps.

For clarity, we remark that the use of an ancilla system S' is underlying the mathematical construction of the isomorphism, but is not required in an experimental determination of $\bar{I}$. Rather than reconstructing the Choi-Jamiołkowski state $\rho_{\mathrm{S}}^{\mathrm{CJ}}$ from quantum state tomography on the enlarged system SS', one can equivalently determine $\rho_{\mathrm{S}}^{\mathrm{CJ}}$ by reconstructing the dynamics $\mathcal{E}_{\mathrm{S}}$ by means of quantum process tomography on the physical system S [257]. Due to the Choi-Jamiołkowski isomorphism in both cases the number of real parameters to determine ($4^N(4^N-1)$) is the same and grows exponentially with the number of qubits. In the following sections we therefore provide alternative strategies to estimate $\bar{I}$ avoiding full tomography.

6.2.3.3 *Lower Bound to $\bar{I}$*

A lower estimate for $\bar{I}$ can be obtained by performing correlation measurements on the subsystems S_1 and S_2. Our central result is that the normalized quantity $\bar{I}(\mathcal{E}_{\mathrm{S}})$ is lower bounded by

$$\bar{I}(\mathcal{E}_{\mathrm{S}}) \geq \frac{1}{8\ln d}\frac{C_{\rho'}^2(X_1,X_2)}{\|X_1\|^2\|X_2\|^2}, \tag{6.31}$$

with two local quantum observables X_1 and X_2 and $C_{\rho'}(X_1,X_2) = \langle X_1 \otimes X_2\rangle_{\rho'} - \langle X_1\rangle_{\rho'}\langle X_2\rangle_{\rho'}$. $\rho' = \mathcal{E}_{\mathrm{S}}(\rho)$ is the evolution of an initial product state ρ according to the dynamical map $\mathcal{E}_{\mathrm{S}}$. Here $\|\cdot\|$ denotes the operator norm (the absolute value of the maximum eigenvalue) and we have taken the logarithms inside $\bar{I}(\mathcal{E}_{\mathrm{S}})$ in Eqn. 6.29 to be binary logarithms $\log_2$ (otherwise the natural logarithm $\ln d$ on the right hand side becomes multiplied by a different factor).

In order to prove Eqn. 6.31, we use the relation between the mutual information and the quantum relative entropy $I(\rho_{\mathrm{AB}}) = S(\rho_{\mathrm{AB}}\|\rho_{\mathrm{A}}\otimes\rho_{\mathrm{B}})$ [258], so that by taking the bipartition $\mathrm{A} = \mathrm{S}_1\mathrm{S}_1'$ and $\mathrm{B} = \mathrm{S}_2\mathrm{S}_2'$, we rewrite Eqn. 6.29 as

$$\bar{I}(\mathcal{E}_{\mathrm{S}}) = \frac{1}{4\log_2 d} S\Big(\rho_{\mathrm{S}}^{\mathrm{CJ}}\Big\|\rho_{\mathrm{S}}^{\mathrm{CJ}}|_{\mathrm{S}_1\mathrm{S}_1'}\otimes\rho_{\mathrm{S}}^{\mathrm{CJ}}|_{\mathrm{S}_2\mathrm{S}_2'}\Big). \tag{6.32}$$

Then the fundamental law that composition with uncorrelated dynamics does not increase the correlatedness of dynamics, as expressed in Eqn. 6.30, yields the inequality

$$\bar{I}(\mathcal{E}_{\mathrm{S}}) \geq \frac{1}{4\log_2 d} S\Big(\tilde{\rho}_{\mathrm{S}}^{\mathrm{CJ}}\Big\|\tilde{\rho}_{\mathrm{S}}^{\mathrm{CJ}}|_{\mathrm{S}_1\mathrm{S}_1'}\otimes\tilde{\rho}_{\mathrm{S}}^{\mathrm{CJ}}|_{\mathrm{S}_2\mathrm{S}_2'}\Big). \tag{6.33}$$

Here, the state $\tilde{\rho}_{\mathrm{S}}^{\mathrm{CJ}} = [(\mathcal{E}_{\mathrm{S}})(\mathcal{R}_{\mathrm{S}_1}\otimes\mathcal{R}_{\mathrm{S}_2})]\otimes\mathbb{1}(|\Phi_{\mathrm{SS}'}\rangle\langle\Phi_{\mathrm{SS}'}|)$ is obtained by composition of the dynamics $\mathcal{E}_{\mathrm{S}}$ with arbitrary local maps $\mathcal{R}_{\mathrm{S}_1}$ and $\mathcal{R}_{\mathrm{S}_2}$, i.e. maps that act only locally on S_1 and S_2, respectively. Now, monotonicity of the relative entropy with respect to the partial trace [45] leads to the bound for the correlation measure

$$\bar{I}(\mathcal{E}_{\mathrm{S}}) \geq \frac{1}{4\log_2 d} S\Big(\tilde{\rho}_{\mathrm{S}}^{\mathrm{CJ}}|_{\mathrm{S}}\Big\|\tilde{\rho}_{\mathrm{S}}^{\mathrm{CJ}}|_{S_1}\otimes\tilde{\rho}_{\mathrm{S}}^{\mathrm{CJ}}|_{S_2}\Big). \tag{6.34}$$

The trace over the subsystem S' on the Choi-Jamiołkowski state yields

$$\begin{aligned}\tilde{\rho}_{\mathrm{S}}^{\mathrm{CJ}}|_{\mathrm{S}} :&= \mathrm{Tr}_{\mathrm{S}'}\left\{[(\mathcal{E}_{\mathrm{S}})(\mathcal{R}_{\mathrm{S}_1}\otimes\mathcal{R}_{\mathrm{S}_2})]\otimes\mathbb{1}(|\Phi_{\mathrm{SS}'}\rangle\langle\Phi_{\mathrm{SS}'}|)\right\}\\ &= (\mathcal{E}_{\mathrm{S}})(\mathcal{R}_{\mathrm{S}_1}\otimes\mathcal{R}_{\mathrm{S}_2})\left(\frac{\mathbb{1}}{d^2}\right) = \mathcal{E}_{\mathrm{S}}(\rho_{\mathrm{S}_1}\otimes\rho_{\mathrm{S}_2}) = \rho'.\end{aligned} \tag{6.35}$$

where the local maps $\mathcal{R}_{\mathrm{S}_1}$ and $\mathcal{R}_{\mathrm{S}_2}$ are chosen such that $\rho_{\mathrm{S}_1,\mathrm{S}_2} := \mathcal{R}_{\mathrm{S}_1,\mathrm{S}_2}(\frac{\mathbb{1}}{d})$. Moreover, since $\tilde{\rho}_{\mathrm{S}}^{\mathrm{CJ}}|_{\mathrm{S}_1,\mathrm{S}_2} = \mathrm{Tr}_{\mathrm{S}_2,\mathrm{S}_1}[\mathcal{E}_{\mathrm{S}}(\rho_{\mathrm{S}_1}\otimes\rho_{\mathrm{S}_2})] := \rho'_{\mathrm{S}_1,\mathrm{S}_2}$, we write Eqn. 6.34 as

$$\bar{I}(\mathcal{E}_{\mathrm{S}}) \geq \frac{1}{4\log_2 d} S(\rho'\|\rho'_{\mathrm{S}_1}\otimes\rho'_{\mathrm{S}_2}). \tag{6.36}$$

Now we use the quantum Pinsker inequality [46]

$$S(\rho\|\sigma) \geq \frac{1}{2\ln 2}\|\rho-\sigma\|_1^2, \tag{6.37}$$

where the relative entropy is measured in bits, ρ and σ are density matrices and the trace norm is $\|A\|_1 = \mathrm{Tr}\sqrt{A^\dagger A}$. Thus, we obtain

$$\begin{aligned}\bar{I}(\mathcal{E}_{\mathrm{S}}) &\geq \tfrac{1}{8(\log_2 d)(\ln 2)}\|\rho'-\rho'_{\mathrm{S}_1}\otimes\rho'_{\mathrm{S}_2}\|_1^2\\ &= \tfrac{1}{8\ln d}\|\rho'-\rho'_{\mathrm{S}_1}\otimes\rho'_{\mathrm{S}_2}\|_1^2.\end{aligned} \tag{6.38}$$

Finally, by considering two arbitrary observables on S_1 and S_2, X_1 and X_2 respectively, the inequality $\|A\|_1 \geq \frac{\mathrm{Tr}(AB)}{\|B\|}$ implies:

$$\begin{aligned}\bar{I}(\mathcal{E}_{\mathrm{S}}) &\geq \frac{1}{8\ln d}\left\{\frac{\mathrm{Tr}[X_1\otimes X_2(\rho'-\rho'_{\mathrm{S}_1}\otimes\rho'_{\mathrm{S}_2})]}{\|X_1\otimes X_2\|}\right\}^2\\ &= \frac{1}{8\ln d}\frac{C^2_{\rho'}(X_1,X_2)}{\|X_1\|^2\|X_2\|^2}.\end{aligned} \tag{6.39}$$

Therefore the inequality from Eqn. 6.31 is recovered. This result is useful because it allows us to estimate a lower bound of the amount of dynamical correlation only by preparing product states and measuring correlation functions. Specifically, the measurement protocol, also shown in Figure 6.23, is as follows:

1. **State preparation**: The bipartite system is initially prepared in a product state $\rho = \rho_{\mathrm{S}_1}\otimes\rho_{\mathrm{S}_2}$.
2. **Evolution**: The state ρ evolves accordingly to the dynamical map $\mathcal{E}_{\mathrm{S}}$ to some state $\rho' = \mathcal{E}_{\mathrm{S}}(\rho)$.
3. **Measurement**: Correlation measurements of two local quantum observables X_1 and X_2 are carried out, $C_{\rho'}(X_1,X_2) = \langle X_1\otimes X_2\rangle_{\rho'} - \langle X_1\rangle_{\rho'}\langle X_2\rangle_{\rho'}$.

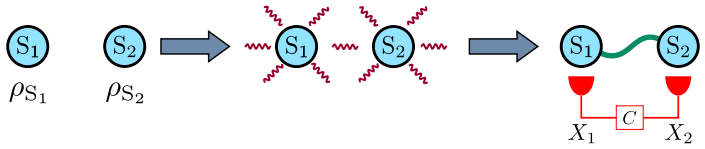

Figure 6.23: Schematic illustration of the measurement of the lower bound of $\bar{I}$. The system is prepared in a separable state $\rho = \rho_{\mathrm{S}_1} \otimes \rho_{\mathrm{S}_2}$ and correlations of the observables X_1 and X_2 are measured after the evolution.

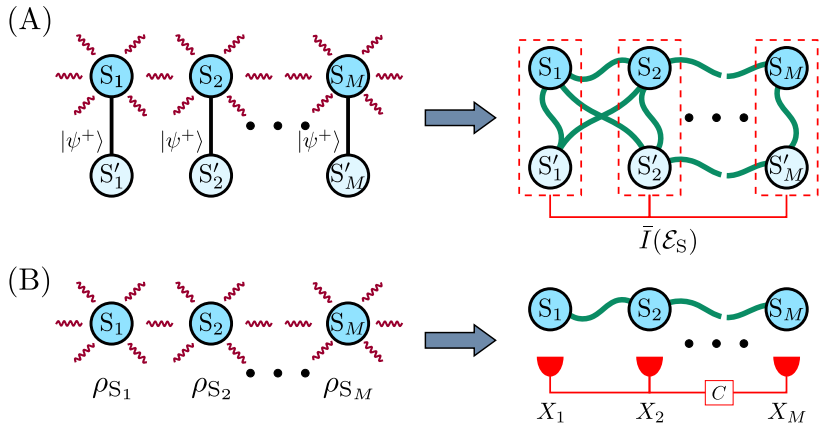

Figure 6.24: Schematic illustration of the multipartite correlation measure. (A) Choi-Jamiołkowski representation of the dynamics. The system is prepared in a product of maximally entangled states of $2M$ parties $\{\mathrm{S}_j|\mathrm{S}'_j\}$ and the dynamics affect only the subsystems S_j. If and only if the dynamics are correlated, the bipartitions $\{\mathrm{S}_i\mathrm{S}'_i|\mathrm{S}_j\mathrm{S}'_j\}$ will be entangled, yielding a nonzero $\bar{I}$. (B) Schematic depiction of the procedure to estimate a lower bound of $\bar{I}$. There, the system is prepared in a separable state $\rho_{\mathrm{S}_1} \otimes \rho_{\mathrm{S}_2} \cdots \otimes \rho_{\mathrm{S}_M}$ and correlations in the dynamics appear as correlations C (see page 153) in a measurement of the observables X_j.

Of course, the tightness of the inequality depends on the choice of X_1 and X_2, so in practice one has to make a well informed choice of observables, taking into account prior information about the system. Typically, one would choose observables that are orthogonal to the dominant noise operator in the system. However there is no simple and universal recipe to determine the observables giving the tightest lower bound. In particular, note that finding non-vanishing values of the lower bound as given by Eqn. 6.31 allows one to reveal unexpected dynamical correlations if suitable observables have been estimated in any experiment.

6.2.3.4 *Extension to multipartite systems*

The approach to measure and estimate bipartite correlations can be extended to the multipartite case. In this situation, one has to specify what kind of correlations are the matter of interest. For instance, one may be interested in the amount of correlations shared between two parties of the system or between all parties. Figure 6.24 illustrates a generic situation where correlations among all systems are investigated.

For definiteness, suppose we consider the total amount of correlations, i.e. the amount of correlations shared by all parties (other cases can be analyzed in a similar manner). In that case, if the system S has M parties $\mathrm{S}_1, \mathrm{S}_2, \ldots, \mathrm{S}_M$, we introduce respective ancillary systems $\mathrm{S}'_1, \mathrm{S}'_2, \ldots, \mathrm{S}'_M$ and prepare a collection of M maximally entangled states between S_1 and S'_1, S_2 and S'_2, etc. [see Figure 6.24(A)]. The dynamics are then applied on the system S we want to study. The amount of total normalized correlations in the dynamics can be assessed by

$$\begin{aligned}\bar{I}(\mathcal{E}_{\mathrm{S}}) &:= \frac{1}{2M\log d} S\left(\rho_{\mathrm{S}}^{\mathrm{CJ}} \middle\| \rho_{\mathrm{S}}^{\mathrm{CJ}}|_{\mathrm{S}_1\mathrm{S}'_1} \otimes \ldots \otimes \rho_{\mathrm{S}}^{\mathrm{CJ}}|_{\mathrm{S}_M\mathrm{S}'_M}\right) \\ &:= \frac{1}{2M\log d}\left\{\left[\sum_{i=1}^{M} S\left(\rho_{\mathrm{S}}^{\mathrm{CJ}}|_{\mathrm{S}_i\mathrm{S}'_i}\right)\right] - S\left(\rho_{\mathrm{S}}^{\mathrm{CJ}}\right)\right\}, \end{aligned} \tag{6.40}$$

where $\rho_{\mathrm{S}}^{\mathrm{CJ}}|_{\mathrm{S}_i\mathrm{S}'_i} = \mathrm{Tr}_{\{\forall \mathrm{S}_{j\neq i}\mathrm{S}'_{j\neq i}\}}(\rho_{\mathrm{S}}^{\mathrm{CJ}})$.

The lower bound for the multipartite setting can be applied as shown in Figure 6.24(B), by measuring correlations. Mathematically the same steps as in the bipartite case (see Eqn. 6.31) can be applied, resulting in

$$\bar{I}(\mathcal{E}) \geq \frac{1}{4M\ln d}\frac{C^2_{\rho'}(X_1,\ldots,X_M)}{\|X_1\|^2\ldots\|X_M\|^2}. \tag{6.41}$$

Here, ρ' is the joint state after the evolution of an initial product state, $X_1, \ldots, X_M$ are local observables for the parties $\mathrm{S}_1, \ldots, \mathrm{S}_M$, respectively, and

$$C_{\rho'}(X_1,\ldots,X_M) = \langle X_1\ldots X_M\rangle_{\rho'} - \langle X_1\rangle_{\rho'}\ldots\langle X_M\rangle_{\rho'}. \tag{6.42}$$

This multipartite bound makes investigating correlation dynamics accessible in systems that are too large for full quantum process tomography, as the number of measurements increases only linearly compared to an exponential scaling for full quantum process tomography.

6.2.3.5 *Application to experiments*

In the following, we study the dynamics of spatial correlations of noise processes in a trapped ion quantum information processor [83]. In Section 6.2.3.5.1 we analyze the temporal development of the spatial correlation estimator $\bar{I}$ to determine the degree of spatial correlations in a two-qubit register. For this, we perform full quantum process tomography on qubit registers with varying degree of correlations which yields following behaviour:

a) Fully correlated noise enables DFSs [259] and thus the correlation quantifier increases with decoherence, eventually reaching a steady state for times larger than the single-qubit coherence time when all single-qubit coherences have vanished but coherences in the DFS survive. For purely dephasing noise the saturation value is $\bar{I} = 0.125$ (see Section D.1).

b) Partially correlated dynamics do not feature a full DFS and thus also, after an initial stage of increasing spatial correlations, the correlations will vanish in the limit of

infinite waiting times. More precisely, the correlations will start to decrease when the individual constituents of the imperfect DFS suffer substantial dephasing.

c) For uncorrelated dynamics the quantifier should not detect any statistically significant correlations.

In 6.2.3.5.2 we utilize the lower bound to $\bar{I}$ to characterize dynamics in a system consisting of four qubits. Initially, we investigate the two-body correlators as a function of qubit distance in the register. Following that, we investigate the four-body spatial correlations for different qubit encodings.

In the experimental platform used to implement the two protocols each qubit is encoded in the $4S_{1/2}$ and $3D_{5/2}$ states of a single $^{40}Ca^{+}$ ion of a string of ions trapped in a macroscopic linear Paul trap [83]. Doppler cooling of the ion crystal is performed on a short-lived cycling transition between the $4S_{1/2}$ and the $4P_{1/2}$ levels, as illustrated in Figure 6.25. The same transition is used to detect the qubit state via the electron shelving scheme [83]. Two additional repumping lasers ensure that the ion does not get trapped in a dark state and enable resetting from the long-lived $3D_{5/2}$ state. A more detailed description of the toolset and the experimental setup used can be found in [83].

To manipulate the state of the qubit two different laser beams are used: A global beam effectively illuminates all ions in the chain with equal power and allows rotations on the Bloch sphere of all qubits simultaneously. Therefore interactions of the following form are possible:

$$R_{\phi}(\theta) = e^{-i\frac{\theta}{2}S_{\phi}}, \tag{6.43}$$

where $S_{\phi} = \sum_{i=0}^{N}(\sigma_x^{(i)}\cos\phi + \sigma_y^{(i)}\sin\phi)$ with $\sigma_{x,y}^{(i)}$ being single-qubit Pauli matrices acting on qubit i.

To perform local operations on single qubits an addressed beam is available. This tightly focused beam is steered along the ion chain via an electro-optical deflector. By driving the qubit transition on resonance or in a detuned way, two types of rotations can be realised:

$$\begin{aligned} R_{\phi}^{(j)}(\theta) =& e^{-i\frac{\theta}{2}(\sigma_x^{(j)}\cos\phi + \sigma_y^{(j)}\sin\phi)} \\ & \text{and} \\ S_z^{(j)}(\theta) =& e^{-i\frac{\theta}{2}\sigma_z^{(j)}}. \end{aligned} \tag{6.44}$$

With this control toolset at hand we are able to prepare the qubits in the required initial state, encode them in different Zeeman sublevels and perform quantum process tomography.

The degree of noise correlations between individual qubits can be tuned by encoding them in Zeeman states with differing magnetic field susceptibility. In $^{40}Ca^{+}$, there exist multiple possibilities to encode a qubit in the Zeeman levels of the $4S_{1/2}$ and $3D_{5/2}$ states as shown in Figure 6.25. The susceptibility of the qubits to the magnetic field ranges from -2.80 MHz/G to +3.36 MHz/G, which allows us to tune not only the coherence time of the individual qubits but also the correlations between qubits, when magnetic field fluctuations are the dominant noise source. Understanding the dephasing dynamics, and in particular noise correlations, in registers containing qubits in different encodings is essential in the context of error mitigation and QEC: this understanding will be needed to determine the viability of an

approach to build, e.g. functional logical qubits, in complementary approaches either based on the use of spectroscopic decoupling of ion qubits, as compared to, e.g., shuttling-based protocols [108].

6.2.3.5.1 *Determining the degree of spatial correlation*

In the following we consider dephasing dynamics that is caused by a magnetic field acting on a string of two ions. The various qubit-states have different susceptibility to magnetic field fluctuations, given by the Landé g factors g_i of the involved Zeeman substates. The phase that qubit i accumulates during the time evolution is

$$\phi_i(t) = \int_0^t d\tau B(\tau)\mu_b g_i$$

with the magnitude of the magnetic field $B(\tau)$ and the Bohr magneton μ_b. The magnetic field fluctuations are modeled by multiple random implementations of $B(t)$. The time evolution for a single implementation can then be expressed as:

$$U = e^{-i\phi_1(\sigma_1^z + g\sigma_2^z)}. \tag{6.45}$$

with the ratio of the Landé factors $g = g_2/g_1$. In order to estimate the dynamics under a dephasing decay, one needs to average the evolution over many noise realizations with random phases. A detailed analysis of the expected decay for qubits with different susceptibility to magnetic fields is given in the Appendix, Section D.1.

In the experiment we are investigating the following qubit configurations that implement dephasing and spontaneous decay dynamics:

a) **Configuration 1:** For the realization of maximally correlated dephasing dynamics, both qubits are encoded in the $\left|4S_{1/2}, m_S = -1/2\right\rangle$ and $\left|3D_{5/2}, m_S = -5/2\right\rangle$ states. This encoding is referred to as encoding **A** hereinafter, and corresponds to the green markers in Figure 6.25. Both qubits have a susceptibility to the magnetic field of -2.80 MHz/G, leading to identical susceptibility coefficients ($g = 1$) (see Eqn. 6.45).

b) **Configuration 2:** To introduce an asymmetric dephasing dynamics, one qubit is encoded in **A** and the second is encoded in the states $\left|3D_{1/2}, m_S = -1/2\right\rangle$ and $\left|3D_{5/2}, m_S = -5/2\right\rangle$ respectively. This encoding is referred to as encoding **B** hereinafter, and corresponds to the blue markers in Figure 6.25. Their different susceptibilities to magnetic field noise of -2.80 MHz/G and +3.36 MHz/G introduce unequal dephasing and therefore affect correlations between the qubits, corresponding to the susceptibility coefficients ($g = -0.83$).

c) **Configuration 3:** Uncorrelated dynamics can be engineered by introducing spontaneous decay. In this scenario, both qubits are encoded in Encoding **A**. A laser pulse resonant with the $3D_{5/2} \leftrightarrow 4P_{3/2}$ transition at 854 nm shortens the effective lifetime of the exited state by inducing a spontaneous decay to the $4S_{1/2}, m_S = -1/2$ level via the $3P_{3/2}, m_S = -3/2$ level. This pump process implements an uncorrelated noise process that can be modeled as spontaneous decay. The effective lifetime depends on the laser power and is in our case set to be $T_{spont} = 7(1)\ \mu$s.

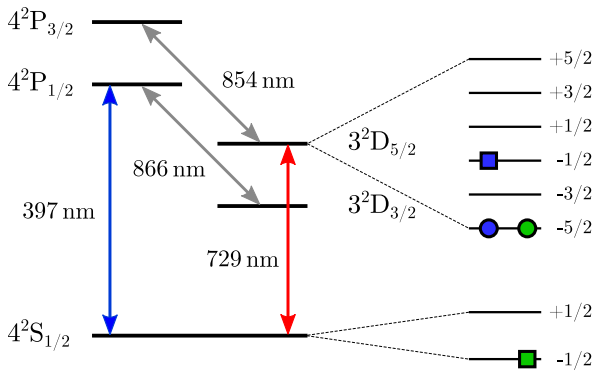

Figure 6.25: Level scheme of $^{40}Ca^{+}$. The green and blue squares and circles indicate different qubit encodings, denoted **A** and **B**, respectively. Squares are marking the qubit state $|1\rangle$ whereas the state $|0\rangle$ is highlighted with circles. The corresponding frequency shifts of the transitions caused by the magnetic field are -2.80 MHz/G and +3.36 MHz/G for the qubits marked with green and blue symbols respectively. For configuration 1 described in the enumeration in the main text for both qubits the encoding marked in green is used. The asymmetry in scenario 2 is introduced by encoding one of the qubits in in the states illustrated in blue. For the third configuration both qubits again use the encoding marked in green and the spontaneous decay from $|0\rangle$ to $|1\rangle$ is enhanced.

The system size of two qubits allows us to perform full process tomography to estimate the correlation measure $\bar{I}$ (see Eqn. 6.29). In our platform for full process tomography in an N qubit system, 12^N measurement settings, each providing $2^N - 1$ measurements, are required. The amplitude of the magnetic field fluctuations is non-stationary as it depends on the entire laboratory environment which cannot be controlled accurately. We engineer a stationary magnetic field noise as the dominating noise source (a situation where laser and magnetic field noise have to be taken into account is described in Section D.1). Thus we can control the single-qubit coherence time as shown in Figure 6.26. The stationary magnetic field noise is engineered by applying a white-noise current to the coils that generate the magnetic field at the ions' positions. We set the noise amplitude such that the coherence time of the qubit encoded in $\left|4S_{1/2}, m_S = -1/2\right\rangle$ and $\left|3D_{5/2}, m_S = -5/2\right\rangle$ is reduced from $59(3)$ ms to $1.98(7)$ ms. The increase of magnetic field noise by a factor of ≈ 30 ensures that laser phase noise is negligible. From the measured data, a process matrix is reconstructed using an iterative Maximum Likelihood method (see Ref. [257]) that ensures trace preservation and positivity of the process matrix.

The estimated quantifier for spatial correlations as defined in Eqn. 6.29 $\bar{I}$ is shown in Figure 6.27 for the decoherence processes of the different configurations described above. These processes are described by an exponential decay and show different timescales. To compare the data from the different configurations we express the free evolution time in units of the respective decay times τ. The temporal development of $\bar{I}$ is studied for evolution times of up to 5 times the decoherence time for configurations 1 and 2 and up to 1.6 times the lifetime for configuration 3, as the differences in the dynamics of different correlation strength are most pronounced on those timescales.

It can be seen in Figure 6.27 that **the symmetric configuration** (Configuration 1), depicted with blue triangles and labeled with *"sym."*, shows the highest degree of correlations that

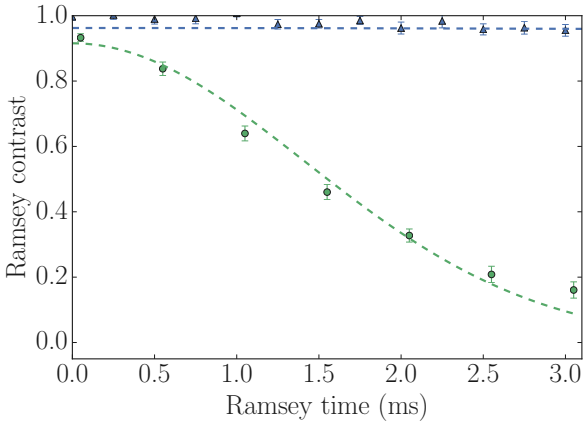

Figure 6.26: Coherence decay of the qubit in encoding A without (blue triangles) and with (green circles) additional magnetic field noise.

reaches a steady state for long evolution times. The correlations converge to a saturation value of 11.2(8) %, which is in agreement with the theoretical value of 12.5 % (as expected in the limit of perfectly correlated dephasing) within 2 standard deviations (see Section D.1).

Measurements using **the asymmetric configuration** (Configuration 2), depicted with green circles and labeled with *"asym."*, show similar dynamics to the symmetric setting for times up to twice the coherence time. For longer evolution times, however, a significant decrease in correlations is observed as no DFS is available in the system.

The third investigated scenario (Configuration 3) implementing engineered **uncorrelated** dynamics by adding spontaneous decay, is depicted with red diamonds. The correlations do not exceed a value of 3.1(6) % in this case. This is significantly lower than the maximum of $\bar{I}$ for fully and partially correlated dephasing dynamics.

The blue shaded area in the figure shows simulated results where random phase fluctuations are acting on a two-qubit system. From the resulting output state of the simulation we generate data including projection noise and the same analysis as for the experimental data is performed. To simulate the asymmetric configuration the applied random phase fluctuations are acting on the qubit weighted according to the different susceptibilities to the magnetic field. For the simulation of uncorrelated spontaneous emission, instead of phase fluctuations, probabilistic, uncorrelated quantum jump trajectories of the individual qubits are simulated. A more detailed description of the simulation can be found in Section D.1. There is qualitative agreement between simulations and measurements, but still there are significant deviations, especially in the case of uncorrelated dynamics, of up to approximately $4\,\sigma$. We assume that this overestimation of the spatial correlations in the system dynamics by the quantifier is due to miscalibration and drifts of experimental parameters. For instance a mismatch between the actual and the calibrated Rabi frequency would lead to additional correlated errors during the process tomography. This effect is best visible for Configuration 3, where the dynamics are expected to show no correlations at all.

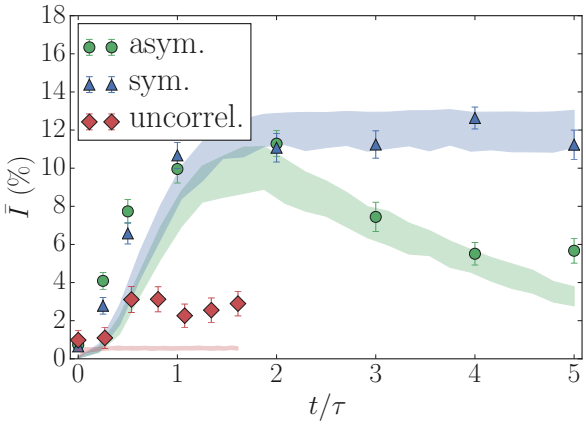

Figure 6.27: Dynamics of the spatial correlation quantifier $\bar{I}$ for different qubit encodings. Three cases are depicted: Both qubits encoded in $\left|4S_{1/2}, m_S = -1/2\right\rangle \leftrightarrow \left|3D_{5/2}, m_S = -5/2\right\rangle$ (green triangles), one qubit encoded in $\left|4S_{1/2}, m_S = -1/2\right\rangle \leftrightarrow \left|3D_{5/2}, m_S = -5/2\right\rangle$ and $\left|3D_{1/2}, m_S = -1/2\right\rangle \leftrightarrow \left|3D_{5/2}, m_S = -5/2\right\rangle$ (blue circles) and both qubits subject to uncorrelated dynamics via spontaneous decay (red diamonds). The horizontal axis is normalized to the coherence time for the first two cases and to the decay time for the third case. Results from a MC based simulation with 500 samples are depicted with shaded areas in the corresponding color.

6.2.3.5.2 *Spatial correlations in multi-qubit systems*

Due to the exponential scaling of the number of measurement settings for a single full process tomography an analysis for a four qubit system would take about 24 hours per waiting time setting and configuration in our system. Therefore, the feasible method to investigate correlations is based on the provided lower bound for the correlation measure as described in Section 6.2.3.4. For these experiments, the free-evolution time is fixed to 10 ms, approximately corresponding to 5 times the coherence time. Inferring from the two-qubit measurements, this evolution time renders a reliable discrimination of encoding configurations, leading to differing degrees of correlations, possible.

First, we investigate the distance dependence of pairwise spatial correlations along the register. For this we evaluate the lower bound for $\bar{I}$ (Eqn. 6.41) between the outermost qubit and subsequently all other qubits. In a four-qubit system this corresponds to evaluating the observables X_1X_i, with $X_i = \left(\begin{smallmatrix}0 & 1\\ 1 & 0\end{smallmatrix}\right)_i$ acting on ion $i \in \{2,3,4\}$, yielding the lower bound $\bar{I}_{LB} = \frac{1}{4\cdot 2\ln 2}\left[\langle X_1X_i\rangle - \langle X_1\rangle\langle X_i\rangle\right]^2$. By applying a global $\pi/2$ pulse around the x axis of the Bloch sphere $R_0(\pi/2)$ the system is prepared in the state $|+\rangle := \frac{1}{\sqrt{d}}\sum_{k=1}^{d}|k\rangle$, where $d = 2^4$ for four ions[†]. After the preparation the system undergoes a free evolution. With this preparation the qubits are in an eigenstate of X_i, the expectation values of these observables are decaying quickly due to the dominant dephasing caused by the excess magnetic field fluctuations. Therefore the lower bound of the dynamical correlations is the tightest for this choice of observables. The data as shown in Figure 6.28 indicate that the spatial correlations do not show any distance dependence. We compare the measured values by numerical simulations which are shown as shaded bars in Figure 6.28 (see also Section D.1). The

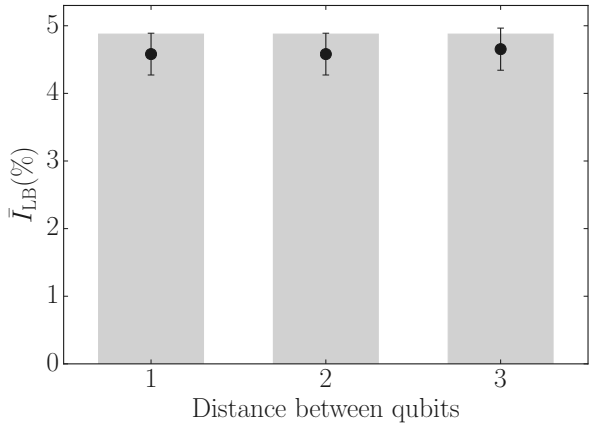

Figure 6.28: Lower bound for pairwise spatial correlations in a four-qubit system as a function of the distance (in terms of ion index difference in the ion string) to qubit 1, depicted with black circles. The corresponding simulations are shown with shaded bars. As all qubits have the same encoding, the correlations between qubit 1 and qubit 2, 3 and 4 respectively are the same within errorbars.

measured values are close to the expected value for a fully dephased state under perfectly correlated noise of 4.5% (see Section D.1).

We then analyze the spatial correlations as given by the four-body observable $X_1X_2X_3X_4$. We investigate three different configurations of qubit encodings which give rise to different DFSs:

- **Configuration 1:** All four qubits encoded in Encoding **A**.
- **Configuration 2:** Qubits 1 and 2 encoded in Encoding **A**, qubits 3 and 4 encoded in Encoding **B**.
- **Configuration 3:** Qubits 1, 2 and 3 encoded in Encoding **A**, qubit 4 encoded in Encoding **B**.

The preparation of the system is the same as in the measurement of the pairwise correlations, but after the waiting time, a four qubit state tomography measurement is performed. From the reconstructed density matrix, we estimate the expectation values of the observables $\langle X_1\rangle$, $\langle X_2\rangle$, $\langle X_3\rangle$, $\langle X_4\rangle$ and $\langle X_1X_2X_3X_4\rangle$, where $X_i = \left(\begin{smallmatrix}0&1\\1&0\end{smallmatrix}\right)_i$ is a Pauli matrix acting on qubit i. The experimental results for the lower bound $\bar{I}_{LB} = \frac{1}{4\cdot 4\ln 2}\left[\langle X_1X_2X_3X_4\rangle - \langle X_1\rangle\langle X_2\rangle\langle X_3\rangle\langle X_4\rangle\right]^2$ but also for the individual expectation values are presented in Figure 6.29. In the left subplot in the top row the lower bound is plotted in green, blue and red for the qubit encoding configurations **1**, **2** and **3**, respectively. The theoretically expected values from numerical simulations of the microscopic noise are depicted with shaded bars. These estimated correlations and single-qubit expectation values lead to a lower bound of 1.66(18) %, 1.05(18) % and 0.84(16) % for the three qubit encoding patterns, respectively. These results show agreement with simulations within 1 standard deviation. Note furthermore that in particular the lower bound value of 1.66(18) % for the

† In that notation the computational basis is numbered consecutively, so $|1\rangle = |0000\rangle, |2\rangle = |0001\rangle, ..., |16\rangle = |1111\rangle$.

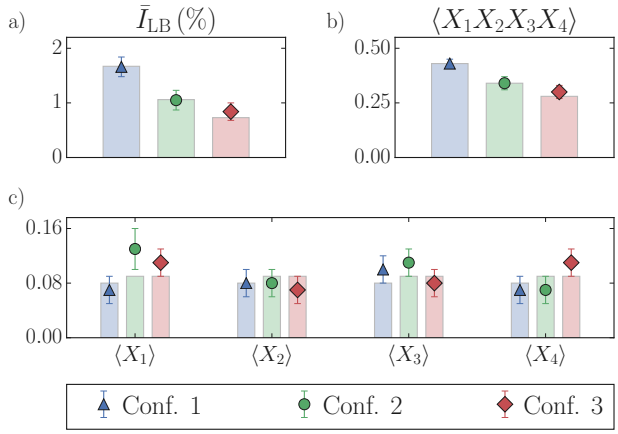

Figure 6.29: a) Lower bound $\bar{I}_{LB}$ for $\bar{I}$ for 3 different qubit encoding configurations described in Section 6.2.3.5.2. b) and c) show the underlying expectation values from which $\bar{I}_{LB}$ is calculated. The expected results from numerical simulations are depicted with shaded bars in the corresponding color.

first encoding pattern in which all four qubits reside in the Encoding **A** (Configuration 1) is a signature of the almost perfectly correlated dynamics - it is close to the theory value predicted for the long time limit of perfectly correlated dephasing dynamics of 1.27 %. In contrast, for two qubits in Encoding **A** and two qubits in **B** (Configuration 2), the observed bound of 1.05(18) % is lower than for Configuration 1 and to be compared with the theory value of 0.56 % predicted for the long time limit (see Section D.1). For the asymmetric Configuration 3 (three qubits in Encoding **A** and one in **B**), one observes with 0.84(16) % the lowest value of the lower bound. As shown in Section D.1, theory predicts the lower bound to fully vanish in the limit of even longer waiting times.

Instead of performing state tomography the expectation values necessary to calculate the lower bound of the correlation quantifier could be measured directly, leading to a linear scaling of the number of measurements with the number of qubits in the worst case. In exchange for the better scaling the correlation estimation gets vulnerable to projection noise. By increasing the number of repetitions of the experiment this error source can be reduced to arbitrary low levels.

6.2.3.6 *Conclusions and Outlook*

We have presented a lower bound for the measure for correlations of quantum dynamics proposed in Ref. [183]. We have shown how this lower bound can be evaluated without full knowledge of the quantum process and how it can be extended to multipartite systems. We have applied both the full measure $\bar{I}$, which requires full tomographic information, as well as the lower bound $\bar{I}_{LB}$ to different electronic qubit encodings in a trapped ion quantum information processor.

Our experimentally measured values are in agreement with expected values from theoretical simulations which are based on a modelling of the various noise sources for different types of qubit encoding patterns. For strings of up to four qubits our measurements confirm that the natural noise in the quantum processor characterized in this work is

dominated by perfectly correlated dephasing noise. Notably, both the values of the exact measure $\bar{I}$, as obtained from quantum process tomography in the two-ion case, as well as the values of the lower bounds obtained for up to four ions, clearly reveal that the noise dynamics is no longer perfectly correlated once a subset of ions is encoded in different electronic states than the others. Furthermore, the observed values for $\bar{I}$ for an asymmetric encoding also reveal the time scale on which this breaking of the perfectly correlated dephasing dynamics takes effect. This quantitative information is valuable, if one is e.g. interested in using sets of ion-qubits for the exploitation of DFSs.

In fact, one of the most intriguing applications of the correlation measure $\bar{I}$ is to characterize noise processes in the context of QEC. It should be noted that the measure itself cannot be directly used to assess the influence of the correlations on a QEC protocol, but it is able to test a specific noise model and to furthermore estimate the model's parameters. In particular, the measure can be used to experimentally determine the behaviour of correlated noise as a function of the distance between the constituent particles. The noise model can then inform a microscopic model to estimate the QEC protocol's performance. This is due to the fact that the effect of correlations on EC procedures depends strongly on the interplay of the actual form of the spatial correlations. The correlation measure quantifies the amount of correlations and thus cannot be directly connected to the threshold of an error correcting code without knowledge of the actual form of the correlations.

In addition, the exact correlation measure (and also the lower bound) can be used to certify that the amount of spatial correlations is reduced in qubit pairs at positions $\mathbf{r}_i$ and $\mathbf{r}_j$ with increasing distance according to certain scalings: Observing the way it decreases, e.g. as a powerlaw $\propto |r_i - r_j|^{-\alpha}$ with a sufficiently large exponent α, allows one then to establish a connection to QEC protocols. Such decay behaviour enters EC protocols as a necessary condition for the provable existence of a regime in which the error correcting codes allow for FT quantum computing [214–220].

Complementary, the lower bound is useful to detect unexpected correlations in systems that do not allow full process tomography. It should be noted that the lower bound can be estimated using data that is taken routinely during system tune-up, such as Ramsey experiments, in many different physical QIP architectures. Based on prior knowledge about the experimental system, one can also design the measured observable to be sensitive to a certain kind of errors.

The presented methods can also be applied to characterize the noise environment in precision measurements. For example in [260], two spatially separated ions are used for dc magnetometry. The authors also investigated the coherence time of the singlet state as a function of the ion distance. For short distances ($\approx 4\,\mu$m) the ions see almost perfectly correlated noise resulting in no measurable decay (an almost perfect DFS). For larger ion separation (≈ 6 mm), the coherence time is reduced by at least one order of magnitude, indicating only partially correlated noise. The spatial correlation measure could be readily applied to this experiment to characterize the correlations in the noise as a function of ion distance. The distance of the qubits in the present work is in the order of 5μm and thus we expect and observe completely correlated noise.

6.2.3.7 *Acknowledgments*

We gratefully acknowledge support by the Austrian Science Fund (FWF), through the SFB FoQuS (FWF Project No. F4002-N16), as well as the Institut für Quanteninformation GmbH.

This research was funded by the Office of the Director of National Intelligence (ODNI), Intelligence Advanced Reasearch Projects Activity (IARPA), through the Army Research Office grant W911NF-16-1-0070. All statements of fact, opinions or conclusions contained herein are those of the authors and should not be construed as representing the official views or policies of IARPA, the ODNI, or the U.S. Government. We also acknowledge support by U.S. A.R.O. through grant W911NF-14-1-0103, the Spanish MINECO grant FIS2015-67411, and the CAM research consortium QUITEMAD+ S2013/ICE-2801.

7

CONCLUSION

It is believed that large-scale quantum computation will require walking the long and rocky road of QEC, where quantum information is distributed among several physical qubits constituting logical qubits. In doing so, redundancy necessary to protect the intrinsically fragile encoded quantum information from undesired disturbances is created. In this thesis, two essential ingredients of FT quantum computation and their experimental implementations using a trapped-ion quantum information processor are discussed:

- First, the repeated readout of information about errors being present on a logical qubit is demonstrated. This procedure allows for continuous correction of errors as they appear throughout the execution of an algorithm.
- And second, the implementation of a universal set of quantum gates on logical qubits is presented. A sequence of gates from such a set allows one to approximate any quantum algorithm with arbitrary accuracy.

Chapter 2 provided a general, hardware-agnostic introduction to QIP and introduced the foundations and building blocks of the QEC protocols discussed throughout this thesis. Chapter 3 discussed the basics of confining ions in free space. Furthermore, the interaction of trapped ions with light and how this interaction can be utilized to implement the building blocks of QIP were described. In Chapter 4, the basic concepts of QEC were explained and the stabilizer formalism, a framework to describe a large class of QEC codes, was introduced. Moreover, the experimental realization of multiple rounds of Steane-type QEC [114] was presented. In this approach, the information about errors on a logical data qubit is copied to an auxiliary logical qubit from which the error syndrome can be extracted. As this syndrome extraction procedure relies on transversal gate operations it is inherently FT, provided that the initialization of the auxiliary logical qubit is FT. This is ensured for the implementations presented herein by using single flag qubits [110–113]. The generality of Steane QEC was illustrated by applying it to different QEC codes. For the distance-3 and distance-5 bit- and phase-flip codes the logical fidelity improved with increasing code distance suggesting an operation of the codes below their respective thresholds. Furthermore, Steane QEC was implemented for the Steane code [36], a seven-qubit QEC code able to correct a single arbitrary error, and compared to a state-of-the-art flag-based QEC protocol [119, 120]. It was shown that Steane EC outperforms the flag-based protocol for the error processes present in the experimental setup. A major contribution to the observed logical error rates can be attributed to measurement and dephasing errors. However, numerical simulations suggest that Steane QEC offers an even larger advantage of up to a factor of two in the regime of dominating two-qubit gate errors. Furthermore, Steane-type QEC can be especially beneficial for architectures providing parallel implementations of logical CNOT gates, as in this case

extracting the error syndrome in only two circuit time steps is possible. The experimental capabilities for efficient Steane EC were recently demonstrated in a neutral atom quantum processor by realizing parallel entangling gates on multiple logical qubit pairs [40].

For the realization of FT quantum computation, FT encoding and syndrome extraction, discussed in Chapter 4, are not sufficient. Also gate operations have to be implemented such that the encoded quantum information is protected against noise throughout the entire execution of a quantum algorithm. Thus, gate operations must be applied directly to encoded qubits. Chapter 5 presented the FT implementation of a universal set of quantum gates in the Steane code. Transversal single-qubit Clifford operations were applied to the state $|0\rangle_{\mathrm{L}}$ to prepare all six cardinal states on the Bloch sphere of the logical qubit. The logical fidelity of the prepared states was compared for FT and non-FT initialization of $|0\rangle_{\mathrm{L}}$. It was observed that the flag-based FT initialization protocol outperforms the non-FT version by approximately a factor of 5. Furthermore, the transversal CNOT gate was characterized by applying it to six different input states of two fault-tolerantly prepared logical qubits. To achieve universality, the set of Clifford gates was amended by the T gate, a rotation with a rotation angle of $\frac{\pi}{4}$ around the Y axis [54]. For the implementation of the T gate, an auxiliary logical qubit was prepared in a magic state, and subsequently, a transversal entangling gate between the logical auxiliary qubit and the target qubit was applied. Along the same lines as for Steane QEC, this magic state injection procedure is FT in case of an FT magic state preparation. The flag-based FT preparation of the magic state proposed in Refs. [110, 119] uses a total of eight flag qubits to capture all dangerously propagating errors. For approximately 13% of the prepared magic states the flag qubits did not indicate a dangerous error and the magic state was accepted. Despite the significantly increased complexity of the FT preparation circuit compared to its non-FT counterpart, an improvement in the magic state fidelity of more than a factor of ten was observed in the experiment.

The application of gates to a qubit register can lead to unintended manipulation of qubits in close proximity to the target qubit, as discussed in Section 6.1. Such crosstalk effects can introduce error processes that break the FT properties of a circuit by introducing error processes that lead to uncorrectable errors. It was shown that crosstalk does not pose a limitation for current error rates in the considered experimental setup. However, simulations showed that for physical error rates decreased by one order of magnitude, crosstalk affects the scaling of the logical error rate with the underlying physical error rates. Nevertheless, reordering the qubit register under consideration of the microscopic structure of the present crosstalk can recover the error rate scaling promised by FT circuit design for some QEC protocols.

Apart from the spatially correlated errors induced by crosstalk, spatially correlated idling errors can significantly impact the performance of QEC procedures [214–220]. In Ref. [183], a measure rigorously quantifying correlations in quantum dynamics for two qubits was proposed. The implementation of this quantification method in a trapped-ion device was discussed in Section 6.2. The correlation strength of idling dynamics between different qubits can be engineering in the trapped-ion device used in this thesis: Encoding qubits in different electronic states of the ions allows one to tune their sensitivity to magnetic fields. With this, the intrinsically fully correlated magnetic field noise present in the setup acts differently along the qubit register. This allows for testing the implemented correlation measure in different correlation-strength regimes. Furthermore, a lower bound to the measure that does not require full knowledge about the quantum dynamics, as well as an extension of the correlation measure to multipartite quantum systems, was introduced. The measure and

its lower bound can be utilized to inform error models that consider spatial correlations in idling dynamics. Such error models will be crucial in future large-scale quantum devices to predict the performance of QEC protocols.

In Ref. [39], error rates of logic qubit initialization and logical CNOT gates were observed that are lower than the respective physical error rates in the same device. The current physical error rates present in the trapped-ion device used to acquire the data in this thesis do not allow us to observe this hallmark feature of beneficial QEC. The main limitations are two-qubit gate error rates, dephasing errors caused by magnetic field noise and mid-circuit measurement errors. To conclude this thesis, future updates to the experimental setup are discussed that hopefully allow us to achieve beneficial QEC, a milestone on the long road towards FT quantum computation.

We suspect that a major contribution to two-qubit gate errors is given by undesired interaction with motional modes. With increasing qubit register size the number of motional modes increases and the mode spectrum gets denser in frequency space. The scheme described in Section 3.2.3 uses a single motional mode to mediate the entangling interaction between qubits. Interactions mediated by other, neglected modes close in frequency can lead to entanglement between electronic and motional state of the ions. An update to the control electronics of the setup is currently in preparation, so that the laser intensity and phase can be modulated during the gate operation. This allows us to decouple the ions' electronic and motional state for multiple modes simultaneously [261, 262] and increase the entangling gate fidelity for trapped-ion devices with dense motional spectra.

Idling errors in the considered setup are dominated by dephasing errors caused by magnetic field noise. The magnetic field at the ion position is generated by a combination of permanent magnets and coils. Currently, the coherence time on the optical qubit transition is on the order of $50\,\mathrm{ms}$, where the limiting factor is noise on the current drivers supplying the coils. By rearranging the permanent magnets, the coils can be superseded, so that the coherence time can be significantly improved [143–145]. Modifying the permanent magnet arrangement requires extensive disassembly of the experimental apparatus and is, therefore, scheduled for a future down-time period of the setup.

Increasing the coherence time also reduces the error rate of mid-circuit measurements, as the measurement contains periods where DD is not applicable. We assume that another major contribution to the error budget of mid-circuit measurements is crosstalk in the single-qubit operations required for switching the data qubit encoding during the measurement procedure. Every single-qubit gate introduces a small undesired rotation on its neighbors. By employing single-qubit operations, that consist of pulses with different rotation axes, the rotation angle of the crosstalk rotation can be reduced [212, 213]. For small Rabi frequencies, as are present on neighboring ions, the consecutive rotations around different axes implement an operation close to the identity operation. On the contrary, the Rabi frequency at the target ion is approximately two orders of magnitude larger and the pulse sequence implements the desired single-qubit operation. As a sequence of rotations around different axes corresponds to a single phase-modulated laser pulse, the update to the control electronics required to implement modulated entangling operations mentioned above also allows us to implement crosstalk-insensitive single-qubit gates.

A

APPENDIX TO PUBLICATION *DEMONSTRATION OF FAULT-TOLERANT STEANE QUANTUM ERROR CORRECTION*

A.1 Quantum error correcting codes

A.1.1 *The seven-qubit color code*

A powerful tool for describing a large group of QEC codes is the stabilizer formalism. In an n-qubit quantum system encoding k logical qubits a group of mutually commuting Pauli operators defining a QEC code, referred to as the stabilizer, can be specified. Any valid code state is a $+1$ eigenstate with respect to all elements of the group, which can be generated by a set of $n-k$ stabilizer generators. By measuring the expectation values of the stabilizer generators, errors can be detected and subsequently corrected through QEC protocols, preserving the integrity of the encoded quantum information. The distance d of the code is given by the minimal weight of a non-trivial operator that does retain the quantum state it is acting on within the subspace of $+1$ eigenstates of the stabilizer. An n-qubit stabilizer code with a distance d encoding k qubits is commonly denoted as an $[[n,k,d]]$ code.

The seven-qubit color code $[[7,1,3]]$ is constructed by placing physical qubits on the vertices of a graph [36]. The encoded logical qubit is defined as the simultaneous $+1$ eigenstate of the six stabilizer generators

$$\begin{aligned} S_X^{(1)} &= X_1X_3X_5X_7, \quad S_Z^{(1)} = Z_1Z_3Z_5Z_7 \\ S_X^{(2)} &= X_4X_5X_6X_7, \quad S_Z^{(2)} = Z_4Z_5Z_6Z_7 \\ S_X^{(3)} &= X_2X_3X_6X_7, \quad S_Z^{(3)} = Z_2Z_3Z_6Z_7, \end{aligned} \tag{A.1}$$

as illustrated in Figure 4.16A and Figure A.1. The logical operators are given by $Z_L = Z^{\otimes 7}$ and $X_L = X^{\otimes 7}$, which can be expressed as weight-3 operators by multiplication with stabilizers. For instance, multiplying $S_X^{(1)}$ with X_L gives the weight-3 logical operator $X_2X_4X_6$. The circuit shown in Figure A.2 is used to encode a logical state in the seven-qubit color code [110].

In the error-free case, a measurement of the set of stabilizer generators will yield the outcome $+1$ for each one, since a valid code state is a $+1$ eigenstate of these operators. If a single Pauli fault occurs, this will anticommute with a set of stabilizers. The measurement outcomes in this case will yield the outcome -1 for a set of stabilizers. This syndrome measurement outcome is unique to the initial single Pauli fault when excluding error configurations of weight greater than one. Therefore, one can correct for this error and

recover the code state. However, higher-weight error configurations break this uniqueness and can lead to logical errors when applying the recovery operation. For instance, the weight-1 error configuration X_5 and the weight-2 configuration X_1X_4 lead to the same Z syndrome $\{S_Z^{(1)} = -1, S_Z^{(2)} = -1, S_Z^{(3)} = 1\}$. Applying the recovery operation X_5 would lead to a logical error for the weight-2 error case, as the weight-3 configuration $X_1X_4X_5 = X_L S_X^{(3)}$ is up to multiplication with a stabilizer generator equivalent to X_L. Table A.1 summarizes the possible Z-syndrome measurement outcomes and the corresponding recovery operation, which corrects any single Pauli-X error. Since the seven-qubit color code is self-dual, i.e. symmetric under exchange of X and Z stabilizers, the lookup table for Pauli-Z corrections based on the measured X syndrome is the same.

The syndrome can be extracted using Steane-type QEC with the circuit shown in Figure A.3, where transversal CNOT gates copy errors onto an auxiliary logical qubit which is then measured projectively. Figure A.4 shows the circuit we use for flagged syndrome readout on the seven-qubit color code [38, 120, 128]. If no error is detected in a first round of flagged stabilizer measurements, we assume that no error has occurred and proceed. If a non-trivial syndrome is measured, the complete syndrome is measured again with unflagged circuits to distinguish the dangerous propagated flag errors from non-flag errors. If the two syndromes agree, we take this as a final syndrome for EC with lookup table Table A.1. If they do not agree and the unflagged syndrome coincides with a flag-error syndrome in Table A.2, we apply the corresponding flag-EC. In case the unflagged syndrome is not in the flag-lookup table, the single-qubit recovery from Table A.1 is used. Note that while one could immediately apply the correction to the data register, it is admissible to just keep track of this in software (known as Pauli frame tracking) as long as no logical non-Clifford gate is applied. The experimental setup currently does not allow for real-time changes of the gate sequence based on outcomes of mid-circuit measurements. For the realization of flagged QEC we experimentally implement both possible circuits, with and without a second unflagged measurement of the stabilizer generators, and all combinations thereof for multiple QEC cycles. In post-selection we discard all implementations where the flagged syndrome was trivial, but an unflagged readout was following, and vice versa.

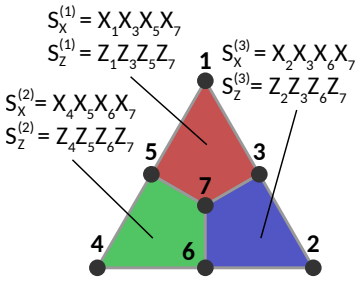

Figure A.1: Stabilizer generators of the seven qubit color code. The seven-qubit color code encodes one logical qubit into seven physical qubits. A code state is a $+1$ eigenstate of all six weight-4 stabilizer generators $\{S_X^{(i)}, S_Z^{(i)}\}$ defined on the colored plaquettes. Pauli-X (-Z) on all qubits corresponds to the logical operator X_L (Z_L), which is up to multiplication with stabilizer generators equivalent to weight-3 operators.

We numerically calculate the fidelities for the limiting case where all error rates except p_{2q} are set to 0, as shown in Figure A.5, in order to estimate the potential advantage of Steane-type QEC over the flag-based approach. Since there is no additional dephasing

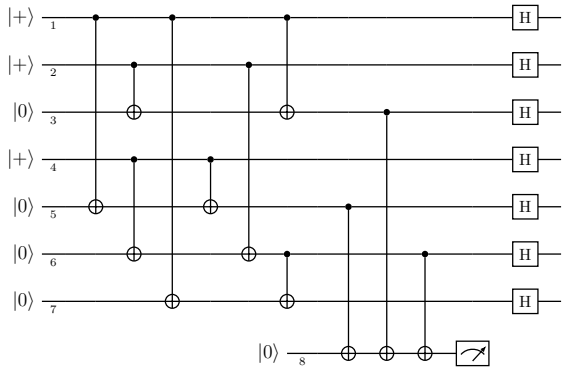

Figure A.2: Circuit for the encoding of a logical state in the seven-qubit color code [110, 128]. The first eight CNOT gates initialize $|0\rangle_L$ on the seven-qubit color code. This is followed by a verification in order to detect single faults that would otherwise propagate onto multiple data qubits and cause a logical failure. Finally, a transversal application of H_L may be applied to prepare $|+\rangle_L$.

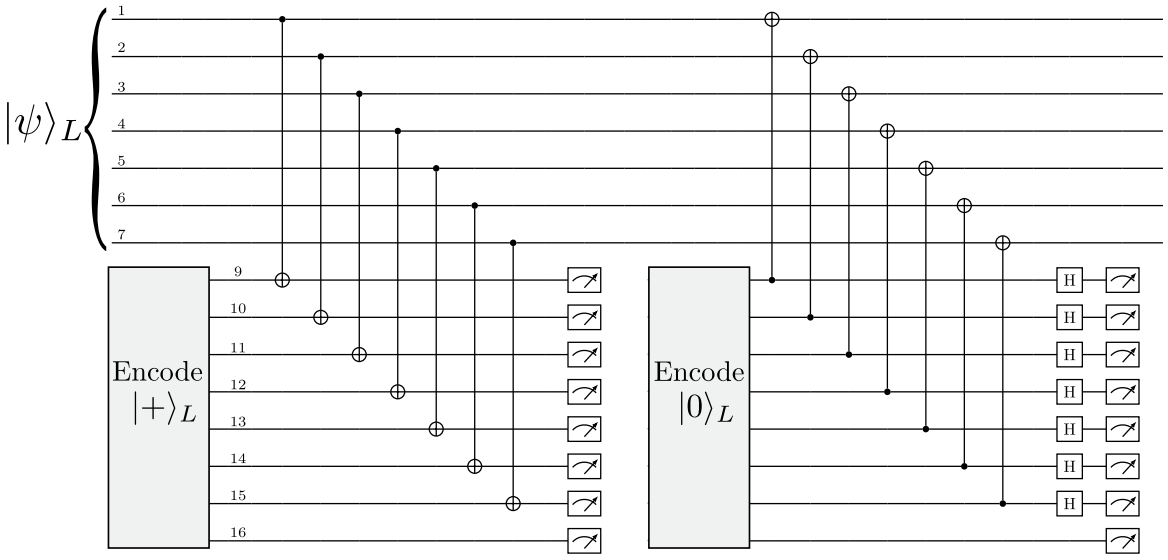

Figure A.3: Circuits for Steane-type syndrome extraction in the seven-qubit color code [114, 116, 118]. A logical auxiliary qubit is initialized using the circuit shown in Figure A.2, coupled to the data qubits and measured.

$S_Z^{(1)}, S_Z^{(2)}, S_Z^{(3)}$	Recovery
$+++$	I
$-++$	X_1
$++-$	X_2
$-+-$	X_3
$+-+$	X_4
$--+$	X_5
$+--$	X_6
$---$	X_7

Table A.1: Lookup table for the seven-qubit color code. For each syndrome measurement with a given set of positive $+$ and negative $-$ outcomes, a single-qubit recovery operation is applied. Since X and Z stabilizers are defined symmetrically on the same support, the Z-type recoveries based on the X syndrome are applied analogously. Any Y error can be considered as a combined X and Z error and be corrected independently.

$S_Z^{(1)}, S_Z^{(2)}, S_Z^{(3)}$	Recovery
$+-+$	X_3X_7
$++-$	X_4X_6

Table A.2: Flag-lookup table for the seven-qubit color code. If the outcomes of flagged and unflagged syndrome readouts do not agree and the measured unflagged syndrome is the table above, the corresponding recovery operation is applied. If the unflagged syndrome is not in the above table, the respective single-qubit recovery operation from Table A.1 is applied. Since X and Z stabilizers are defined symmetrically on the same support, the Z-type recoveries based on the X syndrome are applied analogously.

included, the systematic difference in fidelity between the two logical states $|0\rangle_L$ and $|+\rangle_L$ vanishes. The fidelities for the Steane-type approach are higher than for the flag-based protocol and this difference increases with the number of QEC rounds. After two rounds of QEC, the fidelity for the Steane-type approach is already more than 0.1 higher than for the flag-based protocol. This promises an advantage of Steane-type QEC in the regime of dominating two-qubit error rates.

A.1.2 *The 1D repetition code*

For the n-qubit bit-flip code [45], the logical $|0\rangle_L$ is encoded in n copies of $|0\rangle$ as $|0\rangle_L = |0\rangle^{\otimes n}$. The stabilizer generators are given by pairs of neighboring Pauli-Z operators $\{Z_1Z_2, Z_2Z_3, ...Z_{n-1}Z_n\}$ and the logical operators are $X_L = X^{\otimes n}$ and $Z_L = Z_1$. Analogously, the phase flip code takes repetitions of $|+\rangle$ to encode information redundantly on multiple qubits. In this case, one can define the n-qubit state $|0\rangle_L = |+\rangle^{\otimes n}$ and the stabilizers correspond to pairs of Pauli-X operators $\{X_1X_2, X_2X_3, ...X_{n-1}X_n\}$ and the logical operators are given by $X_L = Z^{\otimes n}$ and $Z_L = X_1$. Steane-type QEC is performed by initializing a second

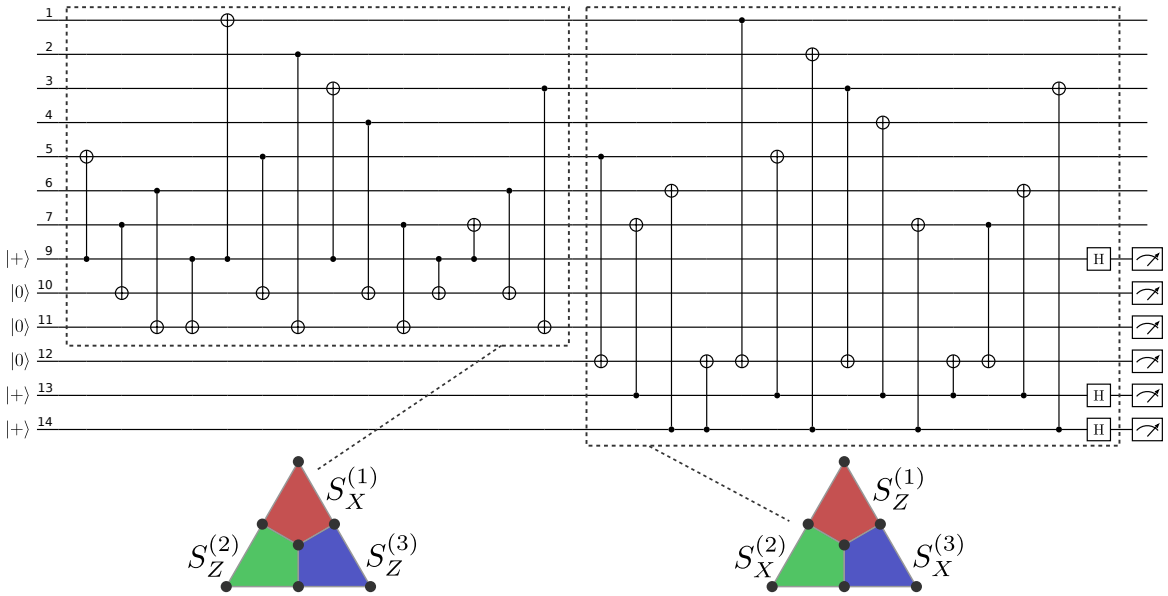

Figure A.4: Circuit for flagged syndrome readout for the syndrome extraction on the seven-qubit color code [38, 120, 128]. The first part of the circuit measures $S_X^{(1)}, S_Z^{(2)}, S_Z^{(3)}$ and the second part extracts $S_Z^{(1)}, S_X^{(2)}, S_X^{(3)}$.

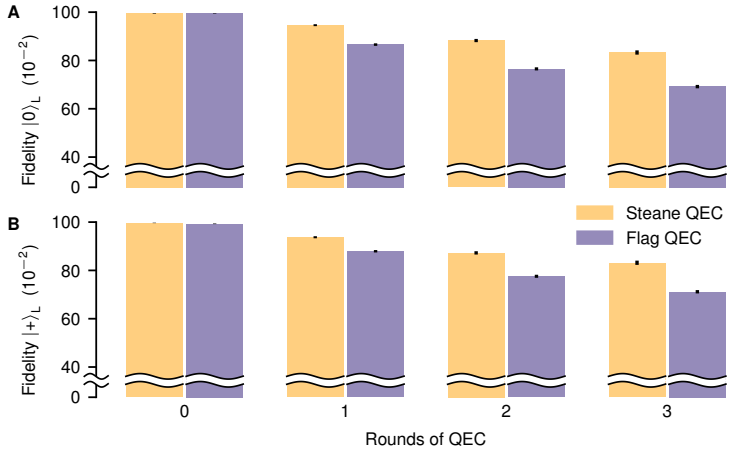

Figure A.5: Fidelities from numerical simulations for Steane-type and flagged syndrome extraction in the limiting case of only accounting for two-qubit gate errors. All error probabilities, apart from the two-qubit gate error probability $p_{2q} = 0.025$, are set to $p_{1q} = p_{\text{init}} = p_{\text{meas}} = p_{\text{mid-circ}} = 0$. Shown are the logical fidelities for the seven-qubit color code after preparing the logical states (**A**) $|0\rangle_L$ and (**B**) $|+\rangle_L$. Steane-type QEC reaches higher fidelities than the flag-based approach and this difference increases with the number of subsequent rounds of QEC. Round 0 corresponds to the encoding of the logical state with no extra round of QEC.

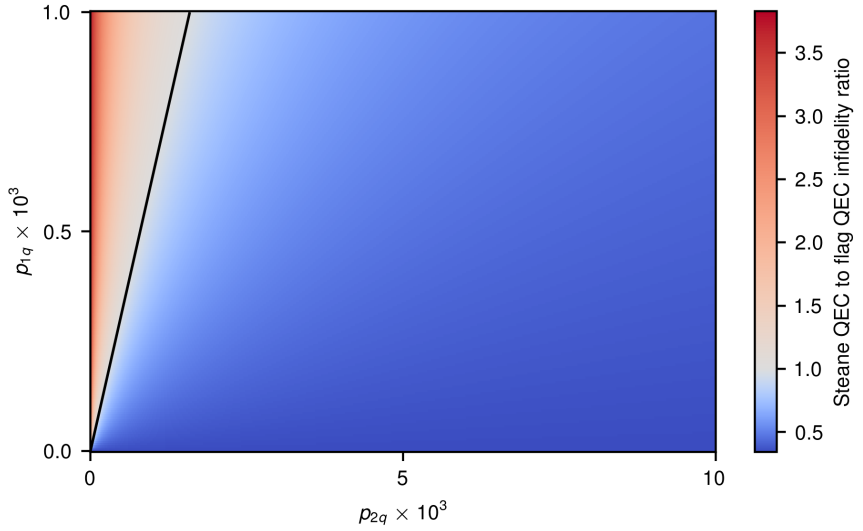

Figure A.6: Infidelity ratio from numerical simulations for Steane-type and flagged syndrome extraction in the limiting case of small two-qubit and single-qubit gate errors. All error probabilities, apart from the gate errors p_{2q}, p_{1q}, are set to $p_{\text{init}} = p_{\text{meas}} = p_{\text{mid-circ}} = 0$. We calculate the leading order in the infidelity for both schemes by performing fault path counting (see Appendix A.2) on the respective circuits. We plot the infidelity ratio of Steane-type over flagged syndrome extraction, such that values below (above) 1 indicated in blue (red) indicate an advantage for Steane-type (flagged) syndrome extraction. The black line indicates the contour of equal infidelity of Steane-type and flagged QEC. The results of our simulations show that when the two-qubit gate error is dominant ($p_{2q} \gg p_{1q}$), Steane-type syndrome readout offers an advantage also at low physical error rates.

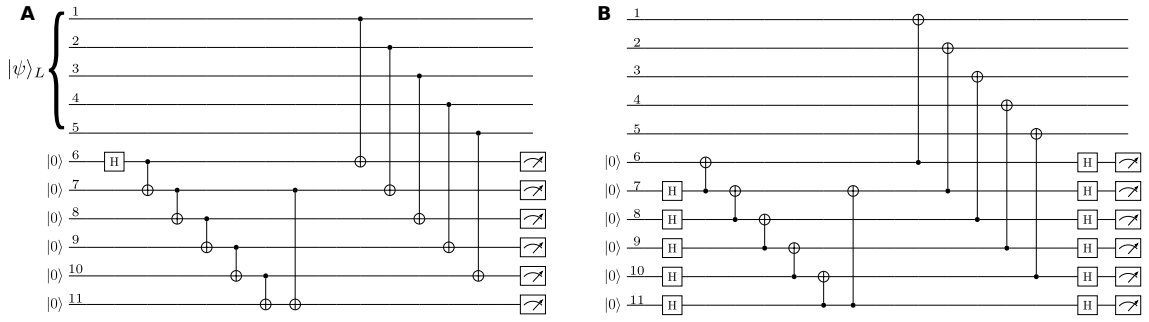

Figure A.7: Circuits for Steane-type syndrome extraction in the repetition code. Syndrome extraction for the **(A)** bit-flip code or **(B)** phase-flip code is performed by initializing a logical auxiliary qubit is in a suitable GHZ state on qubits 6 to 10 and verifying it with an additional flag qubit 11. Sequentially, a transversal CNOT gate is applied and the auxiliary qubit is measured in the corresponding basis. The flag verification (qubit 11) can be left out in the circuits for the respective distance-3 codes without breaking fault tolerance.

logical qubit in the corresponding logical $|+\rangle_L$ and applying a transversal CNOT gate, as shown exemplarily in Figure A.7 for the distance-5 repetition code.

A.2 Effective noise model and simulation methods

In order to estimate the logical fidelities of the discussed EC protocols, we perform MC simulations using STIM [263] and PECOS [198]. Every component in a circuit is modeled as an ideal operation U_{ideal} followed by an error E drawn from an error set with a given probability p. We consider depolarizing noise channels on single- and two-qubit gates

$$\begin{aligned}\mathcal{E}_1(\rho) &= (1-\sum_{j=1}^{3} p_j)\rho + \sum_{j=1}^{3} p_j E_1^j \rho E_1^j \\ \mathcal{E}_2(\rho) &= (1-p_{2q})\rho + \frac{p_{2q}}{15}\sum_{j=1}^{15} E_2^j\,\rho\,E_2^j.\end{aligned} \tag{A.2}$$

with the error sets

$$\begin{aligned}E_1 &\in \{\sigma_k, \forall k \in \{1,2,3\}\} \\ E_2 &\in \{\sigma_k \otimes \sigma_l, \forall k,l \in \{0,1,2,3\}\}\backslash\{\sigma_0\otimes\sigma_0\},\end{aligned} \tag{A.3}$$

where σ_k are the single-qubit Pauli operators $\sigma_k = \{I, X, Y, Z\}$ with $k = 0,1,2,3$. For the single-qubit case we give the more general channel to capture the asymmetric case found for the errors induced during mid-circuit measurements. The general formula reduces to the symmetric depolarizing case by choosing all three Pauli errors with equal probability $p_j = p_{1q}/3$, as we do for the single-qubit gate error. The parameters p_{1q} and p_{2q} specify the probability that any one of the errors of the corresponding error set occurs on the qubits which are acted upon. Qubits are initialized and measured in the computational basis. Faults

Operation	Error rate	Duration
Two-qubit gate	$p_{2q} = 0.027$	$322.5\,\mu\text{s}$
Single-qubit gate	$p_{1q} = 0.0036$	$25\,\mu\text{s}$
Measurement	$p_{\text{meas}} = 0.003$	
Preparation	$p_{\text{init}} = 0.003$	
Mid-circuit detection	$p^{(x)}_{\text{mid-circ}} = 0.011$ $p^{(y)}_{\text{mid-circ}} = 0.024$ $p^{(z)}_{\text{mid-circ}} = 0.035$	

Table A.3: Error rates and duration of operations on a trapped-ion quantum processor. These values correspond to the trapped-ion setup that was used in the experiments and are used in the following simulations. Gate durations are increased by $10\,\mu\text{s}$ compared to the values given in Appendix A.3 to account for settling times of the addressing optics, when the ion being addressed is changed.

on these operations are modeled by applying X errors after state preparations and before measurements with a probability p_{init} and p_{meas}, respectively. Furthermore, we include noise on idling qubits, which are not acted upon with a gate at a given step of the protocol. Since the dominating noise on idling qubits is dephasing due to magnetic field fluctuations, which limits the decoherence time $T_2 \approx 50\,\text{ms}$, we model the noise channel for idling qubits by Pauli-Z faults as

$$\mathcal{E}_{\text{idle}}(\rho) = (1 - p_{\text{idle}})\rho + p_{\text{idle}} Z\rho Z. \tag{A.4}$$

The probability p_{idle} of a Z fault on each idling qubit depends on the execution time t of the performed gate and is given by

$$p_{\text{idle}} = \frac{1}{2}\left[1 - \exp\left(-\frac{t}{T_2}\right)\right]. \tag{A.5}$$

Mid-circuit detections are performed in order to perform multiple rounds of EC, where auxiliary qubits are measured while keeping the data qubits intact. The idling data qubits experience noise during this mid-circuit detection, which we model as an asymmetric depolarizing channel on all data qubits. We estimate the individual Pauli $p^{(x)}_{\text{mid-circ}}, p^{(y)}_{\text{mid-circ}}, p^{(z)}_{\text{mid-circ}}$ error rates in this channel based on single-qubit process tomography. All error rates and gate times are summarized in Table A.3.

For the extrapolation to the limiting case of small gate error rates we additionally perform simulations with a technique known as fault path counting [264]. The goal here is to determine the leading order contributions to the logical infidelity at low physical error rates. Since single faults cannot lead to logical errors by design, this function will be dominated by second order terms when expanding as a polynomial of physical error rates. We focus on the gate errors p_{2q} and p_{1q} and set all other error sources to zero. This implies the leading terms of the function describing the infidelity can be written as $\text{infid}(p_{2q}, p_{1q}) = c_2 p_{2q}^2 + c_1 p_{1q}^2 + c_{12} p_{1q} p_{2q} + \mathcal{O}(p^3)$.

The coefficients c_i are related to the number of corresponding fault configurations resulting in logical failure. For example, c_2 is the sum over all configurations where placing faults on any two two-qubit gates in a given circuit (-sequence) results in a logical error; analogously for c_1 when placing two faults on any two single-qubit gates and c_{12} when placing one two-qubit gate and one single-qubit gate fault. The coefficients furthermore contain a normalization since we write the polynomial as a function of p_{1q} and p_{2q}, which determine the microscopic fault probabilities of a single-qubit gate fault as $p_{1q}/3$ and a two-qubit gate fault as $p_{2q}/15$ via Eqn. A.3. To determine the logical outcome, each fault configuration has to be propagated to the end of the circuit. Fault path counting is viable at low physical error rates when higher order contributions are negligible. In this regime, this allows us to determine the coefficients of the polynomial such that we can explore the influence of different error sources. The coefficients are given in Table A.4. As shown in Figure A.6, we compare Steane and flagged

	c_2	c_1	c_{12}
Steane EC	70.3	684.2	438.3
Flagged EC	204.5	178.7	543.6

Table A.4: Coefficients obtained by fault path counting simulations. As described in the main text, c_k related to the number of fault configurations of two faults leading to a logical error weighted with the probability of occurrence. These coefficients determine the leading order of the polynomial describing the infidelity of each EC scheme at low error rates.

syndrome readout schemes and plot the ratio of infidelities as a function of single and two-qubit gate error strength. We find that there are two regimes where either method is preferable, strikingly for systems dominated by the two-qubit gate error $p_{2q} \gg p_{1q}$ our results show an advantage of Steane over flagged syndrome readout across the board.

A.3 Experimental methods

All experiments presented in this manuscript are conducted on a trapped-ion quantum processor [84]. In a non-segmented macroscopic Paul trap a string of sixteen $^{40}Ca^{+}$ ions is trapped with inter-ion spacing ranging from $3.8\,\mu m$ to $6.0\,\mu m$, set by trap parameters. The COM modes of the ion string in the pseudo-harmonic potential of the trap have oscillation frequencies of $\omega_z = 2\pi \times 369\,\mathrm{kHz}$ and $\omega_x = 2\pi \times 3086\,\mathrm{kHz}$, $\omega_y = 2\pi \times 3165\,\mathrm{kHz}$ for the direction along the ion string (referred to as axial) and the two perpendicular directions (referred to as radial), respectively. The first step of every experimental cycle is a Doppler cooling pulse acting on the $|4^2S_{1/2}\rangle \leftrightarrow |4^2P_{1/2}\rangle$ transition at a wavelength of $397\,\mathrm{nm}$ (see Figure A.8) with a duration of $500\,\mu s$. Simultaneously the ion chain is illuminated with light at $866\,\mathrm{nm}$ to avoid pumping to the dark state $|3^2D_{3/2}\rangle$ by driving any population trapped there back to the state $|4^2S_{1/2}\rangle$. Both laser beams act on all ions simultaneously and have spatial overlap with all motional modes. The two lowest-frequency axial modes and all 32 radial modes are further cooled close to the ground state by resolved sideband cooling [83]. The ions are illuminated by a laser beam red-detuned by the respective motional frequency from the $|4^2S_{1/2}, m_J = -1/2\rangle \leftrightarrow |3^2D_{5/2}, m_J = -5/2\rangle$ transition at $729\,\mathrm{nm}$. For the axial modes the $729\,\mathrm{nm}$ laser propagates along the ion string, whereas the radial modes are cooled by a steerable, addressed $729\,\mathrm{nm}$ beam illuminating only one ion at a time from a direction perpendicular to the ion string. To cool the radial modes the ion having the strongest

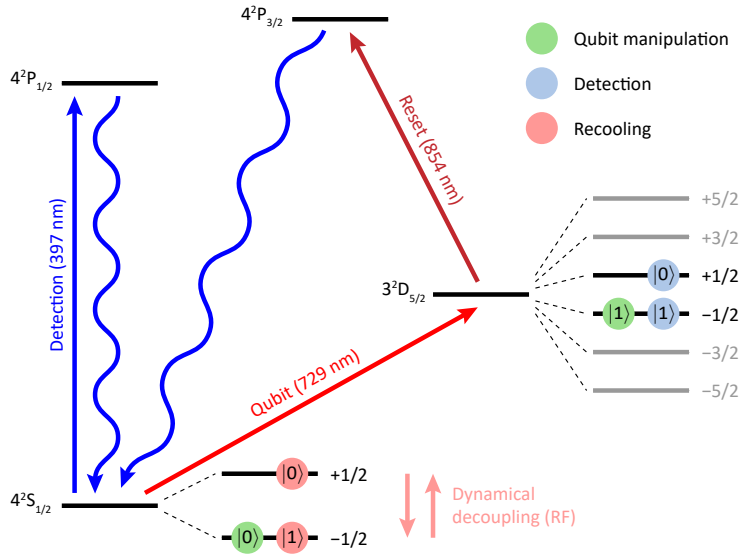

Figure A.8: Energy scheme of $^{40}Ca^+$. Lasers at wavelengths of 729 nm, 854 nm and 397 nm are used for qubit manipulation, qubit reset, and Doppler cooling, respectively. Different encodings are used for the data qubits in different stages of a circuit. Gates are applied to the optical qubit encoding (green symbols). For mid-circuit measurements the data qubits are encoded in different Zeeman sublevels of the states $|0\rangle = |4^2S_{1/2}\rangle$ and $|0\rangle = |3^2D_{5/2}\rangle$ to avoid interaction with laser light for qubit state detection, reset, and recooling illuminating the whole register. Furthermore, a RF drive is available for DD when the qubit is encoded in the Zeeman manifold of the electronic ground state during the sideband recooling stage of mid-circuit measurements.

coupling to the respective motional mode is illuminated. All modes within approximately 50 kHz from the laser frequency are cooled, which allows us to cool 34 modes with only 15 frequency settings. To accelerate the cooling process ions excited to the $|3^2D_{5/2}\rangle$ state are pumped to the state $|4^2P_{3/2}\rangle$ using laser light at 854 nm from where they rapidly decay to one of the ground states. This sideband cooling cycle is repeated up to five times depending on the mode, where one cycle takes 500 µs. The mean phonon number of the COM mode with mode frequency $\omega_y = 2\pi \times 3165$ kHz after sideband cooling is $\bar{n} = 0.05(1)$ and exhibits a heating rate of 3.6(2) phonons per second. For the rocking mode along the same direction, the mode closest in frequency to the COM mode with a relative detuning of 23 kHz, the mean phonon number after sideband cooling is $\bar{n} = 0.02(1)$. Within 50 ms no heating is observed on this mode. This behavior is expected in macroscopic ion traps, as in such traps typically the noise leading to motional heating is spatially correlated along the ion string [265]. Measuring the mean phonon number and heating rate for other motional modes is not trivial due to the crowding of the modes in frequency space. However, we assume that the contribution of those modes to the entangling gate dynamics is negligible. The finalizing step of the state preparation procedure is to prepare all ions in $|4^2S_{1/2}, m_J = -1/2\rangle$ by exciting the transition $|4^2S_{1/2}, m_J = +1/2\rangle \leftrightarrow |3^2D_{5/2}, m_J = +1/2\rangle$ with axial 729 nm light while speeding up the decay to the ground state using 854 nm light, as for sideband cooling.

The coherent manipulation of the individual qubits in the register subsequent to state preparation is exclusively done via tightly focused laser pulses with a propagation direction perpendicular to the ion string addressing the qubit transition $|4^2S_{1/2}, m_J = -1/2\rangle \leftrightarrow |3^2D_{5/2}, m_J = -1/2\rangle$. The experimental setup allows us to illuminate up to two ions simul-

taneously. Addressing a single ion i with light resonant to the qubit transition allows us to implement operations of the form $R_\phi^{(i)}(\theta) = \exp\left(-\mathrm{i}\frac{\theta}{2}(\sigma_x^{(i)}\cos\phi + \sigma_y^{(i)}\sin\phi)\right)$, where $\sigma_\cdot$ are single-qubit Pauli matrices. The rotation axis ϕ can be controlled via the light phase, the rotation angle θ via light intensity and pulse duration. The duration of a pulse with $\theta = \frac{\pi}{2}$ is $15\,\mu\mathrm{s}$. Together with virtual Z rotations [85] this operation allows us to implement arbitrary single-qubit unitary operations. The gate set is completed by adding the entangling MS interaction, where any two ions may be illuminated with bichromatic light slightly detuned from the motional sidebands corresponding to the radial mode at frequency ω_y [168]. Adjusting the gate time to $t_{\mathrm{gate}} = \frac{1}{\delta} = 312.5\,\mu\mathrm{s}$, where δ is the detuning from the motional sidebands, implements the gate $\mathrm{MS}^{(ij)} = \exp(-\mathrm{i}\frac{\pi}{4}\sigma_x^{(i)}\sigma_x^{(j)})$, which is equivalent to the CNOT gate up to single-qubit rotations [88]. Qubit state readout after application of a gate sequence to the qubit register is implemented by simultaneously illuminating the whole register with laser light at wavelengths of $397\,\mathrm{nm}$ and $866\,\mathrm{nm}$. While qubits projected to the computational state $|0\rangle = |4^2\mathrm{S}_{1/2}, m_J = -1/2\rangle$ repeatedly emit photons at a wavelength of $397\,\mathrm{nm}$ after being excited to $|4^2\mathrm{P}_{1/2}\rangle$ and returning to $|4^2\mathrm{S}_{1/2}\rangle$, qubits projected to $|1\rangle = |4^2\mathrm{D}_{5/2}, m_J = -1/2\rangle$ are not affected by those light fields and do not emit photons [83]. Imaging the ion string on an EMCCD camera allows for the spatially resolved detection of light emission from the ion string, and therefore the computational basis bit string the qubit register was projected into can be reconstructed.

Error rates for single-qubit gates are estimated from single-qubit randomized benchmarking on the 16-qubit register. We find an error rate per gate averaged over all 16 qubits of 0.0036 with a standard deviation of 0.0004. The two-qubit error rate is estimated by preparing a 16-qubit GHZ state and comparing the experimentally measured fidelity to simulated fidelities from numerical simulations accounting for errors on single-qubit gates, two-qubit gates, initialization and measurements. As outlined in previous work of ours [266], for the analysis of the fidelity of the prepared GHZ state we perform two measurements: The probabilities to project to one of the two basis states $|0\rangle^{\otimes 16}$ and $|1\rangle^{\otimes 16}$ are determined by a direct projective measurement in the Z basis after preparation. The off-diagonal elements of the density matrix of the GHZ state instead are measured by applying single-qubit gates $R_\varphi^{(i)}(\pi/2)$ to all qubits after preparing the GHZ state. For different phases φ the parity of the prepared state is measured via a projective measurement and a sinusoidal model is fitted to the observed parity oscillations [228]. The mean of the sum of the populations in $|0\rangle^{\otimes 16}$ and $|1\rangle^{\otimes 16}$ and the contrast of the parity oscillations of the coherence measurement gives the fidelity of the GHZ state. Averaging over multiple instances of the prepared GHZ state over the course of around 13 hours gives a mean fidelity of 0.54 with a standard deviation of 0.04, corresponding to an estimated two-qubit error rate $p_{2q} = 0.027$ with a standard deviation of 0.005. Typical values for qubit initialization and measurement fault rates are $p_{\mathrm{init}} = p_{\mathrm{meas}} = 0.003$ in the device under consideration [83].

A.3.1 *Mid-circuit measurements*

For mid-circuit measurements only a part of the register, referred to as auxiliary qubits, is supposed to be projected into the computational basis, while a part of the register, referred to as data qubits, is ideally unaffected. To avoid projecting the data qubits, their qubit encoding is transferred to $|0\rangle_{\mathrm{data,det}} = |3^2\mathrm{D}_{5/2}, m_J = +1/2\rangle$ and $|1\rangle_{\mathrm{data,det}} = |3^2\mathrm{D}_{5/2}, m_J = -1/2\rangle$ by first applying an RF pulse with a pulse area of π (π-pulse) that transfers the population

in $|4^2\mathrm{S}_{1/2}, m_J = -1/2\rangle$ to $|4^2\mathrm{S}_{1/2}, m_J = +1/2\rangle$ followed by a π-pulse on the transition $|4^2\mathrm{S}_{1/2}, m_J = +1/2\rangle \leftrightarrow |3^2\mathrm{D}_{5/2}, m_J = +1/2\rangle$ for all data qubits. Subsequently the same detection pulse as for the final detection is applied. Recoil of scattered photons from bright auxiliary qubits heat up the ion string, which would lead to reduced gate fidelities after the mid-circuit measurement. Therefore a Doppler cooling pulse is applied. To recool the ion string close to the motional ground state an additional sideband cooling step is necessary. The data qubit encoding is transferred to $|0\rangle_{\mathrm{data,cool}} = |4^2\mathrm{S}_{1/2}, m_J = +1/2\rangle$ and $|1\rangle_{\mathrm{data,cool}} = |4^2\mathrm{S}_{1/2}, m_J = -1/2\rangle$ by applying π-pulses on the transitions associated to the states $|4^2\mathrm{S}_{1/2}, m_J = \pm 1/2\rangle$ and $|3^2\mathrm{D}_{5/2}, m_J = \pm 1/2\rangle$ as sideband cooling involves illuminating the ion string with $854\,\mathrm{nm}$ light, which would otherwise destroy any information encoded in the $|3^2\mathrm{D}_{5/2}\rangle$ manifold. Then the same sideband cooling pulse scheme as for state preparation is applied, apart from the fact that axial modes are not cooled and ions encoding data qubits are excluded from the set of allowed cooling ions. Cooling axial modes would require using the axial $729\,\mathrm{nm}$ beam, as the addressed beam does not have overlap with the direction of motion of axial modes, and therefore would also affect data qubits. Prior to every sideband cooling pulse the respective ion is pumped to $|4^2\mathrm{S}_{1/2}, m_J = -1/2\rangle$ by applying two repetitions of a π-pulse on the transition $|4^2\mathrm{S}_{1/2}, m_J = +1/2\rangle \leftrightarrow |3^2\mathrm{D}_{5/2}, m_J = -3/2\rangle$ followed by a $5\,\mu\mathrm{s}$ pulse of $854\,\mathrm{nm}$ light. The mid-circuit measurement is finalized by repeating the pumping cycle for all auxiliary qubits that are supposed to be reused four times, and restoring the encoding of the data qubits by applying a π-pulse on the transition $|4^2\mathrm{S}_{1/2}, m_J = -1/2\rangle \leftrightarrow |3^2\mathrm{D}_{5/2}, m_J = -1/2\rangle$ followed by an RF π-pulse transferring the population in $|4^2\mathrm{S}_{1/2}, m_J = +1/2\rangle$ to $|4^2\mathrm{S}_{1/2}, m_J = -1/2\rangle$. The mid-circuit sideband cooling procedure requires around $15\,\mathrm{ms}$. A detailed timeline of a mid-circuit measurement is shown in Figure A.9.

A.3.2 *Dynamical decoupling*

The coherence time in the optical-qubit encoding and the ground-state encoding is on the order of $50\,\mathrm{ms}$ and $5\,\mathrm{ms}$, respectively. Idling data qubits would thus suffer from significant dephasing during sideband cooling if no countermeasures were taken. Therefore a DD sequence is performed on the data qubits during the recooling procedure to preserve coherence. This decoupling is implemented with an RF antenna radiating at $16.7\,\mathrm{MHz}$ acting on the entire register simultaneously which drives the transition between the two ground states, where the data qubits are encoded during sideband cooling. The antenna with a diameter of about $2\,\mathrm{cm}$ is connected to a resonant circuit and is mounted outside the vacuum chamber as close as possible to the ion string. Driving the resonant antenna with a power of approximately $2\,\mathrm{W}$ allows us to implement a bit flip in $35\,\mu\mathrm{s}$. The maximum relative deviation in Rabi frequency in the 16-qubit register is $\frac{\Omega_{\max}-\Omega_{\min}}{\Omega_{\min}} = 0.002(1)$, where $\Omega_{\max}$ and $\Omega_{\min}$ are the maximum and minimum Rabi frequencies, respectively. The RF source driving the antenna is a direct digital synthesizer integrated in the same control hardware that also generates the RF pulses driving AOMs used to address the optical-qubit transition. The phase of the pulses generated by these RF sources is defined with respect to a common reference enabling coherent operation across different direct digital synthesizer channels. A decoupling pulse is applied approximately every millisecond in between cooling pulses for different motional modes. Under the application of this decoupling scheme we do not see any significant dephasing up to a waiting time of $60\,\mathrm{ms}$, which indicates an effective coherence time larger than $1\,\mathrm{s}$. The effect of a full mid-circuit measurement on data

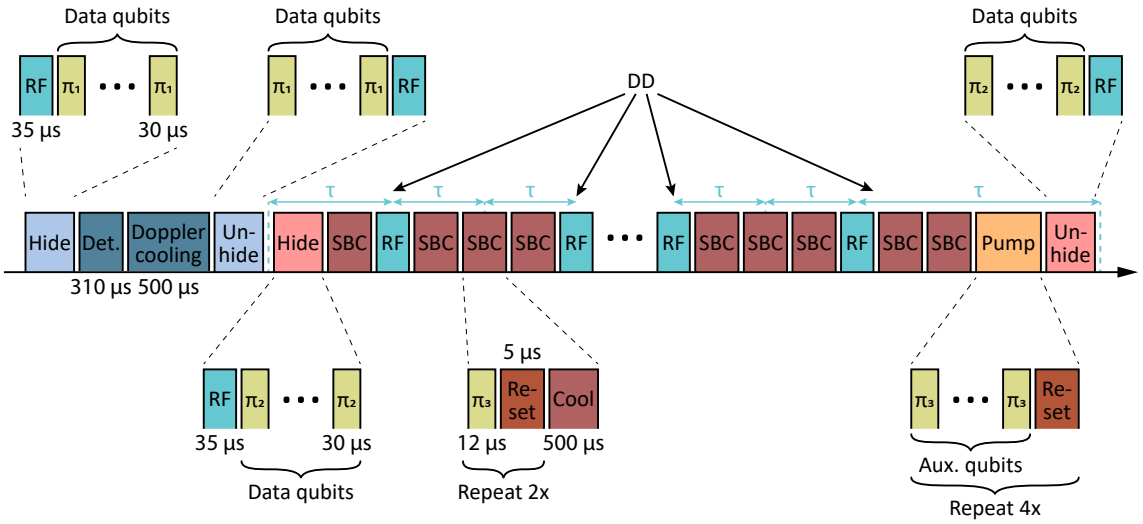

Figure A.9: Sequence timing diagram of a mid-circuit measurement. The first light blue pulse labeled 'Hide' transfers the encoding of the data qubits from the encoding labeled with green symbols in Figure A.8 to the encoding labeled with blue symbols. Instead of directly applying a π-pulse labeled 'π_1' on the transition $|4^2\mathrm{S}_{1/2}, m_J = -1/2\rangle \leftrightarrow |3^2\mathrm{D}_{5/2}, m_J = +1/2\rangle$ an RF pulse with pulse area π followed by π-pulses on the transition $|4^2\mathrm{S}_{1/2}, m_J = +1/2\rangle \leftrightarrow |3^2\mathrm{D}_{5/2}, m_J = +1/2\rangle$ are applied. As the coupling on the $\delta m_J = 0$ transition is significantly higher, this allows us to speed up the hiding process. After applying detection and Doppler cooling pulses the encoding of the data qubits is returned to the encoding shown with green symbols by applying the reverted hiding sequence. Subsequently, the encoding of the data qubits is transferred to the encoding shown with red symbols by applying an RF pulse with pulse area π followed by π-pulses labeled 'π_2' on the transition $|4^2\mathrm{S}_{1/2}, m_J = -1/2\rangle \leftrightarrow |3^2\mathrm{D}_{5/2}, m_J = -1/2\rangle$. Although the two RF pulses implement the identity we do not omit them to retain symmetry with the unhiding pulses at the end of the sequence. Before each sideband cooling cycle a π-pulses labeled 'π_3' on the transition $|4^2\mathrm{S}_{1/2}, m_J = -1/2\rangle \leftrightarrow |3^2\mathrm{D}_{5/2}, m_J = -1/2\rangle$ is applied to the auxiliary qubit used for cooling in the respective sideband cooling cycle. Subsequently a pulse labeled 'Reset' (simultaneous illumination with $854\,\mathrm{nm}$ and $866\,\mathrm{nm}$ light of the entire register) is applied. Together, these two pulses ensure that the auxiliary qubit population is transferred to $|4^2\mathrm{S}_{1/2}, m_J = -1/2\rangle$ and sideband cooling can operate efficiently. After the last sideband cooling cycle all auxiliary qubits that are supposed to be reused are reinitialized to $|4^2\mathrm{S}_{1/2}, m_J = -1/2\rangle$ using the same pulse sequence that optically pumps the population before each sideband cooling cycle. The mid-circuit measurement procedure is concluded with the unhiding sequence returning the data qubit encoding to the encoding labeled with green symbols in Figure A.8. In between sideband cooling cycles RF pulses are applied for DD. The length of the pulse labeled 'Cool' is varied for the first and last sideband cooling cycle to ensure that the refocusing time τ is kept constant for hiding and pumping sequences involving different data and auxiliary qubit numbers.

qubits is characterized via single-qubit process tomography of the data qubits using linear reconstruction. Figure 4.17C shows the chi matrix representation [45] of the process averaged over all data qubits in the Pauli basis, whereas Figure A.10 shows the underlying process matrices for the individual data qubits. The average fidelity is 0.930 with a standard deviation of 0.011. The averaged process matrix data is also used to inform the error model described in Appendix A.2, as there are no salient differences between the individual matrices. These error probabilities are extracted from the experimental process matrix, quantifying the effect of mid-circuit measurements on data qubits, shown in Figure 4.17C.

The DD scheme described above can only be applied when the data qubits are encoded in the ground state, shown with red symbols in Figure A.8. For detection and Doppler cooling the data qubits are transferred to the encoding shown with blue symbols, which is a factor of $\approx \frac{2}{1.2}$ less sensitive to magnetic field fluctuations compared to the ground-state encoding given by the g factors of the states $|4^2\mathrm{S}_{1/2}\rangle$ and $|3^2\mathrm{D}_{5/2}\rangle$. Therefore, assuming a coherence time $T_2 = 8\,\mathrm{ms}$ limited by magnetic field fluctuations and an idling duration of $0.8\,\mathrm{ms}$ the dephasing error probability of the data qubits during detection and Doppler cooling of the auxiliary qubits is 0.05 according to Eqn. A.5. Increasing the coherence time to $T_2 = 1\,\mathrm{s}$ would decrease the error rate on the data qubits to 0.0004. Likely another major contribution to the overall error affecting data qubits during mid-circuit measurements is crosstalk of hiding pulses, where the Rabi frequency of undesired crosstalk is on the order of 100 times smaller than the Rabi frequency on the target ion. Mitigating the effect of hiding pulses on neighboring ions using composite pulses together with an extended coherence time could significantly reduce the error rate on data qubits for mid-circuit measurements.

A.4 Uncertainty estimation

The uncertainties given in this work account for statistical errors under the assumption of an underlying binomial distribution of the measurement outcomes. We make use of the Wilson score interval [267] in order to get error intervals in the interval $[0, 1]$ even for probabilities close to 0 or 1. The upper (referred to as '$+$' in the formula) and lower ('$-$') bound of the interval for a probability p measured with N shots are given by

$$p_\pm(p) = \frac{1}{1 + \frac{z(\alpha)^2}{N}} \left(p + \frac{z(\alpha)^2}{2N} \pm z(\alpha) \sqrt{\frac{p(1-p)}{N} + \frac{z(\alpha)^2}{4N^2}} \right), \tag{A.6}$$

where $z(\alpha) = \Phi^{-1}\left(1 - \frac{\alpha}{2}\right)$ with Φ^{-1} being the quantile function of the normal distribution and α being the target error rate. We choose $z = 1$ which corresponds to a confidence level of $1 - \alpha \approx 0.68$.

A.5 Logical fidelity

The figure of merit for the quality of a logical state we choose in this work is the logical fidelity, which is the probability of retrieving the correct logical state. A single logical qubit state ρ is given by

$$\rho = \frac{1}{2} \left(\sigma_0 + \langle X_L \rangle \sigma_1 + \langle Y_L \rangle \sigma_2 + \langle Z_L \rangle \sigma_3 \right), \tag{A.7}$$

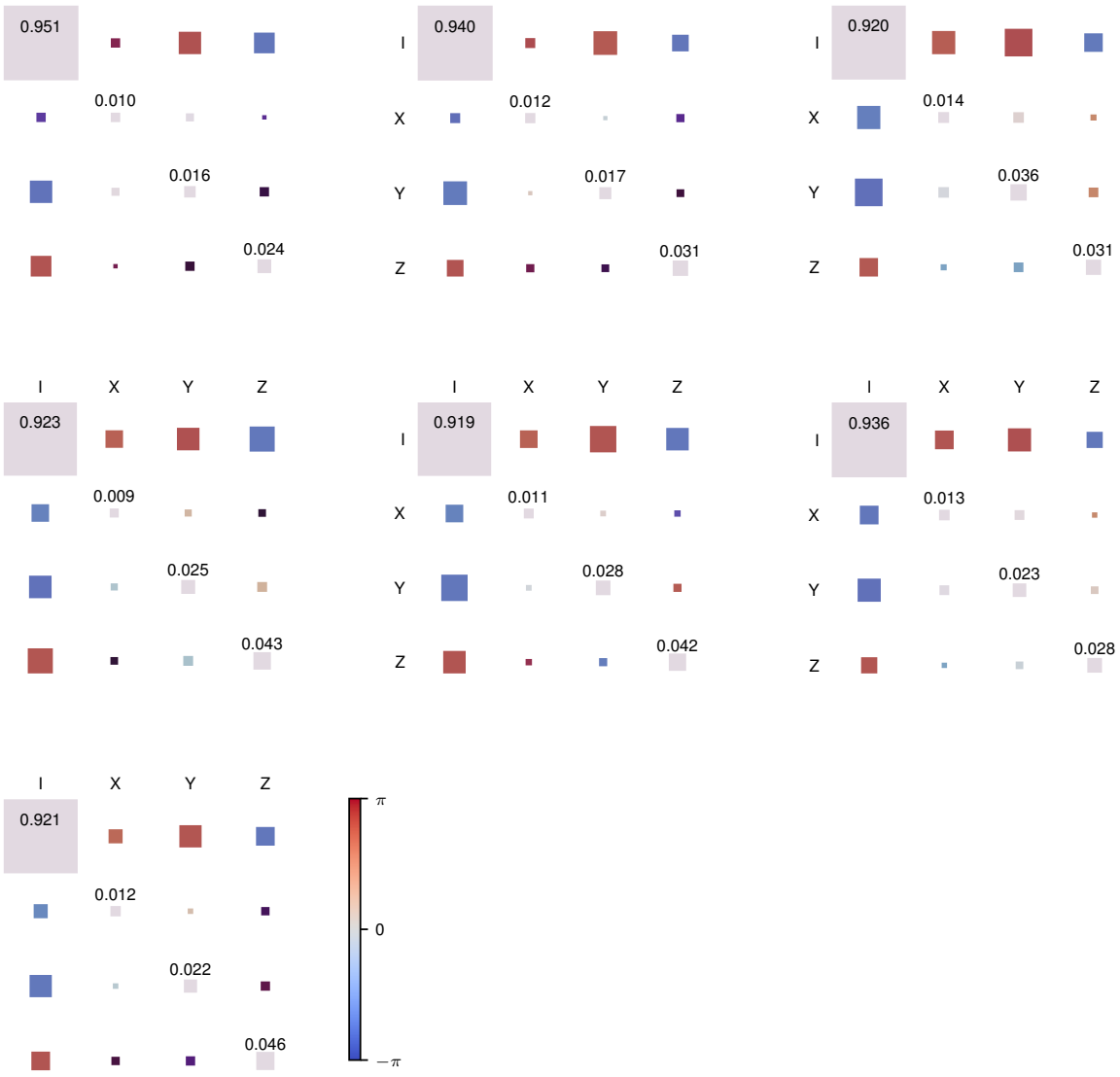

Figure A.10: Single-qubit process tomography of mid-circuit measurements. Chi matrix representation of the process acting on data qubits during mid-circuit measurements shown for all data qubits individually. The process fidelity ranges from 0.919 to 0.951 with an average of 0.930 and a standard deviation of 0.011. The area and the color coding of the squares correspond to the absolute value and the phase of the elements of the chi matrix, respectively.

where X_L, Y_L and Z_L are the logical operators and $\sigma_\cdot$ are single-qubit Pauli matrices. Then the logical fidelity of ρ with respect to a logical target state ρ_t after performing an ideal round of QEC is given by

$$\mathcal{F}_t(\rho) = \langle P_t \rangle = \mathrm{tr}\left(P_t \rho\right), \tag{A.8}$$

with P_t being the projector on the logical target state. For the logical Pauli states $|0\rangle_L$ and $|+\rangle_L$ the projectors read

$$P_{|0\rangle_L} = \frac{1}{2}\left(\mathbb{1} + Z_L\right) \quad \text{and} \quad P_{|+\rangle_L} = \frac{1}{2}\left(\mathbb{1} + X_L\right), \tag{A.9}$$

leading to the expressions

$$\mathcal{F}_{|0\rangle_L} = \frac{1}{2}\left(1 + \langle Z_L \rangle\right) \quad \text{and} \quad \mathcal{F}_{|+\rangle_L} = \frac{1}{2}\left(1 + \langle X_L \rangle\right) \tag{A.10}$$

for the logical fidelities of the logical states considered in this work.

A.6 Additional results

In addition to the implementation of multiple rounds of Steane QEC on the seven-qubit color code we realize repetitive readout of a single type of stabilizer generators, corresponding to executing either the first or the second half of the scheme displayed in Figure 4.16C. The syndrome extraction is applied to a logical Pauli state sensitive to the corrections suggested by the syndrome measurement, e.g. Z-type stabilizer generators are measured for the input state $|0\rangle_L$ and X-type stabilizer generators are measured for the input state $|+\rangle_L$. We refer to one readout as a half-cycle of QEC. We implement up to five half-cycles of QEC with the corresponding logical fidelities being shown in Figure A.11. Again we see good agreement of experiments with data from numerical simulations.

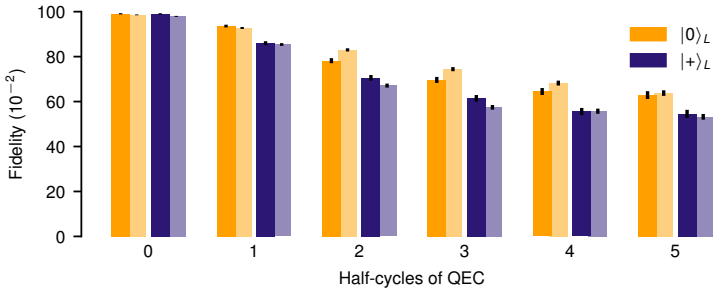

Figure A.11: Logical fidelities for half-cycles of syndrome extraction on the seven-qubit color code. Logical fidelities obtained from Steane-type QEC for the logical input states $|0\rangle_L$ and $|+\rangle_L$. For the input states $|0\rangle_L$ and $|+\rangle_L$ only the syndrome given by the Z-type and X-type stabilizer generators, respectively, is extracted multiple times. Half-cycle 0 corresponds to the encoding of the logical state with no extra round of QEC. The experimental and simulation results are depicted with darker and lighter shades, respectively.

B

METHODS SECTION TO PUBLICATION *DEMONSTRATION OF FAULT-TOLERANT UNIVERSAL QUANTUM GATE OPERATIONS*

B.1 Trapping and cooling

The experiments described in this work are performed on a trapped ion quantum computer. $^{40}Ca^{+}$ ions are trapped in a macroscopic Paul trap and the optical qubit is encoded in two Zeeman sublevels of the $4S_{1/2}$ and $3D_{5/2}$ electronic states. Further details on the experimental setup can be found in the recent publication [84].

For this work, the ion crystal is configured to consist of 16 ions with an axial COM mode frequency $\omega_{\text{ax, COM}} = 2\pi \times 400\,\text{kHz}$ and radial COM mode frequencies of $\omega_{\text{rad1,COM}} = 2\pi \times 3270\,\text{kHz}$ and $\omega_{\text{rad2,COM}} = 2\pi \times 3100\,\text{kHz}$. Before executing any gate sequence, the radial motional modes of the ion chain are cooled nearly to the ground state via Doppler cooling for $2\,\text{ms}$, followed by resolved sideband cooling for $15\,\text{ms}$. Subsequently, the qubits are initialized via optical pumping to the $4S_{1/2,m_j=-1/2}$ ground state.

B.2 Qubit manipulation

Coherent qubit manipulation is performed by individually addressable laser pulses at a wavelength of $729\,\text{nm}$. Pulses resonant with the $4S_{1/2,m_j=-1/2}$ to $3D_{5/2,m_j=-1/2}$ transition enable rotations around an arbitrary axis in the equatorial plane of the Bloch sphere, where the angle between the rotation axis and the X axis is determined by the phase ϕ of the light pulse. Those operations are described by $R_\phi^{(i)}(\theta) = \exp(-i\frac{\theta}{2}(\sigma_x^{(i)}\cos\phi - \sigma_y^{(i)}\sin\phi))$, where $\sigma_x^{(i)}$ and $\sigma_y^{(i)}$ are single-qubit Pauli matrices acting on qubit i. Rotations around the X axis R_x (Y axis R_y) can be implemented by setting ϕ to 0 ($-\pi/2$). A pulse length of $15\,\mu\text{s}$ is required to implement a $\pi/2$-pulse on a single qubit. Randomized benchmarking for single-qubit gates in the 16-ion chain yields an average fidelity of a $\pi/2$-gate of $99.51 \pm 0.05\%$. Additionally, rotations around the Z axis of the Bloch sphere for a specific ion can be implemented *virtually* by introducing a phase shift to all subsequent pulses applied to the ion.

Two-qubit gates are realized by the MS interaction [168] described by $\text{MS}_{ij}(\theta) = \exp(-i\frac{\theta}{2}\sigma_x^{(i)}\sigma_x^{(j)})$. An arbitrary pair of ions is addressed with bichromatic beams slightly detuned from the radial COM mode $\omega_{\text{rad1,COM}}$. Gate time $t_{\text{gate}} = 270\,\mu\text{s}$ and detuning from the COM mode $\Delta \approx 2\pi \times 3.7\,\text{kHz}$ are chosen to allow for simultaneous decoupling of the two closest radial modes $\omega_{\text{rad1,COM}}$, $\omega_{\text{rad1,2}}$ at the end of the interaction. An additional (third) frequency tone, $1.05\,\text{MHz}$ blue-detuned from the carrier transition, compensates the AC Stark shift induced by the bichromatic light field. For $\theta = \pi/2$ this results in an XX gate which is equivalent to a CNOT gate up to single-qubit rotations [88]. A decomposition of

a CNOT gate acting on qubits i and j into an XX gate and local operations with a freely selectable parameter $v = \pm 1$ is the following:

$$\mathrm{CNOT}_{ij} = R_y^i(-v \cdot \pi/2) \cdot R_x^i(\pi/2) \cdot R_x^j(v \cdot \pi/2) \cdot \mathrm{MS}_{ij}(-\pi/2) \cdot R_y^i(v \cdot \pi/2). \tag{B.1}$$

The average Bell state fidelity in a chain of 16 ions is about 97.5% for entangling gates between neighbouring ions.

B.3 State readout

Qubit state readout is performed by illuminating the ions with a light field resonant to the $4S_{1/2}$ to $4P_{1/2}$ transition and collect scattered photons. Due to technical limitations imposed by the EMCCD camera, site-resolved state readout is only possible after the coherent evolution. In-sequence detection events utilizing an avalanche photodiode (APD) can only reveal the number of excitations present in the ion string. A subset of qubits can be read out in-sequence by shelving the population in the $4S$ state of all other ions to the $3D_{5/2,m_j=-3/2}$ Zeeman sublevel prior to the illumination of the ion string with the detection light field. This technique is used for the measurements presented in Section 5.3.4. For the FT initialization of the magic state the auxiliary qubits are measured via the APD. If there are no excited ions detected, the protocol is continued by reusing the measured ions for encoding a second logical qubit state and injecting the magic state. After an illumination time of $2\,\mathrm{ms}$ for the EMCCD measurement and $0.5\,\mathrm{ms}$ for the APD measurement a readout fidelity of $> 99.7\%$ is achieved, where this number refers to the single-qubit readout fidelity for EMCCD measurements and and the discrimination between 0 and > 0 excited qubits for APD measurements.

If the qubit manipulation is supposed to be continued after a detection event that scattered photons, meaning that a qubit was projected to the S state, in-sequence recooling is required as the scattered photons heat up the ion chain, which would prevent subsequent gate operations with high-fidelity. The experimental setup we used to conduct the experiments presented in this work currently does not support in-sequence cooling, therefore preventing the implementation of repeated rounds of EC. We note that upgrades to the setup facilitating in-sequence cooling are about to be carried out and that in-sequence detection and recooling were already implemented in a different recent experiment of the research group [181].

B.4 Error estimation

The errors given throughout this work solely account for statistical errors. For the estimation of the statistical fluctuations all measured outcomes are resampled from a multinomial distribution according to their respective probabilities. The stated errors in the text but also errorbars given in figures correspond to 68% confidence intervals extracted from the resampled datasets.

An additional source of errors are temporal fluctuations of the experimental performance due to varying environmental parameters like magnetic field or ambient temperature. Such fluctuations on the timescale of minutes to hours explain the increased logical infidelity of

$|0\rangle_L$ and $|1\rangle_L$, as compared to the other Pauli eigenstates in Figure 5.6. In our experiment the magnitude of these errors can exceed the contribution from statistical errors.

B.5 Simulation methods

Theoretical simulation results presented in the main text are obtained using stabilizer simulations and statevector simulations for the logical Pauli states and magic state preparation and injection circuits, respectively. We use the "Performance Estimator of Codes On Surfaces" (PECOS) package due to its flexibility in analyzing error propagation in different error models through MC simulation (publicly available at https://github.com/PECOS-packages/PECOS) [198]. In these simulations any ideal circuit element is replaced by a faulty element, consisting of the ideal operation followed by an error operator, with a given probability.

We model circuit errors as depolarizing errors, which reproduces well the experimentally observed infidelities despite its conceptual simplicity which does not take the microscopic physical processes underlying noisy gates and operations in the ion trap into account explicitly. Noise is applied in simulations by randomly placing Pauli errors E according to the experimental physical error rates after every single-qubit and two-qubit gate with their respective error rates p_1 and p_2. These errors can be

$$E_1 \in \{\sigma_k, \forall k \in \{1,2,3\}\} \tag{B.2}$$
$$E_2 \in \{\sigma_k \otimes \sigma_l, \forall k,l \in \{0,1,2,3\}\} \setminus \{I \otimes I\} \tag{B.3}$$

where $\sigma_k = \{I, X, Y, Z\}$ with $k = 0,1,2,3$ are the Pauli matrices. The error channels for our depolarizing noise model read

$$\mathcal{E}_1(\rho) = (1-p_1)\rho + \frac{p_1}{3}(X\rho X + Y\rho Y + Z\rho Z) \tag{B.4}$$
$$\mathcal{E}_2(\rho) = (1-p_2)\rho + \frac{p_2}{15}\left[\sum_{i,j=0}^{3}(\sigma_i \rho \sigma_j) - \rho\right] \tag{B.5}$$

so that any single-qubit error is applied uniformly to the ideal gate with equal probability $p_1/3$ and the single-qubit gate is executed ideally with probability $1-p_1$; two-qubit errors are applied uniformly after the ideal two-qubit gates with equal probability $p_2/15$ and any two-qubit gate is executed ideally with probability $1-p_2$. Results of qubit initializations and measurements are flipped with respective probabilities p_i and p_m. In all simulations we used physical error rates of

$$\begin{aligned} p_1 &= 0.005 \\ p_2 &= 0.025 \\ p_i &= p_m = 0.003 \end{aligned} \tag{B.6}$$

for the corresponding operations.

The logical Pauli state encoding circuits (Figure 5.6a) and logical CNOT circuit (Figure 5.7a) are simulated efficiently using stabilizer simulations. This is possible since we are

preparing eigenstates of Pauli operators, measuring exclusively in one of three possible Pauli bases here and these circuits only contain Clifford gates.

This description as stabilizer states breaks down when arbitrary single-qubit rotations are to be performed by the circuit, especially with regards to the magic state, Eqn. 5.15, that generates the non-Clifford T-gate. The circuits that fault-tolerantly prepare the logical magic state (Figure 5.8a) and perform the gate teleportation (Figure 5.9a) contain non-Clifford operations and thus we are required to run full statevector simulations.

The Y-type teleportation circuit acts as follows on the Y-type magic state, as given by Eqn. 5.15, and an arbitrary single-qubit input state $|\psi\rangle$:

$$|H\rangle|\psi\rangle = (\cos(\pi/8)|0\rangle + \sin(\pi/8)|1\rangle)(\alpha|0\rangle + \beta|1\rangle) \tag{B.7}$$

$$\xrightarrow{\text{CY}} \cos(\pi/8)|0\rangle(\alpha|0\rangle + \beta|1\rangle) + i\sin(\pi/8)|1\rangle(\alpha|1\rangle - \beta|0\rangle) \tag{B.8}$$

$$= \frac{1}{\sqrt{2}}\left(|+i\rangle \exp\left(-i\frac{\pi}{8}Y\right)|\psi\rangle + |-i\rangle \exp\left(i\frac{\pi}{8}Y\right)|\psi\rangle\right) \tag{B.9}$$

$$= \frac{1}{\sqrt{2}}\left(|+i\rangle T|\psi\rangle + |-i\rangle \exp\left(i\frac{\pi}{4}Y\right)T|\psi\rangle\right). \tag{B.10}$$

Thus, in case of measuring the first qubit in the $|+i\rangle$ state, the T-gate is applied as desired to the state $|\psi\rangle$ on the second qubit. In the other case of a -1 measurement result of the first qubit in the Y basis, an additional Clifford operation, namely a $\pi/2$-rotation about the Y axis, $\exp\left(-i\frac{\pi}{4}Y\right)$, must be applied to end up with the desired state $T|\psi\rangle$ on the second qubit.

Therefore, in the teleportation circuit (Figure 5.9a), the logical controlled-Y is followed by measurement of all data qubits of the first register in the Y basis and application of a classically controlled logical Y rotation

$$R \equiv R_Y(\pi/2) = \exp\left(-i\frac{\pi}{4}Y\right) \tag{B.11}$$

depending on the measurement result of the first register where the logical magic state has been prepared previously. The logical gate $R_L \simeq R^{\otimes 7}$ is applied to the second register which carries a logical Pauli state, e.g. $|+\rangle_L$. The resulting output state is the logical T-gate applied to the logical Pauli state, e.g. $T_L|+\rangle_L$. Both in simulation and experiment the effect of the R-gate is taken into account by altering the destructive final data qubit measurements. Since R is a $\pi/2$-rotation about the Y axis, it maps Z-basis states onto X-basis states and vice versa.

In our experimental implementation of the magic state we omitted a $\mathrm{Y}(\pi/2)$-rotation. Therefore we applied logical R in the case of the +1 outcome of the logical Y-basis measurement of the first register.

B.6 Ideal error correction

Whenever performing destructive measurements on encoded data qubits we may reinterpret the measurement result according to the color code look-up table decoder. For example, from measuring the bitstring 0000001 on a seven-qubit register we may conclude for low physical error rates present in our setup that the likeliest error on those qubits has been a single X flip on the first qubit and reinterpret the measurement result as 0000000. This process of ideal or in-software EC is commonly used and possible whenever one aims not to keep running

further quantum circuits on the error-corrected state. In general the corrected bitstring is determined by extracting the syndrome from the overlap of the measured bitstring with the stabilizer generators in binary notation and applying the respective correction. For CSS codes such as the color code the X and Z sectors can be treated distinctly. So when measuring the bitstring 0000001 in the Z basis, the overlap with Z stabilizers in binary notation $s_Z^{(1)} = 1010101, s_Z^{(2)} = 1111000, s_Z^{(3)} = 1100110$ yields the syndrome $[-1, +1, +1]$. Here binary 1s correspond to a Pauli-Z operator for the single qubit at the respective position and binary 0s represent the identity operation. Reinterpreting the measured bitstring as 0000000 is equivalent to applying a X_1 correction operator based on the syndrome information which would correctly recover the original state. Since in this work we are demonstrating FT operations, all final quantum states may only be correct up to an arbitrary single Pauli error. These errors are accounted for via ideal EC.

B.7 Logical Pauli states

When fault-tolerantly encoding logical Pauli states we characterize the output state by categories of errors present after executing the circuit in Figure 5.6a. The categories of errors given in Figure 5.6b refer to the states of distance d to the desired $|0\rangle_L$-state which determines whether or not we can correctly identify the state as $|0\rangle_L$ after ideal EC.

We obtain the distance d to the desired $|0\rangle_L$-state by destructively measuring the data qubit register and finding the minimal Hamming distance D_H of the measurement bitstring m to the bitstrings that label the basis states of

$$\begin{aligned} |0\rangle_L = \frac{1}{\sqrt{8}}\Big(&|0000000\rangle + |1010101\rangle + |0110011\rangle \\ &+ |1100110\rangle + |0001111\rangle + |1011010\rangle \\ &+ |0111100\rangle + |1101001\rangle \Big) \end{aligned} \tag{B.12}$$

in post-processing:

$$\begin{aligned} d \equiv \min \Big(&D_H(m, 0000000), D_H(m, 1010101), \\ &\ldots, D_H(m, 1101001) \Big). \end{aligned} \tag{B.13}$$

Ideal EC will trivially correct the exact $|0\rangle_L$ state, i.e. $d = 0$, and correct all states with single Pauli errors, e.g. $X_2 |0\rangle_L$ ($d = 1$). It will yield the logically flipped $|1\rangle_L$ result when acting on a state of distance $d = 2$ or $d = 3$ from $|0\rangle_L$, i.e. $|0\rangle_L$ carrying two X errors or directly a weight-3 logical bit flip X_L.

For arbitrary logical Pauli states destructive measurements must be performed in their respective basis. However, only Pauli-X (Pauli-Z) errors are visible in the preparation of logical Pauli-Z (Pauli-X) basis states $|0\rangle_1$, $|1\rangle_L$ ($|\pm\rangle_L$).

Note that for all measurements on the characterization of logical Pauli states shown in Figure 5.6 and Extended Data Figure B.1 an accidental redefinition of the rotation direction of physical single-qubit Y rotations is accounted for in post-processing. See Extended Data Figure B.1 for more details.

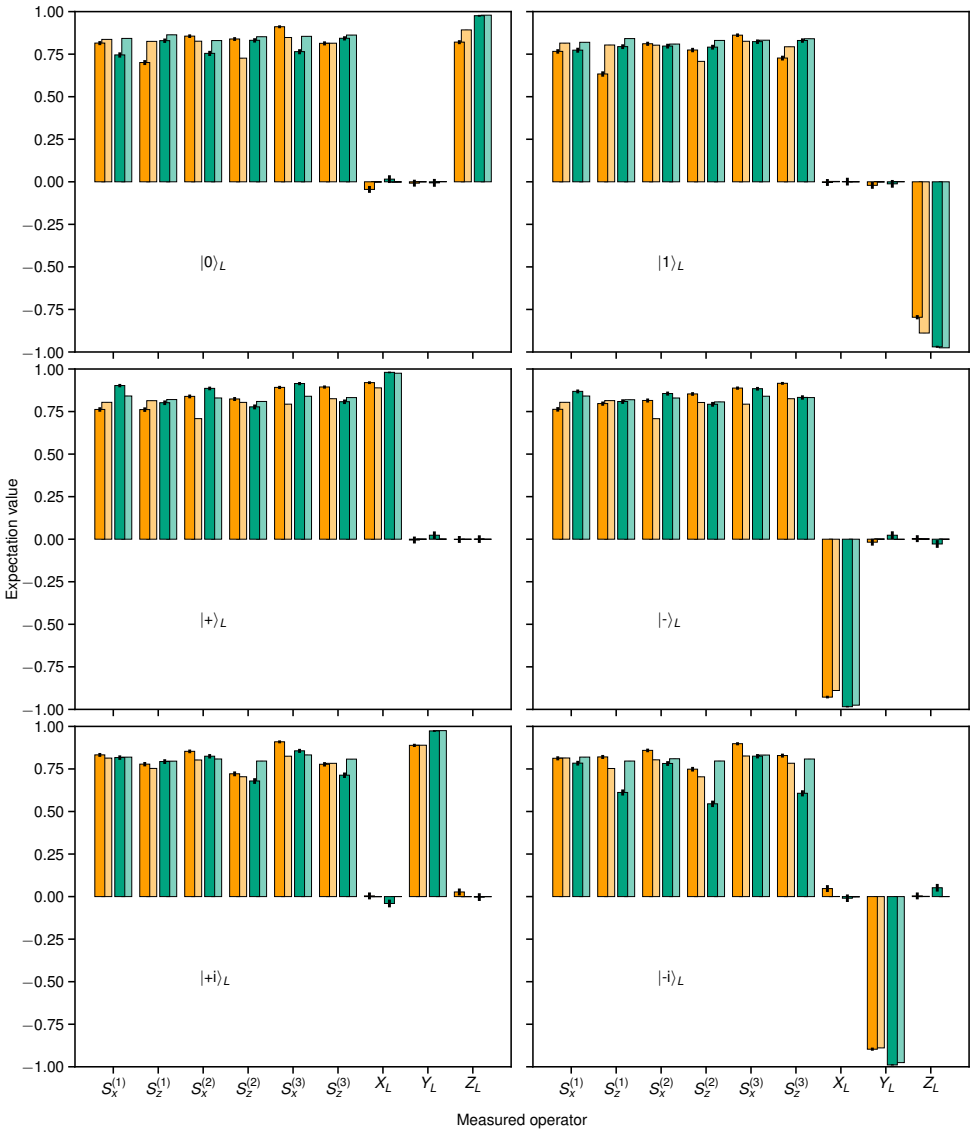

Figure B.1: Stabilizer generators of a single logical qubit. Expectation values of the stabilizer generators and the logical operators of the seven-qubit color code for the six cardinal states of the Bloch sphere. Results for the non-FT and FT preparation scheme are depicted in orange and turquoise respectively, whereas results from numerical simulations are shown in lighter colored bars. 2500 and 10^6 runs were performed in the experiment and for simulations for each prepared state, respectively. For the calculation of the expectation values of the logical operators a round of perfect EC is applied. For the measurements corresponding to the data presented in this figure but also in Figure 5.6 the sign of the rotation angle of physical Y rotations is flipped, effectively implementing an additional deterministic π phase flip on qubit 6 and a π bit flip on qubit 7 at the end of the circuit depicted in Figure 5.6a. The effects of this redefinition do not amount in a change of measurement bases and can be readily accounted for in post-processing.

B.8 Logical fidelities

Single-qubit logical states. – The logical fidelities presented in the main text are obtained by reconstructing the logical Bloch vector of the prepared state ρ and determining the overlap with the Bloch vector of a logical target state. Within the code space, the projector onto an ideal single-qubit logical target state $\rho_t = |t\rangle\langle t|_L$ is given by

$$P_t = \frac{1}{2}(I + O_t) \tag{B.14}$$

with O_t the logical operator that the target state $O_t |t\rangle_L = |t\rangle_L$ is the $+1$ eigenstate to. For the Pauli states considered in this work the projectors are

$$P_{0/1} = \frac{1}{2}(I \pm Z_L) \tag{B.15}$$

$$P_{\pm} = \frac{1}{2}(I \pm X_L) \tag{B.16}$$

$$P_{\pm i} = \frac{1}{2}(I \pm Y_L) \tag{B.17}$$

and logical fidelity of a prepared state ρ follows as

$$\mathcal{F}_t(\rho) = \langle P_t \rangle = \mathrm{Tr}\,(P_t \rho)\,. \tag{B.18}$$

We emphasize that these logical fidelities are *not* equivalent to the full quantum state fidelities $\mathcal{F} = \mathrm{Tr}\,(\rho_t \rho)$ but are the probabilities to be able to correctly conclude which logical state was intended to be prepared or stored.

Combining Eqns. B.15-B.17 with the expression for the logical fidelity in Eqn. B.18, we can see that expectation values of logical Pauli operators O_t need to be determined in order to find the logical fidelities

$$\mathcal{F} = \frac{1}{2}(1 \pm \langle O_t \rangle) \text{ with } O_t \in \{X_L, Y_L, Z_L\}, \tag{B.19}$$

which e.g. evaluates to $\mathcal{F}_0 = \frac{1}{2}(1 + \langle Z_L \rangle)$ for the logical Pauli state $|0\rangle_L$. All six cardinal state logical fidelities are shown in Figure 5.6c. We sample the expectation values of the logical Pauli operators by running stabilizer simulations of the respective preparation circuit $N = 10^6$ times followed by destructive measurement of all data qubits and ideal EC in the respective Pauli basis. The measurement result for a logical operator before EC is determined as $(-1)^{|m|}$ by the number of 1s in the measurement bitstring m modulo 2. Then a round of ideal EC as described in Section B.6 is performed to obtain the final measurement result. Measurement results from each run are averaged to obtain the expectation value of the respective logical operator.

Two-qubit logical states. – In order to characterize the logical CNOT gate through stabilizer simulations single logical qubit states $|x\rangle_L$ and $|y\rangle_L$ are prepared distinctly in two seven-qubit registers. The CNOT gate, acting $|x, y\rangle_L \mapsto |x, y \oplus x\rangle_L$ on the basis states

labelled with $x, y \in \{0, 1\}$, flips the second bit (target) if the first bit (control) is in the 1-state. Thus, $|+, 0\rangle_L$ is mapped to the maximally entangled Bell state

$$|\Phi^+\rangle_L = \frac{1}{\sqrt{2}}(|0, 0\rangle_L + |1, 1\rangle_L), \tag{B.20}$$

which can equivalently be expressed by the logical density operator

$$\rho_{\Phi^+} = |\Phi^+\rangle \langle\Phi^+|_L \simeq \frac{1}{2} \begin{pmatrix} 1 & 0 & 0 & 1 \\ 0 & 0 & 0 & 0 \\ 0 & 0 & 0 & 0 \\ 1 & 0 & 0 & 1 \end{pmatrix} \tag{B.21}$$

where the matrix representation is in the logical two-qubit computational basis. The input-output mapping for the experimentally implemented input states is the following:

$$\begin{pmatrix} |0, 0\rangle_L & \rightarrow |0, 0\rangle_L \\ |0, 1\rangle_L & \rightarrow |0, 1\rangle_L \\ |1, 0\rangle_L & \rightarrow |1, 1\rangle_L \\ |1, 1\rangle_L & \rightarrow |1, 0\rangle_L \\ |+, 0\rangle_L & \rightarrow |\Phi^+\rangle_L \\ |+i, 0\rangle_L & \rightarrow |\Phi^{+i}\rangle_L \end{pmatrix} \tag{B.22}$$

Quantum state tomography has been performed to quantify experimental capabilities to obtain the logical Bell state described by this density matrix as shown in Figure 5.7b. Expectation values of all logical two-qubit Pauli matrices including the identity are measured and subsequently maximum likelihood techniques are used to reconstruct the logical density operator [268]. The Bell state is stabilized by the logical operators $Z_L^1 Z_L^2$ and $X_L^1 X_L^2$ where superscripts $.^{1,2}$ refer to the two logical qubits. Analogously, the CNOT maps input $|+i, 0\rangle_L$ to the Y-basis maximally entangled state

$$|\Phi^{+i}\rangle_L = \frac{1}{\sqrt{2}}(|0, 0\rangle_L + i\,|1, 1\rangle_L). \tag{B.23}$$

Its stabilizers can be obtained by realizing that both states are related via a phase gate

$$|\Phi^{+i}\rangle = S_1\,|\Phi^+\rangle \tag{B.24}$$

so by transforming the stabilizer generators of $|\Phi^+\rangle$ as

$$S_1 Z_1 Z_2 S_1^\dagger = Z_1 Z_2 \tag{B.25}$$

$$S_1 X_1 X_2 S_1^\dagger = Y_1 X_2 \tag{B.26}$$

we obtain the stabilizer generators of $|\Phi^{+i}\rangle$.

The projectors onto the logical two-qubit output states we wish to characterize is now given by the product of the projectors onto the simultaneous $+1$ eigenspace of the logical operators in both registers

$$P_{00} = (P_0 \otimes I)(I \otimes P_0) = \frac{1}{2}\left(I + Z_L^1\right)\frac{1}{2}\left(I + Z_L^2\right) \tag{B.27}$$

$$P_{01} = (P_0 \otimes I)(I \otimes P_1) = \frac{1}{2}\left(I + Z_L^1\right)\frac{1}{2}\left(I - Z_L^2\right) \tag{B.28}$$

$$P_{11} = (P_1 \otimes I)(I \otimes P_1) = \frac{1}{2}\left(I - Z_L^1\right)\frac{1}{2}\left(I - Z_L^2\right) \tag{B.29}$$

$$P_{10} = (P_1 \otimes I)(I \otimes P_0) = \frac{1}{2}\left(I - Z_L^1\right)\frac{1}{2}\left(I + Z_L^2\right) \tag{B.30}$$

$$P_{\Phi^+} = \frac{1}{2}\left(I + X_L^1 X_L^2\right)\frac{1}{2}\left(I + Z_L^1 Z_L^2\right) \tag{B.31}$$

$$P_{\Phi^{+i}} = \frac{1}{2}\left(I + Z_L^1 Z_L^2\right)\frac{1}{2}\left(I + Y_L^1 X_L^2\right) \tag{B.32}$$

Employing Eqn. B.18, the logical fidelities for the output states of the logical CNOT gate follow as expectation values of the logical two-qubit state projectors as

$$\mathcal{F}_{00} = \frac{1}{4}\left(1 + \langle Z_L^1\rangle + \langle Z_L^2\rangle + \langle Z_L^1 Z_L^2\rangle\right) \tag{B.33}$$

$$\mathcal{F}_{01} = \frac{1}{4}\left(1 + \langle Z_L^1\rangle - \langle Z_L^2\rangle - \langle Z_L^1 Z_L^2\rangle\right) \tag{B.34}$$

$$\mathcal{F}_{11} = \frac{1}{4}\left(1 - \langle Z_L^1\rangle - \langle Z_L^2\rangle + \langle Z_L^1 Z_L^2\rangle\right) \tag{B.35}$$

$$\mathcal{F}_{10} = \frac{1}{4}\left(1 - \langle Z_L^1\rangle + \langle Z_L^2\rangle - \langle Z_L^1 Z_L^2\rangle\right) \tag{B.36}$$

$$\mathcal{F}_{\Phi^+} = \frac{1}{4}\left(1 + \langle X_L^1 X_L^2\rangle - \langle Y_L^1 Y_L^2\rangle + \langle Z_L^1 Z_L^2\rangle\right) \tag{B.37}$$

$$\mathcal{F}_{\Phi^{+i}} = \frac{1}{4}\left(1 + \langle Z_L^1 Z_L^2\rangle + \langle X_L^1 Y_L^2\rangle + \langle Y_L^1 X_L^2\rangle\right) \tag{B.38}$$

and are shown in Figure 5.7b as results of $N = 10^6$ stabilizer simulation runs of the logical CNOT circuit followed by destructive measurement of all data qubits and ideal EC in the respective Pauli basis. Averaging over measurement results for the logical operators yields their expectation value.

The logical magic state $|H\rangle_L$ may be denoted by the logical density operator

$$\rho_H = |H\rangle\langle H|_L \simeq \frac{1}{2}\begin{pmatrix} 1 + 1/\sqrt{2} & 1/\sqrt{2} \\ 1/\sqrt{2} & 1 - 1/\sqrt{2} \end{pmatrix} \tag{B.39}$$

where the matrix representation is in the logical computational basis. Quantum state tomography of the experimentally prepared logical magic state is shown in comparison to the theoretical values in Eqn. B.39 in Figure 5.8b, where a logical $\mathrm{Y}(\pi/2)$-rotation is applied

after reconstruction to account for omitted local operations. The fidelity of the logical magic state as shown in Figure 5.8c is given by

$$\mathcal{F}_H = \frac{1}{2}\left(1 + \frac{\langle X_L\rangle + \langle Z_L\rangle}{\sqrt{2}}\right) \tag{B.40}$$

since the logical magic state is the $+1$ eigenstate of the logical Hadamard operator $H_L \left|H\right\rangle_L = \left|H\right\rangle_L$ and its projector reads

$$P_H = \frac{1}{2}\left(I + H_L\right) = \frac{1}{2}\left(I + \frac{X_L + Z_L}{\sqrt{2}}\right). \tag{B.41}$$

When we inject the logical magic state onto logical Pauli states the result is the logical T-gate applied to the previously prepared logical Pauli state

$$\left|\psi\right\rangle_{L,\text{out}} = T_L \left|t\right\rangle_{L,\text{in}}. \tag{B.42}$$

For the four different input logical Pauli states $\left|0\right\rangle_L$, $\left|1\right\rangle_L$, $\left|-\right\rangle_L$ and $\left|-i\right\rangle_L$ the output states are

$$\left|H\right\rangle_L = T_L \left|0\right\rangle_L \tag{B.43}$$
$$\left|-H\right\rangle_L = T_L \left|1\right\rangle_L \tag{B.44}$$
$$Z_L \left|H\right\rangle_L = T_L \left|-\right\rangle_L \tag{B.45}$$
$$\left|-i\right\rangle_L = T_L \left|-i\right\rangle_L \tag{B.46}$$

and their projectors read

$$P_{0/1} = \frac{1}{2}\left(I \pm H_L\right) = \frac{1}{2}\left(1 \pm \frac{X_L + Z_L}{\sqrt{2}}\right) \tag{B.47}$$
$$P_- = Z_L P_0 Z_L = \frac{1}{2}\left(1 - \frac{X_L - Z_L}{\sqrt{2}}\right) \tag{B.48}$$
$$P_{-i} = \frac{1}{2}\left(I - Y_L\right). \tag{B.49}$$

The respective logical T-gate output state fidelities $\mathcal{F}_t$ for input Pauli state $\left|t\right\rangle_L$ are then given by

$$\mathcal{F}_0 = \frac{1}{2}\left(1 + \frac{\langle X_L\rangle + \langle Z_L\rangle}{\sqrt{2}}\right) \tag{B.50}$$
$$\mathcal{F}_1 = \frac{1}{2}\left(1 - \frac{\langle X_L\rangle + \langle Z_L\rangle}{\sqrt{2}}\right) \tag{B.51}$$
$$\mathcal{F}_- = \frac{1}{2}\left(1 - \frac{\langle X_L\rangle - \langle Z_L\rangle}{\sqrt{2}}\right) \tag{B.52}$$
$$\mathcal{F}_{-i} = \frac{1}{2}\left(1 - \langle Y_L\rangle\right). \tag{B.53}$$

To estimate the expectation values of the logical operators occurring in the expressions for the fidelities given above, we run $N = 10^5$ statevector simulations of the FT preparation and injection circuits. Each run is followed by destructive measurement in the respective Pauli basis and ideal EC that determines a measurement outcome of the logical Pauli operator. The expectation value is then calculated as the mean over all measurement outcomes.

The sampling uncertainty ε_L when sampling the expectation value of a logical Pauli operator O_L is $\varepsilon_L = \sqrt{\frac{\mathrm{Var}(\langle O_L \rangle)}{N}}$ and is propagated to their respective fidelities by Gaussian error propagation.

B.9 Logical process matrix

Process matrices can be used to parameterize quantum channels

$$\mathcal{E}(\rho) = \sum_{n=0}^{3} \sum_{m=0}^{3} \chi_{mn} E_m \rho E_n^\dagger \tag{B.54}$$

in the quantum operations formalism. The process matrix χ_{mn} for the logical T-gate that we show in Figure 5.9b is described by the quantum channel

$$\mathcal{E}(\rho) = T\rho T^\dagger = \sum_{n=0}^{3} \sum_{m=0}^{3} \chi_{mn} \sigma_m \rho \sigma_n \tag{B.55}$$

where we expand the channel in terms of the logical Pauli matrices. The matrix representation of χ in the logical Pauli basis reads

$$\chi = \frac{1}{2} \begin{pmatrix} 1 + 1/\sqrt{2} & 0 & i/\sqrt{2} & 0 \\ 0 & 0 & 0 & 0 \\ -i/\sqrt{2} & 0 & 1 - 1/\sqrt{2} & 0 \\ 0 & 0 & 0 & 0 \end{pmatrix}. \tag{B.56}$$

Measurements of expectation values of the logical Pauli basis for the T-gate input states $|0\rangle_L$, $|1\rangle_L$, $|-\rangle_L$ and $|-i\rangle_L$ form a tomographically complete set and allow for the reconstruction of the process matrix χ_{mn} [268].

B.10 Acceptance rates

We define the *acceptance rate* as ratio of circuit runs where all flag qubits are measured as $+1$. The logical Pauli $|0\rangle_L$-state is fault-tolerantly encoded ($|0\rangle_{L,\mathrm{ft}}$) using the circuit given in Figure 5.6a, the logical magic state is prepared both by using the non-FT circuit followed by only the transversal Hadamard measurement ($|H\rangle_{L,\mathrm{nf}}$ & M_H) and by using the full FT protocol ($|H\rangle_{L,\mathrm{ft}}$) as given in Figure 5.8a. Approximate acceptance rates in simulation and experiment are shown in Extended Data Table B.1 for these three different encoding circuits alongside with the respective number of qubits acting as flags as well as number of gates.

encoding	#entangling gates	#flags	simulation	experiment	$\Delta\varepsilon$
$\|0\rangle_{L,\mathrm{ft}}$	8	1	85%	79%	7%
$\|H\rangle_{L,\mathrm{nf}}$ & M_H	20	2	72%	57%	21%
$\|H\rangle_{L,\mathrm{ft}}$	48	8	27%	14%	48%

Table B.1: Acceptance rates of flag encoding circuits. Approximate acceptance rates and relative deviation in simulation and experiment for three encoding circuits with different number of flag qubits and entangling gates.

We observe that the relative deviation $\Delta\varepsilon$ between MC simulation and experimentally measured acceptance rates for the respective circuits increases with longer circuits and a higher number of flag qubits involved.

C

APPENDIX TO PUBLICATION *STRATEGIES FOR PRACTICAL ADVANTAGE OF FAULT-TOLERANT CIRCUIT DESIGN IN NOISY TRAPPED-ION QUANTUM COMPUTERS*

C.1 Noise model details

In the following, we provide more details for the noise model used to perform the simulations of faulty quantum circuits presented in Section 6.1.1.3.2 of the main text. The four independent physical error rates on single-qubit gates, two-qubit gates, qubit initialization and measurement are the sources of error in the simulations accompanying the experimental FT universal gate set realization [128]. For the extended noise model, we also include dephasing noise on idling qubits as well as crosstalk on single- and two-qubit gates. For the latter, we provide two different descriptions, namely as a coherent noise channel and as an incoherent Pauli channel. Overrotations on MS gates are also considered in both a coherent and incoherent model. The derivation of generalized crosstalk noise on gates with arbitrary laser phase, Eqns. 6.7 and 6.8, is the main focus of this Appendix.

The noise channels we state below are examples of quantum operations $\mathcal{E}$ which map an initial qubit state ρ to a final state $\rho' = \mathcal{E}(\rho)$ and thus allow one to formalize evolution of a state under noise. We may express $\mathcal{E}$ as a Kraus map

$$\mathcal{E}(\rho) = \sum_i K_i \rho K_i^\dagger \tag{C.1}$$

where the Kraus operators K_i describe the noise on ρ.

As discussed in Section 6.1.1.3.2, all rotation axes of physical gate operations are parametrized by the phase(s) of the respective qubit laser(s). In the following, we elaborate on the realization of single- and two-qubit gate rotations about axes parametrized by the laser phase(s) which we put to use for the FT magic state preparation circuit in Figure 6.10. It is compiled from a circuit built from CNOT gates to a circuit containing only MS gates. The compiled circuit then contains single-qubit Z rotations which need not be performed physically in the ion trap system, e.g. by AC Stark shifts. All rotation axes, and therefore laser phases, for subsequent gates are changed in order to propagate a Z rotation until the end of the circuit [85]. Here they can be accounted for in software (and when measuring in the Z basis they can be omitted entirely). In order to take advantage of this, we need to allow for different phases φ_1 and φ_2 on the MS target ions and vary the phase φ for single-qubit rotations. We now give a generalization of the standard Pauli-type single- and two-qubit rotations, also including the case of crosstalk. The standard Pauli-X and -Y gates and the

XX-type MS gate shown in Figure 6.2b will be recovered as special cases from this general discussion.

C.1.1 *Single-qubit gates*

Single-qubit rotations are parametrized as a unitary evolution with the operator

$$R_\varphi(\theta) = \exp\left(-\mathrm{i}\frac{\theta}{2}\sigma_\varphi\right) \tag{C.2}$$

$$\sigma_\varphi = X\cos\varphi + Y\sin\varphi \tag{C.3}$$

where σ_φ describes the rotation axis in the equatorial plane of the Bloch sphere. For example, one recovers the $X(Y)$-gate for $\varphi = 0(\pi/2)$ and $\theta = \pi$. With $\varphi = \pi/4$ the resulting spin operator is $\sigma_{\pi/4} = \frac{X+Y}{\sqrt{2}}$, implementing a non-Clifford rotation.

Crosstalk occurs on gates when the laser light intended to only shine on ions in order to perform a qubit rotation cannot be focused tightly enough so that a finite electric field is at the position of a non-targeted ion. Then, neighboring ions also receive a fraction of residual laser light and the rotation intended to the gate ions is partly performed as well on the neighbor ions. The coupling of the laser field $\vec{E}$ to the electric quadrupole of the ion state is measured by the Rabi frequency Ω. The Rabi frequency Ω is proportional to the gradient of the electric field at the location of the neighbor ion. We assume that the main contribution to the gradient of the electric field is given by the longitudinal change in electric field of the electromagnetic wave. Therefore the gradient is proportional to the amplitude of the electric field amplitude. Consequently also the Rabi frequency on a neighbor ion Ω_n is proportional to the electric field amplitude at the location of the neighbor ion. Since the rotation angle θ of the single-qubit gate is given by $\theta = \Omega t$, where t is the time the laser light is on, the rotation angle on the neighbor qubit θ_n is determined by the crosstalk ratio $\varepsilon = \Omega_n/\Omega$ via

$$\theta_n = \varepsilon\theta. \tag{C.4}$$

In our simulations, we assume an average crosstalk ratio of $\varepsilon = 1 \times 10^{-2}$.

For single-qubit crosstalk, the neighboring ions to the target ion, where a rotation about θ shall be performed, see residual laser light which causes the crosstalk rotation of angle $\varepsilon\theta$. The rotation on each neighbor location is

$$R_\varphi(\varepsilon\theta) = \exp\left(-\mathrm{i}\frac{\varepsilon\theta}{2}\sigma_\varphi\right). \tag{C.5}$$

The rotation operator $R_\varphi(\varepsilon\theta)$ acts on a single-qubit density matrix ρ like

$$\begin{aligned}\mathcal{E}(\rho) &= R_\varphi(\varepsilon\theta)\,\rho\,R_\varphi^\dagger(\varepsilon\theta)\\ &= \cos^2\frac{\varepsilon\theta}{2}\rho \;+\sin^2\frac{\varepsilon\theta}{2}\left(\sigma_\varphi\rho\sigma_\varphi\right)+\frac{\mathrm{i}}{2}\sin\varepsilon\theta\;[\rho,\sigma_\varphi]\\ &= \cos^2\frac{\varepsilon\theta}{2}\rho \;+\sin^2\frac{\varepsilon\theta}{2}\left(\cos^2\varphi X\rho X+\sin^2\varphi Y\rho Y\right.\\ &\qquad\qquad\left.+\;\cos\varphi\sin\varphi(X\rho Y+Y\rho X)\right)\\ &\qquad+\frac{\mathrm{i}}{2}\sin\varepsilon\theta\;(\rho(X\cos\varphi+Y\sin\varphi)\\ &\qquad\qquad-\;(X\cos\varphi+Y\sin\varphi)\rho)\,. \end{aligned}\tag{C.6}$$

In order to efficiently simulate the above coherent noise channel $\mathcal{E}$ in a stabilizer simulation, we now perform the Pauli twirling approximation (PTA) [269–273] to obtain the (approximate) incoherent channel of the form

$$\tilde{\mathcal{E}}(\rho)=\frac{1}{4}\sum_{P\in\mathcal{P}}P\mathcal{E}(P\rho P)P\tag{C.7}$$

with $\mathcal{P}=\{I,X,Y,Z\}$. Each term in the sum of Eqn. C.7 of the channel $\tilde{\mathcal{E}}(\rho)$ reads

$$\begin{aligned}P\mathcal{E}(P\rho P)P &= \cos^2\frac{\varepsilon\theta}{2}\rho+\sin^2\frac{\varepsilon\theta}{2}P\sigma_\varphi P\rho P\sigma_\varphi P\\ &\quad+\frac{\mathrm{i}}{2}\sin\varepsilon\theta\,[\rho,P\sigma_\varphi P]\end{aligned}\tag{C.8}$$

for any Pauli matrix $P\in\mathcal{P}$. With the identities

$$I\sigma_\varphi I = X\cos\varphi+Y\sin\varphi\tag{C.9}$$
$$X\sigma_\varphi X = X\cos\varphi-Y\sin\varphi\tag{C.10}$$
$$Y\sigma_\varphi Y = -X\cos\varphi+Y\sin\varphi\tag{C.11}$$
$$Z\sigma_\varphi Z = -(X\cos\varphi+Y\sin\varphi)\tag{C.12}$$

we can calculate the twirled channel. We calculate the sum over the Paulis for each of the three terms in Eqn. C.8 separately to find the Pauli twirled channel

$$\tilde{\mathcal{E}}(\rho) = \cos^2\frac{\varepsilon\theta}{2}\rho+\sin^2\frac{\varepsilon\theta}{2}\left(\cos^2\varphi X\rho X+\sin^2\varphi Y\rho Y\right)\tag{C.13}$$
$$\equiv (1-p_{\mathrm{c}_1})\rho+p_{\mathrm{c}_1}\left(r_xX\rho X+(1-r_x)Y\rho Y\right)\tag{C.14}$$

where we define the physical error rate as before but also introduce the *phase ratios* $r_x=\cos^2\varphi$ and $r_y=1-r_x=\sin^2\varphi$. All terms in the commutator and the off-diagonal terms in the

$\sin^2$-term cancel. This directly corresponds to taking only the diagonal terms of the process matrix χ parametrizing the coherent channel of Eqn. C.6 in the Pauli basis

$$\chi = \begin{pmatrix} \cos^2 \varepsilon\theta/2 & \mathrm{i}/2 \sin \varepsilon\theta \cos\varphi & \mathrm{i}/2 \sin \varepsilon\theta \sin\varphi & 0 \\ -\mathrm{i}/2 \sin \varepsilon\theta \cos\varphi & \sin^2 \varepsilon\theta/2 \cos^2\varphi & \sin^2 \varepsilon\theta/2 \cos\varphi \sin\varphi & 0 \\ -\mathrm{i}/2 \sin \varepsilon\theta \sin\varphi & \sin^2 \varepsilon\theta/2 \cos\varphi \sin\varphi & \sin^2 \varepsilon\theta/2 \sin^2\varphi & 0 \\ 0 & 0 & 0 & 0 \end{pmatrix}. \tag{C.15}$$

As an example for crosstalk on a single-qubit Pauli gate, consider the coherent rotation about a Pauli axis $\sigma \in \{X, Y\}$ (realized via $\varphi \in \{0, \pi/2\}$) as described by the operator

$$R_\sigma(\theta) = \cos\frac{\theta}{2} - \mathrm{i} \sin\frac{\theta}{2}\sigma. \tag{C.16}$$

With a laser beam that affects three qubits, the target ion t and its two neighbor ions $n_1(t)$ and $n_2(t)$ that are subjected to a fraction ε of the laser electric field, the total rotation operator is the product of three single-qubit rotations

$$\begin{aligned} &R_\sigma^{(n,t)}(\theta) \\ &= \exp\left(-\mathrm{i}\frac{\theta}{2}\sigma_t\right) \exp\left(-\mathrm{i}\frac{\varepsilon\theta}{2}\sigma_{\varphi_{n_1(t)}}\right) \exp\left(-\mathrm{i}\frac{\varepsilon\theta}{2}\sigma_{\varphi_{n_2(t)}}\right) \end{aligned} \tag{C.17}$$

where the rotation axes of the neighbor ions are determined by the Pauli operators $\sigma_{\varphi_{n_1(t)}}$ and $\sigma_{\varphi_{n_2(t)}}$ independently from the Pauli operator on the target ion. Let us assume that the phase on neighbor $n_1(t)$ is $\varphi_{n_1(t)} = \pi/2$ so that a Y rotation will be performed. The corresponding rotation operator transforms the state ρ like

$$\begin{aligned} &R_Y^{(n_1)}(\theta)\, \rho\, R_Y^{(n_1)}(\theta)^\dagger = \exp\left(-\mathrm{i}\frac{\varepsilon\theta}{2}Y_{n_1}\right)\, \rho\, \exp\left(+\mathrm{i}\frac{\varepsilon\theta}{2}Y_{n_1}\right) \\ &= \cos^2\frac{\varepsilon\theta}{2}\rho + \sin^2\frac{\varepsilon\theta}{2}Y_{n_1}\rho Y_{n_1} + \frac{\mathrm{i}}{2}\sin\varepsilon\theta\, [\rho, Y_{n_1}]\,. \end{aligned} \tag{C.18}$$

Performing the PTA to this transformation amounts to neglecting the third term containing the commutator. The Pauli-twirled channel is then an incoherent error channel of the form

$$\mathcal{E}(\rho) = (1 - p_{\mathrm{c}_1})\rho + p_{\mathrm{c}_1} Y\rho Y \tag{C.19}$$

for the respective neighbor ion location and the probability

$$p_{\mathrm{c}_1} = \sin^2\frac{\varepsilon\theta}{2} \tag{C.20}$$

of applying the crosstalk fault operator Y.

Since we observe that the phases in Figure 6.6 are distributed across the whole interval of all possible values $\varphi \in [0, 2\pi]$, we use

$$\int_0^{2\pi} \mathrm{d}\varphi \cos^2\varphi = \int_0^{2\pi} \mathrm{d}\varphi \sin^2\varphi = \pi \tag{C.21}$$

to average over the crosstalk phase φ in Eqn. C.13:

$$\begin{aligned}\langle\tilde{\mathcal{E}}\rangle_\varphi(\rho) &= (1-p_{\mathrm{c}_1})\rho \\ &\quad + \frac{p_{\mathrm{c}_1}}{2\pi}\int_0^{2\pi}\mathrm{d}\varphi\,\left(\cos^2\varphi X\rho X + \sin^2\varphi Y\rho Y\right).\end{aligned} \tag{C.22}$$

From this we obtain the incoherent noise channel

$$\mathcal{E}_{\mathrm{c}_1}(\rho) = (1-p_{\mathrm{c}_1})\rho + \frac{p_{\mathrm{c}_1}}{2}\left(X\rho X + Y\rho Y\right) \tag{C.23}$$

which we use in our numerical simulations.

Note that for this channel the physical crosstalk error rate $p_{\mathrm{c}_1} = p_{\mathrm{c}_1}(\theta)$ depends on the rotation angle of the gate as opposed to the depolarizing or our dephasing channel. The quantum circuits in this work contain rotation angles $\theta \in \{\pi, \pi/2, \pi/4\}$ for which we list the approximate probabilities according to Eqn. C.20 in the table below.

rotation angle θ	physical error rate p_{c_1}
π	2.5×10^{-4}
$\pi/2$	6.2×10^{-5}
$\pi/4$	1.5×10^{-5}

For the incoherent channel, both neighbor ions n_1 and n_2 have their own independent single-qubit crosstalk error channel.

c.1.2 *MS gates*

The two-qubit entangling gate in our trapped-ion architecture is the MS gate. We now provide a derivation of our noise model for crosstalk on MS gates based on the gate Hamiltonian. The Hamiltonian of the MS gate reads

$$H(t) = H_0 + H_{\mathrm{int}}(t) \tag{C.24}$$

$$H_0 = \sum_{j=1}^{Q}\frac{\omega_{\mathrm{eg},0}}{2}\sigma_{z,j} + \nu\left(a^\dagger a + \frac{1}{2}\right) \tag{C.25}$$

$$\begin{aligned}H_{\mathrm{int}}(t) = \sum_{j=1}^{Q}\frac{\Omega_j(t)}{2}&\left(e^{\mathrm{i}\left(\vec{k}_1\vec{x}_j - \left(\omega_{\mathrm{eg},0}+\delta\right)t - \varphi_j\right)}\right. \\ &\left. + e^{\mathrm{i}\left(\vec{k}_2\vec{x}_j - \left(\omega_{\mathrm{eg},0}-\delta\right)t - \varphi_j\right)} + \mathrm{h.c.}\right)\left(\sigma_j^+ + \sigma_j^-\right).\end{aligned} \tag{C.26}$$

with $\sigma_j^{\pm} = (X_j \pm \mathrm{i}Y_j)/2$. Here Q is the number of all ions that laser light shines on and the Ω_j are their respective Rabi frequencies. Using $\vec{k}_i\vec{x} = \eta_i(a^\dagger + a)$, we operate in a regime where the detuning $\delta \ll \omega_{\mathrm{eg},0}$ is much smaller than the qubit frequency so that the Lamb-Dicke parameters η_1, $\eta_2 \approx \eta$ are assumed to be the same for both target ions 1 and 2. With the rotated spin operator

$$\sigma_{\varphi_j} = X_j \cos\varphi_j + Y_j \sin\varphi_j \tag{C.27}$$

we can write the sum over the ions explicitly as MS gate target ions $t' \in \{1, 2\}$ and neighbor ions $n \in \{n_1(1), n_2(1), n_1(2), n_2(2)\}$ with their Rabi frequencies $\Omega_{t'}(t) = \Omega$ and $\Omega_n = \varepsilon\Omega$:

$$H_{\mathrm{int}}(t) \approx -\eta\Omega \left(ae^{-\mathrm{i}\epsilon t} + a^\dagger e^{\mathrm{i}\epsilon t}\right) \left(\sum_{t'} \frac{1}{2}\sigma_{\varphi_{t'}} + \sum_n \frac{\varepsilon}{2}\sigma_{\varphi_n}\right) \tag{C.28}$$

where $\epsilon = \nu - \delta$. The final form of the Hamiltonian can now be expressed as

$$H_{\mathrm{int}}(t) = -\eta\Omega \left(ae^{-\mathrm{i}\epsilon t} + a^\dagger e^{\mathrm{i}\epsilon t}\right) S_{\vec{\varphi}} \tag{C.29}$$

with the collective spin operator $S_{\vec{\varphi}} = \frac{1}{2}\sigma_{\vec{\varphi}}$ where $\vec{\varphi} = (\varphi_{t_1}, \varphi_{t_2}, \varphi_{n_1(1)}, \varphi_{n_2(1)}, \varphi_{n_1(2)}, \varphi_{n_2(2)})$ contains all target and neighbor ion phases.

From this Hamiltonian follows the time evolution

$$U(t) = D(\Gamma(t)\sigma_{\vec{\varphi}}) \exp\left(\mathrm{i}\theta(t) S_{\vec{\varphi}}^2\right) \tag{C.30}$$

with $\Gamma(t) = \int_0^t \gamma(t')\mathrm{d}t'$ and $\theta(t) = \Im \int_0^t \gamma(t')\mathrm{d}t' \int_0^{t'} \gamma^*(t'')\mathrm{d}t''$ where $\gamma(t) = \mathrm{i}\eta\Omega e^{\mathrm{i}\epsilon t}$ and the displacement operator $D(\alpha) = \exp\left(\alpha a^\dagger - \alpha^* a\right) \sim 1 + \left(\alpha a^\dagger - \alpha^* a\right)$ for which $D(\alpha)D(\beta) = D(\alpha + \beta)\exp\left(\mathrm{i}\,\Im(\alpha\beta^*)\right)$ holds. The parameters of the gate $\Gamma(t)$ and $\theta(t)$ can be adjusted experimentally to realize the MS gate [274].

The collective spin operator contains both the target and their nearest neighbor ions

$$\begin{aligned} S_{\vec{\varphi}} &= S_{\vec{\varphi}}\Big|_{\text{targets}} + S_{\vec{\varphi}}\Big|_{\text{neighbors}} && \text{(C.31)} \\ &= \frac{1}{2}\left(\sigma_{\varphi_1} + \sigma_{\varphi_2}\right. \\ &\quad \left. + \varepsilon\left(\sigma_{\varphi_{n_1(1)}} + \sigma_{\varphi_{n_2(1)}} + \sigma_{\varphi_{n_1(2)}} + \sigma_{\varphi_{n_2(2)}}\right)\right) && \text{(C.32)} \end{aligned}$$

where the latter have their Rabi frequencies suppressed by the crosstalk ratio ε. Squaring $S_{\vec{\varphi}}$ will create all combinations of target and neighbor ions in first order of ε which we can as well express as

$$S_{\vec{\varphi}}^2 = S_{\vec{\varphi}}^2\Big|_{\text{intended}} + S_{\vec{\varphi}}^2\Big|_{\text{crosstalk}}. \tag{C.33}$$

The MS gate

$$\mathrm{MS}_{\vec{\varphi}}(\theta) = \exp\left(-\mathrm{i}\theta S_{\vec{\varphi}}^2\right) \tag{C.34}$$

transforms the state ρ as

$$\mathcal{E}(\rho) = \exp\left(-\mathrm{i}\theta S_{\vec{\varphi}}^2\right)\ \rho\ \exp\left(\mathrm{i}\theta S_{\vec{\varphi}}^2\right). \tag{C.35}$$

The intended part realizes the MS gate rotation on the target ions. The unitary evolution, which describes the intended MS gate, then reads

$$\mathrm{MS}_{\varphi_1,\varphi_2}(\theta) = \exp\left(-\mathrm{i}\theta S_{\varphi_1,\varphi_2}^2\right) \tag{C.36}$$

with the spin operator

$$S_{\varphi_1,\varphi_2} = \frac{1}{2}\left(\sigma_{\varphi_1} + \sigma_{\varphi_2}\right). \tag{C.37}$$

The MS interaction originates from the square of the spin operator

$$S_{\varphi_1,\varphi_2}^2 \mathrel{\tilde{=}} \frac{1}{2}\sigma_{\varphi_1}\sigma_{\varphi_2} \tag{C.38}$$

where we have omitted terms which either sum to zero as the Pauli operators anticommute on the same qubit or square to the identity and thus only contribute an irrelevant global phase. For the case $\varphi_1 = \varphi_2 = 0$ we find the usual XX-type MS gate

$$\begin{aligned}
\mathrm{MS}_{0,0}(\theta) &= \exp\left(-\mathrm{i}\frac{\theta}{4}(X_1 + X_2)^2\right) && \text{(C.39)}\\
&\mathrel{\tilde{=}} \exp\left(-\mathrm{i}\frac{\theta}{2}X_1X_2\right) && \text{(C.40)}\\
&= \cos\frac{\theta}{2} - \mathrm{i}\sin\frac{\theta}{2}X_1X_2 && \text{(C.41)}
\end{aligned}$$

which has the same form as Eqn. C.16 with $\sigma = X_1X_2$. Another gate relevant to our simulations is, for example, the non-Clifford gate

$$\mathrm{MS}_{0,\pi/4}(\theta) = \exp\left(-\mathrm{i}\frac{\theta}{2}X_1\left(\frac{X_2 + Y_2}{\sqrt{2}}\right)\right) \tag{C.42}$$

which appears in the circuit for deterministic FT magic state preparation in Figure 6.10. Here, the identities used for propagation of Z rotations to the end of the circuit are

$$\begin{aligned}
\mathrm{MS}_{0,0}(-\pi/2)R_Z^{(t_1)}(\alpha) &= R_Z^{(t_1)}(\alpha)\mathrm{MS}_{-\alpha,0}(-\pi/2) && \text{(C.43)}\\
R_\varphi(\theta)R_Z(\alpha) &= R_Z(\alpha)R_{\varphi-\alpha}(\theta). && \text{(C.44)}
\end{aligned}$$

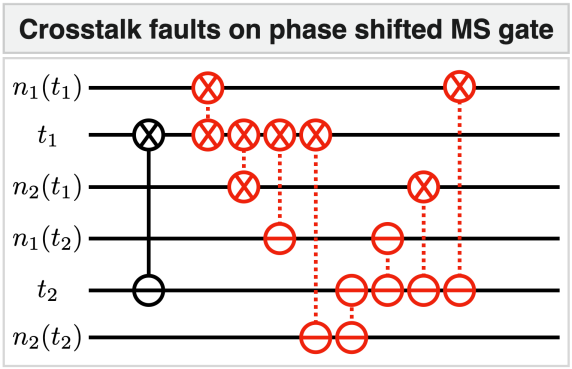

Figure C.1: Crosstalk faults on phase shifted MS gate. Fault locations (red, dotted lines) for an $\mathrm{MS}_{0,-\pi/4}\left(-\frac{\pi}{2}\right)$ gate (black, solid vertical line) originating from the square of the spin operator in Eqn. C.61. The phase of the crosstalk corresponds to the phase of the associated target ion.

The crosstalk term in Eqn. C.33 contains all two-combinations of single-qubit operators in order ε, as depicted as an example in Figure C.1. Neglecting higher orders of ε, each crosstalk location can be treated as an independent coherent two-qubit rotation. For example, the location $t_1,\ n_1(t_1)$ is contained in the squared spin operator as

$$S_{\vec{\varphi}}^2\Big|_{\text{crosstalk}} \supset \frac{\varepsilon}{2}\sigma_{\varphi_1}\sigma_{\varphi_{n_1(1)}} \tag{C.45}$$

and generates the rotation

$$R_{1,n_1(1)} = \exp\left(-\mathrm{i}\frac{\varepsilon}{2}\theta\sigma_{\varphi_1}\sigma_{\varphi_{n_1(1)}}\right). \tag{C.46}$$

For any crosstalk location $t,\ n$ we describe its independent unitary evolution by the coherent channel

$$\begin{aligned}\mathcal{E}(\rho) &= R_{t,n}(\varepsilon\theta)\,\rho\,R_{t,n}^\dagger(\varepsilon\theta) &\text{(C.47)}\\ &= \exp\left(-\mathrm{i}\frac{\varepsilon}{2}\theta\sigma_{\varphi_t}\sigma_{\varphi_n}\right)\,\rho\,\exp\left(\mathrm{i}\frac{\varepsilon}{2}\theta\sigma_{\varphi_t}\sigma_{\varphi_n}\right) &\text{(C.48)}\end{aligned}$$

(analogously to Eqn. C.6). Denoting arbitrary two-qubit Pauli operators $P_2 \in \mathcal{P}\otimes\mathcal{P}$, we can perform the Pauli twirling analogously to the single-qubit crosstalk by calculating the 16 expressions $P_2\mathcal{E}(P_2\rho P_2)P_2$. The resulting incoherent channel for one MS crosstalk location (a red gate in Figure C.1) is

$$\begin{aligned}\tilde{\mathcal{E}}(\rho) = \cos^2\frac{\varepsilon\theta}{2}\rho&\\ + \sin^2\frac{\varepsilon\theta}{2}\big(&\cos^2\varphi_t\cos^2\varphi_n X_tX_n\rho X_tX_n\\ &+\sin^2\varphi_t\sin^2\varphi_n Y_tY_n\rho Y_tY_n\\ &+\cos^2\varphi_t\sin^2\varphi_n X_tY_n\rho X_tY_n\\ &+\sin^2\varphi_t\cos^2\varphi_n Y_tX_n\rho Y_tX_n\big)\end{aligned} \tag{C.49}$$

where we can now define the incoherent noise channel

$$\begin{aligned}\tilde{\mathcal{E}}(\rho) = (1-p_{c_2})\rho + p_{c_2}\,(&r_{xx}X_tX_n\rho X_tX_n \\ &+ r_{xy}X_tY_n\rho X_tY_n \\ &+ r_{yx}Y_tX_n\rho Y_tX_n \\ &+ r_{yy}Y_tY_n\rho Y_tY_n)\end{aligned} \tag{C.50}$$

with phase ratios

$$r_{xx} = \cos^2\varphi_t \cos^2\varphi_n \tag{C.51}$$
$$r_{xy} = \cos^2\varphi_t \sin^2\varphi_n \tag{C.52}$$
$$r_{yx} = \sin^2\varphi_t \cos^2\varphi_n \tag{C.53}$$
$$r_{yy} = \sin^2\varphi_t \sin^2\varphi_n. \tag{C.54}$$

Averaging over phases of neighbor ions φ_n, we use Eqn. C.21 to obtain the incoherent noise channel

$$\begin{aligned}\langle\tilde{\mathcal{E}}\rangle_{\varphi_n}(\rho) = (1-p_{c_2})\rho \\ + \frac{p_{c_2}}{2}\big(&\cos^2\varphi_t\ (X_tX_n\,\rho\,X_tX_n \\ &+\ X_tY_n\,\rho\,X_tY_n) \\ &+ \sin^2\varphi_t\ (Y_tX_n\,\rho\,Y_tX_n \\ &+\ Y_tY_n\,\rho\,Y_tY_n)\big)\,.\end{aligned} \tag{C.55}$$

For a simple noise model which – in the same spirit as depolarizing noise – does not need to take into account the microscopic nature of the gate, we also average over the target ion phases φ_t to obtain the channel

$$\begin{aligned}\mathcal{E}_{c_2}(\rho) = (1-p_{c_2})\rho + \frac{p_{c_2}}{4}\,(&X_tX_n\rho X_tX_n + X_tY_n\rho X_tY_n \\ &+ Y_tX_n\rho Y_tX_n + Y_tY_n\rho Y_tY_n)\end{aligned} \tag{C.56}$$

which we use in our numerical simulations.

We now consider the special case where the two target ions share a common neighbor, i.e. that $n_2(1) = n_1(2)$, which receives laser light from both target ions. If also the phases on target and neighbor ions are the same, the spin operator in Eqn. C.32 changes to read

$$S_{\vec{\varphi}} = \frac{1}{2}\left(\sigma_{\varphi,1} + \sigma_{\varphi,2} + \varepsilon\left(\sigma_{\varphi,n_1(1)} + 2\sigma_{\varphi,n_2(1)} + \sigma_{\varphi,n_2(2)}\right)\right) \tag{C.57}$$

so we get a coherent rotation of doubled angle $\theta \to 2\theta$ on the common neighbor ion. This doubling translates to the incoherent model through $\sin\varepsilon\theta = 4\sin^2\varepsilon\theta/2\cos^2\varepsilon\theta/2$ to a shift in probability $p_{c_2} \to 4p_{c_2}$.

This is, e.g., relevant for the XX crosstalk discussed in Section 6.1.1.5 where for all MS gates $\varphi_1 = \varphi_2 = 0$. On each target-neighbor-pair $t,\, n$ we can expand the unitary evolution operators from the coherent channel

$$\mathcal{E}_{\text{cct}}(\rho) = \exp\left(-\mathrm{i}\frac{\varepsilon}{2}\theta X_t X_n\right)\, \rho\, \exp\left(\mathrm{i}\frac{\varepsilon}{2}\theta X_t X_n\right) \tag{C.58}$$

(cf. Eqn. C.46) to obtain an incoherent noise channel for the MS gate crosstalk after PTA. Every crosstalk location which does not involve a common neighbor ion is then subject to the noise channel

$$\mathcal{E}_{\text{xct}}(\rho) = (1 - p_{\text{c}_2})\rho + p_{\text{c}_2} X_t X_{n(t)} \rho X_t X_{n(t)} \tag{C.59}$$

with $p_{\text{c}_2}(\theta) = \sin^2 \varepsilon\theta/2 = 6.2 \times 10^{-5}$ and $\theta = -\pi/2$. For locations with common neighbor ions the shifts $\theta \to 2\theta$ and $p_{\text{c}_2} \to 4p_{\text{c}_2}$ are taken into account in the numerical simulations respectively.

As another special case, let us consider target ions labeled as qubit 2 and 4 so there is a common neighbor 3 and two outer neighbors 1 and 5. We take $\varphi_1 = 0$ and $\varphi_2 = -\pi/4$ and define the operator $F \equiv \frac{X-Y}{\sqrt{2}}$. Under the assumption that the neighbor ion phases were the same as their associated target ion's phase, we now find all operator combinations that contribute to crosstalk from

$$S_{0,-\pi/4} = \frac{1}{2}\left(X_2 + F_4 + \varepsilon\left(X_1 + X_3 + F_3 + F_5\right)\right) \tag{C.60}$$

$$\begin{aligned} S^2_{0,-\pi/4} \supset \frac{1}{4}\big(2\varepsilon\big(&X_1X_2 + X_2X_3 + X_2F_3 + X_2F_5 \\ &+ X_1F_4 + X_3F_4 + F_3F_4 + F_4F_5\big)\big) \end{aligned} \tag{C.61}$$

in the squared spin operator. Note that both terms X_3F_4 and F_3F_4 occur in Eqn. C.61 so there is no angle doubling on the common neighbor qubit 4 since $\varphi_1 \neq \varphi_2$. Adjusting the phases of target ions could also be used in order to cancel the crosstalk on a common neighbor ion completely with the above assumption.

Overrotations. The above reasoning for deriving noise channels from rotation operators can also be applied for overrotations of a small angle ξ on a rotation about θ on an MS target qubit pair. This effectively implements a rotation of angle $\theta + \xi$ around an axis parametrized by phases $\varphi_1,\, \varphi_2$ for a two-qubit gate. The incoherent noise channel that we employ for simulations of XX overrotation in MS gates (Eqn. C.40) is

$$\mathcal{E}^{(2)}_{\text{ior}}(\rho) = (1 - p_2)\rho + p_2 X_1 X_2 \rho X_1 X_2 \tag{C.62}$$

with

$$p_2 = \sin^2 \frac{\xi}{2}. \tag{C.63}$$

The corresponding coherent channel reads

$$\mathcal{E}_{\text{cor}}^{(2)}(\rho) = \exp\left(-\mathrm{i}\frac{\xi}{2}X_1X_2\right)\,\rho\,\exp\left(+\mathrm{i}\frac{\xi}{2}X_1X_2\right). \tag{C.64}$$

C.2 Simulation methods

In this Appendix, we provide a detailed description of the theoretical methods employed for numerical simulations of logical failure rates. Depending on the range of physical error rates, we make use of either direct MC simulation or SS which is an importance sampling technique focusing on just the most important fault-weight-subsets contributing significantly to the logical failure rate.

Direct Monte Carlo. When using direct MC simulations, we model faulty qubit operations by an ideal unitary U which is followed by a fault operator E to form the faulty operation

$$U_{\text{faulty}} = E \cdot U_{\text{ideal}}. \tag{C.65}$$

The operator E is placed after any ideal unitary gate or qubit initialization (or before a qubit measurement) with probability $\vec{p} = (p_1,\, p_2,\, p_i,\, \dots)$ and then drawn from the set of all possible fault operators according to the noise model. The MC estimator for the logical failure rate $\hat{p}_L$ is given by the number of samples where the stochastic placing of fault operators results in a logical failure divided by the total number of samples

$$\hat{p}_L = \frac{\text{no. logical failures}}{\text{no. MC samples}}. \tag{C.66}$$

The sampling error for MC sampling can be estimated by the Wald interval

$$\varepsilon_{\text{MC}} = \sqrt{\frac{\hat{p}_L\,(1-\hat{p}_L)}{N}} \tag{C.67}$$

so that for a large number of samples $N \to \infty$ the true logical failure rate p_L is likely to be found in the confidence interval $[\hat{p}_L - \varepsilon_{\text{MC}},\, \hat{p}_L + \varepsilon_{\text{MC}}]$. It is known that for $\hat{p}_L$ estimations that are close to or equal to zero or one after a finite but potentially small number of samples the Wald interval suffers from irregularities. These can be prevented using the Wilson score interval [267] instead which is bounded by

$$p_\pm = \frac{1}{1+\frac{z_{\alpha/2}^2}{N}}\left(\hat{p}_L + \frac{z_{\alpha/2}^2}{2N} \pm z_{\alpha/2}\sqrt{\frac{\hat{p}_L(1-\hat{p}_L)}{N} + \frac{z_{\alpha/2}^2}{4N^2}}\right) \tag{C.68}$$

at confidence level α where z is the quantile function of the normal distribution

MC sampling is efficient in a regime of physical failure rates where faults are realized frequently so we only employ it for larger physical failure rates. For low physical failure

rates, in MC sampling one would mostly run the fault-free case, e.g. at $p = 0.1\%$ and a circuit of 100 gates the ideal circuit would be realized $(1-p)^{100} \approx 90\%$ of the time. When realization of fault operations becomes a rare event, we turn towards SS instead.

Subset sampling. The logical failure rate p_L can be written as a sum of so-called subset failure rates $\vec{p}_{\text{fail}}$ that contribute with different weights $A(\vec{w}, \vec{p})$ each, so that

$$p_L = \sum_{\vec{w}} A(\vec{w}, \vec{p}) \vec{p}_{\text{fail}}(\vec{w}) \tag{C.69}$$

where we distinguish subsets by the weight $\vec{w} = (w_1, w_2, w_i, ...)$ of the fault operator that is applied to the respective circuit operations. Each subset failure rate $\vec{p}_{\text{fail}}(\vec{w})$ is obtained by MC sampling fault operations with fixed weight $\vec{w}$. The contribution of each subset is given by the binomial weight

$$A(\vec{w}, \vec{p}) = \prod_{\mu} \binom{N_\mu}{w_\mu} p_\mu^{w_\mu} (1-p_\mu)^{N_\mu - w_\mu} \tag{C.70}$$

where μ iterates over all types of faulty circuit operations since the probability of applying exactly w_μ fault operators is $p_\mu^{w_\mu}(1-p_\mu)^{N_\mu - w_\mu}$ and there are $\binom{N_\mu}{w_\mu}$ possibilities to arrange these configurations for any type $\mu \in \{1, 2, i, ...\}$. The true logical failure rate is bounded by

$$\hat{p}_L = \sum_{\vec{w}=\vec{0}}^{\vec{w}_{\max}} A(\vec{w}, \vec{p}) \vec{p}_{\text{fail}}(\vec{w}) \leq p_L \tag{C.71}$$

$$\leq \sum_{\vec{w}=\vec{0}}^{\vec{w}_{\max}} A(\vec{w}, \vec{p}) \vec{p}_{\text{fail}}(\vec{w}) + \sum_{\vec{w}_{\max}+1}^{\vec{N}} A(\vec{w}, \vec{p}) \tag{C.72}$$

where the weight cutoff error

$$\delta(\vec{p}) = \sum_{\vec{w}_{\max}+1}^{\vec{N}} A(\vec{w}, \vec{p}) \tag{C.73}$$

vanishes for low physical failure rates $\delta(\vec{p}) \to 0$ as $\vec{p} \to \vec{0}$. However, in the opposite regime $\delta(\vec{p})$ becomes large so one must choose an appropriate weight cutoff $\vec{w}_{\max}$ to keep the cutoff error below a desired numerical value. For large weight cutoff $|\vec{w}_{\max}|$ the number of subsets is so large that it becomes advantageous to use MC sampling instead. Subset sampling will be advantageous as long as the fault-free subset $\vec{w} = \vec{0}$ is the largest subset

$$A(\vec{0}, \vec{p}) \geq A(\vec{w}, \vec{p}) \quad \forall \vec{w}. \tag{C.74}$$

The MC sampling errors $\varepsilon_{\text{SS}}(\vec{w}) \sim \sqrt{\frac{\vec{p}_{\text{fail}}(\vec{w})(1-\vec{p}_{\text{fail}}(\vec{w}))}{N_{\text{SS}}(\vec{w})}}$ for all subsets accumulate to the sampling error on the logical failure rate

$$\varepsilon_{\text{SS}} = \sqrt{\sum_{\vec{w}=\vec{0}}^{\vec{w}_{\text{max}}} [A(\vec{w},\vec{p})\varepsilon_{\text{SS}}(\vec{w})]^2} \tag{C.75}$$

so that overall the true logical failure rate p_L will likely be in the interval $[\hat{p}_L - \varepsilon_{\text{SS}},\, \hat{p}_L + \varepsilon_{\text{SS}} + \delta]$.

Practical procedure. For the logical failure rates presented in this work we performed the following sampling procedure. First, we fix a scale of interest for the physical failure rates and the crosstalk ratio parametrized by λ (see Eqn. 6.12). This scale contains the experimental parameters as a reference point at $\lambda = 1$. For the depolarizing noise model we scale the parameters p_1, p_2, p_i, p_m and for the extended noise model we additionally scale the parameters $p_{\text{idle},1}$, $p_{\text{idle},2}$, $p_{\text{idle},m}$, $p_{\text{c}_1}(\pi)$, $p_{\text{c}_1}(\pi/2)$, $p_{\text{c}_1}(\pi/4)$, p_{c_2}. For the XX-type crosstalk model, p_{c_2} is replaced by $p_{\text{c}_2,\text{com}}$ and $p_{\text{c}_2,\text{non}}$ for common and non-common neighbor ion crosstalk locations.

We then start our numerical simulation by using MC at the largest physical failure rates and sample at decreasing physical failure rate until either the target relative error is reached or the previously specified maximum number of samples has been run. In the latter case or when no logical failure was recorded at all, we repeat the simulation at the present physical failure rates using SS. Here, we now choose the maximum weight such that the cutoff error δ at the present physical failure rates accounts for at most half of the target relative error. We perform SS uniformly over all relevant subsets until the sampling error ε_{SS} is also at most half of the target relative error or until the maximum number of samples has been reached. The sampling error for all numerical simulations is given as the Wilson score interval C.68 at a confidence level of 95% ($z_{0.025} \approx 1.96$) in a symmetric form $[\hat{p}_L - \frac{p_+ - p_-}{2}, \hat{p}_L + \frac{p_+ - p_-}{2}]$. This prevents us from irregularities of the Wald interval that may occur at subset failure rate estimations that are close to or equal to zero or one after a finite but potentially small number of samples.

In SS we refrain from actually sampling the fault-free subset but fix its subset failure rate and sampling error to be equal to zero. For a non-FT circuit we exhaustively place all possible weight-1 faults to obtain the subset failure rates for the subsets with total weight $|\vec{w}|$ equal to one exactly, i.e. without sampling error. We do the same for all crosstalk faults since they do not respect the FT property in general. For faults that do respect fault tolerance, we also fix their subset failure rates and sampling error to be equal to zero.

C.3 Deterministic FT magic state preparation

The look up table used for correcting errors during the logical Hadamard measurement as part of the deterministic FT magic state preparation protocol in Figure 6.12 is given in Table C.1. The recovery operation R which is applied directly after an EC block depends not only on the measured syndrome but also on the flag pattern f_0, f_1, f_2, f_3 measured in the M_H block. Note for example that the syndromes 000 001 may lead to either the recovery operation $R = X_2$ or $R = X_1X_3$ depending on said flag measurements. The full six-bit

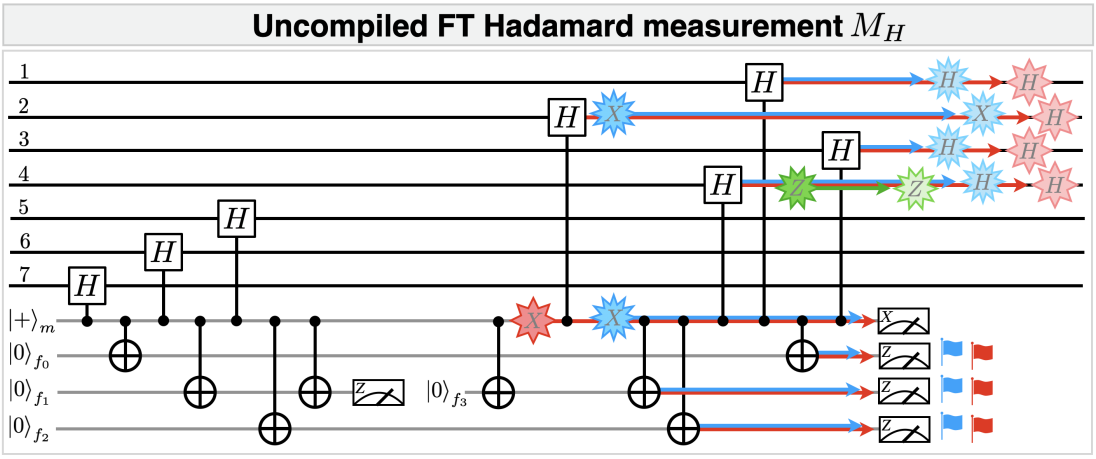

Figure C.2: Uncompiled logical Hadamard measurement circuit. Flag-FT circuit for measuring the logical Hadamard operator according to Ref. [119]. The qubit mapping is not changed because our stabilizers are unchanged compared to Ref. [119]. The faults X_m (red, 8-cornered star), X_2X_m (blue, 12-cornered star) and Z_4 (green, 10-cornered star) as described in the main text are shown with their respective propagated errors $H_1H_2H_3H_4$, $X_2H_1H_3H_4$ and Z_4.

syndrome is necessary to correct all Hadamard errors despite the symmetry of X and Z stabilizers in the Steane code. To see this, consider the Hadamard error

$$H_1H_3 = \frac{1}{2}\left(X_1X_3 + Z_1X_3 + X_1Z_3 + Z_1Z_3\right). \tag{C.76}$$

Since $H = \frac{X+Z}{\sqrt{2}}$ the product of two or more Hadamards mixes all possible combinations of X and Z operators which must be distinguished by the syndrome. At the same time, the flag pattern allows us to distinguish weight-2 errors from weight-1 errors that would cause the same syndrome.

To see why the correction $F = H_1H_3H_4$ from Figure 6.12c is necessary, we consider the uncompiled version of the measurement circuit M_H from Ref. [119] which is reproduced in Figure C.2. Here, an X fault on the measurement qubit can cause the error $H_1H_2H_3H_4$ at the end of M_H as shown in Figure C.2. This error contains all combinations of X- and Z-type operators on qubits 1 to 4, for instance $X_1X_2X_3Z_4 = X_LZ_4$ and $Z_1Z_2Z_3Z_4 = Z_LZ_4$. Both these constituents of the Hadamard error will lead to the same syndrome measurement in the EC block, namely $-{+}{+}\,{+}{+}{+}$, the one matching Z_4, but different logical operators are introduced unnoticed. Applying the F-block will transform the error to $F\,H_1H_2H_3H_4 = H_2 \simeq X_2 + Z_2$. By the subsequent EC block, this superposition will collapse so that either the syndrome ${+}{+}{+}\,{+}{+}{-}$ or ${+}{+}{-}\,{+}{+}{+}$ will be measured and the respective error can be corrected. If instead we had not applied the F operation, we could confuse the error with another one causing the same syndrome, i.e. an error that does not contain logical X or logical Z as shown above but a logical identity or logical Y on qubits 1 to 3. Keep in mind that also the flag pattern needs to be identical so that we cannot use it either to distinguish the errors. Consider the Z_4I_m fault on the third to last controlled Hadamard gate. It will cause the error Z_4 with syndrome $-{+}{+}\,{+}{+}{+}$ which can be distinguished from the X_LZ_4 and Z_LZ_4 errors given above because it will not trigger any flag of M_H. As an example of two faults that lead to the same flag pattern and syndrome if F were not applied, take the fault X_2X_m

f_0, f_1, f_2, f_3	K_1^X, K_2^X, K_3^X	K_1^Z, K_2^Z, K_3^Z	R
1100	000	001	X_2
1110	000	001	X_2
1010	000	001	X_2
1011	000	001	X_2
1100	001	000	Z_2
1110	001	000	Z_2
1010	001	000	Z_2
1011	001	000	Z_2
1000	000	011	X_3
1000	011	000	Z_3
1000	000	111	X_7
1000	111	000	Z_7
1000	000	001	X_1X_3
1000	011	010	X_1Z_3
1000	010	011	X_3Z_1
1000	001	000	Z_1Z_3
1100	110	100	X_4Z_5
1100	100	110	X_5Z_4
1000	000	010	X_6X_7
1100	000	010	X_6X_7
1000	111	101	X_6Z_7
1100	111	101	X_6Z_7
1000	101	111	X_7Z_6
1100	101	111	X_7Z_6
1000	010	000	Z_6Z_7
1100	010	000	Z_6Z_7
1000	010	001	$X_1X_3Z_1$
1000	001	010	$X_1Z_1Z_3$
1000	000	101	$X_1X_3X_4$
1010	000	101	$X_1X_3X_4$
1000	011	110	$X_1X_4Z_3$
1010	011	110	$X_1X_4Z_3$
1000	010	111	$X_3X_4Z_1$
1010	010	111	$X_3X_4Z_1$
1000	001	100	$X_4Z_1Z_3$
1010	001	100	$X_4Z_1Z_3$
1000	100	001	$X_1X_3Z_4$
1010	100	001	$X_1X_3Z_4$
1000	111	010	$X_1Z_3Z_4$
1010	111	010	$X_1Z_3Z_4$
1000	110	011	$X_3Z_1Z_4$
1010	110	011	$X_3Z_1Z_4$
1000	101	000	$Z_1Z_3Z_4$
1010	101	000	$Z_1Z_3Z_4$

f_0, f_1, f_2, f_3	K_1^X, K_2^X, K_3^X	K_1^Z, K_2^Z, K_3^Z	R
1110	000	100	$X_5X_6X_7$
1010	000	100	$X_5X_6X_7$
1100	000	100	$X_5X_6X_7$
1110	101	001	$X_5X_7Z_6$
1010	101	001	$X_5X_7Z_6$
1100	101	001	$X_5X_7Z_6$
1110	110	010	$X_6X_7Z_5$
1010	110	010	$X_6X_7Z_5$
1100	110	010	$X_6X_7Z_5$
1110	011	111	$X_7Z_5Z_6$
1010	011	111	$X_7Z_5Z_6$
1100	011	111	$X_7Z_5Z_6$
1110	111	011	$X_5X_6Z_7$
1010	111	011	$X_5X_6Z_7$
1100	111	011	$X_5X_6Z_7$
1110	010	110	$X_5Z_6Z_7$
1010	010	110	$X_5Z_6Z_7$
1100	010	110	$X_5Z_6Z_7$
1110	001	101	$X_6Z_5Z_7$
1010	001	101	$X_6Z_5Z_7$
1100	001	101	$X_6Z_5Z_7$
1110	100	000	$Z_5Z_6Z_7$
1010	100	000	$Z_5Z_6Z_7$
1100	100	000	$Z_5Z_6Z_7$
1000	101	010	$X_6X_7Z_6$
1000	010	101	$X_6Z_6Z_7$
1100	011	001	$X_5X_7Z_5Z_6$
1100	001	011	$X_5X_6Z_5Z_7$
1000	100	101	$X_1X_3X_4Z_4$
1000	111	110	$X_1X_4Z_3Z_4$
1000	110	111	$X_3X_4Z_1Z_4$
1000	101	100	$X_4Z_1Z_3Z_4$

Table C.1: Look up table for flag-FT measurement of the logical Hadamard operator in the deterministic scheme given in Figure 6.12b. $+1$ and -1 measurement outcomes of flag and syndrome auxiliary qubits are represented as 0 and 1 respectively. The full six bit syndrome needs to be considered in order to choose the appropriate recovery operation R in contrast to the situation where X- and Z-type recoveries are applied independently in standard EC on the Steane code.

on the fourth controlled-Hadamard gate and X_m just before this gate. Both cause the flag pattern 1011. The former will cause the error $X_2H_1H_3H_4$ and the latter will propagate to $H_1H_2H_3H_4$ which is equivalent when acting on the logical magic state to $H_5H_6H_7$ since the magic state is the eigenstate of the logical Hadamard operator $H_L = H^{\otimes 7}$. These two errors can, e.g., be collapsed to $X_1X_2X_3X_4$ and $X_5X_6X_7$ by the EC block and the syndrome $+++\,-++$ will be measured. Since they differ by a logical X they cannot be distinguished by the Hadamard look up table. Applying F will transform the errors according to

$$FX_2H_1H_3H_4 = X_2 \tag{C.77}$$

$$FH_5H_6H_7 = H_1H_3H_4H_5H_6H_7$$

$$\Leftrightarrow FH_1H_2H_3H_4 = H_2 \tag{C.78}$$

which can both be corrected. As another example, these two faults could also collapse to $X_1X_2X_3Z_4$ and $Z_1Z_2Z_3Z_4$ respectively by the EC block yielding syndrome $-++\,+++$. Confusing one for the other we would in total apply a logical Y operation to the logical magic state which is prevented by the F flip.

The steps involved in the deterministic FT magic state preparation are depicted as a flowchart in Figure C.3. The overall correction strategy works as follows: If the Hadamard measurement flags and there exists an entry in the Hadamard look up table C.1 for the measured flag pattern and syndrome, apply the corresponding recovery operation. Else, if the EC flags, run the non-FT syndrome readout (Figure C.5) and apply the correction according to the flag error set if the flags and syndrome disagree. Otherwise, apply the standard Steane look up table recovery operation. For the EC block, X- and Z-type syndromes can be read out independently from each other.

C.4 Quantum state fidelity

The full quantum state fidelity of the data qubit state is defined as

$$\mathcal{F}(\rho_t, \rho) = \mathrm{Tr}(\rho_t\rho) = \langle\rho_t\rangle \tag{C.79}$$

the expectation value of our logical target state $\rho_t = |t\rangle\langle t|$. Eqn. C.79 is in contrast to the logical fidelity which is the overlap of the output state with the desired logical Bloch vector. The quantum state fidelity is the standard quantity that characterizes a quantum state independently of any QEC framework. It contains information about the full state including local properties which the logical fidelity fails to provide since it is merely understood as the overlap of the logical Bloch vector with the desired logical target state, i.e. the projection onto this state. Although the logical fidelity reflects the probability to successfully recover the state after a noisy circuit, it is defined only in the code space but not the full n-qubit Hilbert space [37]. Since the stabilizers subdivide the Hilbert space to form the code space in the first place, it is important to quantify how well the code space itself is prepared, i.e. how close to unity are the expectation values of the stabilizer generators.

We expand the general n-qubit target state ρ_t in the operator basis formed by all possible n-qubit Pauli operators W_k where $k = 1, ..., 4^n$. The quantum state fidelity then reads

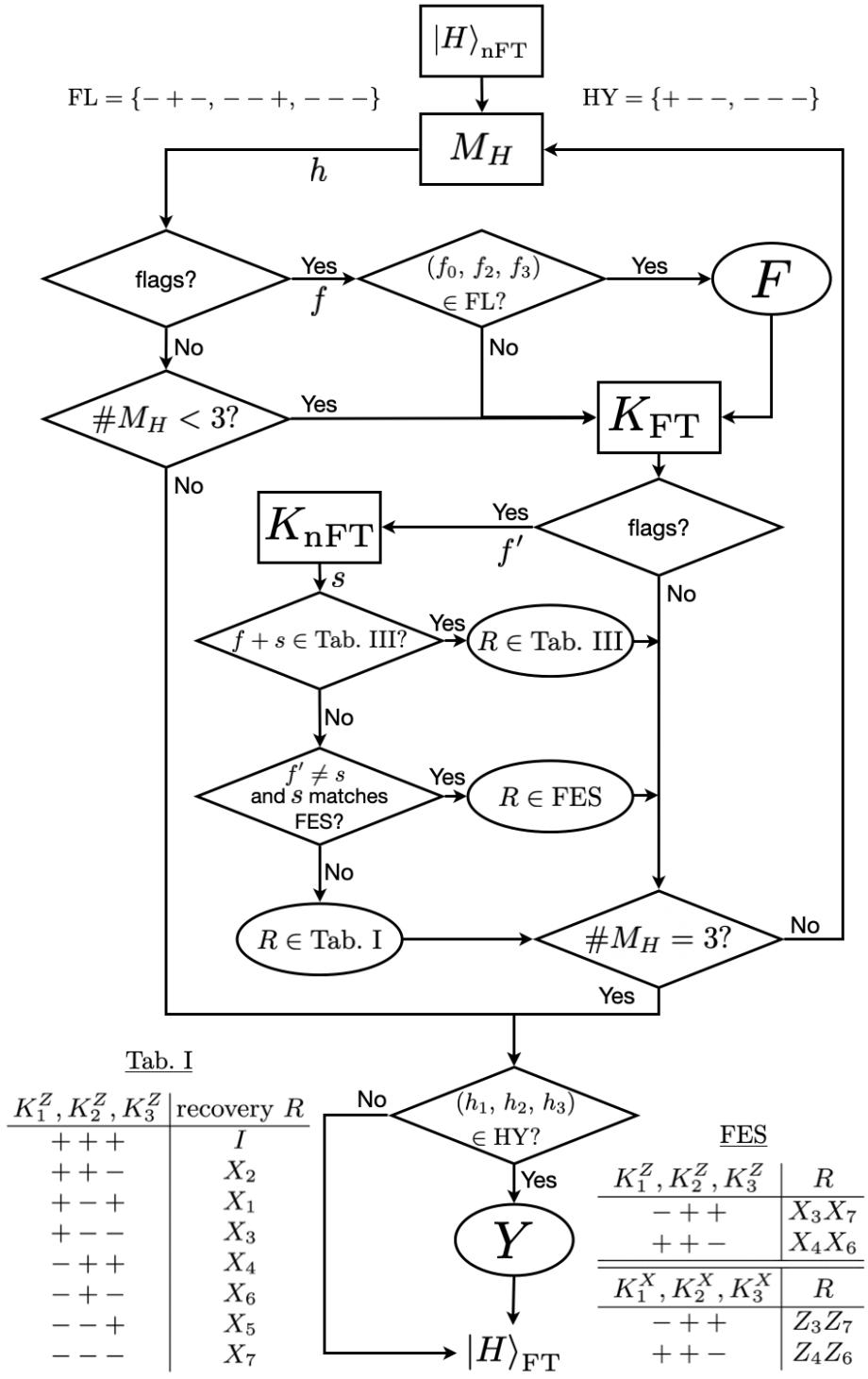

Figure C.3: Flowchart for the deterministic FT magic state preparation procedure. In-sequence measurements determine the circuits of the noisy protocol chosen dynamically during runtime (rectangles). The measurement outcome of an individual M_H circuit is labeled h. Measurements of flag circuits are shown as outputs f and f'. Denoted by s is the syndrome output by K_{nFT}. Additional corrections need to be applied (ovals) depending on the intermediate measurement results: R is drawn from the Steane look up table 6.1, the Hadamard error set (Table C.1) or the flag error set (FES) and F and Y are given in Figure 6.12. The sets of measurement results that cause application of F and Y are labeled FL and HY respectively.

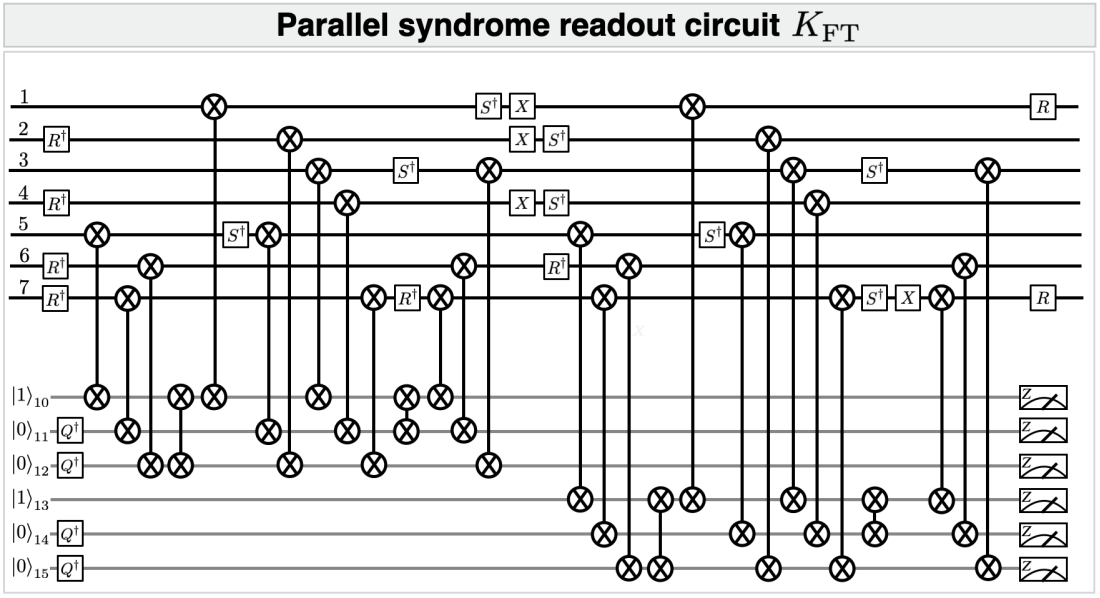

Figure C.4: Parallel stabilizer readout. Fault-tolerant circuit for interleaved measurement of all six stabilizers. Auxiliary qubits simultaneously act as measurement and flag qubits for the deterministic FT magic state preparation protocol (see Figure 6.12).

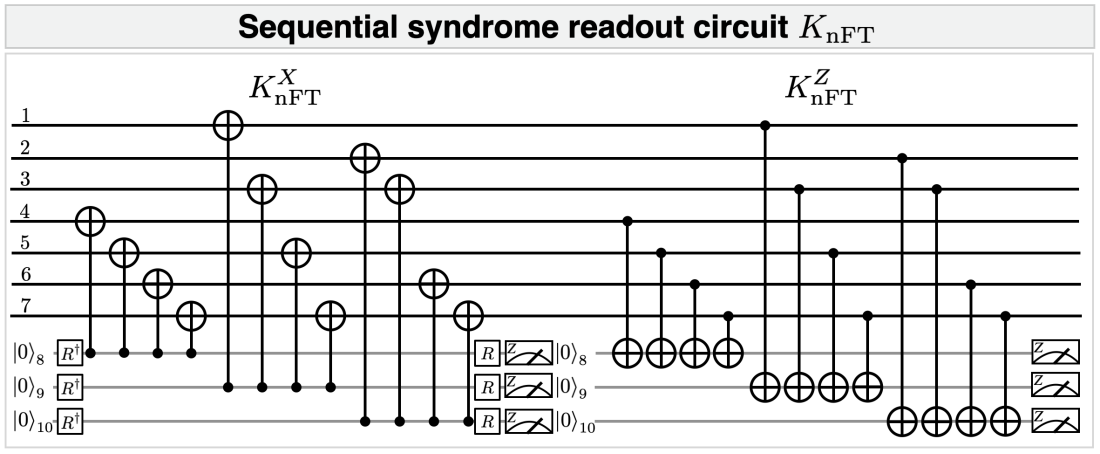

Figure C.5: Sequential stabilizer readout. The circuit is used for non-FT stabilizer readout of the six bit syndrome as part of the deterministic FT magic state preparation protocol shown in Figure 6.12. Each CNOT gate is directly compiled into the sequence of MS gates and local rotations as given in Figure 6.2c.

$$\mathcal{F}(\rho_t, \rho) = \frac{1}{4^n} \operatorname{Tr}\left(\sum_{k=1}^{4^n} \left[\operatorname{Tr}\left(W_k \rho_t \right) W_k \right] \rho \right). \tag{C.80}$$

For stabilizer states $\rho = |\psi\rangle \langle\psi|$ with $W_k |\psi\rangle = \pm |\psi\rangle$ being the elements of the stabilizer group, only the 2^n coefficients corresponding to the set of all stabilizer elements W_k are non-zero $\operatorname{Tr}(W_k \rho) = \pm 1$. The fidelity can then be expressed as

$$\mathcal{F}(\rho_t, \rho) = \frac{1}{2^n} \sum_{k=1}^{2^n} \langle W_k \rangle \tag{C.81}$$

where the W_k are all possible products of combinations of stabilizer elements of the logical state, i.e. combinations of code stabilizer generators with the respective logical operators or the identity:

$$\sum_{k=1}^{2^n} W_k = \prod_{i=1}^{n} \frac{I + S_i}{2} \tag{C.82}$$

$$S_i \in \{K_1^X, K_1^Z, K_2^X, K_2^Z, K_3^X, K_3^Z, O_t\} \tag{C.83}$$

For stabilizer states we only need to evaluate Eqn. C.81 to obtain the quantum state fidelity. For a single logical qubit in an $n = 7$-qubit register ρ_t may be factorized by projectors onto the code space and the logical subspace

$$\rho_t = P_{\pm O_t} P_{\text{CS}} \tag{C.84}$$

$$P_{\text{CS}} = \prod_{i=1}^{6} \frac{I + K_i}{2} \tag{C.85}$$

$$P_{\pm O_t} = \frac{I \pm O_t}{2}. \tag{C.86}$$

The density operator for the logical zero state $|0\rangle_L$ reads

$$\rho_{|0\rangle_L} = |0\rangle \langle 0|_L = \frac{I + Z_L}{2} P_{\text{CS}} \tag{C.87}$$

and the state fidelity for each of these cases reduces to

$$\mathcal{F}(\rho_t, \rho) = \frac{1}{128} \sum_{k=1}^{128} \langle W_k \rangle \tag{C.88}$$

with the respective $W_k = I, \ldots, Z_L K_1^X K_1^Z K_2^X K_2^Z K_3^X K_3^Z$. The code space population p_{CS} and the fidelity within the code space $\mathcal{F}_{\text{CS}}$ is obtained via

$$p_{\text{CS}} = \text{Tr}\left(P_{\text{CS}}\rho_t\right) = \frac{1}{64}\sum_{k=1}^{64}\langle W_k\rangle \tag{C.89}$$

$$\mathcal{F}_{\text{CS}}(\rho_t) = \frac{\text{Tr}\left(\rho_t\rho\right)}{p_{\text{CS}}} \tag{C.90}$$

where the 64 terms for the code space population are the Pauli operators W_k which do not contain the logical operator $W_k = I, \ldots, K_1^X K_1^Z K_2^X K_2^Z K_3^X K_3^Z$.

C.5 Single-qubit randomized benchmarking

The fidelity of single-qubit operations is extracted from randomized benchmarking experiments as described in Ref. [275], where a single Clifford operation is decomposed into 2.167 laser pulses on average. In Figure 6.3 we combined data for all 16 qubits to a single dataset, whereas in Figure C.7 we show the underlying datasets for all qubits individually. The numerical values for single-qubit gate fidelities are given in Table C.2. As there is no pattern of single-qubit gate fidelity with respect to the position in the ion chain apparent, all error models discussed in this work feature only a single fidelity for all single-qubit gates.

Qubit number	Single-qubit gate fidelity
1	0.9978(3)
2	0.9978(3)
3	0.9975(3)
4	0.9973(3)
5	0.9977(3)
6	0.9980(3)
7	0.9975(3)
8	0.9969(4)
9	0.9976(3)
10	0.9977(3)
11	0.9975(3)
12	0.9977(3)
13	0.9975(3)
14	0.9974(3)
15	0.9979(3)
16	0.9975(3)

Table C.2: Single-qubit gate fidelities estimated from randomized benchmarking in a 16-qubit register. The number of Clifford operations used in the generation of the benchmarking sequences ranges from 2 to 20. The given errors are 95% confidence intervals.

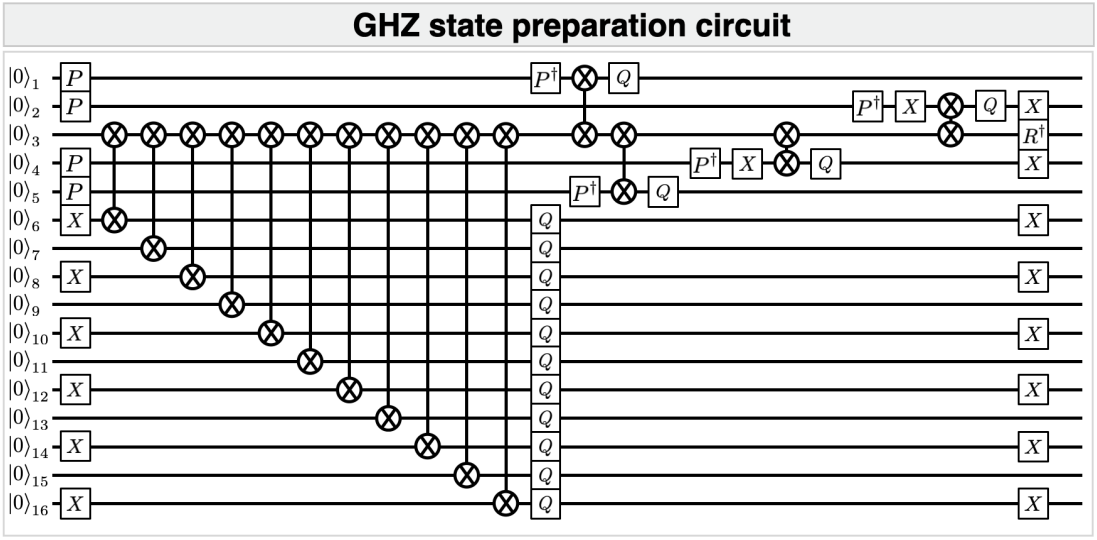

Figure C.6: 16-qubit GHZ state preparation circuit. The circuit is used to estimate the fidelity of a single entangling gate. The operations $P^{(\dagger)}$ are resonant pulses with a rotation angle of π (and opposite rotation direction) on the transition $4S_{1/2,m_j=-1/2}$ to $3D_{5/2,m_j=-3/2}$ used for (un)hiding of qubits. This shelving procedure reduces noise due to crosstalk from multiple entangling gates acting on qubit 3.

C.6 Estimation of entangling gate fidelity

To estimate the mean fidelity of entangling operations without using time-consuming benchmarking techniques the following approach is used: We prepare the 16-qubit GHZ state $|\psi_{\mathrm{GHZ}}\rangle = (|0\rangle^{\otimes 16} - i\,|1\rangle^{\otimes 16})/\sqrt{2}$ across the entire register by using 15 two-qubit MS gates and 40 single-qubit resonant operations. The corresponding circuit is depicted in Figure C.6. For the analysis of the fidelity of the prepared GHZ state we perform two measurements: The probabilities to project to the basis states $|0\rangle^{\otimes 16}$ and $|1\rangle^{\otimes 16}$ are determined by a direct projective measurement in the Z basis. The off-diagonal elements of the density matrix of the GHZ state instead are measured by applying single-qubit gates $R_\varphi^{(i)}(\pi/2)$ to all qubits after preparing the GHZ state. For different phases φ the parity of the prepared state is measured via a projective measurement and a sinusoidal model is fitted to the observed parity oscillations [228]. The mean of the sum of the populations in $|0\rangle^{\otimes 16}$ and $|1\rangle^{\otimes 16}$ and the contrast of the parity oscillations of the coherence measurement gives the fidelity of the GHZ state. The fidelity of a single two-qubit gate is estimated as [276]

$$\mathcal{F}_{\mathrm{tq}} = \left(\frac{\mathcal{F}_{\mathrm{GHZ}}}{\mathcal{F}_{\mathrm{sq}}^{40}}\right)^{\frac{1}{15}}, \tag{C.91}$$

where $\mathcal{F}_{\mathrm{GHZ}} = 0.62(3)$ and $\mathcal{F}_{\mathrm{sq}} = 0.99760(8)$ are fidelity of the GHZ state and mean single-qubit gate fidelity estimated from randomized benchmarking respectively. The estimated two-qubit gate fidelity in the 16-qubit register is $\mathcal{F}_{\mathrm{tq}} = 0.975(3)$.

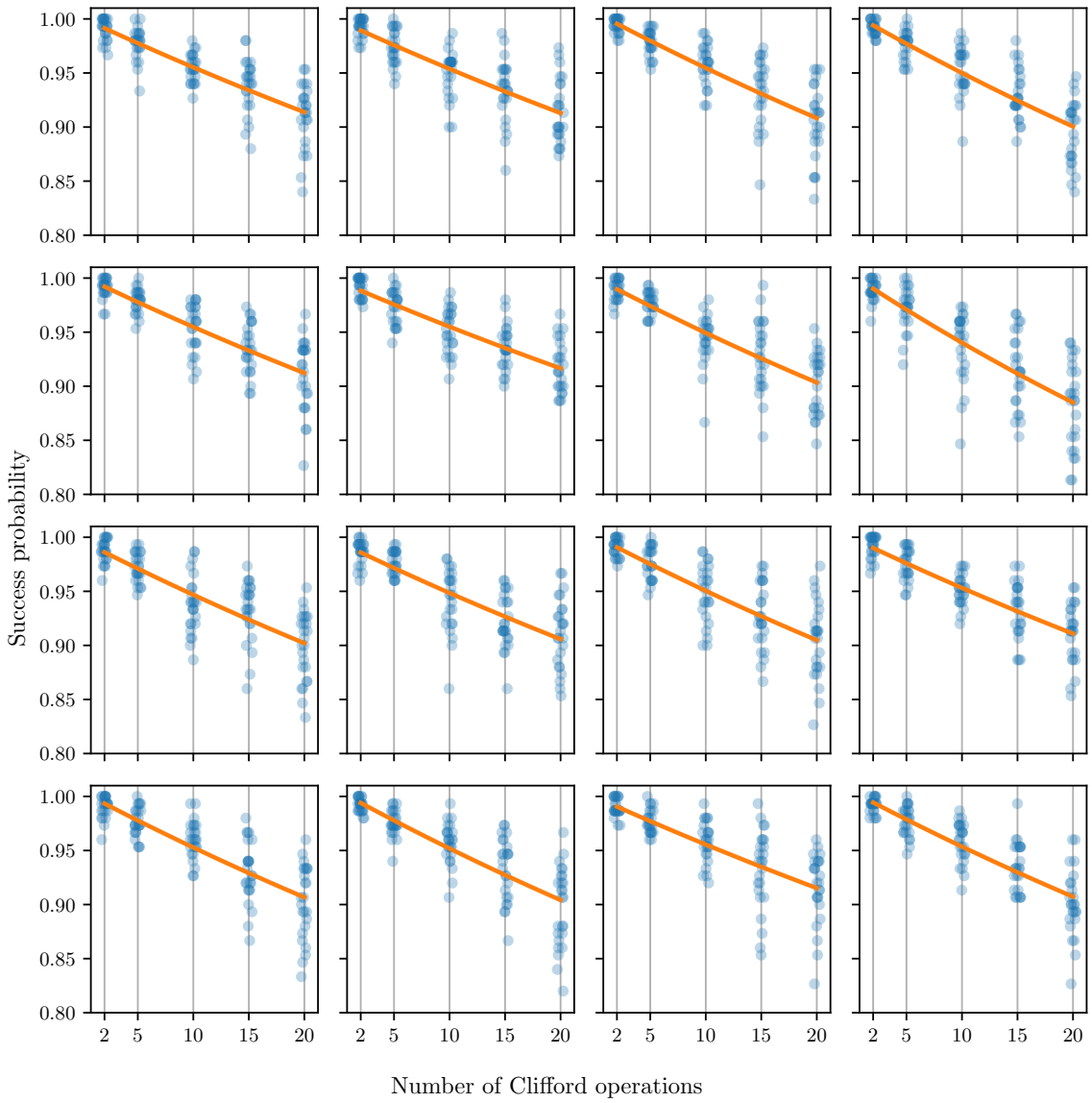

Figure C.7: Single-qubit gate benchmarking. Success probability decay of randomized benchmarking sequences in a 16-qubit register (qubit 1 in the top-left corner, qubit 16 in the bottom-right corner). The scatter on the horizontal axis around the sequence lengths 2, 5, 10, 15 and 20 is introduced for better visibility of the success probability of the individual random sequences. The discretization on the vertical axis is given by averaging over 150 executions per random sequence.

D

APPENDIX TO PUBLICATION *EXPERIMENTAL QUANTIFICATION OF SPATIAL CORRELATIONS IN QUANTUM DYNAMICS*

D.1 Simulations

It is common to find more than one source of dephasing in ion trap architectures. Here we consider the case where one type of dephasing is caused by the external and global magnetic field fluctuations and the other due to the laser frequency fluctuations of the addressing laser source. In particular, with respect to the contribution from magnetic field fluctuations, it is important to note that trapped ion qubits encoded in the electronic qubit levels $S_{1/2}(m_j = -1/2) = |1\rangle \rightarrow D_{5/2}(m_j = -1/2) = |0\rangle$ will undergo a different dephasing dynamics than temporarily spectroscopically decoupled ("hidden") qubits. Spectroscopical decoupling has been commonly employed e. g. in the context of repetitive QEC [102], entangling subsets of qubits [37] and quantum teleportation [277].

Here, we consider a string of two ions, the first of which is spectroscopically decoupled, and the second one residing in the standard qubit subspace. Thus, we effectively consider two ions with a laser field addressing the second one. The joint state of the ions ρ undergoes the evolution which corresponds to accumulating random phases,

$$e^{-i\phi_B(a\sigma_1^z+b\sigma_2^z)}e^{-i\phi_L\sigma_2^z}, \tag{D.1}$$

where ϕ_B is due to the global magnetic field fluctuations and ϕ_L to frequency fluctuations of the laser source addressing the second ion. The constants a and b depend on the specific energy levels on each ion taken into consideration. If those are the same, we have $a = b = 1$. Denoting by $p_B(\phi_B)$ and $p_L(\phi_L)$ the probability distributions for ϕ_B and ϕ_L, respectively, we have the noisy dynamics

$$\mathcal{E}(\rho) = \int d\phi_B p_B(\phi_B) \int d\phi_L p_L(\phi_L)[e^{-i\phi_B(a\sigma_1^z+b\sigma_2^z)}e^{-i\phi_L\sigma_2^z}]\rho[e^{i\phi_B(a\sigma_1^z+b\sigma_2^z)}e^{i\phi_L\sigma_2^z}]. \tag{D.2}$$

We can write

$$e^{-i\phi_B a\sigma_1^z} = \cos(a\phi_B) - i\sin(a\phi_B)\sigma_1^z, \tag{D.3}$$

$$e^{-i(b\phi_B+\phi_L)\sigma_2^z} = \cos(b\phi_B + \phi_L) - i\sin(b\phi_B + \phi_L)\sigma_2^z, \tag{D.4}$$

so that

$$\begin{aligned} e^{-i\phi_B a\sigma_1^z} e^{-i(b\phi_B+\phi_L)\sigma_2^z} &= \cos(a\phi_B)\cos(b\phi_B+\phi_L) \\ &- i\sin(a\phi_B)\cos(b\phi_B+\phi_L)\sigma_1^z \\ &- i\cos(a\phi_B)\sin(b\phi_B+\phi_L)\sigma_2^z \\ &- \sin(a\phi_B)\sin(b\phi_B+\phi_L)\sigma_1^z\sigma_2^z, \end{aligned}$$

and then

$$\mathcal{E}(\rho) = \sum_{\alpha,\beta=0,\ldots 3} \chi_{\alpha\beta} G_\alpha \rho G_\beta, \tag{D.5}$$

with $G_0 = \mathbb{1}\otimes\mathbb{1}$, $G_1 := \sigma_1^z$, $G_2 := \sigma_2^z$, and $G_3 := \sigma_1^z\sigma_2^z$. The coefficients $\chi_{\alpha\beta}$ form a self-adjoint matrix with the following components:

$$\begin{aligned} \chi_{00} &= \int\int d\phi_B d\phi_L p_B(\phi_B) p_L(\phi_L) \cos^2(a\phi_B)\cos^2(b\phi_B+\phi_L), \\ \chi_{01} &= \frac{i}{2}\int\int d\phi_B d\phi_L p_B(\phi_B) p_L(\phi_L) \sin(2a\phi_B)\cos^2(b\phi_B+\phi_L), \\ \chi_{02} &= \frac{i}{2}\int\int d\phi_B d\phi_L p_B(\phi_B) p_L(\phi_L) \cos^2(a\phi_B)\sin[2(b\phi_B+\phi_L)], \\ \chi_{03} &= -\frac{1}{4}\int\int d\phi_B d\phi_L p_B(\phi_B) p_L(\phi_L) \sin(2a\phi_B)\sin[2(b\phi_B+\phi_L)], \\ \chi_{11} &= \int\int d\phi_B d\phi_L p_B(\phi_B) p_L(\phi_L) \sin^2(a\phi_B)\cos^2(b\phi_B+\phi_L), \\ \chi_{12} &= \frac{1}{4}\int\int d\phi_B d\phi_L p_B(\phi_B) p_L(\phi_L) \sin(2a\phi_B)\sin[2(b\phi_B+\phi_L)], \\ \chi_{13} &= \frac{i}{2}\int\int d\phi_B d\phi_L p_B(\phi_B) p_L(\phi_L) \sin^2(a\phi_B)\sin[2(b\phi_B+\phi_L)], \\ \chi_{22} &= \int\int d\phi_B d\phi_L p_B(\phi_B) p_L(\phi_L) \cos^2(a\phi_B)\sin^2(b\phi_B+\phi_L), \\ \chi_{23} &= \frac{i}{2}\int\int d\phi_B d\phi_L p_B(\phi_B) p_L(\phi_L) \sin(2a\phi_B)\sin^2(b\phi_B+\phi_L), \\ \chi_{33} &= \int\int d\phi_B d\phi_L p_B(\phi_B) p_L(\phi_L) \sin^2(a\phi_B)\sin^2(b\phi_B+\phi_L). \end{aligned} \tag{D.6}$$

If we consider a Gaussian distribution for every random phase

$$f(\phi_B) = \frac{1}{\sqrt{2\pi}\sigma_B} e^{-\frac{\phi_B^2}{2\sigma_B^2}} \quad \text{and} \quad f(\phi_L) = \frac{1}{\sqrt{2\pi}\sigma_L} e^{-\frac{\phi_L^2}{2\sigma_L^2}}, \tag{D.7}$$

we obtain $\chi_{01} = \chi_{02} = \chi_{13} = \chi_{23} = 0$ because of the odd parity of the integrating functions.

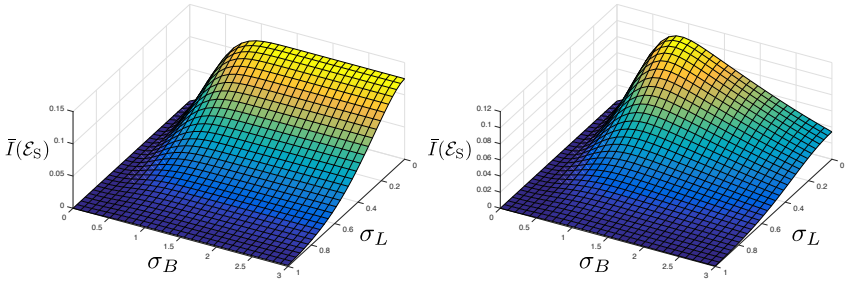

Figure D.1: Amount of correlations for $a = \pm b$ (left) and $a = 1$, $b = -0.83$ (right), as a function of σ_B and σ_L.

As we assumed to have pure dephasing dynamics the Choi-Jamiołkowski state can be written as:

$$\begin{aligned}\rho_S^{CJ} &= \mathcal{E}_Z \otimes \mathbb{1}(|\Phi_{SS'}\rangle\langle\Phi_{SS'}|) \\ &= \frac{1}{d^2}\sum_{k,l,m,n=1}^{d} \alpha_{klmn} |kl\rangle \langle mn| \otimes |kl\rangle \langle mn|\end{aligned}$$

All diagonal elements are $\alpha_{klkl} = 1$, and the remaining integrals in Eqn. D.6 can analytically be performed, yielding the following components of the Choi-Jamiołkowski state ρ_S^{CJ}:

$$\begin{aligned}\alpha_{1112} = \alpha_{2122} &= \chi_{00} + \chi_{11} - \chi_{22} - \chi_{33} = e^{-2(b^2\sigma_B^2+\sigma_L^2)} \\ \alpha_{1121} = \alpha_{1222} &= \chi_{00} - \chi_{11} + \chi_{22} - \chi_{33} = e^{-2a^2\sigma_B^2} \\ \alpha_{1122} &= \chi_{00} + 2\chi_{03} - \chi_{11} - 2\chi_{12} - \chi_{22} + \chi_{33} = e^{-2[(a+b)^2\sigma_B^2+\sigma_L^2]} \\ \alpha_{1221} &= \chi_{00} - 2\chi_{03} - \chi_{11} + 2\chi_{12} - \chi_{22} + \chi_{33} = e^{-2[(a-b)^2\sigma_B^2+\sigma_L^2]}.\end{aligned} \tag{D.8}$$

This allows us to compute the measure of correlation $\bar{I}$ from the Choi-Jamiołkowski state. The results are shown in Figure D.1 for $a = \pm b$, and for $a = 1$, $b = -0.83$. For $a \neq \pm b$ the amount of correlations has a maximum for some value of σ_B and $\sigma_L = 0$, and decays for large σ_B or σ_L. In the case of $a = \pm b$, where both systems have the same susceptibility to magnetic field fluctuations, a maximum value for $\bar{I}$ of 0.125 is reached in the limit of $\sigma_B \to \infty$ and $\sigma_L = 0$. For the experimental implementations from section 6.2.3.5 enhanced magnetic field noise, engineered by applying white current noise to coils in the ion's surrounding, was added, rendering the laser phase noise described by σ_L negligible. Therefore, the presented experimental results correspond to a cut through these 3D figures at $\sigma_L = 0$. Configurations 1 in section 6.2.3.5.1 corresponds to $a = b$ (see left part of Figure D.1). The asymptotic limit of 0.125 is in agreement with the experimental results in Figure 6.27. Configuration 2 is corresponding to $\frac{b}{a} = -0.83$.

To simulate the dynamics of the build-up of space correlations in Figure 6.27 a different simulation method is used: Random phase fluctuations are acting on both qubits, where the experimental waiting time is corresponding to the width of the phase distribution from which the samples are drawn. After 1000 realizations of random dephasing dynamics, the

resulting density matrix is used to generate simulated measurement results by calculating expectation values for all combinations of Pauli operators acting on the two qubits, which correspond to the probabilities to measure a certain output state. From this set of probabilities measurement results are generated using a multinomial distribution. We estimate the error arising from this statistical error (projection noise) by performing 100 realizations of the simulation. The methods used to simulate results for the asymmetric configuration are the same, apart from the fact that the phase fluctuation of random strength is applied to qubit 1 directly and multiplied by the factor to include the different susceptibilities to the magnetic field due to the different Landé g factors of the included states before acting on qubit 2. For the simulation of the uncorrelated case a slightly different procedure is used: Instead of random dephasing, an independent decay to the ground state of the two qubits is applied to reflect the uncorrelated dynamics due to enhanced spontaneous decay.

Analytical expectations for the long-time limit under dephasing dynamics

4-qubit correlations - It is instructive to consider also the long-time dynamics in the case of perfectly correlated dephasing dynamics, and the situation in which one is interested in obtaining the lower bound of the correlation measure. Let us first focus on **Configuration 1**, in which all four qubits are encoded in Encoding A. The initial product state of the four qubits, $|\psi\rangle = |+\rangle^{\otimes 4}$, can be written as

$$|\psi\rangle = \frac{1}{4}(|\psi_0\rangle + |\psi_4\rangle) + \frac{1}{2}(|\psi_1\rangle + |\psi_3\rangle) + \sqrt{\frac{3}{8}}\,|\psi_2\rangle \tag{D.9}$$

with the Dicke states $|\psi_j\rangle$ of $j = 0$ up to $j = 4$ excitations,

$$\begin{aligned}
|\psi_0\rangle &= |0000\rangle\,,\\
|\psi_1\rangle &= \frac{1}{2}(|1000\rangle + |0100\rangle + |0010\rangle + |0001\rangle),\\
|\psi_2\rangle &= \frac{1}{\sqrt{6}}(|0011\rangle + |0101\rangle + |0110\rangle + |1001\rangle + |1010\rangle + |1100\rangle),\\
|\psi_3\rangle &= \frac{1}{2}(|0111\rangle + |1011\rangle + |1101\rangle + |1110\rangle),\\
|\psi_4\rangle &= |1111\rangle\,.
\end{aligned}$$

Under spatially perfectly correlated dephasing, the initial state $|\psi\rangle$ evolves for times much longer than the single-qubit coherence time, but still shorter than the life-time of the metastable qubit state, into

$$|\psi\rangle\langle\psi| \overset{t\to\infty}{\longrightarrow} \frac{1}{16}(|\psi_0\rangle\langle\psi_0| + |\psi_4\rangle\langle\psi_4|) + \frac{1}{4}(|\psi_1\rangle\langle\psi_1| + |\psi_3\rangle\langle\psi_3|) + \frac{3}{8}\,|\psi_2\rangle\langle\psi_2|\,, \tag{D.10}$$

i.e. the subspaces of a fixed excitation number j are decoherence-free, so that the initial coherences between basis states within one and the same excitation number j subspace are preserved, whereas coherences between subspaces of different j and j' are eventually fully lost. From this it is straightforward to see that the single-qubit coherences vanish for all four

qubits, $\langle X_j \rangle = 0$. In contrast, the four-qubit operator $X_1X_2X_3X_4$ has a non-zero expectation value, $\langle X_1X_2X_3X_4 \rangle = 3/8$, which results in a lower bound

$$\bar{I}_{LB} = \frac{1}{4 \cdot 4 \ln 2} \left[\langle X_1X_2X_3X_4 \rangle - \langle X_1 \rangle \langle X_2 \rangle \langle X_3 \rangle \langle X_4 \rangle \right]^2 = 0.0127. \tag{D.11}$$

For **Configuration 2** (qubits 1 and 2 encoded in Encoding A, qubits 3 and 4 encoded in Encoding B) the initial four-qubit state $|\psi\rangle = |+\rangle^{\otimes 4}$ will evolve into the density matrix $\rho = \rho_{12} \otimes \rho_{34}$ for long times. The state of the first and second, and third and fourth qubits, respectively, is given by

$$\rho_{12} = \rho_{34} = \frac{1}{4}(|00\rangle \langle 00| + |11\rangle \langle 11|) + \frac{1}{2}(|\Psi^+\rangle\langle\Psi^+|), \tag{D.12}$$

Therefore, all four single-qubit coherences vanish, $\langle X_j \rangle = 0$. However, due to the presence of the component which corresponds to the pair of Bell-states in the partially decohered four-qubit density matrix, the four-qubit operator $X_1X_2X_3X_4$ has again a non-zero expectation value, $\langle X_1X_2X_3X_4 \rangle = 1/4$, which in this case leads to

$$\bar{I}_{LB} = \frac{1}{4 \cdot 4 \ln 2} \left[\langle X_1X_2X_3X_4 \rangle - \langle X_1 \rangle \langle X_2 \rangle \langle X_3 \rangle \langle X_4 \rangle \right]^2 = \frac{1}{256 \cdot \ln 2} = 0.0056 = 0.56\%. \tag{D.13}$$

Finally, for **Configuration 3**, with qubits 1, 2 and 3 encoded in Encoding A, and qubit 4 in Encoding B, one can show that the initial state $|\psi\rangle = |+\rangle^{\otimes 4}$ evolves for long enough times into

$$\rho = \left[\frac{1}{8} \left(|000\rangle \langle 000| + |111\rangle \langle 111| \right) + \frac{3}{8} \left(|\psi_1'\rangle \langle \psi_1'| + |\psi_2'\rangle \langle \psi_2'| \right) \right]_{123} \otimes \frac{1}{2} \mathbb{1}_4 \tag{D.14}$$

with the Dicke-type 3-qubit states

$$|\psi_1'\rangle = \frac{1}{\sqrt{3}}(|100\rangle + |010\rangle + |001\rangle),$$
$$|\psi_2'\rangle = \frac{1}{\sqrt{3}}(|110\rangle + |101\rangle + |011\rangle).$$

Since for this state both the single-qubit coherences and $\langle X_1X_2X_3X_4 \rangle$ vanish, one expects a vanishing spatial correlation measure, $\bar{I}_{LB} = 0$, in this limit.

2-qubit correlations - Similarly, it is straightforward to obtain the expected behaviour for the long-time dynamics of two qubits undergoing perfectly correlated dephasing. In this case, the initial state $|\psi\rangle = |+\rangle^{\otimes 2}$ of a pair of qubits evolves for long times into

$$|\psi\rangle \langle \psi| \overset{t \to \infty}{\longrightarrow} \frac{1}{4}(|00\rangle \langle 00| + |11\rangle \langle 11|) + \frac{1}{2}(|\Psi^+\rangle\langle\Psi^+|), \tag{D.15}$$

with the Bell state $|\Psi^+\rangle = \frac{1}{\sqrt{2}}(|01\rangle + |10\rangle)$. Again, the single-qubit coherences vanish, $\langle X_1\rangle = \langle X_2\rangle = 0$, whereas the two-qubit operator X_1X_2 saturates at $\langle X_1X_2\rangle = 1/2$, resulting in a lower bound for the two-qubit correlations of

$$\bar{I}_{LB} = \frac{1}{4 \cdot 2\ln 2}\left[\langle X_1X_2\rangle - \langle X_1\rangle\langle X_2\rangle\right]^2 = 0.0451. \tag{D.16}$$

BIBLIOGRAPHY

[1] G. E. Moore. "Cramming more components onto integrated circuits, Reprinted from Electronics, volume 38, number 8, April 19, 1965, pp.114 ff." *IEEE Solid-State Circuits Society Newsletter* **11**, 33–35 (2006).

[2] B. Lojek. *History of Semiconductor Engineering*. Berlin, Heidelberg: Springer Berlin Heidelberg, 2007.

[3] L. Wilson et al. "Executive Summary". In: *IEEE International Roadmap for Devices and Systems Outbriefs*. IEEE, 2021, pp. 1–64.

[4] J. Wu, Y.-L. Shen, K. Reinhardt, and H. Szu. "A NANO enhancement to Moore's law". In: *Independent Component Analyses, Compressive Sampling, Wavelets, Neural Net, Biosystems, and Nanoengineering X*. SPIE, 2012, 84010P.

[5] R. P. Feynman. "Simulating physics with computers". *International Journal of Theoretical Physics* **21**, 467–488 (1982).

[6] D. Deutsch and R. Jozsa. "Rapid solution of problems by quantum computation". *Proceedings of the Royal Society of London. Series A: Mathematical and Physical Sciences* **439**, 553–558 (1992).

[7] R. Cleve, A. Ekert, C. Macchiavello, and M. Mosca. "Quantum algorithms revisited". *Proceedings of the Royal Society of London. Series A: Mathematical, Physical and Engineering Sciences* **454**, 339–354 (1998).

[8] P. Shor. "Algorithms for quantum computation: discrete logarithms and factoring". In: *Proceedings 35th Annual Symposium on Foundations of Computer Science*. IEEE, 1994, pp. 124–134.

[9] C. Pomerance. "A tale of two sieves". *Notices of the American Mathematical Society* **43**, 1473–1485 (1996).

[10] R. L. Rivest, A. Shamir, and L. Adleman. "A method for obtaining digital signatures and public-key cryptosystems". *Communications of the ACM* **21**, 120–126 (1978).

[11] P. J. J. O'Malley et al. "Scalable Quantum Simulation of Molecular Energies". *Physical Review X* **6**, 031007 (2016).

[12] Z. Jiang, K. J. Sung, K. Kechedzhi, V. N. Smelyanskiy, and S. Boixo. "Quantum Algorithms to Simulate Many-Body Physics of Correlated Fermions". *Physical Review Applied* **9**, 044036 (2018).

[13] B. Bauer, S. Bravyi, M. Motta, and G. K.-L. Chan. "Quantum Algorithms for Quantum Chemistry and Quantum Materials Science". *Chemical Reviews* **120**, 12685–12717 (2020).

[14] T. Ayral, P. Besserve, D. Lacroix, and E. A. Ruiz Guzman. "Quantum computing with and for many-body physics". *The European Physical Journal A* **59** (2023).

[15] D. P. DiVincenzo. "The Physical Implementation of Quantum Computation". *Fortschritte der Physik* **48**, 771–783 (2000).

[16] D. Loss and D. P. DiVincenzo. "Quantum computation with quantum dots". *Physical Review A* **57**, 120–126 (1998).

[17] C. Kloeffel and D. Loss. "Prospects for Spin-Based Quantum Computing in Quantum Dots". *Annual Review of Condensed Matter Physics* **4**, 51–81 (2013).

[18] J. Wrachtrup, S. Y. Kilin, and A. P. Nizovtsev. "Quantum computation using the 13C nuclear spins near the single NV defect center in diamond". *Optics and Spectroscopy* **91**, 429–437 (2001).

[19] S. Pezzagna and J. Meijer. "Quantum computer based on color centers in diamond". *Applied Physics Reviews* **8**, 011308 (2021).

[20] N. Peters, J. Altepeter, E. Jeffrey, D. Branning, and P. Kwiat. "Precise creation, characterization, and manipulation of single optical qubits". *Quantum Information and Computation* **3**, 503–517 (2003).

[21] S. Slussarenko and G. J. Pryde. "Photonic quantum information processing: A concise review". *Applied Physics Reviews* **6**, 041303 (2019).

[22] J. Clarke and F. K. Wilhelm. "Superconducting quantum bits". *Nature* **453**, 1031–1042 (2008).

[23] M. Kjaergaard et al. "Superconducting Qubits: Current State of Play". *Annual Review of Condensed Matter Physics* **11**, 369–395 (2020).

[24] A. Blais, A. L. Grimsmo, S. M. Girvin, and A. Wallraff. "Circuit quantum electrodynamics". *Reviews of Modern Physics* **93**, 025005 (2021).

[25] L. Henriet et al. "Quantum computing with neutral atoms". *Quantum* **4**, 327 (2020).

[26] K. Wintersperger et al. "Neutral atom quantum computing hardware: performance and end-user perspective". *EPJ Quantum Technology* **10**, 32 (2023).

[27] J. I. Cirac and P. Zoller. "Quantum Computations with Cold Trapped Ions". *Physical Review Letters* **74**, 4091–4094 (1995).

[28] R. Blatt and D. Wineland. "Entangled states of trapped atomic ions". *Nature* **453**, 1008–1015 (2008).

[29] C. D. Bruzewicz, J. Chiaverini, R. McConnell, and J. M. Sage. "Trapped-ion quantum computing: Progress and challenges". *Applied Physics Reviews* **6**, 021314 (2019).

[30] M. E. Beverland et al. "Assessing requirements to scale to practical quantum advantage". arXiv:2211.07629 (2022).

[31] J. Preskill. "Reliable quantum computers". *Proceedings of the Royal Society of London. Series A: Mathematical, Physical and Engineering Sciences* **454**, 385–410 (1998).

[32] A. M. Steane. "Quantum Error Correction". In: *Introduction to Quantum Computation and Information*. Ed. by H.-K. Lo, T. Spiller, and S. Popescu. Singapore: World Scientific, 1998.

[33] D. Gottesman. "An introduction to quantum error correction and fault-tolerant quantum computation". In: *Quantum Information Science and Its Contributions to Mathematics*. Ed. by S. J. Lomonarco. Proceedings of Symposia in Applied Mathematics. Providence, RI: American Mathematical Society, 2010.

[34] J. Preskill. "Crossing the Quantum Chasm: From NISQ to Fault Tolerance". Conference session. Q2B23 Silicon Valley. Santa Clara, United States, 2023.

[35] P. Shor. "Fault-tolerant quantum computation". In: *Proceedings of 37th Conference on Foundations of Computer Science*. IEEE, 1996, pp. 56–65.

[36] A. Steane. "Multiple-particle interference and quantum error correction". *Proceedings of the Royal Society of London. Series A: Mathematical, Physical and Engineering Sciences* **452**, 2551–2577 (1996).

[37] D. Nigg et al. "Quantum computations on a topologically encoded qubit". *Science* **345**, 302–305 (2014).

[38] C. Ryan-Anderson et al. "Realization of Real-Time Fault-Tolerant Quantum Error Correction". *Physical Review X* **11**, 041058 (2021).

[39] C. Ryan-Anderson et al. "Implementing Fault-tolerant Entangling Gates on the Five-qubit Code and the Color Code". arXiv:2208.01863 (2022).

[40] D. Bluvstein et al. "Logical quantum processor based on reconfigurable atom arrays". *Nature* **626**, 58–65 (2023).

[41] I. Pogorelov et al. "Experimental fault-tolerant code switching". arXiv:2403.13732 (2024).

[42] J. Preskill. "Fault-Tolerant Quantum Computation". In: *Introduction to Quantum Computation and Information*. Ed. by H.-K. Lo, T. Spiller, and S. Popescu. Singapore: World Scientific, 1998.

[43] B. Eastin and E. Knill. "Restrictions on Transversal Encoded Quantum Gate Sets". *Physical Review Letters* **102**, 110502 (2009).

[44] P. A. M. Dirac. "A new notation for quantum mechanics". *Mathematical Proceedings of the Cambridge Philosophical Society* **35**, 416–418 (1939).

[45] M. A. Nielsen and I. L. Chuang. *Quantum Computation and Quantum Information: 10th Anniversary Edition*. Cambridge: Cambridge University Press, 2010.

[46] M. M. Wilde. *Quantum Information Theory*. Cambridge: Cambridge University Press, 2013.

[47] B. C. Hall. *Quantum Theory for Mathematicians*. New York: Springer, 2013.

[48] Qiskit contributors. "Qiskit: An Open-source Framework for Quantum Computing". https://dx.doi.org/10.5281/zenodo.2573505. 2023.

[49] D. Gottesman. "Theory of fault-tolerant quantum computation". *Physical Review A* **57**, 127–137 (1998).

[50] D. Gottesman. "The Heisenberg representation of quantum computers". In: *XXII International Colloquium on Group Theoretical Methods in Physics*. International Press, 1998, pp. 32–43.

[51] S. Aaronson and D. Gottesman. "Improved simulation of stabilizer circuits". *Physical Review A* **70**, 052328 (2004).

[52] J. Preskill. "Quantum information and computation". In: *Lecture Notes for Physics 229*. 2015.

[53] A. Barenco et al. "Elementary gates for quantum computation". *Physical Review A* **52**, 3457–3467 (1995).

[54] E. T. Campbell, H. Anwar, and D. E. Browne. "Magic-State Distillation in All Prime Dimensions Using Quantum Reed-Muller Codes". *Physical Review X* **2**, 041021 (2012).

[55] P. Boykin, T. Mor, M. Pulver, V. Roychowdhury, and F. Vatan. "On universal and fault-tolerant quantum computing: a novel basis and a new constructive proof of universality for Shor's basis". In: *40th Annual Symposium on Foundations of Computer Science*. IEEE, 1999, pp. 486–494.

[56] M. Hamada. "The minimum number of rotations about two axes for constructing an arbitrarily fixed rotation". *Royal Society Open Science* **1**, 140145 (2014).

[57] S. J. Devitt, W. J. Munro, and K. Nemoto. "Quantum error correction for beginners". *Reports on Progress in Physics* **76**, 076001 (2013).

[58] W. Paul, O. Osberghaus, and E. Fischer. "Ein Ionenkäfig". *Forschungsberichte des Wirtschafts- und Verkehrsministeriums Nordrhein-Westfalen* **415** (1958).

[59] D. Leibfried, R. Blatt, C. Monroe, and D. Wineland. "Quantum dynamics of single trapped ions". *Reviews of Modern Physics* **75**, 281–324 (2003).

[60] J. D. Jackson. *Classical electrodynamics*. New York: Wiley, 2009.

[61] W. Paul and H. Steinwedel. "Notizen: Ein neues Massenspektrometer ohne Magnetfeld". *Zeitschrift für Naturforschung A* **8**, 448–450 (1953).

[62] Y. Huang, G.-Z. Li, S. Guan, and A. G. Marshall. "A combined linear ion trap for mass spectrometry". *Journal of the American Society for Mass Spectrometry* **8**, 962–969 (1997).

[63] G. Werth, V. N. Gheorghe, and F. G. Major. *Charged Particle Traps II: Applications*. Berlin, Heidelberg: Springer Berlin Heidelberg, 2009.

[64] H. Li, Y. Zhang, S. He, and X. Tong. "Determination of the geometric parameters and of a linear Paul trap". *Chinese Journal of Physics* **60**, 61–67 (2019).

[65] F. G. Major, V. N. Gheorghe, and G. Werth. *Charged Particle Traps. Physics and Techniques of Charged Particle Field Confinement*. Berlin, Heidelberg: Springer Berlin Heidelberg, 2005.

[66] D. James. "Quantum dynamics of cold trapped ions with application to quantum computation". *Applied Physics B: Lasers and Optics* **66**, 181–190 (1998).

[67] A. Steane. "The ion trap quantum information processor". *Applied Physics B: Lasers and Optics* **64**, 623–643 (1997).

[68] S.-L. Zhu, C. Monroe, and L.-M. Duan. "Trapped Ion Quantum Computation with Transverse Phonon Modes". *Physical Review Letters* **97**, 050505 (2006).

[69] M. Hettrich et al. "Measurement of Dipole Matrix Elements with a Single Trapped Ion". *Physical Review Letters* **115**, 143003 (2015).

[70] Z. Meir, M. Sinhal, M. S. Safronova, and S. Willitsch. "Combining experiments and relativistic theory for establishing accurate radiative quantities in atoms: The lifetime of the 2P3/2 state in Ca+40". *Physical Review A* **101**, 012509 (2020).

[71] A. Kreuter et al. "Experimental and theoretical study of the $3d\,^2D$–level lifetimes of $^{40}Ca^+$". *Physical Review A* **71**, 032504 (2005).

[72] C. A. Blockley, D. F. Walls, and H. Risken. "Quantum Collapses and Revivals in a Quantized Trap". *Europhysics Letters (EPL)* **17**, 509–514 (1992).

[73] R. Loudon. *The quantum theory of light*. Oxford: Oxford University Press, 2006.

[74] C. F. Roos. *Controlling the quantum state of trapped ions*. PhD thesis. Universität Innsbruck, 2000.

[75] K. Sengstock et al. "Optical Ramsey spectroscopy on laser-trapped and thermal Mg atoms". *Applied Physics B Lasers and Optics* **59**, 99–115 (1994).

[76] N. F. Ramsey. "A Molecular Beam Resonance Method with Separated Oscillating Fields". *Physical Review* **78**, 695–699 (1950).

[77] H. Y. Carr and E. M. Purcell. "Effects of Diffusion on Free Precession in Nuclear Magnetic Resonance Experiments". *Physical Review* **94**, 630–638 (1954).

[78] R. Gerritsma et al. "Precision measurement of the branching fractions of the $4p\,^2P_{3/2}$ decay of Ca II". *The European Physical Journal D* **50**, 13–19 (2008).

[79] A. D. Gingell, M. T. Bell, J. M. Oldham, T. P. Softley, and J. N. Harvey. "Cold chemistry with electronically excited Ca+ Coulomb crystals". *The Journal of Chemical Physics* **133** (2010).

[80] P. A. Barton et al. "Measurement of the lifetime of the $3d^2D_{5/2}$ state in $^{40}Ca^+$". *Physical Review A* **62**, 032503 (2000).

[81] P. Staanum, I. S. Jensen, R. G. Martinussen, D. Voigt, and M. Drewsen. "Lifetime measurement of the metastable $3d\,^2D_{5/2}$ state in the $^{40}Ca^+$ ion using the shelving technique on a few-ion string". *Physical Review A* **69**, 032503 (2004).

[82] I. Marzoli, J. I. Cirac, R. Blatt, and P. Zoller. "Laser cooling of trapped three-level ions: Designing two-level systems for sideband cooling". *Physical Review A* **49**, 2771–2779 (1994).

[83] P. Schindler et al. "A quantum information processor with trapped ions". *New Journal of Physics* **15**, 123012 (2013).

[84] I. Pogorelov et al. "Compact Ion-Trap Quantum Computing Demonstrator". *PRX Quantum* **2**, 020343 (2021).

[85] D. C. McKay, C. J. Wood, S. Sheldon, J. M. Chow, and J. M. Gambetta. "Efficient Z gates for quantum computing". *Physical Review A* **96**, 022330 (2017).

[86] A. Sørensen and K. Mølmer. "Quantum Computation with Ions in Thermal Motion". *Physical Review Letters* **82**, 1971–1974 (1999).

[87] G. Kirchmair et al. "Deterministic entanglement of ions in thermal states of motion". *New Journal of Physics* **11**, 023002 (2009).

[88] D. Maslov. "Basic circuit compilation techniques for an ion-trap quantum machine". *New Journal of Physics* **19**, 023035 (2017).

[89] W. Nagourney, J. Sandberg, and H. Dehmelt. "Shelved optical electron amplifier: Observation of quantum jumps". *Physical Review Letters* **56**, 2797–2799 (1986).

[90] R. Stricker et al. "Characterizing Quantum Instruments: From Nondemolition Measurements to Quantum Error Correction". *PRX Quantum* **3**, 030318 (2022).

[91] K. X. Wei, E. Pritchett, D. M. Zajac, D. C. McKay, and S. Merkel. "Characterizing non-Markovian off-resonant errors in quantum gates". *Physical Review Applied* **21**, 024018 (2024).

[92] C. Gidney and M. Ekerå. "How to factor 2048 bit RSA integers in 8 hours using 20 million noisy qubits". *Quantum* **5**, 433 (2021).

[93] D. W. Berry, C. Gidney, M. Motta, J. R. McClean, and R. Babbush. "Qubitization of Arbitrary Basis Quantum Chemistry Leveraging Sparsity and Low Rank Factorization". *Quantum* **3**, 208 (2019).

[94] I. H. Kim et al. "Fault-tolerant resource estimate for quantum chemical simulations: Case study on Li-ion battery electrolyte molecules". *Physical Review Research* **4**, 023019 (2022).

[95] A. G. Fowler, M. Mariantoni, J. M. Martinis, and A. N. Cleland. "Surface codes: Towards practical large-scale quantum computation". *Physical Review A* **86**, 032324 (2012).

[96] P. M. Shah, P. D. Vyavahare, and A. Jain. "Modern error correcting codes for 4G and beyond: Turbo codes and LDPC codes". In: *Radio and Antenna Days of the Indian Ocean (RADIO)*. IEEE, 2015, pp. 1–2.

[97] D. E. Gottesman. *Stabilizer Codes and Quantum Error Correction*. PhD thesis. California Institute of Technology, 1997.

[98] D. J. Robinson. *Abstract Algebra: An Introduction with Applications*. Berlin: De Gruyter, 2022.

[99] J. L. Park. "The concept of transition in quantum mechanics". *Foundations of Physics* **1**, 23–33 (1970).

[100] A. Peres. "Reversible logic and quantum computers". *Physical Review A* **32**, 3266–3276 (1985).

[101] G. A. Paz-Silva, G. K. Brennen, and J. Twamley. "Fault Tolerance with Noisy and Slow Measurements and Preparation". *Physical Review Letters* **105**, 100501 (2010).

[102] P. Schindler et al. "Experimental Repetitive Quantum Error Correction". *Science* **332**, 1059–1061 (2011).

[103] C.-K. Li, M. Nakahara, Y.-T. Poon, N.-S. Sze, and H. Tomita. "Recovery in quantum error correction for general noise without measurement". *Quantum Information and Computation* **12**, 149–158 (2012).

[104] D. Crow, R. Joynt, and M. Saffman. "Improved Error Thresholds for Measurement-Free Error Correction". *Physical Review Letters* **117**, 130503 (2016).

[105] H. E. Ercan et al. "Measurement-free implementations of small-scale surface codes for quantum-dot qubits". *Physical Review A* **97**, 012318 (2018).

[106] S. Heußen, D. F. Locher, and M. Müller. "Measurement-Free Fault-Tolerant Quantum Error Correction in Near-Term Devices". *PRX Quantum* **5**, 010333 (2024).

[107] S. Veroni, M. Müller, and G. Giudice. "Optimized measurement-free and fault-tolerant quantum error correction for neutral atoms". *Physical Review Research* **6**, 043253 (2024).

[108] A. Bermudez et al. "Assessing the Progress of Trapped-Ion Processors Towards Fault-Tolerant Quantum Computation". *Physical Review X* **7**, 041061 (2017).

[109] A. Paetznick and B. W. Reichardt. "Fault-tolerant ancilla preparation and noise threshold lower bounds for the 23-qubit Golay code". *Quantum Information and Computation* **12**, 1034–1080 (2012).

[110] H. Goto. "Minimizing resource overheads for fault-tolerant preparation of encoded states of the Steane code". *Scientific Reports* **6** (2016).

[111] C. Chamberland and M. E. Beverland. "Flag fault-tolerant error correction with arbitrary distance codes". *Quantum* **2**, 53 (2018).

[112] R. Chao and B. W. Reichardt. "Quantum Error Correction with Only Two Extra Qubits". *Physical Review Letters* **121**, 050502 (2018).

[113] R. Chao and B. W. Reichardt. "Fault-tolerant quantum computation with few qubits". *npj Quantum Information* **4** (2018).

[114] A. M. Steane. "Active Stabilization, Quantum Computation, and Quantum State Synthesis". *Physical Review Letters* **78**, 2252–2255 (1997).

[115] A. R. Calderbank and P. W. Shor. "Good quantum error-correcting codes exist". *Physical Review A* **54**, 1098–1105 (1996).

[116] P. Aliferis, D. Gottesman, and J. Preskill. "Quantum accuracy threshold for concatenated distance-3 code". *Quantum Information and Computation* **6**, 97–165 (2006).

[117] A. Cross, D. DiVincenzo, and B. Terhal. "A comparative code study for quantum fault tolerance". *Quantum Information and Computation* **9**, 541–572 (2009).

[118] Chamberland, Christopher. *New methods in quantum error correction and fault-tolerant quantum computing*. PhD thesis. University of Waterloo, 2018.

[119] C. Chamberland and A. W. Cross. "Fault-tolerant magic state preparation with flag qubits". *Quantum* **3**, 143 (2019).

[120] B. W. Reichardt. "Fault-tolerant quantum error correction for Steane's seven-qubit color code with few or no extra qubits". *Quantum Science and Technology* **6**, 015007 (2020).

[121] Z. Chen et al. "Exponential suppression of bit or phase errors with cyclic error correction". *Nature* **595**, 383–387 (2021).

[122] S. Krinner et al. "Realizing repeated quantum error correction in a distance-three surface code". *Nature* **605**, 669–674 (2022).

[123] Y. Zhao et al. "Realization of an Error-Correcting Surface Code with Superconducting Qubits". *Physical Review Letters* **129**, 030501 (2022).

[124] R. Acharya et al. "Suppressing quantum errors by scaling a surface code logical qubit". *Nature* **614**, 676–681 (2023).

[125] R. S. Gupta et al. "Encoding a magic state with beyond break-even fidelity". *Nature* **625**, 259–263 (2024).

[126] J. Hilder et al. "Fault-Tolerant Parity Readout on a Shuttling-Based Trapped-Ion Quantum Computer". *Physical Review X* **12**, 011032 (2022).

[127] L. Egan et al. "Fault-tolerant control of an error-corrected qubit". *Nature* **598**, 281–286 (2021).

[128] L. Postler et al. "Demonstration of fault-tolerant universal quantum gate operations". *Nature* **605**, 675–680 (2022).

[129] D. H. Menendez, A. Ray, and M. Vasmer. "Implementing fault-tolerant non-Clifford gates using the [[8,3,2]] color code". arXiv:2309.08663 (2023).

[130] Y. Wang et al. "Fault-Tolerant One-Bit Addition with the Smallest Interesting Colour Code". arXiv:2309.09893 (2023).

[131] B. Pokharel and D. A. Lidar. "Better-than-classical Grover search via quantum error detection and suppression". *npj Quantum Information* **10** (2024).

[132] V. Negnevitsky et al. "Repeated multi-qubit readout and feedback with a mixed-species trapped-ion register". *Nature* **563**, 527–531 (2018).

[133] J. M. Pino et al. "Demonstration of the trapped-ion quantum CCD computer architecture". *Nature* **592**, 209–213 (2021).

[134] S. D. Erickson et al. "High-Fidelity Indirect Readout of Trapped-Ion Hyperfine Qubits". *Physical Review Letters* **128**, 160503 (2022).

[135] D. Zhu et al. "Interactive cryptographic proofs of quantumness using mid-circuit measurements". *Nature Physics* **19**, 1725–1731 (2023).

[136] M. Riebe et al. "Deterministic entanglement swapping with an ion-trap quantum computer". *Nature Physics* **4**, 839–842 (2008).

[137] T. Monz et al. "Realization of a scalable Shor algorithm". *Science* **351**, 1068–1070 (2016).

[138] T. Manovitz, Y. Shapira, L. Gazit, N. Akerman, and R. Ozeri. "Trapped-Ion Quantum Computer with Robust Entangling Gates and Quantum Coherent Feedback". *PRX Quantum* **3**, 010347 (2022).

[139] S. Meiboom and D. Gill. "Modified Spin-Echo Method for Measuring Nuclear Relaxation Times". *Review of Scientific Instruments* **29**, 688–691 (1958).

[140] J. Kelly et al. "State preservation by repetitive error detection in a superconducting quantum circuit". *Nature* **519**, 66–69 (2015).

[141] E. Knill. "Quantum computing with realistically noisy devices". *Nature* **434**, 39–44 (2005).

[142] H. Bombin and M. A. Martin-Delgado. "Topological Quantum Distillation". *Physical Review Letters* **97**, 180501 (2006).

[143] T. P. Harty et al. "High-Fidelity Preparation, Gates, Memory, and Readout of a Trapped-Ion Quantum Bit". *Physical Review Letters* **113**, 220501 (2014).

[144] T. Ruster et al. "A long-lived Zeeman trapped-ion qubit". *Applied Physics B* **122**, 254 (2016).

[145] P. Wang et al. "Single ion qubit with estimated coherence time exceeding one hour". *Nature Communications* **12** (2021).

[146] S. Wimperis. "Composite pulses with rectangular excitation and inversion profiles". *Journal of Magnetic Resonance (1969)* **83**, 509–524 (1989).

[147] S. Wimperis. "Broadband, Narrowband, and Passband Composite Pulses for Use in Advanced NMR Experiments". *Journal of Magnetic Resonance, Series A* **109**, 221–231 (1994).

[148] J. T. Anderson, G. Duclos-Cianci, and D. Poulin. "Fault-Tolerant Conversion between the Steane and Reed-Muller Quantum Codes". *Physical Review Letters* **113**, 080501 (2014).

[149] A. Kubica and M. E. Beverland. "Universal transversal gates with color codes: A simplified approach". *Physical Review A* **91**, 032330 (2015).

[150] H. Bombín. "Dimensional jump in quantum error correction". *New Journal of Physics* **18**, 043038 (2016).

[151] S. Bravyi and A. Kitaev. "Universal quantum computation with ideal Clifford gates and noisy ancillas". *Physical Review A* **71**, 022316 (2005).

[152] B. M. Terhal. "Quantum error correction for quantum memories". *Reviews of Modern Physics* **87**, 307–346 (2015).

[153] R. Chao and B. W. Reichardt. "Flag Fault-Tolerant Error Correction for any Stabilizer Code". *PRX Quantum* **1**, 010302 (2020).

[154] M. H. Abobeih et al. "Fault-tolerant operation of a logical qubit in a diamond quantum processor". *Nature* **606**, 884–889 (2022).

[155] P. W. Shor. "Polynomial-Time Algorithms for Prime Factorization and Discrete Logarithms on a Quantum Computer". *SIAM Journal on Computing* **26**, 1484–1509 (1997).

[156] D. Aharonov and M. Ben-Or. "Fault-Tolerant Quantum Computation with Constant Error Rate". *SIAM Journal on Computing* **38**, 1207–1282 (2008).

[157] A. Paetznick and B. W. Reichardt. "Universal Fault-Tolerant Quantum Computation with Only Transversal Gates and Error Correction". *Physical Review Letters* **111**, 090505 (2013).

[158] M. E. Beverland, A. Kubica, and K. M. Svore. "Cost of Universality: A Comparative Study of the Overhead of State Distillation and Code Switching with Color Codes". *PRX Quantum* **2**, 020341 (2021).

[159] R. Harper and S. T. Flammia. "Fault-Tolerant Logical Gates in the IBM Quantum Experience". *Physical Review Letters* **122**, 080504 (2019).

[160] A. Erhard et al. "Entangling logical qubits with lattice surgery". *Nature* **589**, 220–224 (2021).

[161] K. J. Satzinger et al. "Realizing topologically ordered states on a quantum processor". *Science* **374**, 1237–1241 (2021).

[162] C. K. Andersen et al. "Repeated quantum error detection in a surface code". *Nature Physics* **16**, 875–880 (2020).

[163] J. F. Marques et al. "Logical-qubit operations in an error-detecting surface code". *Nature Physics* **18**, 80–86 (2021).

[164] D. Gottesman. "Quantum fault tolerance in small experiments". arXiv:1610.03507 (2016).

[165] M. Takita, A. W. Cross, A. D. Córcoles, J. M. Chow, and J. M. Gambetta. "Experimental Demonstration of Fault-Tolerant State Preparation with Superconducting Qubits". *Physical Review Letters* **119**, 180501 (2017).

[166] C. Vuillot. "Is error detection helpful on IBM 5Q chips?" *Quantum Information and Computation* **18**, 949–964 (2018).

[167] N. M. Linke et al. "Fault-tolerant quantum error detection". *Science Advances* **3** (2017).

[168] A. Sørensen and K. Mølmer. "Entanglement and quantum computation with ions in thermal motion". *Physical Review A* **62**, 022311 (2000).

[169] V. Nebendahl, H. Häffner, and C. F. Roos. "Optimal control of entangling operations for trapped-ion quantum computing". *Physical Review A* **79**, 012312 (2009).

[170] A. Bermudez, X. Xu, M. Gutiérrez, S. C. Benjamin, and M. Müller. "Fault-tolerant protection of near-term trapped-ion topological qubits under realistic noise sources". *Physical Review A* **100**, 062307 (2019).

[171] L. Riesebos, X. Fu, S. Varsamopoulos, C. G. Almudever, and K. Bertels. "Pauli Frames for Quantum Computer Architectures". In: *Proceedings of the 54th Annual Design Automation Conference 2017*. ACM, 2017, pp. 1–6.

[172] P. Parrado-Rodríguez, C. Ryan-Anderson, A. Bermudez, and M. Müller. "Crosstalk Suppression for Fault-tolerant Quantum Error Correction with Trapped Ions". *Quantum* **5**, 487 (2021).

[173] B. E. A. Saleh and M. C. Teich. *Fundamentals of Photonics*. New York: Wiley, 1991.

[174] E. T. Campbell, B. M. Terhal, and C. Vuillot. "Roads towards fault-tolerant universal quantum computation". *Nature* **549**, 172–179 (2017).

[175] D. Bluvstein et al. "A quantum processor based on coherent transport of entangled atom arrays". *Nature* **604**, 451–456 (2022).

[176] H. Häffner, C. F. Roos, and R. Blatt. "Quantum computing with trapped ions". *Physics Reports* **469**, 155–203 (2008).

[177] R. Ozeri. "The trapped-ion qubit tool box". *Contemporary Physics* **52**, 531–550 (2011).

[178] N. M. Linke et al. "Experimental comparison of two quantum computing architectures". *Proceedings of the National Academy of Sciences* **114**, 3305–3310 (2017).

[179] D. Kielpinski, C. Monroe, and D. J. Wineland. "Architecture for a large-scale ion-trap quantum computer". *Nature* **417**, 709–711 (2002).

[180] Negnevitsky, Vlad. *Feedback-stabilised quantum states in a mixed-species ion system*. PhD thesis. ETH Zurich, 2018.

[181] M. Ringbauer et al. "A universal qudit quantum processor with trapped ions". *Nature Physics* **18**, 1053–1057 (2022).

[182] C. Figgatt et al. "Parallel entangling operations on a universal ion-trap quantum computer". *Nature* **572**, 368–372 (2019).

[183] Á. Rivas and M. Müller. "Quantifying spatial correlations of general quantum dynamics". *New Journal of Physics* **17**, 062001 (2015).

[184] L. Postler et al. "Experimental quantification of spatial correlations in quantum dynamics". *Quantum* **2**, 90 (2018).

[185] A. K. Pal et al. "Relaxation times do not capture logical qubit dynamics". *Quantum* **6**, 632 (2022).

[186] J. Emerson, R. Alicki, and K. Życzkowski. "Scalable noise estimation with random unitary operators". *Journal of Optics B: Quantum and Semiclassical Optics* **7**, S347–S352 (2005).

[187] K. X. Wei et al. "Verifying multipartite entangled Greenberger-Horne-Zeilinger states via multiple quantum coherences". *Physical Review A* **101**, 032343 (2020).

[188] C. J. Ballance. *High-Fidelity Quantum Logic in Ca+*. Cham: Springer International Publishing, 2017.

[189] M. Li, M. Gutiérrez, S. E. David, A. Hernandez, and K. R. Brown. "Fault tolerance with bare ancillary qubits for a [[7,1,3]] code". *Physical Review A* **96**, 032341 (2017).

[190] D. M. Debroy, M. Li, S. Huang, and K. R. Brown. "Logical performance of 9 qubit compass codes in ion traps with crosstalk errors". *Quantum Science and Technology* **5**, 034002 (2020).

[191] B. Zhang. *Improving circuit performance in a trapped-ion quantum computer*. PhD thesis. Duke University, 2021.

[192] E. Hecht. *Optics*. Boston: Pearson, 2016.

[193] J. C. Wyant and K. Creath. "Basic Wavefront Aberration Theory for Optical Metrology". In: *Applied Optics and Optical Engineering, Volume XI*. Ed. by R. R. Shannon and J. C. Wyant. New York: Academic Press, 1992.

[194] C. F. Roos, M. Chwalla, K. Kim, M. Riebe, and R. Blatt. "'Designer atoms' for quantum metrology". *Nature* **443**, 316–319 (2006).

[195] S. J. Beale, J. J. Wallman, M. Gutiérrez, K. R. Brown, and R. Laflamme. "Quantum Error Correction Decoheres Noise". *Physical Review Letters* **121**, 190501 (2018).

[196] J. K. Iverson and J. Preskill. "Coherence in logical quantum channels". *New Journal of Physics* **22**, 073066 (2020).

[197] C. Ryan-Anderson. "PECOS: Performance estimator of codes on surfaces". https://github.com/PECOS-packages/PECOS. 2019.

[198] C. Ryan-Anderson. *Quantum algorithms, architecture, and error correction*. PhD thesis. The University of New Mexico, 2018.

[199] H. Bombin and M. A. Martin-Delgado. "Topological quantum error correction with optimal encoding rate". *Physical Review A* **73**, 062303 (2006).

[200] A. M. Steane. "Error Correcting Codes in Quantum Theory". *Physical Review Letters* **77**, 793–797 (1996).

[201] D. Amaro, M. Müller, and A. K. Pal. "Scalable characterization of localizable entanglement in noisy topological quantum codes". *New Journal of Physics* **22**, 053038 (2020).

[202] M. Sarovar et al. "Detecting crosstalk errors in quantum information processors". *Quantum* **4**, 321 (2020).

[203] R. Solovay. "Lie Groups and Quantum Circuits". Conference session. Mathematics of Quantum Computation. Berkeley, United States, 2000.

[204] A. Y. Kitaev. "Quantum computations: algorithms and error correction". *Russian Mathematical Surveys* **52**, 1191–1249 (1997).

[205] C. J. Trout et al. "Simulating the performance of a distance-3 surface code in a linear ion trap". *New Journal of Physics* **20**, 043038 (2018).

[206] M. Gutiérrez, M. Müller, and A. Bermúdez. "Transversality and lattice surgery: Exploring realistic routes toward coupled logical qubits with trapped-ion quantum processors". *Physical Review A* **99**, 022330 (2019).

[207] A. Katabarwa and M. R. Geller. "Logical error rate in the Pauli twirling approximation". *Scientific Reports* **5** (2015).

[208] M. Gutiérrez, C. Smith, L. Lulushi, S. Janardan, and K. R. Brown. "Errors and pseudothresholds for incoherent and coherent noise". *Physical Review A* **94**, 042338 (2016).

[209] A. S. Darmawan and D. Poulin. "Tensor-Network Simulations of the Surface Code under Realistic Noise". *Physical Review Letters* **119**, 040502 (2017).

[210] G. P. Wadsworth, J. G. Bryan, and A. C. Eringen. "Introduction to Probability and Random Variables". *Journal of Applied Mechanics* **28**, 319–319 (1961).

[211] N. Lang and H. P. Büchler. "Strictly local one-dimensional topological quantum error correction with symmetry-constrained cellular automata". *SciPost Physics* **4**, 007 (2018).

[212] C. Fang, Y. Wang, S. Huang, K. R. Brown, and J. Kim. "Crosstalk Suppression in Individually Addressed Two-Qubit Gates in a Trapped-Ion Quantum Computer". *Physical Review Letters* **129**, 240504 (2022).

[213] B. T. Torosov and N. V. Vitanov. "Narrowband composite two-qubit gates for crosstalk suppression". *Physical Review A* **107**, 032618 (2023).

[214] J. P. Clemens, S. Siddiqui, and J. Gea-Banacloche. "Quantum error correction against correlated noise". *Physical Review A* **69**, 062313 (2004).

[215] R. Klesse and S. Frank. "Quantum Error Correction in Spatially Correlated Quantum Noise". *Physical Review Letters* **95**, 230503 (2005).

[216] D. Aharonov, A. Kitaev, and J. Preskill. "Fault-Tolerant Quantum Computation with Long-Range Correlated Noise". *Physical Review Letters* **96**, 050504 (2006).

[217] E. Novais and H. U. Baranger. "Decoherence by Correlated Noise and Quantum Error Correction". *Physical Review Letters* **97**, 040501 (2006).

[218] E. Novais, E. R. Mucciolo, and H. U. Baranger. "Resilient Quantum Computation in Correlated Environments: A Quantum Phase Transition Perspective". *Physical Review Letters* **98**, 040501 (2007).

[219] E. Novais and E. R. Mucciolo. "Surface Code Threshold in the Presence of Correlated Errors". *Physical Review Letters* **110**, 010502 (2013).

[220] J. Preskill. "Sufficient condition on noise correlations for scalable quantum computing". *Quantum Information and Computation* **13**, 181–194 (2013).

[221] M.-D. Choi. "Completely positive linear maps on complex matrices". *Linear Algebra and its Applications* **10**, 285–290 (1975).

[222] A. Jamiołkowski. "Linear transformations which preserve trace and positive semidefiniteness of operators". *Reports on Mathematical Physics* **3**, 275–278 (1972).

[223] D. Nigg. *Towards fault tolerant quantum computation*. PhD thesis. Universität Innsbruck, 2016.

[224] M. Plenio and S. Virmani. "An introduction to entanglement measures". *Quantum Information and Computation* **7**, 1–51 (2007).

[225] K. Modi, A. Brodutch, H. Cable, T. Paterek, and V. Vedral. "The classical-quantum boundary for correlations: Discord and related measures". *Reviews of Modern Physics* **84**, 1655–1707 (2012).

[226] R. Horodecki, P. Horodecki, M. Horodecki, and K. Horodecki. "Quantum entanglement". *Reviews of Modern Physics* **81**, 865–942 (2009).

[227] R. H. Dicke. "Coherence in Spontaneous Radiation Processes". *Physical Review* **93**, 99–110 (1954).

[228] T. Monz et al. "14-Qubit Entanglement: Creation and Coherence". *Physical Review Letters* **106**, 130506 (2011).

[229] A. Crubellier, S. Liberman, D. Pavolini, and P. Pillet. "Superradiance and subradiance. I. Interatomic interference and symmetry properties in three-level systems". *Journal of Physics B: Atomic and Molecular Physics* **18**, 3811–3833 (1985).

[230] F. Caruso, A. W. Chin, A. Datta, S. F. Huelga, and M. B. Plenio. "Highly efficient energy excitation transfer in light-harvesting complexes: The fundamental role of noise-assisted transport". *The Journal of Chemical Physics* **131** (2009).

[231] P. Rebentrost, M. Mohseni, and A. Aspuru-Guzik. "Role of Quantum Coherence and Environmental Fluctuations in Chromophoric Energy Transport". *The Journal of Physical Chemistry B* **113**, 9942–9947 (2009).

[232] A. Nazir. "Correlation-Dependent Coherent to Incoherent Transitions in Resonant Energy Transfer Dynamics". *Physical Review Letters* **103**, 146404 (2009).

[233] P. Nalbach, J. Eckel, and M. Thorwart. "Quantum coherent biomolecular energy transfer with spatially correlated fluctuations". *New Journal of Physics* **12**, 065043 (2010).

[234] C. Olbrich, J. Strümpfer, K. Schulten, and U. Kleinekathöfer. "Quest for Spatially Correlated Fluctuations in the FMO Light-Harvesting Complex". *The Journal of Physical Chemistry B* **115**, 758–764 (2010).

[235] J. Jeske, Á. Rivas, M. H. Ahmed, M. A. Martin-Delgado, and J. H. Cole. "The effects of thermal and correlated noise on magnons in a quantum ferromagnet". *New Journal of Physics* **20**, 093017 (2018).

[236] S. Diehl et al. "Quantum states and phases in driven open quantum systems with cold atoms". *Nature Physics* **4**, 878–883 (2008).

[237] F. Verstraete, M. M. Wolf, and J. Ignacio Cirac. "Quantum computation and quantum-state engineering driven by dissipation". *Nature Physics* **5**, 633–636 (2009).

[238] B. Olmos, D. Yu, and I. Lesanovsky. "Steady-state properties of a driven atomic ensemble with nonlocal dissipation". *Physical Review A* **89**, 023616 (2014).

[239] T. E. Lee, C.-K. Chan, and S. F. Yelin. "Dissipative phase transitions: Independent versus collective decay and spin squeezing". *Physical Review A* **90**, 052109 (2014).

[240] P. Schindler et al. "Quantum simulation of dynamical maps with trapped ions". *Nature Physics* **9**, 361–367 (2013).

[241] J. Jeske, J. H. Cole, and S. F. Huelga. "Quantum metrology subject to spatially correlated Markovian noise: restoring the Heisenberg limit". *New Journal of Physics* **16**, 073039 (2014).

[242] D. A. Lidar and T. A. Brun, eds. *Quantum Error Correction*. Cambridge: Cambridge University Press, 2013.

[243] P. Zanardi and M. Rasetti. "Noiseless Quantum Codes". *Physical Review Letters* **79**, 3306–3309 (1997).

[244] D. A. Lidar, I. L. Chuang, and K. B. Whaley. "Decoherence-Free Subspaces for Quantum Computation". *Physical Review Letters* **81**, 2594–2597 (1998).

[245] D. A. Lidar, D. Bacon, J. Kempe, and K. B. Whaley. "Decoherence-free subspaces for multiple-qubit errors. II. Universal, fault-tolerant quantum computation". *Physical Review A* **63**, 022307 (2001).

[246] D. Kielpinski et al. "A Decoherence-Free Quantum Memory Using Trapped Ions". *Science* **291**, 1013–1015 (2001).

[247] H. Häffner et al. "Robust entanglement". *Applied Physics B* **81**, 151–153 (2005).

[248] F. G. S. L. Brandão and M. B. Plenio. "Entanglement theory and the second law of thermodynamics". *Nature Physics* **4**, 873–877 (2008).

[249] G. Gour and R. W. Spekkens. "The resource theory of quantum reference frames: manipulations and monotones". *New Journal of Physics* **10**, 033023 (2008).

[250] F. G. S. L. Brandão, M. Horodecki, J. Oppenheim, J. M. Renes, and R. W. Spekkens. "Resource Theory of Quantum States Out of Thermal Equilibrium". *Physical Review Letters* **111**, 250404 (2013).

[251] V. Veitch, S. A. Hamed Mousavian, D. Gottesman, and J. Emerson. "The resource theory of stabilizer quantum computation". *New Journal of Physics* **16**, 013009 (2014).

[252] T. Baumgratz, M. Cramer, and M. B. Plenio. "Quantifying Coherence". *Physical Review Letters* **113**, 140401 (2014).

[253] J. I. de Vicente. "On nonlocality as a resource theory and nonlocality measures". *Journal of Physics A: Mathematical and Theoretical* **47**, 424017 (2014).

[254] G. Gour, M. P. Müller, V. Narasimhachar, R. W. Spekkens, and N. Yunger Halpern. "The resource theory of informational nonequilibrium in thermodynamics". *Physics Reports* **583**, 1–58 (2015).

[255] T. Monz et al. "Realization of the Quantum Toffoli Gate with Trapped Ions". *Physical Review Letters* **102**, 040501 (2009).

[256] B. Schumacher and M. D. Westmoreland. "Relative entropy in quantum information theory". In: *Quantum computation and information*. Ed. by S. J. Lomonaco and H. E. Brandt. Contemporary Mathematics. Providence, RI: American Mathematical Society, 2002.

[257] M. Ježek, J. Fiurášek, and Z. Hradil. "Quantum inference of states and processes". *Physical Review A* **68**, 012305 (2003).

[258] V. Vedral. "The role of relative entropy in quantum information theory". *Reviews of Modern Physics* **74**, 197–234 (2002).

[259] C. F. Roos et al. "Bell States of Atoms with Ultralong Lifetimes and Their Tomographic State Analysis". *Physical Review Letters* **92**, 220402 (2004).

[260] T. Ruster et al. "Entanglement-Based dc Magnetometry with Separated Ions". *Physical Review X* **7**, 031050 (2017).

[261] A. R. Milne et al. "Phase-Modulated Entangling Gates Robust to Static and Time-Varying Errors". *Physical Review Applied* **13**, 024022 (2020).

[262] C. D. B. Bentley et al. "Numeric Optimization for Configurable, Parallel, Error-Robust Entangling Gates in Large Ion Registers". *Advanced Quantum Technologies* **3**, 2000044 (2020).

[263] C. Gidney. "Stim: a fast stabilizer circuit simulator". *Quantum* **5**, 497 (2021).

[264] A. Van Rynbach, A. Muhammad, A. C. Mehta, J. Hussmann, and J. Kim. "A Quantum Performance Simulator based on fidelity and fault-path counting". arXiv:1212.0845 (2012).

[265] M. Brownnutt, M. Kumph, P. Rabl, and R. Blatt. "Ion-trap measurements of electric-field noise near surfaces". *Reviews of Modern Physics* **87**, 1419–1482 (2015).

[266] S. Heußen et al. "Strategies for a practical advantage of fault-tolerant circuit design in noisy trapped-ion quantum computers". *Physical Review A* **107**, 042422 (2023).

[267] E. B. Wilson. "Probable Inference, the Law of Succession, and Statistical Inference". *Journal of the American Statistical Association* **22**, 209–212 (1927).

[268] Z. Hradil, J. Řeháček, J. Fiurášek, and M. Ježek. "Maximum-Likelihood Methods in Quantum Mechanics". In: *Quantum State Estimation*. Ed. by M. Paris and J. Řeháček. Berlin, Heidelberg: Springer Berlin Heidelberg, 2004.

[269] C. H. Bennett, D. P. DiVincenzo, J. A. Smolin, and W. K. Wootters. "Mixed-state entanglement and quantum error correction". *Physical Review A* **54**, 3824–3851 (1996).

[270] J. Emerson et al. "Symmetrized Characterization of Noisy Quantum Processes". *Science* **317**, 1893–1896 (2007).

[271] M. Silva, E. Magesan, D. W. Kribs, and J. Emerson. "Scalable protocol for identification of correctable codes". *Physical Review A* **78**, 012347 (2008).

[272] C. Dankert, R. Cleve, J. Emerson, and E. Livine. "Exact and approximate unitary 2-designs and their application to fidelity estimation". *Physical Review A* **80**, 012304 (2009).

[273] M. R. Geller and Z. Zhou. "Efficient error models for fault-tolerant architectures and the Pauli twirling approximation". *Physical Review A* **88**, 012314 (2013).

[274] F. Martínez-García et al. "Analytical and experimental study of center-line miscalibrations in Mølmer-Sørensen gates". *Physical Review A* **105**, 032437 (2022).

[275] Z. Chen. *Metrology of quantum control and measurement in superconducting qubits*. PhD thesis. University of California, Santa Barbara, 2018.

[276] C. H. Baldwin, K. Mayer, N. C. Brown, C. Ryan-Anderson, and D. Hayes. "Re-examining the quantum volume test: Ideal distributions, compiler optimizations, confidence intervals, and scalable resource estimations". *Quantum* **6**, 707 (2022).

[277] M. Riebe et al. "Deterministic quantum teleportation with atoms". *Nature* **429**, 734–737 (2004).